UNIVERSITÀ
DEGLI STUDI
DI PADOVA

Sede amministrativa: Università degli Studi di Padova
Dipartimento di Fisica e Astronomia

SCUOLA DI DOTTORATO DI RICERCA IN: ASTRONOMIA
CICLO XXVII

ELLIPSOIDAL COLLAPSE OF DARK MATTER HALOES IN COSMOLOGICAL SIMULATIONS

Direttore della scuola: Ch.mo Prof. Giampaolo Piotto
Supervisore: Ch.mo Prof. Giuseppe Tormen

Dottoranda: Giulia Despali

may you build a ladder to the stars
and climb on every rung
and may you stay
forever young

Contents

Abstract

Nowadays different observational campaigns agree on the standard cosmological model to explain and describe the formation and evolution of large scale structures in our Universe. In this scenario, almost 95% of the energy content of the Universe is in unknown forms of energy and matter, generally called dark energy and dark matter. The structures observed today are assumed to have grown gravitationally from small and initially Gaussian density fluctuations. As the universe expands, sufficiently overdense regions expand until they reach a maximum size and then collapse under the action of their own gravity: since dark matter is believed to be the dominant matter component of the universe, it leads the gravitational collapse process, forming structures called dark matter haloes. It is within the potential wells of these haloes that gas can shock, cool and eventually form stars and galaxies.

The main theoretical models on the gravitational collapse of dark matter haloes are the spherical collapse [24] and the ellipsoidal collapse (EC) [70] models. The former describes haloes as spherical overdense regions embedded in an uniform background, while the latter allows more possible shapes, defining haloes as homogeneous ellipsoids. Moreover, the ellipsoidal collapse model predicts that there is a direct connection between the evolution of an halo and the properties of the corresponding region in the initial conditions. Despite the fact that a triaxial modelling is obviously more realistic, the spherical approximation is still the most common choice.

In this work we analysed the results of several cosmological simulations (the GIF2 [20], Le SBARBINE - designed and run in Padova by our group - and the Millennium XXL [3] simulations), with the aim of study the triaxiality of dark matter haloes in detail. In particular, we developed a new halo finder, called “Ellipsoidal Overdensity Halo Finder” (EO), which identifies dark matter haloes as triaxial ellipsoids at all times, thus following the prescription of the EC model. Using its results, we studied the properties of protohaloes in the initial conditions and their evolution through the whole history of the Universe: this is crucial to understand the role of the initial density peaks, which are believed to be the seeds of all the observed structures. Our results help to understand the dynamics of halo collapse, confirming many predictions of the EC model, but also provide hints for a more realistic modelling.

As the issue of halo triaxiality is still not completely solved in theory and simulations, it started to be considered very recently in observational studies. Galaxy clusters are the largest virialized systems in the Universe and, following hierarchical clustering, also the last to form; almost 80% of their mass is attributed to dark matter, while the rest to baryons. The estimate of mass of clusters is still an open problem and the uncertainties are also related to the triaxiality of the haloes that surrounds them. For example, the estimated mass is on average biased to be lower than the true one, due to the fact that the haloes are embedded are typically prolate and so the spherical modelling is not able to capture their real structure. We studied the shape distributions of dark matter haloes at all times and for different cosmologies, using Le SBARBINE and the MXXL simulations. In this way, we derived some universal relations between the shape parameters and the mass of haloes, independent from the cosmological model and redshift. These results will be useful to generate mock halo catalogues

with given triaxial properties and can be used in triaxial mass reconstruction methods that require priors for the axial ratio distributions. Then, we concentrated on very massive haloes to provide more accurate predictions for cluster-size haloes.

Finally, we studied the halo mass function [52, 8, 60, 59] and tested its universality. With this purpose, we identified dark matter haloes at six different density thresholds (the virial one and other multiples of the background and the critical densities, which are commonly used in literature). Our results confirm the universality of the halo mass function, when measured with virialized haloes, while it does not hold for other halo identifications. We provide the fitting formulae for all the overdensity, believing that they could be useful for observers, and a method to rescale from one to the others.

This work is organised as follows: the first two Chapters give an overview of the standard cosmological model and of the principal theories of structure formation; Chapter 3 describes cosmological simulations (both the state of the art and the data used in this work); from Chapter 4 to Chapter 7, we present our results. In particular:

- Chapter 1 describes the current cosmological model and the standard theoretical model of structure formation:
- Chapter 2 focuses on the ellipsoidal collapse model for gravitational collapse, which is the starting point of this work; we describe the original formulation by White & Silk (1979,[70]) and the more recent works that developed the model;
- Chapter 3 discusses the state of the art of cosmological simulations and then presents our new set of six simulations (Le SBARBINE simulations), completed by our group during the last year, and finally the post-processing pipeline. This last includes the Ellipsoidal Overdensity Halo finder, developed in this work: it identifies triaxial dark matter haloes, making a comparison with the EC model easier and more straightforward;
- Chapter 4 adress the problem of halo triaxiality both from a numerical and an observational point of view: we use galaxy clusters - and in particular the mass estimate through strong gravitational lensing - as an example of the importance of taking triaxiality into account. Then we sum up the main findings on halo triaxiality obtained by previous works and show the results obtained with the EO finder, focusing on the differences between the spherical and ellipsoidal halo identification:
- Chapter 5 studies the evolution of dark matter protohaloes, from the initial conditions to the present time, in a direct comparison with the predictions of the EC model;
- Chapter 6 presents some universal distributions of the shape parameters, independent of redshift and cosmology, which may be used to obtain priors and estimates for observations and theoretical modelling;
- Chapter 7 adressed the universality of the halo mass function, testing its validity at many density thresholds and providing an accurate fitting formula.

The results presented in this thesis have been partially published in three papers:

1. Despali, Tormen & Sheth MNRAS 2013: “Ellipsoidal halo finders and implications for models of triaxial halo formation” [15]
2. Despali, Giocoli & Tormen MNRAS 2014: “Some like it triaxial: the universality of dark matter halo shapes and their evolution along the cosmic time” [14]

3. Bonamigo, Despali et al. MNRAS 2015: “The Universality of the Shape of Dark Matter Haloes over six decades in Mass: Insights from the Millennium XXL and Sbarbine Simulations” [7]

Sommario

Al giorno d'oggi molte campagne di osservazioni convergono su quale sia il modello cosmologico standard, che sia in grado di spiegare e descrivere la formazione e l'evoluzione delle strutture su grande scala nel nostro Universo. In questo scenario, circa il 95 % del contenuto energetico dell'Universo è sotto forma di materia ed energia oscura, ancora in parte sconosciute. Le strutture che formano l'Universo attuale si sono formate a partire da piccole fluttuazioni Gaussiane nel campo di densità iniziale e sono cresciute sotto l'azione della gravità. Durante l'espansione dell'universo, le regioni sufficientemente sovradense - dopo un periodo iniziale di espansione - collassano a causa della loro autogravità: la materia oscura, ritenuta la principale componente di materia nell'Universo, domina il processo di collasso gravitazionale formando strutture chiamate aloni di materia oscura. E' all'interno delle buche di potenziale create da questi aloni che il gas può subire processi di shock e condensazione, che portano alla formazione di stelle e galassie.

I principali modelli teorici di collasso gravitazionale per gli aloni di materia oscura sono il modello di collasso sferico [24] e di collasso ellissoidale [70]. Il primo considera gli aloni come regioni sferiche sovradense immerse in un background uniforme, mentre il secondo permette una descrizione più completa della forma dato che definisce gli aloni come ellissoidi triassiali e omogenei. Inoltre, secondo il modello del collasso ellissoidale, l'intera evoluzione di un alone dipende direttamente dalle sue proprietà iniziali. Nonostante il fatto che l'utilizzo di forme triassiali anzichè sferiche sia indubbiamente più realistico, queste ultime sono spesso le più utilizzate. In questo lavoro abbiamo analizzato i risultati di diverse simulazioni cosmologiche (le GIF2 [20], Le SBARBINE - prodotte a Padova dal nostro gruppo - e la Millennium XXL [3]), con lo scopo di studiare nel dettaglio la triassialità degli aloni di materia oscura. In particolare, abbiamo sviluppato un nuovo codice per l'identificazione degli aloni, chiamato “Ellipsoidal Halo Finder”, in grado di identificare gli aloni come ellissoidi triassiali ad ogni tempo, in linea con il modello teorico. In questo modo abbiamo studiato le proprietà dei proto-aloni alle condizioni iniziali delle simulazioni, e la loro evoluzione attraverso tutta la storia dell'Universo: questo tipo di analisi è cruciale per comprendere il ruolo dei picchi di densità iniziali, ritenuti i “semi” da cui si sono originate le strutture che osserviamo oggi. I nostri risultati aiutano a comprendere la dinamica del collasso, confermando molte predizioni del modello ellissoidale, ma forniscono anche la traccia per una modellizzazione più realistica.

Se per il caso delle simulazioni e dei modelli teorici, il problema della triassialità degli aloni non è del tutto risolto, in campo osservativo si è iniziato a considerarlo molto recentemente. Gli ammassi di galassie sono i più massicci sistemi del nostro Universo e quindi, seguendo il clustering gerarchico, anche quelli che si sono formati più recentemente; circa l'80% della loro massa è attribuita alla materia oscura e solo la restante percentuale alla componente barionica. La determinazione della massa degli ammassi è un problema ancora aperto, le cui incertezze sono legate anche alla triassialità degli aloni di materia oscura che li circondano. Per esempio, la massa stimata tende ad essere inferiore a quella reale, dal momento che gli aloni sono tipicamente prolati, e quindi una modellizzazione sferica non è in grado di descriverne la struttura con precisione. In questo lavoro abbiamo analizzato le

distribuzioni della forma degli aloni a tutti i tempi e per diverse cosmologie, usando la MXXL simulation e Le SBARBINE. In questo modo, abbiamo ricavato alcune relazioni universali tra i parametri che descrivono la forma di un alone e la massa, che risultano essere indipendenti dal modello cosmologico e dal redshift. Questi risultati possono essere utili per generare cataloghi simulati e possono essere inseriti nei metodi di ricostruzione della massa che richiedono delle distribuzioni a priori per i rapporti assiali. Abbiamo poi studiato nel dettaglio gli aloni di grande massa, per fornire predizioni più accurate nell'intervallo di massa degli ammassi di galassie.

Infine, abbiamo studiato la funzione di massa degli aloni [52, 8, 60, 59] e testato la sua universalità. Con questo scopo, abbiamo identificato gli aloni usando sei diverse soglie di densità (la sovradensità viriale e altri multipli della densità di background e della densità critica, che sono comunemente usati in letteratura). I nostri risultati confermano l'universalità della funzione di massa, se misurata per gli aloni virializzati; questa non si mantiene invece per le altre identificazioni. Presentiamo le formule di best fit per tutte le sovradensità, ritenendo che possano essere molto utili in campo osservativo, e un metodo per riscalare da una sovradensità all'altra.

Questa tesi è organizzata come segue: i primi due Capitoli danno una panoramica del modello cosmologico standard e delle principali teorie di formazione delle strutture; il Capitolo 3 descrive le simulazioni cosmologiche (sia lo stato dell'arte che, più in dettaglio, i dati usati in questo lavoro); nei Capitoli dal 4 al 7, presentiamo i risultati. In particolare:

- il Capitolo 1 descrive il modello cosmologico attuale e i modelli standard di formazione delle strutture;
- il Capitolo 2 si concentra sul modello di collasso ellissoidale (EC), che costituisce il punto di partenza di questo lavoro; presenta la formulazione originale di White & Silk [70] e i più recenti lavori che hanno ulteriormente sviluppato il modello:
- nel Capitolo 3 si discute lo stato dell'arte delle simulazioni cosmologiche e in seguito viene presentato il nostro nuovo set di sei simulazioni (Le SBARBINE simulations), completato dal nostro gruppo durante lo scorso anno; e infine la pipeline per il post-processing delle simulazioni. Quest'ultima include il codice Ellipsoidal Overdensity Halo Finder, sviluppato per questo lavoro;
- il Capitolo 4 illustra il problema della triassialità degli aloni, sia da un punto di vista numerico che osservativo: usiamo gli ammassi di galassie - e in particolare la stima della loro massa dall'effetto di strong gravitational lensing - come esempio dell'importanza del considerare la triassialità. Infine riassumiamo i principali risultati ottenuti da precedenti lavori e mostriamo le differenze che si ottengono identificando gli aloni come ellissoidi (usando il codice menzionato al punto precedente) o come sfere;
- nel Capitolo 5 studiamo l'evoluzione dei proto-aloni di materia oscura, dalle condizioni iniziali fino al tempo presente, confrontando i risultati con le predizioni del collasso ellissoidale:
- il Capitolo 6 presenta le distribuzioni universali dei parametri della forma, indipendenti da redshift e cosmologia, che possono essere usati come stime a priori per studi teorici e osservativi;
- il Capitolo 7 descrive l'universalità della funzione di massa degli aloni e ti test sulla sua validità a varie soglie di densità, fornendo una modellizzazione molto accurata.

I risultati presentati in questa tesi sono stati parzialmente pubblicati in tre articoli:

1. Despali, Tormen & Sheth MNRAS 2013: "Ellipsoidal halo finders and implications for models of triaxial halo formation" [15]

2. Despali, Giocoli & Tormen MNRAS 2014: “Some like it triaxial: the universality of dark matter halo shapes and their evolution along the cosmic time” [14]
3. Bonamigo, Despali et al. MNRAS 2015: “The Universality of the Shape of Dark Matter Haloes over six decades in Mass: Insights from the Millennium XXL and Sbarbine Simulations” [7]

Structure formation scenario 1

1.1 Standard cosmological model

Cosmology is a branch of science studying the origin and the evolution of the Universe; it is strictly related to theoretical physics and to other branches of astrophysics, as galaxy formation and evolution Modern cosmology is founded upon Einstein's theory of General Relativity and so cosmology adopts its own metric (the Robertson-Walker metric) to describe space-time. Yet, the GR formulation for the space-time of the Universe is quite simple, due to the common assumption of homogeneity and isotropy of the matter distribution, called *cosmological principle*. Observing the Universe on galactic and extragalactic scales we see that the matter is distributed in an irregular way, forming clumps of matter as galaxies and galaxy clusters. On the other hand, from observations on larger scales, we notice that the properties of the Universe are similar at any point and in any direction. This concept has been introduced for the first time by Albert Einstein to ensure a simple basic structure of the universe. The most important confirmation of the cosmological principle comes from the Cosmic Microwave Background (CMB), which was discovered by Penzias and Wilson in 1965 and has been measured with high precision by satellites as WMAP and Planck [48, 46]. The CMB, a trace of the early universe, is highly homogeneous: the temperature fluctuations have an amplitude $\leq 10^{-5}$. Figure 1.1 shows the all-sky measurements of the CMB done by Planck and, below, a stripe of the CMB superposed to the image of our own galaxy.

Robertson-Walker metric and Friedmann equations

The strongest force of nature on large scales is gravity, so Einstein's General Relativity, is the most important part of the physical description of the universe. While in Newton's theory gravitation is a force, in General Relativity it is considered ad a property of space-time:the geometry of space-time is determined by the matter-energy content of the Universe through the Einstein field equation

$$R_{\mu\nu} - \frac{1}{2} g_{\mu\nu} R - g_{\mu\nu}\Lambda = \frac{8\pi G}{c^4} T_{\mu\nu}. \tag{1.1}$$

$R_{\mu\nu}$ is the Ricci tensor, which describes the local curvature of space-time, R is the curvature scalar, $g_{\mu\nu}$ is the metric , $T_{\mu\nu}$ is the energy-momentum tensor and Λ the cosmological constant. The most general form of the space-time metric can be written as:

$$\mathrm{d}s^2 = g_{\mu\nu} \mathrm{d}x^\mu \mathrm{d}x^\nu \tag{1.2}$$

where repeated suffixes imply summation and μ, ν both run form 0 to 3; $x^0 = ct$ is the time coordinate and x^1, x^2, x^3 are space coordinates. In this equation, $\mathrm{d}s^2$ represent the space-time interval between two points labelled by x^μ and $x^\mu + dx^\mu$. If $\mathrm{d}s^2 > 0$, then the interval is timelike, if $\mathrm{d}s^2 < 0$ the interval

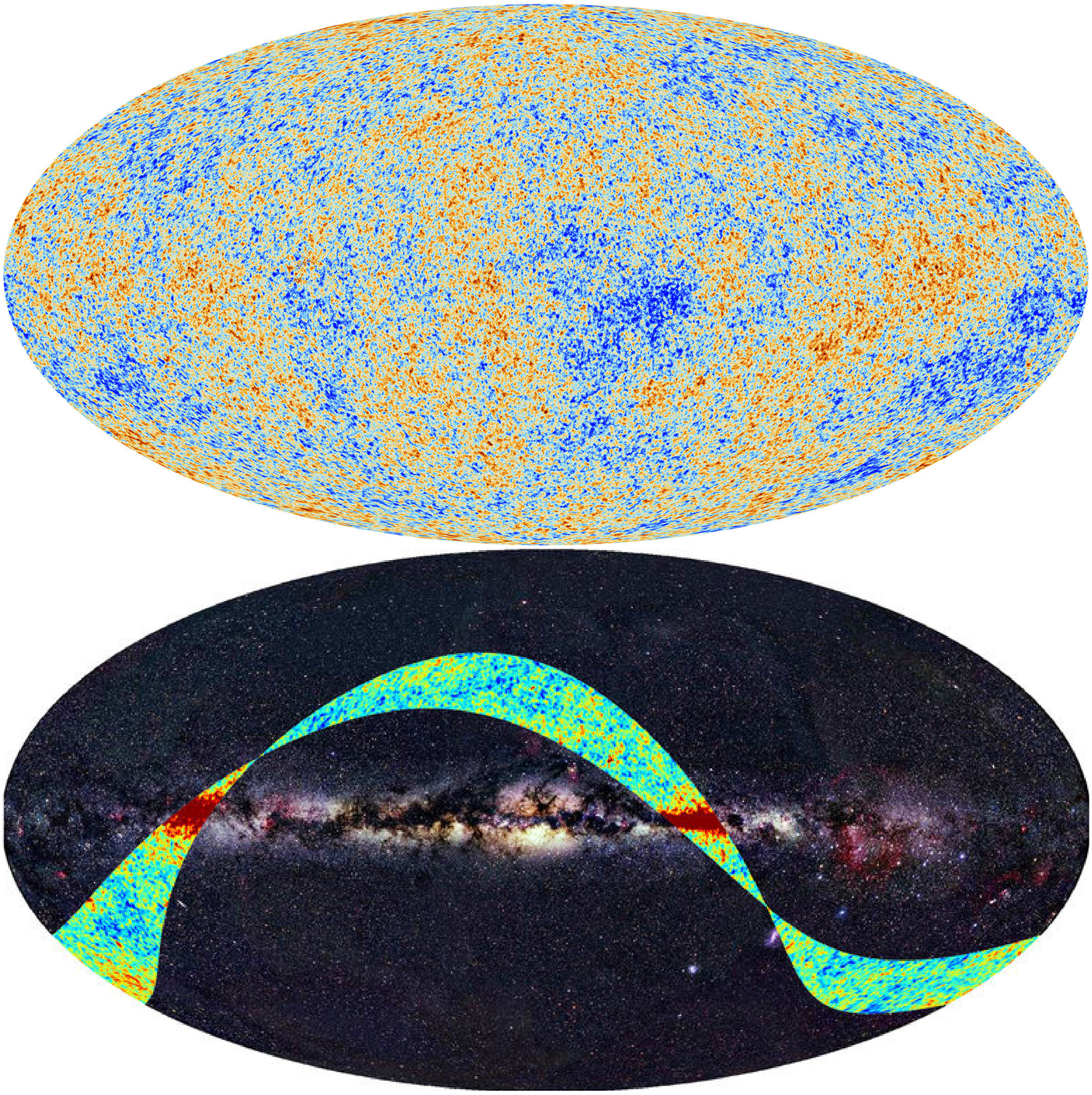

Figure 1.1: *Top*: All-sky CMB measurements from Planck. *Bottom*: First light measurements from Planck: a stripe of CMB superposed to out galaxy.

is spacelike and if $\mathrm{d}s^2 = 0$ the interval is lightlike, that means that the two points are connected by a light ray.

In our case we need the appropriate metric to describe the geometry of our universe, so we must construct a universe in which the cosmological principle holds. The first thing to do is investigating the geometry of a homogenueous and isotropic space; then we assume that we can consider the universe as a continuous fluid and assign to each fluid element the three spatial coordinates x^α and a time parameter (the proper time measured by a clock moving with the fluid element). The coordinates x^α are called *comoving coordinates.* It can be shown that the most general space-time metric describing a universe in wich the cosmological principle holds is, in spherical polar coordinates:

$$\boxed{\mathrm{d}s^2 = (c\mathrm{d}t)^2 - a(t)^2\left[\frac{\mathrm{d}r^2}{1-Kr^2} + r^2(\mathrm{d}\theta^2 + sin^2\theta\mathrm{d}\phi^2)\right]} \tag{1.3}$$

where r, θ and ϕ are the comoving coordinates, t is the proper time, $a(t)$ is the cosmic scale factor and K is the curvature parameter (which takes only the values 1, 0 or -1). This metric is called the *Robertson-Walker metric.* The curvature value $K = 0$ represents the Euclidean space, with its well known properties; for $K = 1$ we have a hypershpere, that is a closed space with finite volume, but no boundaries: this property allows us to make an analogy with the case of a sphere; finally, for $K = -1$ we have the hyperbolic space, open and infinite.

Thus, the geometry of an homogeneous and isotropic universe is described by the Robertson-Walker metric, which in turn is specified by the curvature and the expression for $a(t)$. For this, we need to solve the Einstein's equation, considering the case of a uniform ideal flluid with rest-mass energy density ρc^2 and pressure p. These solutions are called *Friedmann cosmological equations* and are:

$$\boxed{\begin{array}{l} \frac{\ddot{a}}{a} = -\frac{4}{3}\pi G\left(\rho + 3\frac{p}{c^2}\right) + \frac{\Lambda c^2}{3} \\[2ex] \left(\frac{\dot{a}}{a}\right)^2 = \frac{8}{3}\pi G\rho - Kc^2 + \frac{\Lambda c^2}{3}. \end{array}} \tag{1.4}$$

From the last equations we can obtain some important cosmological parameters. The first is the *critical density* which comes from the second Friedmann equation (neglecting the Λ term:

$$\rho_c = \frac{3}{8\pi G}\left(\frac{\dot{a}}{a}\right)^2 \tag{1.5}$$

Then, using ρ_c we can write the *demsity parameter* Ω as

$$\Omega(t) = \frac{\rho}{\rho_c} \tag{1.6}$$

The value of Ω depends on the curvature K:

- if $K = -1$ (closed space) then $\Omega > 1$
- if $K = 0$ (flat space) then $\Omega = 1$
- if $K = 1$ (open space) then $\Omega < 1$.

Recent measurements agree on the fact that $\Omega \simeq 1$ for our Universe, meaning that the geometry of space-time is flat. Moreover, the critical density of the Universe is estimated as $\rho_c \simeq 2.7710^{11} M_\odot h^{-1} Mpc^{-1}$, while the background density can be calculated as $\rho_b = \rho_c\Omega_m(z = 0)$.

The components of the Universe

In the current "standard cosmological model" the vast majority of the energy content of the universe is in unknown forms of matter and energy, commonly called "dark matter" and "dark energy". The first one - called "dark" for its property of not emitting any kind of radiation - has been first proposed by the swiss astronomer Fritz Zwicky in the 30s and is now used to explain a number of effects, which cannot be due to the presence of the sole ordinary baryonic matter: the high value of velocity dispersion in galaxy clusters, the rotation velocity curves of spiral galaxies, strong deflections due to gravitational lensing and so on. Apart from being "dark", the dark matter particles are thought to be very heavy and thus to move at quite low velocities. Nevertheless, the exact composition of dark matter is still unknown and it is widely studied in particle physics; one of the most favoured hypothesis comes from the model of supersymmetry, which would allow the existence of particles with the right properties, called WIMPs (Weakly Interacting Massive Particles). Dark energy comes from more recent theories and has been introduced as a cosmological-constant factor in the Friedmann equations. It is thought to be responsible of the accelerated expansion of the Universe and to be some form of vacuum energy, originated in the very first phases of our Universe. Dark energy constitutes the $70-75\%$ of the whole energy content fo the Universe, while dark matter the $20-30\%$, leaving a very small contribution to baryonic matter - even if this last actually builds up all the visible structures of the Universe.

For many years, the standard combination of values has been $\Omega_m = 0.3$, $\Omega_\Lambda = 0.7$ and $H_0 = 70 kms^{-1}Mpc^{-1}$. The Planck mission furnished the last estimate of the density of components of the universe:

$$\boxed{\begin{aligned} \Omega_m &= 0.315 \pm 0.016 \\ \Omega_\Lambda &= 0.665 \pm 0.016 \\ H_0 &= 67.3 \pm 1.2 kms^{-1}Mpc^{-1} \\ \Omega_b h^2 &= 0.02205 \pm 0.00028 \\ \sigma_8 &= 0.828 \pm 0.012 \\ age &= 13.817 \pm 0.048 Gyrs. \end{aligned}} \tag{1.7}$$

1.2 Standard scenario for cosmic structure formation

In the standard cosmological model, the Universe is assumed to be highly homogeneous at early times: the structures observed today are assumed to have grown from small initial density perturbations due to the action of gravity. In this scenario, structure formation involves the properties of the initial density perturbations and the evolution of these perturbation in the expanding universe. A full description of the growth of perturbations requires General Relativity, in particular if we want to consider perturbations larger than the cosmological horizon. We will start considering a simpler situation: Newtonian perturbation theory in the linear regime. This applies to structures smaller than the horizon size and with an overdensity $\delta << 1$ (so in the linear regime). The easier way to perform the calculations is to decompose the cosmological perturbations into Fourier modes; doing this, we find that some modes are amplified during the linear evolution while other are damped. The evolution therefore acts as a filter of the primordial density perturbations generated in the early universe.

In this model, dark matter leads structure formation, controlling the gravitational collapse process: gravitational instability makes the first systems collapse and reach an equilibrium, forming dark matter $haloes$. The formation of visible galaxies happens next, when the baryonic matter (that is, gas) feels the gravitational potential of dark matter haloes and falls in the potential wells: kinetic energy is transformed into termic energy by shock processes and adiabatic compression; the gas heats up, reaches the equilibrium temperature of the system and then looses heat by radiation and forms clouds and stars. This process is the starting point of galaxy formation, which continues until there is gas available in the interstellar medium.

In this Chapter we will first present the results of perturbation theory in the linear regime: (i) the simple case of a static universe, which does not describe our actual universe, but is useful to understand which scales determine the behaviour of perturbations: (ii) the model of an expanding universe and its components, which presents more complex and realistic solutions. Despite a certain degree of accuracy in the simple linear regime description, many objects in the present-day Universe, including galaxies and clusters, have densities orders of magnitude higher than the average density of the Universe. These objects are thus in the highly nonlinear regime, where $\delta >> 1$. To complete our description of structure formation in the Universe, we therefore need to go beyond perturbation growth in the linear regime. In general, nonlinear gravitational dynamic is difficult to deal with analytically, and so in many applications computer simulations have to be used to follow the evolution in detail. However, by making simple assumptions about the symmetry of the system, analytical models can be constructed: these will not give an accurate description of the true non-linear evolution, but will provide a valuable approximation to the complex processes involved. In particular, the Zel'dovich approximation [71] and the Spherical Collapse model [24] will be described in this Chapter. The next and more complicated model - the Ellipsoidal Collapse model [70] - will be described in more detail in the next Chapter, since it constitutes the starting point of this work.

1.3 The Jeans scale and a static universe

Perturbations do not collapse and form objects everywhere in the universe: it depends on the energy balance, because gravitation and kinetic energy (in the form of peculiar motions) always fight against each other. There is a scale separating the two regimes: the one in which gravity dominates leading the system to collapse and the one in which the kinetic energy wins against gravity. This is called the *Jeans scale*. To explain how we find the Jeans scale definition, we consider an uniform fluid, presenting small density fluctuations on every scale; then we choose a certain spherical region (with radius R, mass M and density ρ) in which dark matter is overdense compared with the background. The fluid description is valid as long as the mean free path of the particles is much smaller than the scale of interest: this applies to a baryonic gas and also to a pressureless dust, as dark matter.

As we already said, gravity between particles tries to compress the region, while peculiar motions of particles tend to move each particle away from the others; if these last dominate the region expands and the overdensity is reduced. The gravitational and the kinetic energy of the overdense spherical region are:

$$E_g \simeq -\frac{GM^2}{R} \simeq -\frac{GM}{R} \simeq -GM\rho R^2 \tag{1.8}$$

$$E_k \simeq \frac{Mv^2}{2} \tag{1.9}$$

and so, using the total energy at equilibrium and energy conservation, we get

$$E = E_g + E_k = 0 \qquad \rightarrow \qquad E_k = -E_g \qquad \rightarrow \qquad \frac{v^2}{2} = G\rho R^2. \tag{1.10}$$

Inverting the last equation, we find the *Jeans radius*

$$\boxed{R_J = v\sqrt{\frac{1}{2G\rho}}}. \tag{1.11}$$

R_J separates two regimes:

- if $R > R_J$, the right side of equation 2.3 dominates: gravity wins and the pertubation collapses due to its own gravity;

- if $R < R_J$, the left side of equation 2.3 dominates: kinetic energy wins and the pertubation is disperded.

In the standard cosmological model we have a ΛCDM universe. We should use this model to solve the conservation equations , but if we need only a qualitative solution for the Jeans scale we can start from the simplest model: a static universe. We consider the matter of the universe as a perfect fluid and so the quantities required to fully describe it are: density, velocity, pressure, entrophy and the gravitational potential. Then, we need the following conservation equations:

- the continuity equation, expressing the mass conservation:

$$\frac{\partial \rho}{\partial t} + \nabla \cdot (\rho v) = \frac{\mathrm{D}\rho}{\mathrm{D}t} + \rho \nabla \cdot v = 0; \tag{1.12}$$

- the Euler equation, showing the momentum conservation

$$\frac{\partial v}{\partial t} + (v \cdot \nabla) v = \frac{\mathrm{D}v}{\mathrm{D}t} = -\frac{1}{\rho}\nabla p - \nabla \phi; \tag{1.13}$$

- the Poisson equation, which relates the gravitational field to its source

$$\nabla^2 \phi = 4\pi G \rho; \tag{1.14}$$

- the state equation of the fluid

$$p = p(\rho, S); \tag{1.15}$$

In all the equations $\mathrm{D}/\mathrm{D}t$ stands for the lagrangian derivative, that is the time derivative as a quantity moves with the fluid:

$$\frac{\mathrm{D}w}{\mathrm{D}t} = \left.\frac{\partial w}{\partial t}\right\|_r + \frac{\partial w}{\partial r}\frac{\partial r}{\partial t} = \left.\frac{\partial w}{\partial t}\right\|_r + (u \cdot \nabla) w \qquad . \tag{1.16}$$

This description, based on the assumption that the matter content of the universe is a non-relativistic fluid, could also be extended to cases where the universe contains a smooth background of relativistic particles or vacuum energy; in such a case, both the continuity and the Euler equations would mantain the same form, while we should add the new density terms in the Poisson equation.

Considering the simple case of adiabatic and isoentropic systems (which imply $\mathrm{d}S/\mathrm{d}t = 0$), we remain with only four equations and the state equation reduces to $p = p(\rho)$. The unperturbed equations of motion in such a static universe are

$$\left\{ \begin{array}{c} \rho = \rho_b = const \\ p = p_b = const \\ v = 0 \\ \phi = \phi_b = const \\ S = const. \end{array} \right. \tag{1.17}$$

This solution, representing a perfectly static, homogeneous and isotropic universe, is physically inconsistent: the presence of a constant potential ϕ_b implies $\nabla^2\phi = 0$, and this does not agree with $\rho \neq 0$. However, this approximation is useful to study what happens to a simple model when introducing small perturbations. Perturbing the previous system we have

$$\left\{ \begin{array}{c} \rho = \rho_b(1+\delta) = \rho_b + \delta\rho \\ p = p_b + \delta p \\ v = \delta v \\ \phi = \phi_b + \delta\phi \end{array} \right.$$

(1.18)

where the density fluctuation (assumed $\delta << 1$) is defined as

$$\delta = \delta(r,t) = \frac{\rho(r,t) - \rho_b}{\rho_b} = \frac{\delta\rho(r,t)}{\rho_b}. \tag{1.19}$$

We insert these values in the conservation equations, linearize them and remove the unperturbed terms; what we obtain at the end is a new formulation of the conservation equations, which describes the perturbation evolution:

- continuity equation:
$$\frac{\partial\delta\rho}{\partial t} + \rho_b \nabla\delta v = 0 \tag{1.20}$$
- Euler equation:
$$\frac{\partial\delta v}{\partial t} = -\frac{v_s^2}{\rho_b}\nabla\delta\rho - \nabla\delta\phi \tag{1.21}$$
- Poisson equation:
$$\nabla^2\delta\phi = 4\pi G\delta\rho \tag{1.22}$$

The easiest way to solve this system is switching to the Fourier space and writing each perturbation w as a plane wave

$$\delta w(r,t) = \delta w_k \exp(i\vec{k}\cdot\vec{r} + i\omega t) \tag{1.23}$$

where $k = 2\pi/\lambda$ is the wave number, determining the wavelenght of the oscillation, $\omega = 2\pi\nu$ is the frequence and w_k the amplitue of the plane wave. The final result is

$$\boxed{\omega^2 = k^2 v_s^2 - 4\pi G\rho_b} \tag{1.24}$$

in which we can distinguish the two regimes separated by the jeans scale: $\omega^2 < 0$ and $\omega^2 > 0$. The value $\omega^2 = 0$ defines the *Jeans wave number* k_J and the *Jeans wavelenght* λ_J:

$$\omega^2 = 0 \qquad \rightarrow \qquad k_J^2 = \frac{4\pi G\rho_b}{v_s^2} \tag{1.25}$$

and so

$$k_J = \sqrt{\frac{4\pi G\rho_b}{v_s^2}} \quad , \quad \lambda_J = \frac{2\pi}{k_J} = v_s\sqrt{\frac{\pi}{G\rho_b}} \quad . \tag{1.26}$$

To understand what happens in the two situations, it is useful to rewrite ω as

$$\omega^2 = k^2 v_s^2 \left[1 - \frac{4\pi G\rho_b}{k^2 v_s^2}\right] = k^2 v_s^2 \left[1 - \left(\frac{\lambda}{\lambda_J}\right)^2\right]. \tag{1.27}$$

Now, if $\lambda < \lambda_J$, $\omega^2 > 0$ and so ω has the real value

$$\omega = \pm k v_s \left[1 - \left(\frac{\lambda}{\lambda_J}\right)^2\right]^{1/2} . \tag{1.28}$$

In this case $\delta\rho$ is represented by a couple of progressive sound waves, of amplidude $\delta\rho_k = const$, moving in the directions $\pm k$. In the limit $\lambda \rightarrow 0$ the propagation velocity of the wave tends to the sound propagation velocity of the fluid, and so the wave tends to a pure sound wave. On the other hand, when $\lambda \to \lambda_J$ the propagation velocity tends to zero and we have a stationary wave. If $\lambda > \lambda_J$, $\omega^2 < 0$ and ω is imaginary

$$\omega = \pm i(4\pi G\rho_b)^{1/2}\left[1-\left(\frac{\lambda_J}{\lambda}\right)^2\right]^{1/2}. \tag{1.29}$$

This time the wave is stationary, because only the real part of a wave has a physical meaning, and this makes the amplitude grow exponentially with time because

$$\delta\rho(r,t) = \delta\rho_k \exp(\pm\|\omega\| t) exp(ik \cdot r). \tag{1.30}$$

We have **gravitational instability**.

1.4 Expanding universe

Important scales and epochs

Obviously, as Edwin Hubble first noticed, our universe is expanding; so we must generalize the results of a static universe to the case of an expanding universe, in particular ΛCDM. This implies the introduction of two new important scales, apart from the Jeans scale λ_J: the *cosmological horizon* $R_H(t)$ and the *dissipation scale* λ_D. The first is defined as

$$R_H(t) = a(t)\int_0^t \frac{c\mathrm{d}t'}{a(t')} = a(t)\int_0^t c\tau \tag{1.31}$$

where $\mathrm{d}\tau = \mathrm{d}t/a(t)$ is the conformal time, that is, a time scale independent of the expansion of the universe. On scales $\lambda > R_H$ acts only gravity, because the points outside the horizon are too far to be causally connected to the observer. The dissipation scale separates scales $\lambda_D < \lambda < \lambda_J$, in which perturbations propagate as sound waves, from scales $\lambda < \lambda_D$, where a wave is calcelled by irreversible processes.

In this model the relevant epochs are those in which the universe, or one of its components, switch from a relativistic regime to a non-relativistic regime: one example is the equivalence moment t_{eq} which separates radiation and matter dominated epochs.

An approximate solution for $\lambda > R_H$

As we said, gravity dominates on scales $\lambda > R_H$ and so in these regions we can use the Friedmann equations, which are relativistic (so we can apply them in every epoch and on every scale, regarding that gravity dominates). We consider a perturbation as a denser universe contained in another less dense universe: the perturbation will be a sphere whith radius $\lambda > R_H$ and mean density $\rho > \rho_{cr}$, embedded in an unperturbed Eistein-de Sitter universe. The Friedmann equations for these two universes are:

$$H^2_{pert} = \frac{8\pi G}{3}\rho_{pert} - \frac{c^2}{a^2} \tag{1.32}$$

$$H^2_b = \frac{8\pi G}{3}\rho_b. \tag{1.33}$$

Choosing the moment in which $H_{pert} == H_b$ we can rewrite the system as

$$\frac{8\pi G}{3}\rho_{pert} - \frac{c^2}{a^2} = \frac{8\pi G}{3}\rho_b \qquad \to \qquad \rho_{pert} - \rho_b = \frac{3c^2}{8\pi G a^2} \tag{1.34}$$

from which, defining as usual $\delta(t) = (\rho_{pert} - \rho_b)/\rho_b$, we have the solution

$$\delta(t) = \frac{3c^2}{8\pi G\rho_b a^2} \quad . \tag{1.35}$$

The evolution of the perturbation in different epochs can be obtained knowing that the equation of state has the form $p = w\rho c^2$ (from which $\rho_b \propto a^{-3(1+w)}$). This implies, for the perturbation:

$$\delta(t) \propto a^{3(1+w)-2} \propto a^{1+3w}. \tag{1.36}$$

On scales larger than the cosmological horizon, perturbations of all the components are coupled to the ones of the dominant component, which is radiation for $t < t_{eq}$ and dark matter for $t > t_{eq}$, and so:

1. for $t < t_{eq}$

$$\rho \simeq \rho_{rad} \quad \rightarrow \quad w = \frac{1}{3} \quad \rightarrow \tag{1.37}$$

$$\delta(t) \simeq \delta_R(t) \propto a^2 \propto t \quad \rightarrow \quad a \propto t^{1/2} \tag{1.38}$$

2. for $t > t_{eq}$

$$\rho \simeq \rho_M \quad \rightarrow \quad w = 0 \quad \rightarrow \tag{1.39}$$

$$\delta(t) \simeq \delta_{DM}(t) \propto a \propto t^{2/3} \tag{1.40}$$

On the contrary, on scales smaller than the horizon, but larger than the Jeans scale, perturbations of non-dominant components behave in a different way, depending on the interaction between them and the dominant component. For example, until recombination, baryon fluctuations are coupled to the radiation ones (because the hydrogen ions are coupled to electrons by Coulombian forces and these are coupled to radiation by Thomson scattering); then, after recombination, baryons follow the gravity of dark matter.

Newtonian equations

A complete and precise description on the evolution of the universe (in the expanding model) requires General Relativity; there are, as we said, some spatial and temporal regimes in which Newtonian Gravity, which simplifies the calculations, is enough: if we consider non relativistic perturbations, only on scales $\lambda < R_H$.

We decide to call $\vec{r}$ the spatial coordinate in the physical reference frame and $\vec{x}$ the coordinate in the comoving system; they are related by the equation $\vec{r} = a\vec{x}$. The velocity $\vec{u}$ of an element of fluid is formed by two terms: $H\vec{r}$ is the velocity caused by the universe expansion, while $\vec{v}$ is the peculiar velocity, due to gravitational attraction of the matter:

$$\frac{\mathrm{d}\vec{r}}{\mathrm{d}t} = \dot{a}\vec{x} + a\dot{\vec{x}} = H\vec{r} + \vec{v} = \vec{u}. \tag{1.41}$$

Knowing this, the fluid equation in the physical reference frame can be written as:

$$\left.\frac{\partial \rho}{\partial t}\right\|_r + \vec{\nabla}_r(\rho\vec{u}) = 0 \qquad \text{Continuity} \qquad \text{equation} \tag{1.42}$$

$$\frac{\mathrm{D}\vec{u}}{\mathrm{D}t} = \left.\frac{\partial \vec{u}}{\partial t}\right\|_r + (\vec{u}\,.\,\vec{\nabla}_r)\vec{u} = -\frac{1}{\rho}\vec{\nabla}_r p - \vec{\nabla}_r\Phi \qquad \text{Euler} \qquad \text{equation} \tag{1.43}$$

$$\nabla_r^2\Phi = 4\pi G\rho \qquad \text{Posso}n \qquad \text{equation} \tag{1.44}$$

Matter universe, inside the horizon

The first case that we consider is the solution for the matter component, and for $\lambda < R_H$. As done for the static universe, the fluid equations must be perturbed and then the solution for $\delta(t)$ is found by switching to the Fourier space ; since we are interested in the solutions for the density field, we must assume that the rotational part of velocity is not coupled with δ and decays: we remain with an irrotational field, which is linear. This expresses the conservation of the angular momentum in an expanding universe. At the end of the calculations we find a single equation for the change of δ, which is

$$\boxed{\ddot{\delta}_k + 2\frac{\dot{a}}{a}\dot{\delta}_k + \delta_k\left[\frac{k^2 v_s^2}{a^2} - 4\pi G\rho_b\right] = 0}. \tag{1.45}$$

The second term is the Hubble drag term, which tends to suppress perturbation growth due to the expansion of the universe; the sign of the third term, which contains the gravitation and pressure contributions, determines which kind of solution we have. The change of δ, of course, depends on the value of Ω and so on the kind of universe that we consider. The general solution, which considers any possible value of Ω, is

$$\delta_+(z) = \frac{H_0}{a_0^2}(1+z)(1+\Omega_0 z)^{1/2}\int_z^\infty \frac{dz(1+z)}{H_0^3(1+z)^3(1+\Omega_0 z)^{3/2}} \tag{1.46}$$

which holds for $t > t_{eq}$ and $\lambda > \lambda_J$. δ_+ indicates the growing mode, since we are not interested in the decaying solutions. The last equation always admits an analytical solution, but in general the solutions can be distinguished in three possible behaviours, corresponding to the most common choices for Ω:

1. $\Omega_0 = 1$: the solution for a flat universe is

$$\delta_+(z) = (1+z)^{3/2}\int_z^\infty \frac{dz}{(1+z)^{7/2}} \propto (1+z)^{-1} \propto t^{2/3} \tag{1.47}$$

2. $\Omega_0 < 1$: for an open universe we have

$$\delta_+(z) = 1 + \frac{3}{x} + \frac{3(1+x)^{1/2}}{x^{3/2}}\ln\left[(1+x)^{1/2} - x^{1/2}\right] \qquad x = \left\|\Omega^{-1}(z) - 1\right\| ; \tag{1.48}$$

3. $\Omega_0 > 1$: the last case is the close universe, for which

$$\delta_+(z) = -1 + \frac{3}{x} - \frac{3(1-x)^{1/2}}{x^{3/2}}\tan^{-1}\left[\left(\frac{x}{1-x}\right)^{1/2}\right] \qquad 0<\theta<\pi \tag{1.49}$$

$$\delta_+(z) = -1 + \frac{3}{x} - \frac{3(1-x)^{1/2}}{x^{3/2}}\left\{\tan^{-1}\left[\left(\frac{x}{1-x}\right)^{1/2}\right] - \pi\right\} \qquad \pi<\theta<2\pi \quad . \tag{1.50}$$

Considering a flat Einstein-de Sitter universe we can easly understand from where these results come from and what is their physical meaning: of course the results are different for the other universes, but the general meaning and the length scales involved remain the same. The calculations are particularly simple, because $\Omega = 1$ and we can substitute in the equations:

$$\rho_b(t) = \frac{1}{6\pi G t^2} \tag{1.51}$$

$$a(t) = a_0\left[\frac{3H_0 t}{2}\right]^{2/3} \tag{1.52}$$

with $a \propto t^{2/3}$. Equation 1.45 can be rewritten as

$$\ddot{\delta}_k + \frac{4}{3t}\dot{\delta}_k + \frac{2}{3t^2}\delta_k\left(\frac{k^2 v_s^2}{4\pi G\rho_b} - 1\right) = 0 \tag{1.53}$$

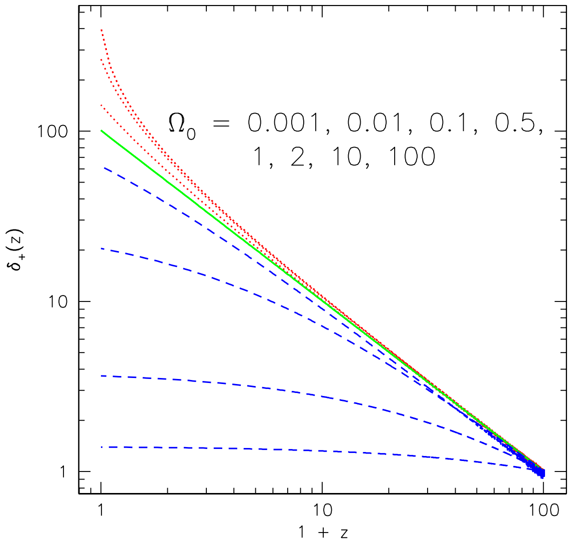

Figure 1.2: Growth of fluctuations in matter-dominated universes, for different values of Ω. The green line represents the $\Omega = 1$ solution, the dashed blue lines the $\Omega < 1$ solutions and the dotted red lines the $\Omega > 1$.

This equation admits a power-law solution for the fluctuation: $\delta \propto t^{\alpha}$. We substitute this solution, and its derivatives, in the equation and solve for α; for $\lambda < \lambda_J$ the solutions are imaginary and correpond to progressive sound waves, while for $\lambda > \lambda_J$ the solutions are real and gravitational instability takes place. In the limit of scales in which pressure in negligible with respect to gravity ($\lambda >> \lambda_J$), the solution is much simpler and goes like

$$\delta_{\pm}(\vec{x}, t) \propto \exp(i\vec{k} \cdot \vec{x})\, t^{-(1\pm5)/6}. \tag{1.54}$$

This tells us that one solution is growing with time, while the other is decaying. As we already said, the interesting one is the growing solution, which determines the growth of perturbations:

$$\delta_{k,+}(t) \propto t^{2/3} \propto a. \tag{1.55}$$

This result holds for any matter-dominated universe, so both for baryons and dark matter. The only difference is the interpretation of the sound speed term: for baryons this is the actual sound speed, while for dark matter, which is non-collisional, this term gives an estimate of the typical velocity dispersion σ_v which acts against gravity.

Going back to the general solution, and looking at Figure 3.1, we can characterize the evolution of universes with different Ω with respect to the flat Einstein-de Sitter universe:

1. Ω=**1** : perturbations in an expanding flat universe have a linear growth. If if was static, the growth would have been exponential, but the underneath expansion of the universe slows it down.

2. Ω >**1** : the growth of perturbations is faster, because this universe contains more matter, which contributes to decelerate the expansion

3. Ω <**1** : contrary to the previous case, perturbations grow slower in an open universe, because the expansion tends to dissipate them.

Dark matter: stagnation effect and free streaming

Before equivalence, so in the radiation dominated epoch, also dark matter behaves in a very peculiar way: dark matter perturbations almost don't grow. Considering all the universe components together and solving the $\ddot{\delta}$ Equation 1.45, we find

$$\delta_{k,DM,+}(a < a_{eq}) \propto 1 + \frac{3}{2}\frac{a}{a_{eq}}. \tag{1.56}$$

The total growth of the perturbations from the entrance in the horizon a_H to the equivalence is given by

$$\boxed{\frac{\delta(a_{eq})}{\delta(a_H)} = \frac{1+3/2}{1+3a_h/2a_{eq}} \leq \frac{5}{2}} \tag{1.57}$$

which is exactly 5/2 when $a_H \to 0$. This shows that dark matter fluctuation almost don't grow before equivalence (and inside the horizon). Physically, this happens because, before equivalence, the expansion time scale is shorter than the gravitational free-fall time scale: this last is $t_{ff} \sim \sqrt{1/G\rho_{DM}(t)}$, while the expansion time comes from

$$\rho(t) \sim \rho_R(t) = \frac{3}{32\pi G t^2} \sim \frac{1}{Gt^2} \qquad \to \qquad t_H \sim \sqrt{(}1/G\rho_R). \tag{1.58}$$

Knowing that, before equivalence, $\rho_R > \rho_{DM}$, we have $t_{ff} > t_H$; this means that dark matter perturbation do not manage to grow in an Hubble time: this is called stagnation effect or Meszaros effect (Meszaros,1974).

Since the universe is not an ideal fluid, we can oberve some dissipation phenomena, in particular on small scales: the dissipation for dark matter is called free streaming. Particles of dark matter move from overdense regions to underdense regions, smoothing the perturbations: after decoupling from radiation, dark matter particles move influenced only by the mean gravitational field and not by the local field; moving in this way they destroy the perturbations which are smaller than the scale that they cover in a time interval Δt. The definition of the free streaming scale is similar to the one of the cosmological horizon, and is:

$$\lambda_{FS}(t) = a(t) \int_0^t \frac{v(t^{'})}{a(t^{'})} dt^{'}. \tag{1.59}$$

The free streaming mass is then defined as $M_{FS} \propto \lambda_{FS}^3 \rho_{DM}$. For dark matter, the Jeans scale and the free streaming scale are determined by the same physical process, that is particles diffusion, and so they both depend on the mean particle velocity. There is, however, a difference: the first is found, at every t, by the $\ddot{\delta}$ Equation 1.45, while the second is defined by the distance covered by the particles from $t = 0$ to t, which is more physical. This means that, while M_J can decrease with time, M_{FS} can only increase, or remain constant.

In the Cold Dark Matter model, the maximum value of the Jeans mass is negligible ($M_J(a_{eq}) \sim 10^{-6} M_\odot$): this means that all the perturbation which are interesting for cosmology are able to grow.

Baryons behaviour

After recombination, baryons are decoupled from radiation: their behaviour will from now on be influenced by dark matter gravity. For baryons, the solution is $\delta_B \propto a$, and in particular δ_B is in some way proportional to δ_{DM}:

$$\delta_B(a) = \delta_{DM}(1 - a_{dec}/a). \tag{1.60}$$

This means that, after recombination and decoupling, δ_B has a period of accelerated growth, because baryons are subjected to the gravitational attraction of dark matter; soon the baryon's growth slows down to follow the normal dark matter growth. This is called baryon *catch up*.

1.5 Zel'dovich approximation

Zel'dovich (1970) [71] provided an approximate solution to the problem of perturbations growth, which is correct even if the perturbations are not small. The calculation mixes linear and non-linear elements, allowing to describe the growth of perturbations also in the non-linear regime (and in particular until they become strongly non linear): we use non-linear equations, but we assume that the acceleration in the Euler equation remains the linear one, derived from the Poisson equation.

Given that all fluctuations were small at early times, it is reasonable to assume that at more recent epochs only the growing mode has a significant amplitude. From linear theory, the evolution can be written as:

$$\delta(\mathbf{x}, a) = D(a)\delta_0(\mathbf{x}) \tag{1.61}$$

where $\delta_0(\mathbf{x})$ is the density perturbation at some initial time t_0 and $D(a)$ is normalized such that $D(a_0) = 1$. Thus the density field grows self-similarly with time. The same is also true both for the gravitational acceleration and the peculiar velocity, this can be seen by substituting the last expression for δ into the Poisson equation:

$$\nabla^2\Phi(\mathbf{x}, a) = 4\pi G\bar{\rho}a^2\delta = 4\pi G\bar{\rho}a^2 D(a)\delta_0(\mathbf{x}) \qquad \rightarrow \qquad \Phi(\mathbf{x}, a) = \frac{D(a)}{a}\Phi_0(\mathbf{x}) \tag{1.62}$$

where $\nabla^2\Phi_0(\mathbf{x}) = 4\pi G\bar{\rho}a^3\delta_0(\mathbf{x})$. In an Einstein-de Sitter universe, where $D \propto a$ this implies that Φ is independent of a, and so of time. We find Φ also in the definition of the Euler equation (perturbed and linearized):

$$\dot{\mathbf{v}} + \frac{\dot{a}}{a}\mathbf{v} = -\frac{\nabla\Phi}{a}. \tag{1.63}$$

This can be integrated for fixed $\mathbf{x}$ to give

$$\mathbf{v} = -\frac{\nabla\Phi_0}{a}\int\frac{D}{a}\mathrm{d}t. \tag{1.64}$$

By definition, $D(a)$ satisfies the already seen fluctuation growth equation:

$$\ddot{\delta} + \frac{2\dot{a}}{a}\dot{\delta} = 4\pi G\bar{\rho}\delta. \tag{1.65}$$

Knowing this we can write the Euler equation in a different way:

$$\int\frac{D}{a}\mathrm{d}t = \frac{\dot{D}}{4\pi G\bar{\rho}a} \qquad \rightarrow \qquad \mathbf{v} = -\frac{\dot{D}}{4\pi G\bar{\rho}a^2}\nabla\Phi_0(\mathbf{x}) = -\frac{1}{4\pi G\bar{\rho}}\frac{\dot{D}}{D}\nabla\Phi_0(\mathbf{x}). \tag{1.66}$$

We can see that the peculiar velocity is poportional to the current gravitational acceleration. Since $\mathbf{v} = a\dot{\mathbf{x}}$, integrating another time gives us the solution for $\mathbf{x}$:

$$\mathbf{x} = \mathbf{x_0} - \frac{D(a)}{4\pi G\bar{\rho}a^3}\nabla\Phi_0(\mathbf{x_0}) \tag{1.67}$$

This reformulation of linear perturbation theory is due to Zel'dovich (1970) [71]. It is a Lagrangian description that specifies the growth of structures by giving the displacement $\mathbf{x} - \mathbf{x_0}$ and the peculiar velocity $\mathbf{v}$ for each mass element in terms of the initial position. As we mentioned, Zel'dovich suggested that this formulation could be used to extrapolate the evolution of structures up to the regime $\delta \sim 1$: this procedure is known as the *Zel'dovich approximation*. Assuming that the acceleration remains the linear one, particle's trajectories are straight lines, with the distance travelled proportional to D. This can be seen also in Equation (4.8), where the position $\mathbf{x}$ at a certain time t is determined by the initial position $\mathbf{x_0}$, then by a second term which expresses the displacement: $\nabla\Phi$ determines the direction of the displacement and D its absolute value.

The solution for the density field can be found by calculating the deformation tensor and its eigenvalues $\lambda_1 \geq \lambda_2 \geq \lambda_3$: this means that we calculate the derivatives of the physical coordinate $\mathbf{r} = a\mathbf{x}$ with respect to the comoving coordinate $\mathbf{x}$, getting

$$\frac{\partial\mathbf{r_i}}{\partial\mathbf{x_k}} = \frac{\partial}{\partial\mathbf{x_k}}(a\mathbf{x}) = a - aD\partial_j\partial_k(\Phi_0/4\pi G\bar{\rho}a^3). \tag{1.68}$$

We then choose the coordinate system along the principal axes defined by the deformation tensor and so get the reduced form

$$Def = \begin{Vmatrix} a-\lambda_1 D & 0 & 0 \\ 0 & a-\lambda_2 D & 0 \\ 0 & 0 & a-\lambda_3 D \end{Vmatrix}.$$

From this we finally obtain the solution for the density field:

$$\boxed{1+\delta = \left\| \frac{\partial \mathbf{x}}{\partial \mathbf{x_0}} \right\|^{-1} = \frac{1}{(1-\lambda_1 D)(1-\lambda_3 D)(1-\lambda_3 D)}}. \tag{1.69}$$

In the linear case, where $\lambda_1 D << 1$, we get $\delta(\vec{x}) = D(a)(\lambda_1+\lambda_2+\lambda_3) = D(a)\delta_0(\mathbf{x})$, as expected. Zel'dovich (1970) [71] proposed that this equation holds also for $\lambda_1 D \sim 1$: in this case the density becomes infinite when $\lambda_1 D == 1$. At this point the first non-linear structures form: these will be two dimensional *sheets*, called *pancakes*. Then, when also $\lambda_2 D == 1$, the structure will become a *filament*.

However, the Zel'dovich approximation is obviously no longer valid after the formation of *pancakes*, when shell crossing occours. In reality, particles falling into pancakes will oscillate in the gravitational potential, rather than move out along the directions of their initial velocities as it would be predicted by the approximation.

1.6 Spherical collapse

The first and simplest model that can give a valuable approximation of gravitational collapse is the spherical collapse: it describes the evolution of a spherical mass shell in an expanding universe. Considering the perturbation as spherical, and not triaxial, allows to ignore the shape-related inhomogeneities and to concentrate on the collapse dynamics.

Collapse in a universe with $\Lambda = 0$

We consider the perturbation as a spherical universe, embedded in a larger expanding universe, with lower background density. The evolution of a tophat perturbation like this is given by

$$\frac{\mathrm{d}^2 R}{\mathrm{d}t^2} = -\frac{GM}{R^2} \tag{1.70}$$

where M is the mass within the shell. In this model, concentric shells remain concentric as they evolve, so the total mass and the mass of each shell are constant. The equation of motion can be integrated once, to yield:

$$\frac{1}{2}\left(\frac{\mathrm{d}R}{\mathrm{d}t}\right)^2 - \frac{GM}{R} = E = \text{const.} \tag{1.71}$$

If $E = 0$ we obtain the classic solution for R:

$$R = \left(\frac{9GM}{2}\right)^{1/3} t^{2/3}. \tag{1.72}$$

The perturbation evolves like $t^{2/3} \propto a^{3/2}$, as we already found for the Einstein-de Sitter universe. Otherwise, if $E < 0$ the derivative $\mathrm{d}R/\mathrm{d}t$ can change sign, and so, if the perturbation is sufficiently denser than the background, it will expand initially, but will eventually pull away from the background expansion, and collapse after reaching a maximum size. As we saw in Jeans theory, the perturbation collapses if the gravitational potential energy wins over the kinetic energy; if $\delta_i << 1$ and if we assume that the initial velocities are simply given by the Hubble flow ($(\mathrm{d}R/\mathrm{d}t)_i \simeq H_i R_i$), then we can write:

$$K_i = \frac{(H_i R_i)^2}{2}$$
$$W_i = -\frac{GM}{R_i} = -\Omega_i(1+\delta_i)\frac{(H_i R_i)^2}{2} \tag{1.73}$$

where K stands for the kinetic energy and W for th gravitational potential. The total energy is

$$E_i = K_i + W_i = K_i(1-\Omega_i(1+\delta_i)). \tag{1.74}$$

Collapse will occour if $E_i < 0$ and so if $(1+\delta_i) > 1/\Omega_i$. The exact time evolution of each shell can be written also in a parametric form:

$$\begin{aligned}\frac{R}{R_i} &= A(1-cos\theta)\\ \frac{t+T}{t_i} &= B(\theta - \sin\theta)\end{aligned} \tag{1.75}$$

where θ grows from 0 to 2π. This form of the equations allows a simple and useful interpretation of the problem.

Turnaround and virialization

The *turnaround* is defined as the instant of maximum expansion of the perturbation; this corresponds to the moment when in which the kinetic energy is zero and all the energy is contained in the gravitational potential term. Using energy conservation we can calculate the perturbation size at turnaround; the total energy in this moment is

$$E = -\frac{GM}{R_{max}} = E_i. \tag{1.76}$$

After turning around, the perturbation will collapse, trajectories of particles in different shells will cross and the object will virialize. Again from energy conservation, we know that at virial equilibrium:

$$2K_{vir} = -W_{vir} \tag{1.77}$$

and

$$E = K_{vir} + W_{vir}. \tag{1.78}$$

Therefore

$$E = K_{vir} + W_{vir} = -\frac{W_{vir}}{2} \sim \frac{GM}{2R_{vir}} = -\frac{GM}{R_{max}} \rightarrow \boxed{R_{vir} \sim \frac{R_{max}}{2}}. \tag{1.79}$$

Thus, at virialization, the system is half the size and eight time denser than it was at turnaround. Obviously, in the parametric form of Equation 1.76, turnaround corresponds to $\theta = \pi$ and collapse to $\theta = 2\pi$: at turnaround we set A by requiring $R_{max}/R = 2A$ and then we set B using the relation above. In an Einstein de-Sitter model we have $\Omega = 1$ and $\bar{\rho}(t) = 1/(6\pi G t^2)$, so the overdensity grows as

$$1+\delta = \frac{\bar{\rho}_i}{\bar{\rho}(t)}\left(\frac{R_i}{R}\right)^3 \simeq \frac{(t/t_i)^2}{A^3(1-\cos\theta)^3} = \frac{B^2(\theta-\sin\theta)^2}{A^3(1-\cos\theta)^3} = \frac{9}{2}\frac{(\theta-\sin\theta)^2}{(1-\cos\theta)^3} \tag{1.80}$$

Considering the limit of small time intervals, we can calculate the Taylor expansions of the last expression and then remove high order terms; doing these approximation we can derive the prediction of the spherical collapse model for the case of linear growth. We get, for the growing mode:

$$\delta \simeq \frac{3\theta^2}{20} \simeq \frac{3}{5}\delta_i\left(\frac{t}{t_i}\right)^{2/3}. \tag{1.81}$$

The linear results, calculated from the last equation, are:

- $\theta = \pi$: at turnaround $\delta_L = 1.062$
- $\theta = 2\pi$: at virialization $\delta_L = 1.686$.

The last result comes from the equation describing the overdensity for a mass shell to collapse at time t_{vir}:

$$\delta_c(t_{vir}) = \frac{3g(t_{vir})}{5}\left\{\left[\frac{\pi}{\Omega^{1/2}(t_{vir})H(t_{vir})t_{vir}}\right]^{2/3} - \left[1-\Omega^{-1}(t_{vir})\right]\right\}. \tag{1.82}$$

Since $H(t)$ and $g(t)$ depend only on $\Omega(t)$ in matter dominated epochs, the critical overdensity for collapse depends only on $\Omega(t_{vir})$ and it can be approximated by:

$$\delta_c(t_{vir}) = \frac{3}{5}\left(\frac{3\pi}{2}\right)^{2/3}[\Omega(t_{vir})]^{0.0185} \sim 1.686[\Omega(t_{vir})]^{0.0185} \tag{1.83}$$

with a very weak dependence on Ω.

Without doing any approximation, we can now calculate the nonlinear values of the perturbation density with respect to the background:

- at turnaround, so for $\theta = \pi$

$$\boxed{1+\delta_{max} = \frac{9}{2}\left(\frac{\pi^2}{2^3}\right) = \frac{9\pi^2}{16} \simeq 5.55} \tag{1.84}$$

- at virialization, so for $\theta = 2\pi$, we cannot use directly Equation 1.81, because $(2\pi - \cos(2\pi)) \to 0$ and so we make use of some considerations: since $\delta > 1$, the object is already significantly non linear at tournaround. If $\Omega = 1$, then the universe expands by a factor of $2^{2/3}$ between t_{max} and t_{vir} and so at virialization the background universe is less dense by a factor 4. Knowing this, we find that the perturbation at virialization is denser than the background by a factor

$$\boxed{1+\delta_{vir} = \frac{9\pi^2}{16}\left(\frac{R_{max}}{R_{vir}}\right)^3\left(\frac{\bar{\rho}_{max}}{\rho_{vir}}\right) = \frac{9\pi^2}{16} \times 8 \times 4 \sim 178} \tag{1.85}$$

These results do not depend on the mass of the object and so suggest that all virialized objects will have the same density relative to the background, whatever their mass and the underestimate increases as the collapse proceeds. It is clear how the linear theory underestimates the growth of δ: at the turnaround the linear theory predicts $\delta_{max} \simeq 1.062$, while the nonlinear result is $\delta_{max} \simeq 4.55$; at virialization the difference is eve bigger, since the linear result is $\delta_{vir} \simeq 1.686$, while in the non linear case $\delta_{vir} \simeq 178$. This means that, as the collapse proceeds, the estimation error of the linear theory becomes bigger: we have a confirmation of what we have always said, that is linear theory works well only until $\delta \sim 1$.

Despite the limits of the spherical collapse model these values (1.686 and 178 - usually approximated to 200) have become the references ones for the identification of dark matter haloes in simulations and for the definition of the mass.

Some limits of the spherical model

As the mass shell turns around and begins to collapse, particles in the mass shell can cross the mass shells that were originally inside it, and consequently the mass enclosed by the initial mass shell is no longer constant, making the assumption of a constant M invalid. This is a first limit in the accuracy of the spherical collapse model. Another one can be seen noticing that, formally, $\theta \to 2\pi$ implies $\delta \to \infty$, but in practice an infinite density is not physical and the object will virialize at a certain finite radius and density value. A common way to deal with this last problem is to stop the evolution at a “freeze-out” moment, chosen in order to reproduce the virial density contrast.

Extension to a flat universe with $\Lambda > 0$

In a universe with a non-zero cosmological constant, the equation of motion of the mass shell has one extra-term and becomes:

$$\frac{\mathrm{d}^2R}{\mathrm{d}t^2} = -\frac{GM}{R^2} + \frac{\Lambda}{3}R, \tag{1.86}$$

where we have used the fact that the cosmological constant contributed to the gravitational acceleration through an effective density $\rho + 3P/c^2 = -2\rho = -\Lambda c^2/4\pi G$. Integrating the previous equation we have, as before, $E = const$:

$$\frac{1}{2}\left(\frac{\mathrm{d}R}{\mathrm{d}t}\right)^2 - \frac{GM}{R} - \frac{\Lambda c^2}{6} = E. \tag{1.87}$$

With this new contribution, the solution for the density contrast becomes

$$\delta_i = \frac{3}{5}(1+\zeta)\left(\frac{\omega_i}{\zeta}\right)^{1/3} \tag{1.88}$$

where $\omega_i = \Omega_\Lambda(t_i)/\Omega_m(t_i)$, $\zeta = \Lambda c^2 R^3_{max}/6GM$ and $R_i/R_{max} \sim (\omega_i/\zeta)^{1/3}$. From this, the overdensity at the time of collapse can be approximated by

$$\delta_c(t_{coll}) = \frac{3}{5}\left(\frac{3\pi}{2}\right)^{2/3}[\Omega_m(t_{col})]^{0.0055} \sim 1.686[\Omega_m(t_{col})]^{0.0055}. \tag{1.89}$$

As for cosmologies with zero cosmological constant, the dependence on Ω_m is extremely weak and therefore, to good approximation $\delta_c(t_{col}) \sim 1.686$ for all realistic cosmologies.

Spherical collapse with shell crossing

As we said, the spherical collapse assumes that shells of matter do not cross. Of course this assumption is not physically realistic, because a mass shell of collisionless particles will oscillate about the center after collapse, with an amplitude that may change with time. Gunn (1977) [24] considered a simple model in which the oscillation amplitude is assumed to be a constant proportional to the radius of the mass shell at its first turnaround. The mean density within a radius r can be written as

$$\bar{\rho}(r) = \frac{3M}{4\pi r^3(M)} \tag{1.90}$$

where $r(M) \propto r_{ta}(M)$. The density profile can then be obtained knowing how r_{ta} changes with M. As an example, we consider a perturbation $\delta_i \propto r_i^{-3\epsilon} \propto M^{-\epsilon}$ in an Einstein-de Sitter universe. In thi case $r_{ta} \propto r_i/\delta_i \propto M^{(\epsilon+1/3)}$ and the density profile is

$$\rho(r) \propto r^{-\gamma} \qquad \text{with} \qquad \gamma = 9\epsilon/(1+3\epsilon). \tag{1.91}$$

For the special case in which the initial perturbation is assoiciated with a point mass embedded in an Einstein-de Sitter background, $\epsilon = 1$ and $\rho(r) \propto r^{-9/4}$.

Unfortunately, this treatment of shell crossing is not accurate. It assumes that the original mass enclosed by the shell is almost the same as the total mass enclosed by the shell at the apocenter, since the mass shell is expected to spend most time near its apocenter. However, the total mass at apocenter includes not only the particles initially enclosed by the mass shell, but also those which were initially outside it but have current radii smaller than its apocentric radius. Because of this additional mass, the apocentric radius in general changes with time and so the density profile will be a bit different.

1.7 Relaxation processes

In dynamics, relaxation is the process by which a system approaches equilibrium or by which it returns it returns to equilibrium after a disturbance. So far in this chapter we have discusses the gravitational collapse of collisionless systems and the properties of virialized equilibrium systems. We now turn our attention for a while to the relaxation mechanisms that operate during the collapse process and lead to these equilibrium configurations. It is clear that statistical mechanics alone cannot determine exactly the relaxed equilibrium state of a collisionless system. This state must depend on the details of the collapse process and on the initial conditions that determine how efficient the relaxation will be. We study two extensions of the collapse model, the *secondary infall model* and the *violent relaxation.* One of the main difference between these two model is whether the final configuration preservs the memory of the initial conditions or not, and thus if it is possible to correlate the two epochs. Even if now it is known that they do not work perfectly, they are still useful to give a more physical description of the collapse process.

Secondary infall model

The secondary infall model of collapse tries to give a more realistic description of the collapse process, starting from two simple considerations: first of all, there is no real motivation for the assumption that the virial radius equals half the turnaround radius, and that virialization happens at twice the turnaround time; secondly, at any given time the mass of the collapsing object is made up of two types of particles, those which spend most of their time close to the center and those which are just passing by, which are assumed to be not dominating. The secondary infall model attempt to account correctly for the effects of these extra particles.

Let $M_{add}(r)$ be the mass due to particles on orbits with large radii which spend some of their time within the halo radius r. A particle on an orbit which carries it out to a maximum distance $r' > r$ from the center, spends within r the fraction of time given by

$$p(r|r') = \int_0^r \frac{\mathrm{d}r}{v(r)} \Bigg/ \int_0^{r'} \frac{\mathrm{d}r}{v(r)} . \tag{1.92}$$

The velocity v is obtained by integrating the equation of motion of the shell: $\mathrm{d}r^2/\mathrm{d}t = -GM/r^2$. If $M_x(r)$ denotes the mass in particles which do not go further away from the center more than r', we set

$$v^2(r) = \frac{GM_x(r)}{r} - \frac{GM_x(r')}{r'} = \frac{GM_x(r')}{r'}\left(\frac{M_x(r)r'}{M_x(r')r} - 1\right). \tag{1.93}$$

If we assume a density profile $\rho_x(r) = \rho_x r^{-\gamma}$, we have $M_x(r) \propto r^{3-\gamma}$ and

$$p(r|r') = \int_0^{r/r'} \frac{\mathrm{d}r/r'}{\sqrt{(r/r')^{2-\gamma} - 1}} \Bigg/ \int_0^1 \frac{\mathrm{d}r/r'}{\sqrt{(r/r')^{2-\gamma} - 1}} . \tag{1.94}$$

The contribution to the total mass from particles just passing through r is given by taking tha total mass in particles within r', multiplying by the fraction of time that these particles spend within r, and integrating over all $r' > r$ out to the turnatound radius R_{max}:

$$\frac{M_{add(r)}}{M_x(r)} = \frac{4\pi \int_r^{R_{max}} \mathrm{d}r'\, r'^2 \rho_x(r') P(r|r')}{4\pi \int_0^r \mathrm{d}r'\, r'^2 \rho_x(r')}. \tag{1.95}$$

This expression shows that the additional mass, when expressed as a fraction of the total mass, depends on r. This additional effective mass in the inner regions of the object means that the outer shells actually contract a little more than they would have done otherwise. Since this depends on r, the assumption of a constant collapse factor must be modified.

Violent relaxation

Calculations could be complicated also by the fact that, even if we usually assume the energies of the individual paricles to be conserved during collapse, the relaxation processes are generally accompained by changes of the gravitational potential $\Phi(\mathbf{x},t)$. If we let $\epsilon = v^2/2+\Phi$ be the specific energy for a given particle, then

$$\frac{\mathrm{d}\epsilon}{\mathrm{d}t} = \frac{\partial\epsilon}{\partial\mathbf{v}}\cdot\frac{\mathrm{d}\mathbf{v}}{\mathrm{d}t} + \frac{\partial\epsilon}{\partial\Phi}\frac{\mathrm{d}\Phi}{\mathrm{d}t} = -\mathbf{v}\cdot\nabla\Phi + \frac{\mathrm{d}\Phi}{\mathrm{d}t} = -\mathbf{v}\cdot\nabla\Phi + \frac{\partial\Phi}{\partial t} + \mathbf{v}\cdot\nabla\Phi = \frac{\partial\Phi}{\partial t} \tag{1.96}$$

where we have used $\mathrm{d}\mathbf{v}/\mathrm{d}t = -\nabla\Phi$. Thus, a time-dependent potential of a collisionless system can induce a change in the energies of the particles involved: in a time-varying potential, energy is no longer an integral of motion. Exactly how the energy of a particle changes depends in a complex way on the initial position and energy of the particle: particles can both gain or loose energy, and some particles can even become unbound. Overall, the effect is to broaden the range of energies. The additional relaxation mechanism, provided by this potential variation, is called *violent relaxation*. As evident from the last equation, $\mathrm{d}\epsilon/\mathrm{d}t$ is independent of the particle mass, so violent relaxation has no tendency to segregate particles of differing mass during the relaxation process. This is different from collisional relaxation, where the momentum exchange associated with the two-body gravitational encounters drives the system towards equipartition of kinetic energy. The time scale for violent relaxation can be defined as

$$t_{vr} = \langle \frac{1}{\epsilon^2}\left(\frac{\partial\Phi}{\partial t}\right)^2\rangle^{-1/2}, \tag{1.97}$$

where the average is taken over all the particles that make up the collective potential. As shown by Lynden-Bell (1967), this is approximately equal to the free-fall time of the system, $t_{ff} = (3\pi/32G\bar{\rho})^{1/2}$, showing that the relaxation process is very fast, and so $violent$.

In general, during relaxation processes, most information regarding the initial condition is erased. However, the mixing associated with violent relaxation is self-limiting, because as soon as the system approaches any equilibrium state, the large scale potential fluctuations, which drive the evolution, vanish. Mixing destroys the coherent motions required to maintain these variations, for example, in the later phases of the collapse of a system ot the merger of two systems. As a result it is difficult to predict the extent to which the properties of the initial conditions are reflected in the final equilibrium state. Numerical simulations have shown that violent relaxation is never *complete*, in the sense that the final energies of particles are correlated with their initial values and the shape of the final system clearly remembers that of the initial conditions. The simulations show also that the final density profile depends strongly on the initial conditions, in particular on the initial virial ratio $|2T/W|$, which basically expresses how far the initial system is from virial equilibrium (virialized systems have a virial ratio of unity). During the early stages of the collapse, the system rapidly contracts to a compact configuration; the initial collapse is followed by a series of expansion and contraction phases, during which the particles either gain or loose energy resulting in a final distribution of particles energies, which is much broader than the initial distribution. The time it takes for the system to settle in equilibrium depends on the initial virial ratio; in addition, the large potential fluctuations cause a larger fraction of particles to be flung out to large radii, giving rise to a more extended halo which takes longer time to set in equilibrium. The final distribution extends well beyond the outer boundary of the initial configuration, with the central density comparable to the density of the system at the time when it first collapses. The velocity field of the equilibrated structure is nearly isotropic in the inner regions, but dominated by radial orbits in the outer part: this is a natural consequence of the fact that the particles in the outskirts were launched there due to potential fluctuations.

1.8 *Excursion sets* model and the halo mass function

We have seen that the linear theory holds until $\delta \sim 1$; thereafter the nonlinear effects become important and the collapsing region separates from the background universe to form a collapsed halo. When the halo starts to form, δ has already reached the critical value $\delta_c = 1.686$, predicted by the spherical collapse model. We have seen that, following the exact evolution of a perturbation in the non-linear regime is extremely difficult; we need a statistical way to characterise the halo population without following the nonlinear dynamics in detail. With this aim, we should look at the problem from a new point of view: instead of considering an evolving field δ and a fixed critical value δ_c, we can imagine a time-dependent critical value, or barrier, $\delta_c(t)$. On the contrary, the density fluctuation field is rescaled at the initial time t_0: $\delta(\mathbf{x}) = \delta(\mathbf{x}, t_0)$. Using this model, a mass element located at **x**, is contained in a halo of mass M at time t if the linear density fluctuation $\delta(\mathbf{x}, R)$, centered in **x** and filtered on scale $R \propto M^{1/3}$ is

$$\delta(\mathbf{x}, R) \geq \delta_c(t). \tag{1.98}$$

In this picture we are assuming that haloes form from peaks in the initial density field, obtained after smoothing with a window function of characteristic scale R. The abundance and the clustering properties of these density peaks can ben calculated as a function of their height and shape. It is tempting to interpret the number density of peaks in terms of a number density of collapsed objects of mass $M \propto \rho R^3$. However, there is a serious problem with this identification, because a mass element which is associated with a peak of $\delta_1(\mathbf{x}) = \delta(\mathbf{x}, R_1)$ can also be associated with a peak of $\delta_2(\mathbf{x}) = \delta(\mathbf{x}, R_2)$, where $R_2 > R_1$. If $\delta_2 < \delta_1$ the mass element can be considered part of both M_1 and M_2: the overdensity will first reach the critical values for collapse on scale R_1 and then on scale R_2. This situation reflects the fact that M_1 is the mass of a collapsed object at t_1 which merges to form a bigger object of mass M_2 at t_2: so M_1 should no longer be considered as a separate object. In the opposite case, when $\delta_2 > \delta_1$, the mass can never be a part of a collapsed object of mass M_1 and must be incorporated directly into the larger system M_2. This problem turns to be quite difficult to be solved rigorously.

Press-Schechter formalism

What is required to predict the mass function of collapsed objects is a method to partition the density field at some early time into a set of disjoint patches, each of which will form a single collapsed object at some later time; then we must calculate the statistical properties of this partition. The Press-Schechter formalism (1974, [52]) allows to describe in a simpler and less rigorous way the mass function calculation. The filtered density field is given by the convolution of $\delta(\mathbf{x})$ with a window function $W(\mathbf{x}, R)$. Using Fourier theory we can write:

$$\delta(\mathbf{x}, R) = \frac{1}{(2\pi)^3} \int d^3k exp(i\mathbf{k}.\mathbf{x}) \hat{\delta}(k) \hat{W}(kR) \simeq \int_0^{k_f} dk k^2 \hat{\delta}(k). \tag{1.99}$$

This shows that $W(\mathbf{x}, R)$ acts as a filter and erases the contribution of all the perturbations with $k \geq k_f$. The ansatz of the Press-Schechter formalism is that the probability that $\delta > \delta_c(t)$ is the same as the fraction of mass elements that at time t are contained in haloes with mass greater than M. If $\delta_0(\mathbf{x})$ (and so $\delta(\mathbf{x})$) is a Gaussian random field, then the probability that $\delta > \delta_c(t)$ is given by:

$$P = \frac{1}{\sqrt{2\pi}\sigma(M)} \int_{\delta_c(t)}^{\infty} \exp\left[-\frac{\delta^2}{2\sigma^2(M)}\right] \mathrm{d}\delta = \frac{1}{2} \mathrm{erfc}\left[\frac{\delta_c(t)}{\sqrt{2}\sigma(M)}\right]. \tag{1.100}$$

Here

$$\sigma^2(M) =< \delta^2(\mathbf{x}, R) >= \frac{1}{2\pi^2} \int_0^{\infty} P(k) \hat{W}(\mathbf{k}, R) k^2 \mathrm{d}k \tag{1.101}$$

is the mass variance of the smoothed density filed; $P(k)$ is the power spectrum of the density perturbations. The probability 1.101 is equal to $F(> M)$, that is the mass fraction of collapsed objects with mass greater than M. The resulting formula for the number density of collapsed objects with masses in the range $[M, M + \mathrm{d}M]$ is

$$\begin{aligned} n(M,t)dM &= \frac{\rho}{M}\frac{\partial F(>M)}{\partial M}\mathrm{d}M = 2\frac{\rho}{M}\frac{\partial P(>\delta_c(t))}{\partial \sigma}\left|\frac{\mathrm{d}\sigma}{\mathrm{d}M}\right|\mathrm{d}M \\ &= \sqrt{\frac{2}{\pi}}\frac{\rho}{M^2}\exp\left(-\frac{\delta_c^2}{2\sigma^2}\right)\left|\frac{\mathrm{d}\ln\sigma}{\mathrm{d}\ln M}\right|\mathrm{d}M. \end{aligned} \tag{1.102}$$

This is known as the Press and Schechter mass function. Using the variable $\nu = \delta_c(t)/\sigma(M)$, it can also be written in the compact form:

$$\boxed{n(M,t)\mathrm{d}M = \frac{\rho}{M^2}\sqrt{\frac{2}{\pi}}\nu\exp(-\nu^2/2)\left|\frac{\mathrm{d}\ln\nu}{\mathrm{d}\ln M}\right|\mathrm{d}M.} \tag{1.103}$$

The PS formalism provides a useful way to understand how nonlinear structures develope in a hierarchical model. From Equation 1.104 we can see that halos with mass M can only form in significant number when $\sigma(M) \gtrsim \delta_c(t)$; if we define the characteristic mass $M_\star(t)$ by $\sigma(M_\star) = \delta_c(t) = \delta_c/D(t)$, then only haloes with $M \leq M_\star$ can have formed in significat number at time t. Since, in hierarchical models, $D(t)$ increases with t and $\sigma(M)$ decreases with M, the characteristic mass increases with time. Thus, as time passes, more and more massive haloes start to form.

The *excursion sets* model

An alternative derivation of the halo mass function was obtained by Bond et al. (1991, [8]), using what is called the excursion set formalism. In this model $S(M) = \sigma^2(M)$ is used as the mass variable: since in hierarchical models S is a monotonically declining function of M, a larger value of S corresponds to a smaller mass. Each location $\mathbf{x}$ in the density field corresponds to a trajectory $\delta(S)$, which reflects the value of the density field at that location when smoothed with a filter of mass S. We consider a set of random walks (S,δ), starting from $S = \delta = 0$ and growing with increasing S; a random walk which crosses for the first time the barrier $\delta_c(t)$ at a certain point (S,δ) corresponds to a fluid element cointained in haloes of mass $M(S)$ at time t. This means that each time t determines a horizontal barrier $\delta_c(t)$. It is important to remark that the right mass value that is associated with a trajectory corresponds to the first barrier crossing (Figure 1.3). This is because three different kind of trajectories are possible: trajectories which cross the value at some k and remain over the barrier, trajectories which have always been under the barrier and finally trajectories which cross the barrier at some k, but then return under it. In order to calculate the correct number of objects at some time t, we need to exclude these last trajectories. For this we can use the fact that, since we are using random walks, all trajectories may have a mirror trajectory: at any time the trajectories have equal probability of moving upwards or downwards. These $virtual$ trajectories correspond, for example, to random walks starting from $(S,\delta) = (0, 2\delta_c)$ and they satisfy the same equations of $normal$ trajectories: we can use their probability distribution to exclude the third kind of walks which intersect the barrier more than once. Thus our probability will be:

$$P = \frac{1}{\sqrt{2\pi S}}\int_{\delta_c(t)}^{\infty}\exp\left[-\frac{\delta^2}{2S}\right] - \exp\left[-\frac{(\delta - 2\delta_c(t))^2}{2S}\right]\mathrm{d}\delta. \tag{1.104}$$

Excluding those trajectories corresponds to assume that all the walks which cross the barrier $\delta_c(t)$ are $absorbed$.

1.9 Scaling relations for hierarchical clustering

Now that we have described various models for the evolution of cosmic density perturbations, we can use these results to examine how gravitational collapse proceeds and what kind of structures are to be expected from such collapse. In particular, in the current standard model of structure formation, large scale structures form through **hierarchical clustering**: objects on small scales form first and then they merge to form always more massive structures. This can be seen from

$$\sigma^2(r,t) = \left[\frac{r}{r_\star(t)}\right]^{-(n+3)} = \left[\frac{M}{M_\star(t)}\right]^{-(n+3)/3} \tag{1.105}$$

where

$$P(k) \propto k^n \qquad M_\star(t) \propto [D(t)]^{6/(n+3)}. \tag{1.106}$$

$M_\star(t)$ is the mass on which $\sigma = 1$ at time t. Since the critical linear overdensity of gravitational collapse is ~ 1.68, according to spherical collapse model, we can imagine that nonlinear structures with mass $\sim M$ begin to form in significant numbers when the linear value of $\sigma(M;t)$ reaches ~ 1.68. Therefore, the time dependence of $M_\star$ can be used to understand how nonlinear structures develop with time for a given linear power spectrum. Since $D(t)$ increases with t, the mass scale of nonlinearity $M_\star(t)$ increases with t for $n > -3$: in this case structure formation is *bottom-top*, in the sense that smaller structures form prior to larger ones. For cold dark matter, the effective spectral index is larger than -3 over all lenght scales. From the last equation we can derive scaling laws for the other significant quantities:

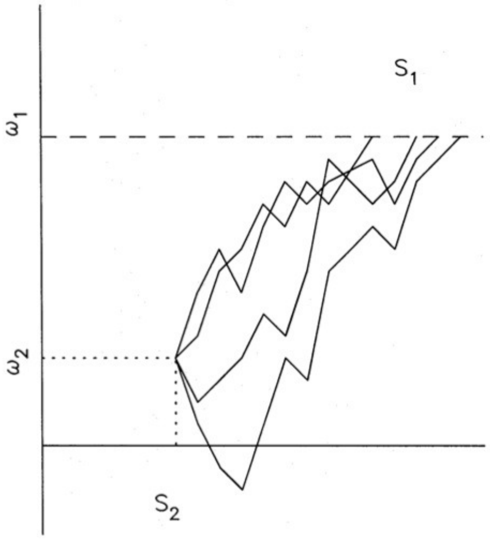

Figure 1.3: Trajectories of δ versus S for a subset of walks that make their first upcrossing of a barrier height ω_2 at S_2, and then continue until they eventually cross through a second barrier of height $\omega_1 > \omega_2$ at various values of S_1. From Lacey & Cole (1993,[30]).

$$D(t) \propto M^{(n+3)/6} \qquad t \propto M^{(n+3)/4} \tag{1.107}$$

$$\rho \propto [1+z(t)]^3 \propto M^{-(n+3)/2} \tag{1.108}$$

$$r \propto (M/\rho)^{1/3}. \tag{1.109}$$

If $n > -3$ smaller objects formed earlier and have higher densities. At any given time t, the Universe contains collapsed objects of variuos masses up to the characteristic value $M_\star(t)$; as time goes by, $M_\star$ increases and larger and larger objects form by accretion and merger of smaller objects. Another limitation of the range of possible n is given by the fact that the binding energy of an object must not be dominated by that of its progenitors, and so $n < 1$ must hold: in this way the typical binding energy increases as larger objects form.

We can then divide the evolution of the cosmic density field in three different regimes:

1. $M >> M_\star$: on these scales the density fluctuations are still in the linear regime
2. $M << M_\star$: the density fluctuations corresponding to low mass objects have already collapsed to form virialized objects
3. $M \sim M_\star$: the fluctuations are in the quasi-linear regime and the structure is dominated by large-scale pancake and filaments; so $M_\star$ can be considered the typical mass of haloes that are forming now.

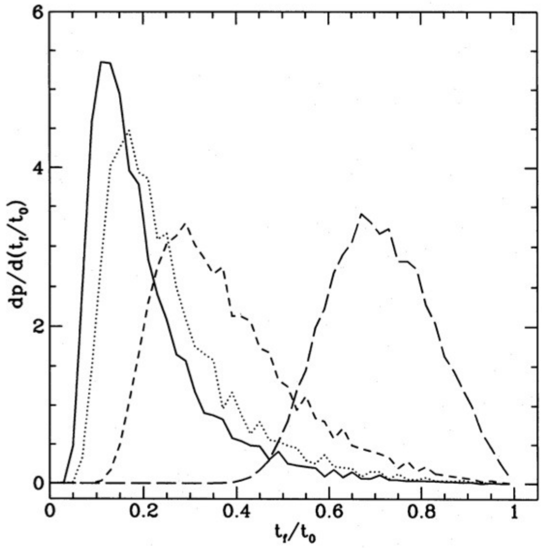

Figure 1.4: The distribution of formation times of haloes in a CDM universe; the solid, dotted, short-dashed and long-dashed curves are stand for present halo masses $M_0/h^{-1}M_\odot = (10^6, 10^9, 10^{12}, 10^{15})$. (Lacey & Cole, 1993 [30])

At any gien time, the cosmic density field is therefore a complicated web consisting of virialized haloes, large scale filaments and pancakes, that surround low density regions (voids). A confirmation of the hierarchical model can be seen in Figure 1.4, where Lacey & Cole (1993) plotted the distribution of formation times for haloes of four different masses. Knowing that the formation time is defined as the moment at which the main progenitor of an halo has accreted half of the final halo mass, we note that more massive haloes form evidently later than low-mass haloes.

1.10 Dark matter haloes

Dark matter haloes are the fundamental "units" of large scale structures: haloes form under the action of gravity, evolve and merge, forming the ever-changing cosmic web. They are also biased tracers of galaxies and so of the distribution of baryonic matter. Understanding their basic properties is - and has been - one of the main issues in cosmology. In thi Section we will recall the main features of dark matter haloes and the works that led to their determination (the aspect of halo triaxiality - which is the focus of this work - will be treated in detail in the following chapters and so we do not mention it here).

Density profile

As a first approximation, we can model a dark matter halo as a spherical object. In this way, the internal mass distribution is fully described by a density profile such as $\rho(r)$. Since different haloes have different formation histories, we may expect a significant halo-to-halo variation of the density profile. On the other hand, virialized dark matter haloes are highly nonlinear objects and so the information regarding their formation histories may have been erased by the nonlinear collapse, in particular during the relaxation process (as we mentioned, talking about violent relaxation). Physically, we observe that matter is more concentrated in the central part of the halo than in the outskirts; this could be model by a general profile:

$$\boxed{\rho(r) = \frac{\rho_0}{\left(\frac{r}{r_s}\right)^\gamma \left[1 + \left(\frac{r}{r_s}\right)^\alpha\right]^{(\beta-\gamma)/\alpha}}} \tag{1.110}$$

where r_s is a scale radius. This equation describes also the density profile of elliptical galaxies and it represents a sphere with a double broken power-law density distribution: at small radii $\rho \propto r^{-\gamma}$, while at large radii $\rho \propto r^{-\beta}$; α determines the sharpness of the break. All the most common parametrisation of the density profile can be reduced to this general formula, for different combinations of α, β, γ.

Since we can approximately model dark matter haloes as spheres, we should derive some initial guesses on the density profile using the spherical collapse model. This suggests that the ratio of the inital radius of a shell to the radius at which it turns around is related to its initial density:

$$\frac{R}{R_{max}} \propto \delta_i(R). \tag{1.111}$$

Suppose that, on average, after turnaround, the matter collapses and virializes at some fraction of the turnaround radius, and that this fraction is independent of the initial radius: for the spherical tophat model we know that this fraction is 1/2. Then, the final density profile must satisfy

$$\frac{\rho(<r)}{\rho(<r_{vir})} = \frac{M(r)}{M(r_{vir})}\left(\frac{r_{vir}}{r}\right)^3 \sim \left(\frac{\delta_i(R)}{\delta_i(R_{vir})}\right)^3 \tag{1.112}$$

where the last comes from the previous equation; in these equations R indicates the initial radius, while r indicates the final radius. As we said, a reasonable choice for fluctuations in a Gaussian random field with $P(k) \propto k^n$ is $\delta(R) \propto R^{-(n+3)}$. Using this

$$\frac{\rho(<r)}{\rho(<r_{vir})} \simeq \left(\frac{\delta_i(R)}{\delta_i(R_{vir})}\right)^3 \simeq \left(\frac{R_{vir}}{R}\right)^{3(3+n)} = \left(\frac{r}{r_{vir}}\right)^{-3(3+n)/(4+n)}. \tag{1.113}$$

When $n = -1$ the final slope is -2. The typical halo profile will then be

$$\rho(r) \propto \begin{cases} r^{-2} & \mathrm{n} = -1 \\ r^{-(3n+9)/(n+4)} & \mathrm{n} > -1. \end{cases}$$

Over the range of interest, $-3 < n < 0$, this model thus predicts that virialized haloes resemble isothermal spheres: the simplest model is therefore to assume that dark matter haloes are truncated singular isothermal spheres:

$$\rho(r) \propto r^{-2}. \tag{1.114}$$

This holds up to the *limiting radius* of the halo, which is defined as distance from the center within which the mean matter density is $\rho_h = \delta_h \rho_{crit} \Omega_m$ (a reasonable choice would be to take $\delta_h = \delta_{vir}$; however, since the criterion for virialization is not strict, other definitions are also in use in the literature).

Of course the isothermal model is, at best, an approximation: many effects may cause deviations from this simple profile. For example:

- collapse may never reach an equilibrium in the outer region of a dark halo
- non-radial motions may be important
- merging events associated with the hierarchical formation process may render the spherical collapse model invalid.

An extension of the isothermal model is the **Hernquist profile**, proposed by Hernquist [25] starting from the observed luminosity distribution for elliptical galaxies and bulges. His resulting form for the density profile is

$$\boxed{\rho(r) \propto \frac{\rho_0}{\left(\frac{r}{r_s}\right)\left(1+\frac{r}{r_s}\right)^3}}. \tag{1.115}$$

This model does not suppose the existence of a defined core and two broken power-laws, but a gently changing logaritmic slope. This happened because the isothermal sphere model, charaterized by the core radius and the velocity dispersion, has been challenged by numerical simulations of the formation of haloes, which provided no firm evidence of the existence of a core. The slope of the density profile changes from $\rho \propto r^{-1}$ at small radii, to $\rho \propto r^{-4}$ at large r. Since Herniquist profile has been derived analytically, we could go backwards and compute the distribution function, which can be expressed in terms of elementary functions.

Using high resolution N-body simulations of structure formation, Navarro et al. (1996) [43] showed that the density profiles of the simulated dark matter haloes are shallower than r^{-2} at small radii and steeper at large radii. Their new formula for the density profile, known as the **NFW profile**, rapidly became the standard definition of the density profile and is:

$$\boxed{\rho(r) = \frac{\rho_c \delta_c}{\left(\frac{r}{r_s}\right)\left(1+\frac{r}{r_s}\right)^2}} \tag{1.116}$$

where r_s is a scale radius and δ_{char} is a characteristic overdensity. The logarithmic slope of the NFW profile changes gradually from -1 to -3 at large radii (rather than -4 as in the Hernquist profile), and only resembles that of an isothermal sphere at radii $r \sim r_s$. This profile is found to be a good representation of the equilibrium density profiles of dark matter halos of all masses and in all CDM-like cosmologies. We can see that this formula resemble the general density profile, that we proposed at the beginning, with $\alpha = 1$, $\beta = 3$ and $\gamma = 1$. Thus, haloes formed by dissipationless hierarchical clustering seem to have a universal density profiles.

Recently, many works started to use a third parametrisation of the density profile : the Einasto profile [16]. It has an extra free parameter, the shape parameter α, and may be written as:

$$\ln\left(\frac{\rho_E}{\rho_{-2}}\right) = -\frac{2}{\alpha}\left[\left(\frac{r}{r_{-2}}\right)^{\alpha} - 1\right], \tag{1.117}$$

where r_{-2} marks the radius where the logarithmic slope of the profile is equal to -2.

Halo substructure

Cold dark matter haloes are not smooth, but they contain a lot of self-bound substructures. The centers of these substructures should correspond to the locations of galaxies or satellites. Subhaloes have cuspy, NFW-like density profiles, but they are also subjected to tidal stripping and so they tend to be less extended than comparable haloes in the field. The subhalo population has also been accreted recently and so is much less concentrated than the halo, since subhaloes tend to reside in the outskirts of the parent halo. A widely known problem is the excess of subhaloes with respect to the number of satellite galaxies. A plausible explanation for the discrepancy is that galaxy formation is extremely inefficient in small halos: various forms of feedback (such as reionization or the injection of supernova energy) render all but a handful of the largest subhalos invisible. Although deprived of stars, these dark subhalos are, in principle, detectable from their gravitational lensing effects.

The ellipsoidal collapse model 2

As seen in the previous chapter, the spherical evolution model improves the description of gravitational collapse by introducing non-linearity, but it is however an approximation: wherever large-scale structures in the universe can be delineated, they turn out to be far from spherically symmetric. This is the reason why we need a more realistic model of gravitational collapse: an example of such a model is the Ellipsoidal Collapse model (EC). It considers structures as homogeneous ellipsoidal regions embedded in a background universe, bringing to light several features which are not present in the spherical models. Certainly this model maintains some approximations or simplifications, which have to be pointed out: first of all, real density fluctuations evolve through configurations that are far from being homogeneous as they separate from the Hubble flow and begin to collapse - any protosystem is composed by a number of subunits which have already collapsed and come to equilibrium and this could make a homogeneous ellipsoid a poor approximation. Secondly, the assumption of a smooth universe outside the perturbation may eliminate some non-negligible effects. Nevertheless, as we will describe in this chapter, this approach offers many advantages: first of all, even with the limit of triaxial symmetry, it allows a variety of shapes for dark matter haloes. The origin of this model lies in a work of White & Silk 1979 [70], who for the first time used a triaxial model for dark matter halo evolution. It has been used and further developed in many other works, as for example Bond et al. 1991 [8], Sheth & Tormen 1999 [60], Sheth et al. 2001 [59], Porciani et al. 2002 [50], Shen et al. 2006 [57], Rossi et al. 2011 [54], Despali et al. 2013 [15], Despali et al. 2014 [14], Ludlow et al. 2014 [36], Borzyszkowski et al. 2014[10] and Bonamigo et al. 2015 [7].

2.1 The origin: White and Silk 1979

The ellipsoidal collapse model has been introduced in the work of White and Silk (1979,[70]), which considers ellipsoidal density perturbation for the first time: such perturbations evolve through a series of increasingly eccentric homogeneous ellipsoids until their shortest axis goes to zero and a "pancake" is formed. The evolution of the ellipsoidal perturbation is treated separately from the background evolution, as a overdense closed universe (as already in the spherical collapse model).

The gravitational potential within a uniform ellipsoid (and for a zero pressure fluid) may be written as

$$\Phi_e = -\pi G \rho_e \sum_{i=1}^{3} \alpha_i x_i^2, \tag{2.1}$$

where ρ_e is the density of the ellipsoid, the coordinate axes coincide with the principal axes and V_e

has been set equal to zero at the origin. The coefficients α_i are given by

$$\alpha_i = a_1 a_2 a_3 \int_0^\infty (a_i^2+\lambda)^{-1} \prod_{j=1}^{3} (a_j^2+\lambda)^{-1/2} d\lambda, \tag{2.2}$$

where the a_i are the half-lengths of the principal axes, with $a_1 \le a_2 \le a_3$. Substituting this potential into Poisson's equation shows that

$$\sum_i \alpha_i = 2. \tag{2.3}$$

The potential due to the smooth background density within the spherical surface which contains the perturbation is

$$\Phi_b = -\frac{2}{3}\pi G \rho_b \sum_i x_i^2. \tag{2.4}$$

Summing the two potential contributions, we obtain the total potential within a homogeneous ellipsoidal overdensity in an unperturbed universe:

$$\boxed{V = -\pi G \sum_i \left[\left(\rho_e - \rho_b\right) \alpha_i + \frac{2}{3}\rho_b \right] x_i^2 = -\pi G \sum_i \left[\alpha_i \rho_e + \left(\frac{2}{3} - \alpha_i \right) \rho_b \right] x_i^2}. \tag{2.5}$$

To obtain the equations of motion from this potential, we assume that, as the perturbation evolves, the background remains uniform and that the external density can be calculated from the usual comological equations. Of course this is only approximately correct, because the background becomes inhomogeneous once the perturbation enters in the nonlinear regime. Anyway, at this point, the evolution of the perturbation is governed mostly by its own self-gravity, and so the last assumption introduces only a small error. The perturbation evolves through a serie of homogeneous ellipsoidal configurations (provided that the initial velocity field is linear in the coordinates: for the initial velocity field here we use only the Hubble flow). The evolution of the ellipsoidal perturbation is then described by the equations:

$$\begin{aligned} \frac{\mathrm{d}^2 a_i}{\mathrm{d}t^2} &= -2\pi G \left[\alpha_i \rho_e + \left(\frac{2}{3} - \alpha_i \right) \rho_b \right] a_i, \\ \frac{\mathrm{d}^2 R_b}{\mathrm{d}t^2} &= -\frac{4\pi}{3} G \rho_b R_b, \\ \rho_e a_1 a_2 a_3 &= const, \\ \rho_b R_b^3 &= const, \end{aligned} \tag{2.6}$$

where R_b is the scale factor of the background universe. The first equation represent the evolution of the ellipsoidal perturbation (and so the evolution of its axes), the second equation is one of the Friedmann equations and stands for the evolution of the background; the last two equations are the conservation of mass for the perturbation and for the background. For the numerical results White & Silk (1979) [70] integrated these equations using a fourth-order Runge-Kutta scheme; moreover, the evaluation of the integrals α_i can be avoided by integrating the auxiliary equation given by Fujimoto (1968):

$$\frac{\mathrm{d}\alpha_i}{\mathrm{d}t} = -\frac{2}{\alpha_i}\frac{\mathrm{d}\alpha_i}{\mathrm{d}t} - \sum_{j\neq i} \frac{\alpha_i - \alpha_j}{a_i^2 - a_j^2} \left(a_i \frac{\mathrm{d}a_i}{\mathrm{d}t} - a_j \frac{\mathrm{d}a_j}{\mathrm{d}t} \right) + \frac{\alpha_i}{a_1 a_2 a_3} \frac{\mathrm{d}(a_1 a_2 a_3)}{\mathrm{d}t}. \tag{2.7}$$

In this approach particular model is specified by giving initial values of Ω, ρ_e/ρ_b, a_2/a_1 and a_3/a_1. The initial values of α_i are calculated and the equations of motion are integrated until the shortest axis of the ellipsoid approaches zero and a *pancake* is formed.

After these considerations, White & Silk (1979) [70] give an approximate solution of the equations of motion: they assume that the time dependence of the α_i can be neglected and that $\rho_e a_i$ and $\rho_b a_i$

have the same time dependence of the spherical perturbations of density ρ_e and ρ_b respectively; then the equations may be written as

$$\frac{\mathrm{d}^2 a_i}{\mathrm{d}t^2} = \left\{ \frac{3}{2}\alpha_i(t_0)\frac{\mathrm{d}^2 R_e}{\mathrm{d}t^2} + \left[1 - \frac{3}{2}\alpha_i(t_0)\right]\frac{\mathrm{d}^2 R_b}{\mathrm{d}t^2} \right\} a_i(t_0), \tag{2.8}$$

that is, they apply the Friedmann equations both for ρ_e and ρ_b. t_0 is the initial time and R_e is the scale factor for a universe with the given initial Hubble constant but with initial density $\rho_e(t_0)$. Now, assuming $R_e = R_b = 1$ and integrating twice the last equation, the resulting approximate solution is

$$\frac{a_i(t)}{a_i(t_0)} = \frac{3}{2}\alpha_i(t_0)R_e(t) + \left[1 - \frac{3}{2}\alpha_i(t_0)\right]R_b(t) = \tag{2.9}$$

$$R_b(t) - \frac{3}{2}\alpha_i(t_0)\left[R_b(t) - R_e(t)\right]. \tag{2.10}$$

These equations clearly describe the evolution fo homogeneous spherical perturbations exactly, and they resemble the linearised equations which Zel'dovich (1970, [71]) suggested could be extrapolated to give a qualitative description of the nonlinear evolution of a general inhomogeneous density field. These equations also describe the evolution of ellipsoidal perturbations quite well. Zel'dovich theory (1970, [71]) predicts evolution through a series of homogeneous coaxial ellipsoids with

$$a_i(t) \propto R_b(t) - \alpha_i b(t) \tag{2.11}$$

where $b(t)$ is proportional to the amplitude of growing perturbations in linear perturbation theory; for an Einstein-de Sitter universe we have $b(t) \propto R_b^2 \propto t^{4/3}$, giving

$$\frac{a_i(t)}{a_i(t_0)} = \frac{\left[R_b(t) - \frac{3}{10}\alpha_i\left(\frac{\rho_e}{\rho_b} - 1\right)\frac{b(t)}{b(t_0)}\right]}{1 - \frac{3}{10}\alpha_i\left(\frac{\rho_e}{\rho_b} - 1\right)} \tag{2.12}$$

In Figure 2.1 we see the numerical solutions for two typical cases compared with the approximate solutions of White & Silk (1979, [70]). Some general points are illustrated by the figure: first of all, the shape of the perturbation does not change much until it ha s a significant overdensity with respect to the background; an important consequence of this observation is that deviations from self-similar evolution are much larger in an open universe, in which a perturbation can obtain a significant overdensity early in its evolution. Thus, in the Einstein-de Sitter model, both the longest and the medium axes are contracting when the perturbation pancakes, while in the open model both of them are still expanding. Another important conclusion considers the collapse time: the collapse time of perturbation - with fixed initial overdensity - decreases with increasing eccentricity meaning that near oblate configurations collapse faster than near prolate ones. In addition, the evolution is faster in a lower-density universe; however, the scale factor also increases more rapidly when Ω is small and - unless the perturbation is highly eccentric - collapse occurs at larger values of R_b in lower-density universes. The ratio of the uncollapsed axes at the instant of pancaking is 2.07:1 for both models: this is an example of a surprising regularity. They find that

$$\frac{a_2(t_c)}{a_3(t_c)} \sim \frac{a_2(t_0) - a_1(t_0)}{a_3(t_0) - a_1(t_0)} \tag{2.13}$$

where we find t_c setting $a_1(t_c) = 0$; this results confirms a regular behaviour. From this it is clear that the kinematic properties of a pancaked ellipsoid depend both on the initial shape of the perturbation and on the density of the background universe.

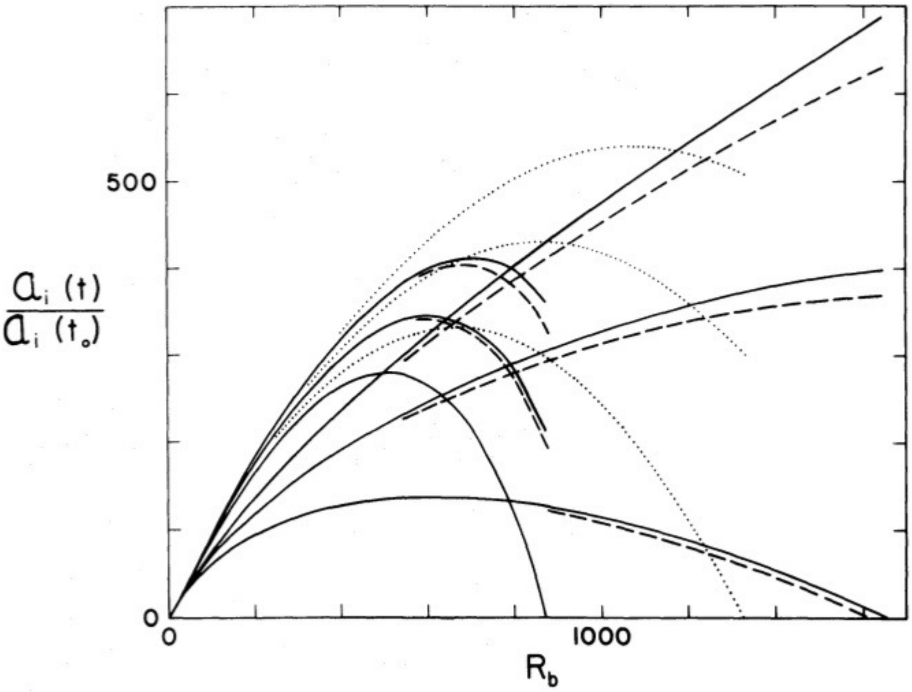

Figure 2.1: Evolution of homogeneous ellipsoidal perturbations in an expanding universe. Two models with the same initial density and Hubble constant are plotter; each has initial axes in the ratio 1:1.25:1.5. The solid lines stopping at $R_b = 873$ give numerical solutions for the relative expansion factors along the three axes of a perturbation in an Einstein-de Sitter universe as a function of the background scale factor. The other three solid lines stopping at $R_b = 1650$ refer to a universe with $\Omega < 1$ ($\Omega = 0.97$ initially and $\Omega = 0.02$ at collapse). The dashed lines are the predictions of the approximate equations and the dotted lines the predictions for the EdS case. (White and Silk 1979)

2.2 *Excursion sets* approach in ellipsoidal collapse: a moving barrier

The *excursion sets model* (Bond et al. 1991, [8]) describes how the assumption that objects form by spherical collapse (Press and Schechter) can be combined with the fact that the initial fluctuations distribution is gaussian, in order to predict $n(m,z)$. They assume that a region collapses at a time z if the initial overdensity within it exceeds a critical value $\delta_{sc}(z)$. This critical value depends on z, but is independent of the initial size of the region; the dependence is given by the spherical collapse model. They also assume that, given the Gaussian nature of the fluctuation field, a simple approximation of $n(m,z)$ is obtained by considering the barrier crossing statistics of many independent, uncorrelated random walks: the barrier shape $B(m.z)$ is given by the fact that δ_{sc} is independent of m. Numerical simulations show that the mass function predicted by this model may fail for small haloes (Lacey and Cole 1994 [31]; Sheth and Tormen 1999 [60]). This is not surprising, because many approximation are requested to reach a reasonably simple analytic solution. In particular, the spherical collapse model may not be accurate enough to describe the dynamics, because perturbation in Gaussian density field are triaxial. To incorporate the effects of non-spherical collapse in the standard formalism, Sheth, Mo and Tormen (2001) [59] consider the possibility of using a *moving barrier* for ellipsoidal collapse, instead of the fixed barrier of spherical collapse. In this approach, the effects of the background cosmology and power spectrum can be neatly separated: the cosmological model determines how δ_{sc} depends on z, whereas the shape of the power spectrum tells how the variance depends on scale r, so it fixes how σ depends on mass $m \propto r^3$.

Thus, in this excursion sets approach, to incorporate the effects of ellipsoidal collapse we need to determine the new barrier shape associated with the non-spherical dynamics. The initial shape of an ellipsoid can be specified by its initial overdensity and by the parameters e and p that characterize the asymmetry of the tidal field:

$$\boxed{\delta_i = \lambda_1 + \lambda_2 + \lambda_3, \qquad e = \frac{\lambda_1 - \lambda_3}{2\delta_i}, \qquad p = \frac{\lambda_1 + \lambda_3 - 2\lambda_2}{2\delta_i}} \tag{2.14}$$

where $\lambda_1 \geq \lambda_2 \geq \lambda_3$. Thus defined, e (≥ 0) is a measure of the ellipticity in the (λ_1, λ_3) plane, and p determines the oblateness ($0 \leq p \leq e$) or prolateness ($0 \geq p \geq -e$) of the tidal ellipsoid. Oblate spheroids have $p = e$, prolate spheroids have $p = -e$ and spheres have $e = p = 0$. In general the shortest axis (the one parallel to λ_1) will be the first to collapse to zero. When this happens our equations are no longer valid. However, in order to study the collapse of the whole ellipsoid, we need to make additional assumptions so as to integrate the equations of motion all the way to when the longest axis is considered to have collapsed. A common practice is to assume that all axes are frozen at the same radius equal to $(200)^{1/3}$ times the Lagrangian radius, so that the mean density within it is about 200 times the mean density of the universe at the time of collapse. This choice is somewhat arbitrary but tries to reproduce the virial density contrast obtained from the spherical collapse model, which was approximately 178.

Using the Bond & Myers (1996) [9] formalism, for an Einstein-de Sitter model a good approximation of the ellipsoidal barrier is given by solving

$$\boxed{\frac{\delta_{ec}(e,p)}{\delta_{sc}} = 1 + \beta \left[5(e^2 \pm p^2) \frac{\delta_{ec}^2(e,p)}{\delta_{sc}^2} \right]^{\gamma}} \tag{2.15}$$

for $\delta_{ec}(e,p)$; $\beta = 0.47$, $\gamma = 0.615$ and the plus (minus) sign is used if p is negative (positive) (Sheth, Mo & Tormen 2001, [59]).

As we can see in Figure 2.2, this approximate fitting formula is good to better than 10 percent or so. This figure shows also the dependence of δ_{ec} on σ and so on mass: low-mass haloes have a grater value of σ, which corresponds to higher ellipticities and also to a higher barrier.

Then the barrier height for the ellipsoidal collapse depends on the three numbers δ, e and p and in principle the problem of estimating the corresponding mass function is one of crossing a barrier in a higher dimensional space. However Sheth, Mo and Tormen (2001, [59]) suggested that the computational complexity could be reduced significantly if one used suitably chosen representative values for e and p. Thus, they derived s a reformulation of the fitting formula for the case $p = 0$: this is useful because in a Gaussian field on average $p = 0$. This can be seen from the distribution function of the three deformation tensor eigenvalues in a Gaussian density field, obtained by Doroshkevich

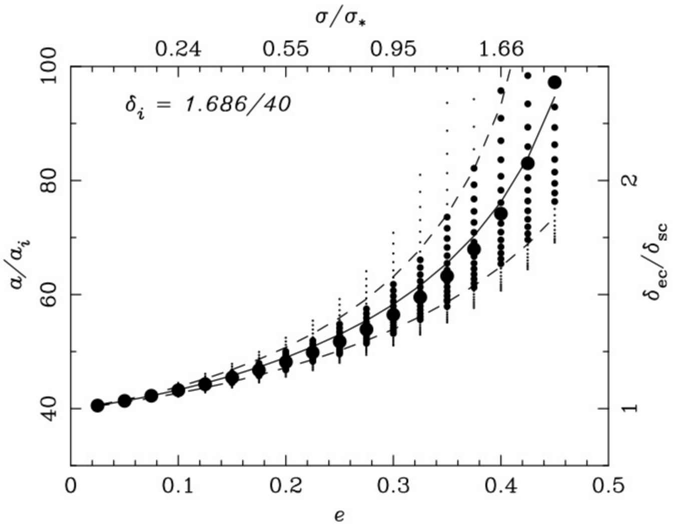

Figure 2.2: The evolution of an ellipsoidal perturbation in an Einstein-de Sitter universe. We see the expansion factor when the longest axis collapses and virializes, as a function of initial e and p. At a given e, the large, medium and small circles show the relation at $p = 0$, $|p| \leq e/2$, $|p| \geq e/2$, respectively. The solid curve show SMT fitting formula for the $p = 0$ result, and the dashed curves show $|p| = e/2$.

(1970):

$$P(\lambda_1,\lambda_2,\lambda_3) = \frac{675\sqrt{5}}{8\pi\sigma^6}\exp\left(-\frac{3I_1^2}{\sigma^2}+\frac{15I_2}{2\sigma^2}\right)(\lambda_1-\lambda_2)(\lambda_2-\lambda_3)(\lambda_1-\lambda_3) \tag{2.16}$$

where $\sigma^2 =< \delta_s^2 >$, $I_1 = \lambda_1+\lambda_2+\lambda_3$ and $I_2 = \lambda_1\lambda_2+\lambda_2\lambda_3+\lambda_3\lambda_1$. The equivalent expression, in terms of (e,p,δ) - Eq. 2.14 - is:

$$g(e,p,\delta|\sigma) = p(\delta|\sigma)g(e,p|\delta,\sigma) = \frac{\exp\left(-\frac{\delta^2}{2\sigma^2}\right)}{\sigma\sqrt{2\pi}}\frac{1125}{\sqrt{10\pi}}e(e^2-p^2)\left(\frac{\delta}{\sigma}\right)^5\exp\left[\frac{5}{2}\frac{\delta^2}{\sigma^2}(3e^2+p^2)\right]. \tag{2.17}$$

Doroshkevich's formula is the product of two independent distributions, a Gaussian for δ/σ, and another one made by a combination of the other five independent elements of the deformation tensor. Integrating the lastformula over δ yields the joint distribution of e and p (given δ_s):

$$P(e,p|\delta_s) = \frac{1125}{\sqrt{10\pi}}e(e^2-p^2)\left(\frac{\delta_s}{\sigma}\right)^5\exp\left[-\frac{5\delta_s^2}{2\sigma^2}(3e^2+p^2)\right] \tag{2.18}$$

Now, for all e this distribution peaks at $p = 0$. We must now find a suitable approximate value for e, which possibly relates it to the mass m: due to Gaussian probability, regions initially having a given value of δ/σ most probably have an ellipticity $e_{mp} = (\sigma/\delta)/\sqrt{5}$. To collapse and form a bound object at z, the initial overdensity of such a region must have been $\delta_{ec}(e_{mp},z)$. If we require that δ on the right-hand side for e_{mp} is equal to this critical value $\delta_{ec}(e_{mp},z)$, then this sets $\sigma^2(R_f)$. This provides a relation between e and mass, anche hence between δ_{ec} and mass. Inserting $p = 0$ and $e_{mp} = (\sigma/\delta)/\sqrt{5}$ in Equation 2.15, it is straightforward to compute the associated $\delta_{ec}(e,z)$.

$$\boxed{\delta_{ec}(\sigma,z) = \delta_{sc}(z)\left\{1+\beta\left[\frac{\sigma^2}{\sigma_\star^2(z)}\right]^\gamma\right\}} \tag{2.19}$$

where $\sigma_\star(z) = \delta_{sc}(z)$. We notice that, as in the spherical case, the power spectrum enters only in the relation between σ and m, whereas the effects of cosmology enter only in the relation between δ_{sc} and z. The last equation has a number of noticeable features:

- for massive objects, which have $\sigma/\sigma_\star < 1$, the equation suggests $\delta_{ec}(\sigma,z) \sim \delta_{sc}(z)$ and so the critical overdensity required for collapse at z si approximately independent of mass: this means that massive objects are well described by the spherical collapse model;
- we know that the critical overdensity increases with $\sigma(m)$, so it is larger for less massive objects: smaller objects are more influenced by external tides and so they must have a greater internal density if they have to hold themselves together as they collapse.

Now, using Equation 2.19 when setting $B(\sigma,z) = \delta_{ec}(\sigma,z)$, we can write a new mass function, for the ellipsoidal collapse *moving barrier*:

$$\boxed{\nu f(\nu) = 2A\left(1+\frac{1}{\nu^{2q}}\right)\left(\frac{\nu^2}{2\pi}\right)^{1/2} exp\left(-\frac{\nu^2}{2}\right)} \tag{2.20}$$

where $q = 0.3$ and $A \sim 0.32222$. This first crossings distribution differs from that predicted by the standard constant barrier model, for which $q = 0$ and $A = 1/2$. Using this equation, once the barrier shape is known, all the predictions of the excursions sets model can be derived easily.

2.3 The initial density field

Much about the halo evolution can bee understood by looking at the properties of the initial density field of the Universe; this is represented by the Initial Conditions (hereafter IC) of a simulation, which are generated at a sufficiently high redshift. As shown in the previous section, the Ellipsoidal Collapse model predicts that the properties of initial protohaloes are determinant for the entire evolution of large scale structures [59].

Moreover, according to the Tidal Torque Theory (hereafter TTT) [49], the origin of angular momentum can be found in the initial conditions and in particular from the cross-talk between the inertia **I** and shear **T** tensors. According to the TTT, the i-th component of the angular momentum can be written as:

$$L_i(t) = a^2(t)\dot{D}(t)\epsilon_{ijk}\mathrm{D}_{jl}\mathrm{I}_{lk} \tag{2.21}$$

where ϵ_{ijk} is the antisymmetric tensor and the two key quantities are the $deformation$ tensor and the $inertia$ tensor:

$$\mathrm{D}_{ij} = -\left.\frac{\partial^2\Phi}{\partial q_i^{'}\partial q_j^{'}}\right|_{\mathbf{q}^{'}=0}, \qquad \mathrm{I}_{ij} = \bar{\rho}_0 a_0^3 \int_\Gamma q_i^{'} q_j^{'} \mathrm{d}^3 q^{'} \tag{2.22}$$

where $\mathbf{q}$ is the Lagrangian position and $\mathbf{q}^{'} = \mathbf{q} + \bar{\mathbf{q}}$. Here we assume that the potential is varying smoothly within the volume Γ, such that it can be approximated by an expansion around the center of mass:

$$\Phi(\mathbf{q}^{'}) \simeq \Phi(\mathbf{0}) + \left.\frac{\partial\Phi}{\partial q_i^{'}}\right|_{\mathbf{q}^{'}=0} q_i^{'} + \frac{1}{2}\left.\frac{\partial^2\Phi}{\partial q_i^{'}\partial q_j^{'}}\right|_{\mathbf{q}^{'}=0} q_i^{'} q_j^{'}. \tag{2.23}$$

Only the traceless parts of the two tensor matter for the calculation of $L_i(t)$; these are the velocity $shear$ or $tidal$ tensor $T_{ij} = \mathrm{D}_{ij} - (\mathrm{D}_{ij}/3)\delta_{ij}$, and the traceless quadrupolar inertia tensor $\mathrm{I}_{ij} - (\mathrm{I}_{ij}/3)\delta_{ij}$. This means that, at first order, the angular momentum of the protohalo is generated by the gravitational coupling of the quadrupole moment of its mass distribution with the tidal field coming from the neighbouring density fluctuations: it is due to the misalignment of the principal axes of the two tensors.

In simulations, the protohalo regions are defined by tracing all the particles of the final virialized haloes back to the ICs, and so to their Lagrangian positions. Then, for each protohalo, one can compute the Lagrangian inertia tensor as

$$\mathrm{I}_{ij} = m\sum_{n=1}^{N} q_i^{'(n)} q_j^{'(n)}, \tag{2.24}$$

where the $\mathbf{q}^{'(n)}$ are the positions of each particles with respect to the center of mass. The shear tensor of the protohalo is calculated by smoothing the potential and differentiating it twice with respect to the spatial coordinates. The equivalent of this is smoothing the initial (Zel'dovich) displacements and differentiating them once with respect to the coordinates. Porciani et al. (2002, [50]) calculated the misalignments between the two tensors, as shown in Figure 2.3. The eigenvectors $\hat{i}_k$ and $\hat{t}_k$ are labelled in sich a way that the corresponding eigenvalues are $i_1 \geq i_2 \geq i_3$ and $t_1 \leq t_2 \leq t_3$. Thus, i_1 is the longest axis of the protohalo mass distribution and t_1 is the direction of maximum compression.

The highest correlation is in the bottom-right panel (cosine almost equal to 1), indicating a very strong alignment between the minor axes of the two tensor and thus between the smallest axis of the mass distribution and the direction of least compression/expansion. The second highest correlation indicates a quite strong alignment also between the two major axes, while the alignment between the intermediate ones is weaker. These values show a tendency for orthogonality between the major axis of one tensor and the minor axis of the other, which is confirmed by the anti-correlations in the

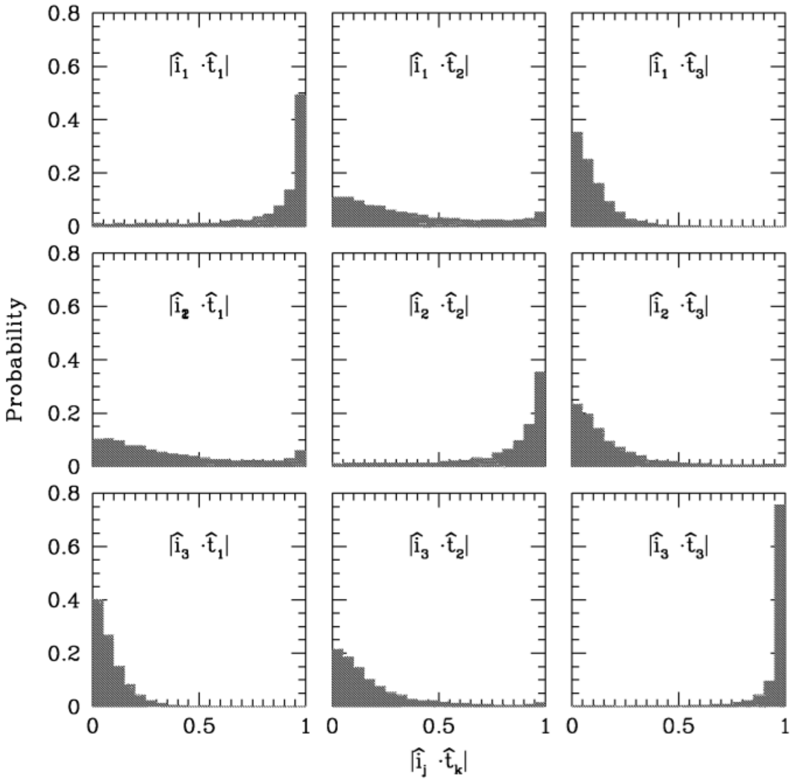

Figure 2.3: Alignments of I and T. The eigenvectors $\hat{\imath}_k$ and $\hat{t}_k$ are labelled in sich a way that the corresponding eigenvalues are $i_1 \geq i_2 \geq i_3$ and $t_1 \leq t_2 \leq t_3$. From Porciani et al. 2002 [50].

bottom-left and top-right panels. Figure 2.4 shows a few examples of the correlation between the two fields, ina regions of the simulation box.

The implication of the alignment between the two tensors is that protohalo spins are due to small residuals from this correlation. It also indicates that the tidal field plays an important role in determining the positions and shapes of protohaloes: the largest compression flow towards the center is along the major inertia axis, since this is required to compress the elongated protohalo into the more spherical and concentrated shape at virialization.

2.4 Evolution equations

The equations giving a full description of triaxial collapse must be solved numerically in general, since the evolution does not have a simple analytical solution. In this section we discuss an accurate analytical approximation to the evolution, developed by Shen et al. (2006) [57] and then by Rossi et al. (2011) [54], which results to more accurate than the Zel'dovich approximation [71].

The initial shear field is usually characterised by the ellipticity e and prolateness p of the initial potential field: the components of the 3×3 initial deformation tensor are the second derivatives of the potential field. Its eigenvalues can thus be expressed as a function of (δ_i, e, p), as already explained

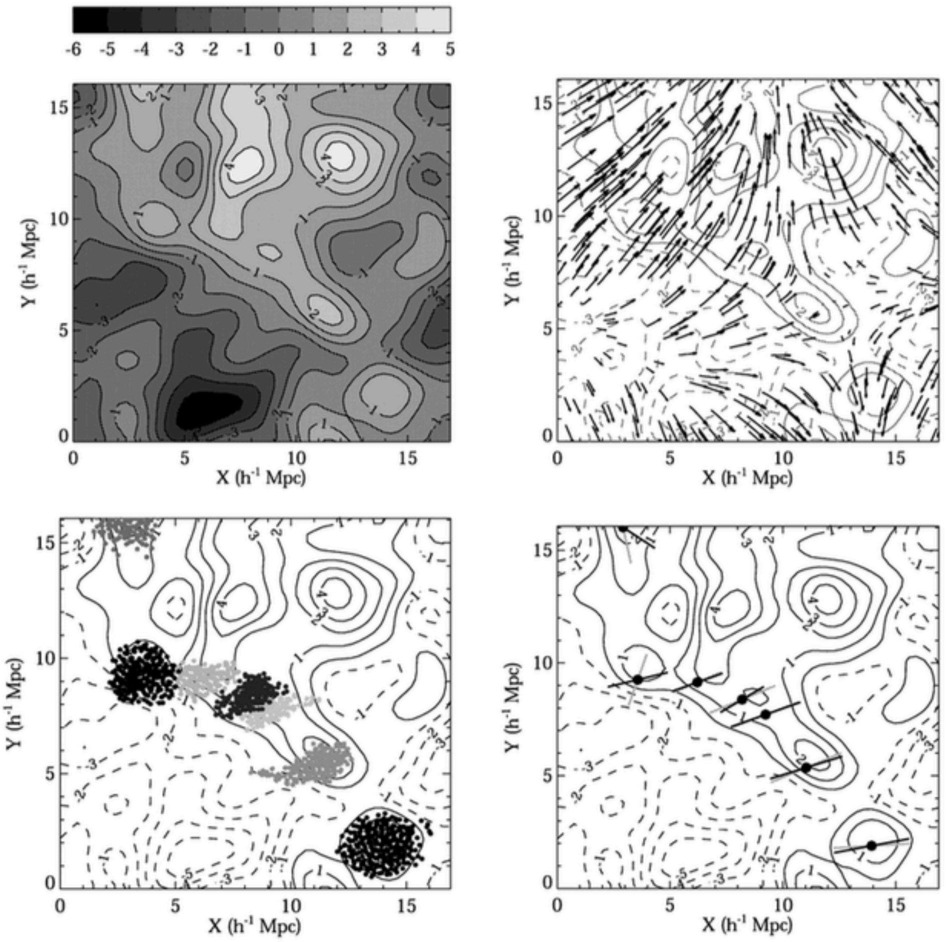

Figure 2.4: Examples of the correlation between the two fields. The top panels show maps of the density ($left$) and velocity $right$) fields at $z = 50$; the contours refer to the density contrast linearly extrapolated to $z = 0$. The bottom panels show all the protohaloes whose contres of masses lie within one smoothing length of the plane; the left panel shows the projection of the protohalo particle positions and the right panel the projections of the major axes of the inertia tensor (dark lines) and the shear tensor (light lines). From Porciani et al. 2002 [50].

in the previous sections:

$$\begin{aligned} \lambda_1 &= \frac{\delta_i}{3}(1+3e+p) \\ \lambda_2 &= \frac{\delta_i}{3}(1-2p) \\ \lambda_3 &= \frac{\delta_i}{3}(1-3e+p) \end{aligned} \tag{2.25}$$

with $\lambda_1 > \lambda_2 > \lambda_3$,$\sum_j \lambda_j = \delta_i$ and so $e \geq 0$, $-e \leq p \leq e$. Then, the scale factors of the three principal axes of the ellipsoid are set by the Zel'dovich approximation [71]:

$$A_k(t_i) = a(t_i)([1-\lambda_k(t_i)] \tag{2.26}$$

where now $A_3 \geq A_2 \geq A_3$, meaning that at the initial conditions the shortest axis of the ellipsoid is aligned with the direction of maximum compression of the potential field and $viceversa$ the longest axis is aligned with the minimum compression. The full evolution is given by (Bond & Myers 1996

[9]):

$$\boxed{\frac{\mathrm{d}^2 A_k}{\mathrm{d}t^2} = -4\pi G\bar{\rho}A_k\left(\frac{1+\delta}{3} + \frac{b_k^{'}}{2}\delta + \lambda_{ext,k}^{'}\right)} \tag{2.27}$$

where $r\bar{h}o = a^{-3}$ is the mean density of the universe and the two last terms account, respectively, for the interior and exterior tidal forces. More precisely

$$b_k^{'}(t) = b_k(t) - \frac{2}{3} = A_1(t)A_2(t)A_3(t)\int_0^\infty \frac{d\tau}{[A_k^2(t)+\tau]\prod_{m=1}^{3}[A_m^2(t)+\tau]^{1/2}} \tag{2.28}$$

and

$$\lambda_{ext,k}^{'}(t) = \frac{a}{a_i}\lambda_k^{'}(t) = \frac{a}{a_i}\left[\lambda_k(t) - \frac{\delta_i}{3}\right]. \tag{2.29}$$

If the tidal force terms are not included, these equations reduce to the spherical collapse ones: if $e = p = 0$ all the three eigenvalues are equal to $\delta_i/3$ and an initially spherical object remains spherical. Otherwise, an initially spherical regions is deformed by the tidal forces into a collapsing homogeneous ellipsoid.

Given an initial set of (δ, e, p) values, equation 2.27 must be solved numerically for each axis: the result can be seen in Figure 2.5 which shows the physical evolution of axis lengths for many combinations of the initial values. However, a similar result can be obtained using an analytic approximation: Shen et al. (2006, [57]) show how to extend the approximation provided by White & Silk (1979, [70] - already described in the previous sections - so that it redices self-consistently to the Zel'dovich approximation at early times. The axis lengths can then be written as:

$$A_k(t) \simeq \frac{a(t)}{a_i}A_k(t_i)[1 - D(t)\lambda_k] - \frac{a(t)}{a_i}A_h(t_i)\left[1 - \frac{D(t)\delta_i}{3} - \frac{a_e(t)}{a(t)}\right], \tag{2.30}$$

where $A_h(t_i) = 3/\sum_k A_k(t_i)^{-1}$, $D(t)$ is the linear theory growth mode and $a_e(t)$ is the expansion factor of a universe with initial density contrast $\delta_i = \sum_k \lambda_k(t_i)$. We can see that the first term is the Zel'dovich approximation [71] to the evolution and that this approximation is exact for the case of a sphere (for which $\lambda_i = \lambda = \delta_i/3$. The left panel of Figure 2.6 show the approximation together with the full numerical solution of the EC model and the Zel'dovich approximation [71]: it is easy to see that equation 2.30 is significantly more accurate than the Zel'dovich approximation. The right panel shows the results from Rossi et al. (2011, [54]), where δ_0 is equal to 1.6753 instead of 2; again, the approximation given by Equation 2.30 works very well for the adopted ΛCDM model. The numerical solution would allow each axis to shrink to arbitrarily small sizes, but all works stop collapse along each axis at a non-negligible freeze-out radius, which is $A_k = 0.177a$ for and Einstein-de Sitter model: in this way the final object is 178 times denser than the background universe, as in the Spherical Collapse model. This $freeze - out$ moment can be seen both in Figure 2.5 and in the right panel of Figure 2.6. The critical density required for collapse by the present time is well approximated by

$$\delta_{ec}(e,p) \simeq \frac{\delta_{sc}}{1 - \beta\sqrt{5(e^2 \pm p^2)}}. \tag{2.31}$$

Since the initial values of λ_k and a_i yield the initial (δ_i, e, p), the collapse model provides an estimate of the freeze-out time for each axis. Figure 2.7 (from Shen et al. 2006 [57]) shows the critical densities for collapse along one, two and three axes (from bottom to top) at $z = 0$, for $p = 0$ and $e = (\sigma/\delta)/\sqrt{5}$.

From equation 2.30, we can also derive - to first order in $\delta(t_i)$:

$$\frac{A_{1,3}(t)}{A_{1,3}(t_i)}\frac{a(t_i)}{a(t)} \simeq \frac{a_e(t)}{a(t)} - \frac{\delta(t_i)}{3}(p \pm 3e)\left[1 + \frac{D(t)}{D(t_i)} - \frac{a_e(t)}{a(t)}\right] \tag{2.32}$$

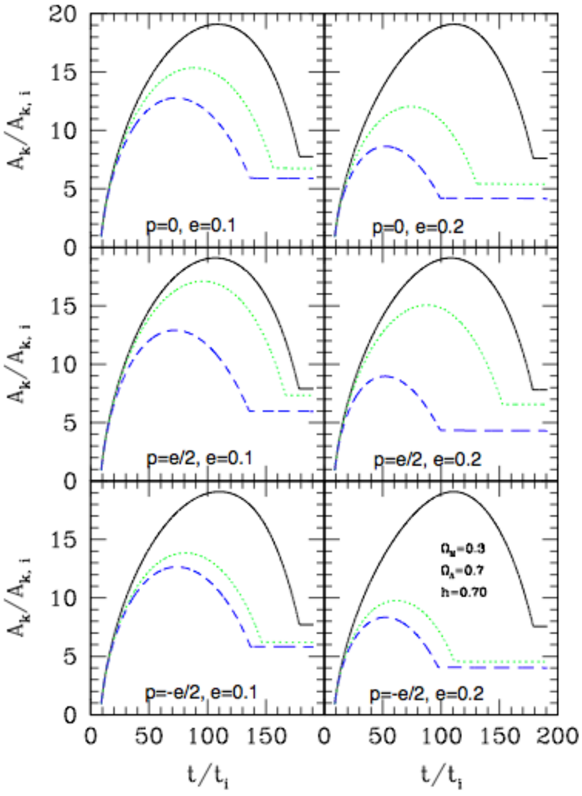

Figure 2.5: Evolution (in physical coordinates) of axis lengths in the EC model; the initial (δ,e,p) values are specified in each panel (from Rossi et al. 2011 [54]).

$$\frac{A_2(t)}{A_2(t_i)}\frac{a(t_i)}{a(t)} \simeq \frac{a_e(t)}{a(t)} + \frac{\delta(t_i)}{3}2p\left[1+\frac{D(t)}{D(t_i)} - \frac{a_e(t)}{a(t)}\right]. \tag{2.33}$$

It is easy to notice that, when $p = 0$, the second axis evolves exactly as in the spherical model:

$$\frac{A_2(t)}{A_2(t_i)} \simeq \frac{a_e(t)}{a(t)}. \tag{2.34}$$

In this respect, a spherical collapse can be imagined as an imperfect ellipsoidal collapse, where the virialization is identified with the collapse of the second axis.

2.5 A recent extension of the EC model

We have seen how one of the limitation of the EC model is considering initially spherical protohaloes. In 2014, two works by Ludlow, Borzyszkowski and Porciani [36, 10] presented an extension of the model which aims to fill this gap. The initial motivation for this extended model resides in the fact that, even if the agreement between the EC model and simulations is quite remarkable, there are still some inconsistencies. Even though their results are extremely interesting, their works have been published very recently and so we will not directly compare with them in this thesis. Nevertheless, we find it worth to mention some of their results between the others on ellipsoidal collapse and we plan to make a comparison with their work in the future.

In the EC model, the initial overdensity δ_i is a fundamental quantity: it is thought to depend on the properties of the tidal field, rather than on those of (proto)haloes. In the left panel of Figure 2.8,

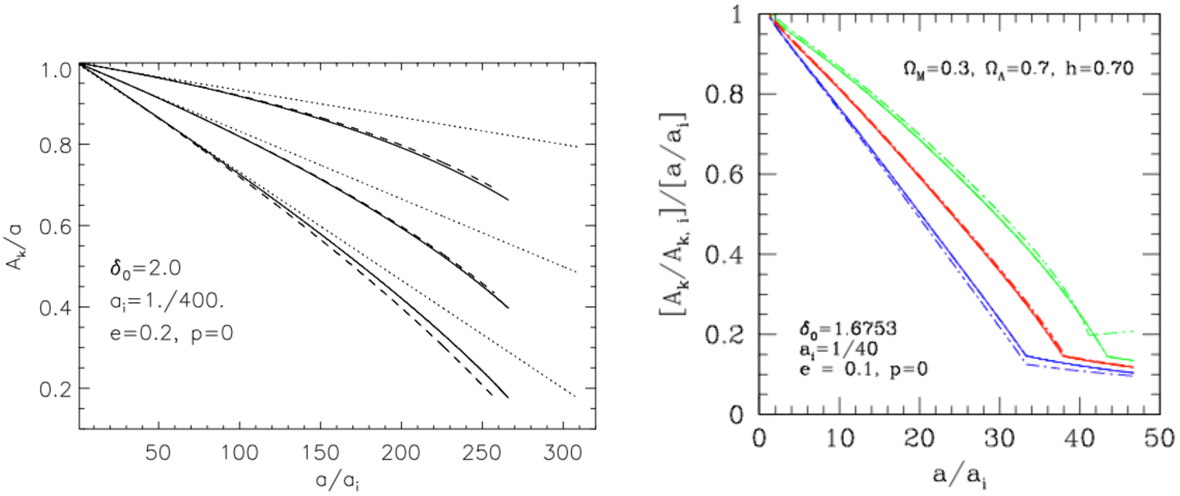

Figure 2.6: Comoving evolution of axis lengths in the ellipsoidal model. *Left*: results from Shen et al. 2006 [57] - the full EC model is represented by the solid lines, the Zel'dovich approximation [71] by the dotted ones and the analytic approximation (for an Einsten-de Sitter model) by the dashed lines. *Right*: from Rossi et al. 2011 [54] - the solid line show the numerical solution of equation 2.27, while the dashed-dotted ones show the analytic approximation; in this case δ_0=1.6753 instead of 2.

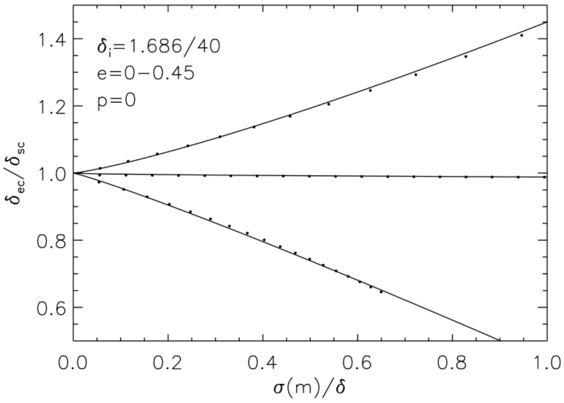

Figure 2.7: Dependence of barrier height on mass for collapse along one, two or three axes (bottom to top) at $z = 0$, for $p = 0$ and $e = (\sigma/\delta)/\sqrt{5}$ (Shen et al. 2006 [57]).

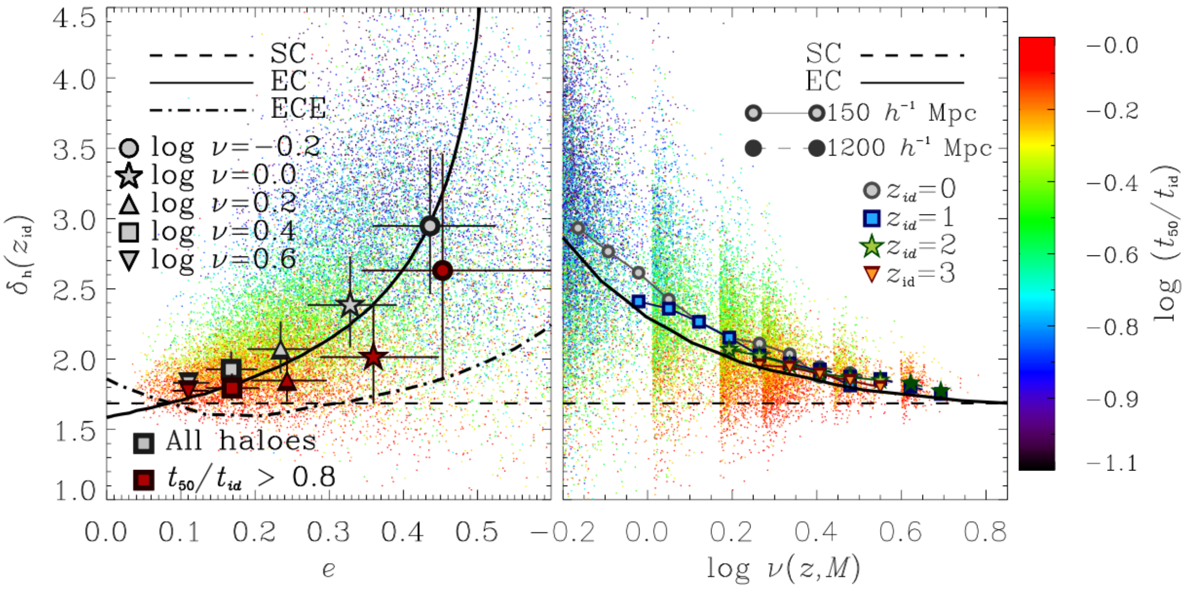

Figure 2.8: Lagrangian overdensities of protohaloes plotted as a function of the ellipticity (left) and overdensity (right) of the surrounding tidal field. $Left$: the authors plot the linear overdensity (extrapolated to $z = 0$), as a function of ellipticity. The cloud of points shows the distribution of all the haloes with more than 500 particles (FOF), identified at redshifts z=0, 1, 2, 3; the points are colour-coded with respect to formation time (t_{50}/t_{id}). The heavier and bigger symbols show the median values for five bins in ν, for all haloes (gray) or only for recently formed ones (red). The solid lines corresponds to the collapse threshold predicted by Bond & Myers 1996 [9], while the horizontal dashed lines indicates $\delta_i = 1.686$. $Right$: mss dependence of the initial overdensity. The colour code is the same of the left panel, while here different symbols represent the median values for haloes identified at each redshift.

the authors plot the linear overdensity (extrapolated to $z = 0$), as a function of ellipticity. the cloud of points shows the distribution of all the haloes with more than 500 particles (FOF), identified at redshifts z=0, 1, 2, 3. The heavier and bigger points show the median values for five bins in ν. The solid lines corresponds to the collapse threshold predicted by Bond & Myers 1996 [9]. The agreement between the theoretical model and the simulations is remarkable, even if there is still large scatter both in δ anf e. The points are colour-coded with respect to formation time (t_{50}/t_{ide}) and it is interesting to note that the majority of recently collapsed objects (both the red dots and the big red points) lie below the theoretical prediction, even if they are expected to trace the solid lines better than haloes which formed earlier. Finally, the right panel of Figure 2.8, shows the mass dependence of the initial overdensity: as expected and as found in other works, the median overdensity decreases with increasing mass, even if the scatter is still considerable.

To partially reduce the scatter and design a more realistic model, in these two works the authors include many effects into the theoretical formulation of the EC model, such as initial triaxiality, the effect of the external field and of the formation time. They consider an uniform density perturbation in an otherwise unperturbed Friedmann-Robertson-Walker background whose energy content is dominated by the matter density ρ_m and a cosmological constant, Λ. They model the perturbation as a homogeneous ellipsoid with semi-axes of physical length r_i (i = 1,2,3) and density contrast δ: thus, the initial protohaloes have a triaxial shape given by the r_is and is not a sphere. In this framework, the axis lengths will obey the following equation of motion:

$$\frac{\ddot{r}_i}{r_i} = \frac{\Lambda c^2}{3} - 4\pi G\rho_b\left(\frac{1+\delta}{3} + \frac{\beta_i}{2}\delta + \lambda_i^{ext}\right), \tag{2.35}$$

as in equation 2.27. They assume that external tides are dominated by large-scale structure and approximate their evolution ac- cording to linear theory, i.e. $\lambda^{ext}(t) \simeq \lambda^{ext} D(t)$. The perturbation therefore remains homogeneous at all times and satisfies

$$1 + \delta = \frac{q_1 q_2 q_3}{r_1 r_2 r_3} (1+z)^3, \tag{2.36}$$

where the q_is denote the initial comoving principal axis lengths of the ellipsoid. In Figure 2.9 we can see the resulting evolution of the axis lengths for collapsing ellipsoids, when the initial shape varies; the numerical calculations start at t0 = 0.250 Myr and assume always the same initial density contrast δ. Comparing these curves with the ones in Figure 2.5 , we see how relaxing the assumption of spherical symmetry substantially changes the collapse times of each axis: the left panels assume an initial triaxiality with axial ratios $q_2/q_1 = q_3/q_2 = 0.8$ and this is enough to perturb the collapse order and the general form of the curves. What it is clear at first sight is that an initial triaxiality allows a greater variety of evolution patterns: the axis ordering may change in time and this could give an interpretation to the misalignments between the initial and final axes. As we wil see in Chapter 6, when examining the axis evolution of individual haloes, we found that they do not follow a fixed pattern and that the three axes may cross and reorder: a future comparison between our numerical results and the prediction of Ludlow, Borzyszkowski and Porciani [36, 10] will be important to test their validity.

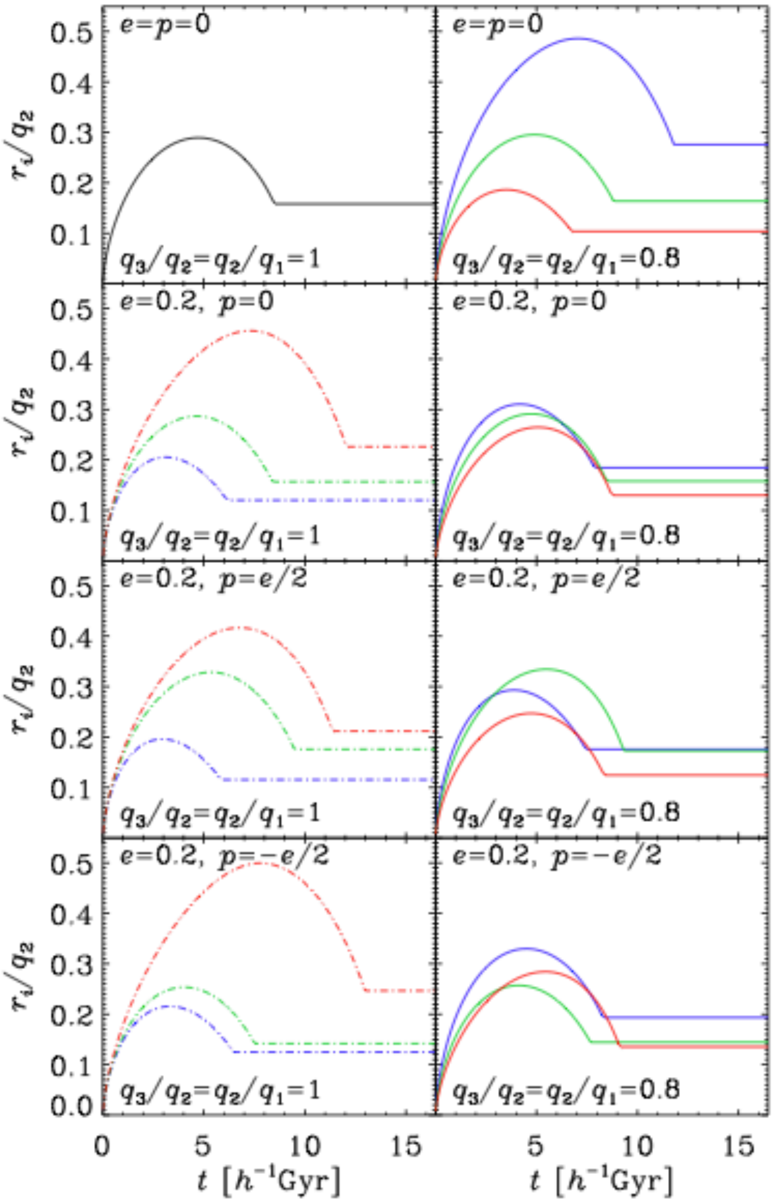

Figure 2.9: Evolution of the axis lengths for collapsing ellipsoids, expressed in units of the initial intermediate axis length, q_2. Left panels assume the initial overdensity is a uniform sphere, as in the model of Bond & Myers 1996 [9]; right-hand panels adopt an initially triaxial overdensity with axis ratios $q_2/q_1 = q_3/q_2 = 0.8$. Top panels assume negligible tidal forces. Lower panels have a (total) tidal field ellipticity of e = 0.2, and show results for three different prolaticities. Note that relaxing the assumption of spherical symmetry substantially changes the collapse times of each axis (from Ludlow et al. 2014 [36]).

Cosmological simulations 3

In this chapter we will describe the state of the art of cosmological simulations in general and the data used in this work. We used data from the GIF2 simulation [20] and the Millennium XXL simulation [3]; then, we run our own set of cosmological simulations, called Le SBARBINE simulations, which will be described in detail in section 3.4.

3.1 State of the art

Cosmological simulations constitute the natural tool to study structure formation. Analytical models are able to describe it up to a certain level, but the equations cannot be fully solved in the non-linear regime. Thanks to new technologies and the increase of computational resources, simulations have developed to an unprecedented level in the last years, becoming larger, faster to run and better resolved. Moreover, more physics has been included in the codes, providing a more and more precise reproduction of the real Universe.

GADGET

GADGET, in its first [62] and second [61] versions, is one of the most common codes to run cosmological simulations. Designed and developed by Volker Springel, it can be use to adress many astrophysical and cosmological problems, ranging from merging galaxies to the evolution of large scale structures.

It describes the dynamics of a collisionless component (dark matter or stars in galaxies) and of an ideal gas (baryons - mostly hydrogen and helium):

1. the non-interacting dark matter is described by the collisionless Boltzmann equation coupled to the Poisson equation, in an expanding background universe; the problem is multi-dimensional and so the equations are solved with the N-body method, where phase-space density is sampled with a finite number N of tracer particles. Their dynamic is described by the Hamiltonian:

   $$H = \sum_i \frac{p_i^2}{2m_i a(t)^2} + \frac{1}{2}\sum_{ij} m_i m_j \phi(x_i - x_j) a(t) \tag{3.1}$$

   where x_i are the comoving coordinate vectors, and the corresponding momenta are given by $p_i = a^2 m_i \dot{x}_i$. The gravitational force is computed with a TreePM method, where the tree is used for short-range gravitational forces only, while long-range forces are computed with a FFT-based particle-mesh (PM) scheme.

2. fluids are represented by means of Smoothed Particles Hydrodynamics (SPH): a set of discrete tracer particles describes the state of a fluid, while continuous fluid quantities are defined by an

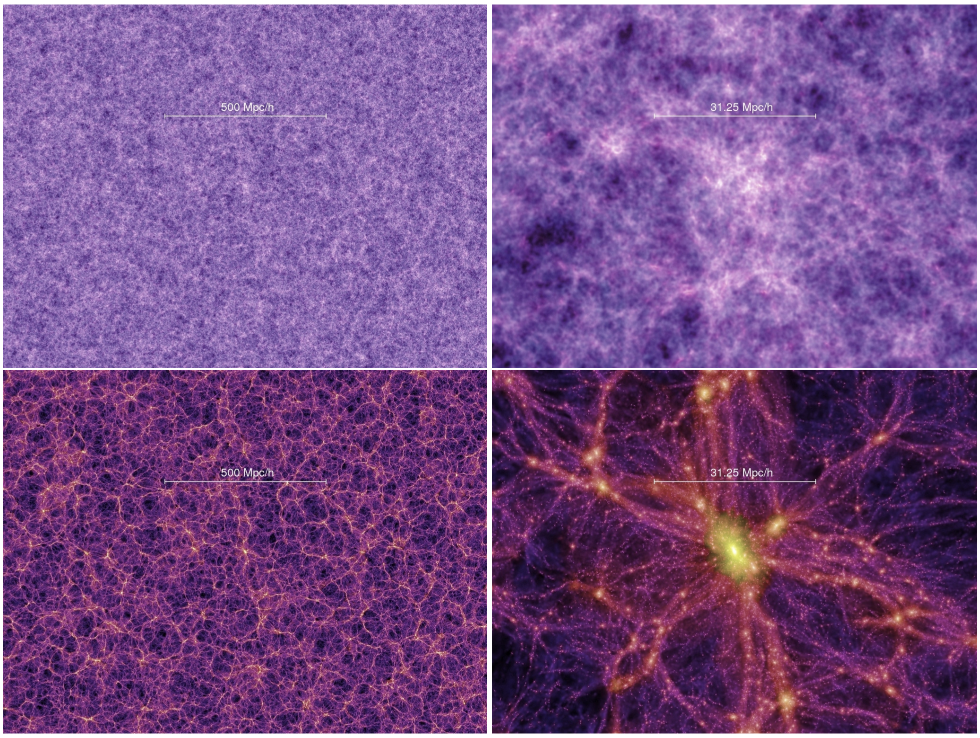

Figure 3.1: Snapshots from the Millennium Simulation (Springel, 2005), created with 2163^3 particles in a box of $500 Mpch^{-1}$. On top we see the dark matter distribution at z=18.3; a big region on the left and a smaller enlarged region on the right. Below we can see the same, but for $z = 0$. It is clear that, as time goes by, more and more structure are formed and the web of filaments and pancakes develops.

name	year	N	box[Mpc/h]	z_i	$m_p[M_\odot/h]$	soft[kpc/h]	Ω_m	Ω_Λ	h	σ_8
GIF2	2004	400^3	110	49	1.73×10^9	7	0.3	0.7	0.7	0.9
Mill	2005	2163^3	500	127	8.6×10^8	5	0.25	0.75	0.73	0.9
Mill-II	2009	2163^3	100	127	6.89×10^6	1	0.25	0.75	0.73	0.9
MXXL	2012	6720^3	3100	63	8.46×10^9	13.7	0.25	0.75	0.73	0.9
Bolshoi	2010	2048^3	250	80	1.35×10^8	1	0.27	0.73	0.7	0.82

Table 3.1: Features of some of the main simulations used in the field. The GIF2 [20] Millennium Simulation [61], the Millennium II [11], Bolshoi simulation [29] and the the Millennium XXL [3] .

interpolation technique. The equations of motion for the SPH particles are given by

$$\frac{dv_i}{dt} = -\sum_{j=1}^{N} m_j \left[f_i \frac{P_i}{\rho_i^2} \nabla_i W_{ij}(h_i) + f_j \frac{P_j}{\rho_j^2} \nabla_i W_{ij}(h_j) \right]. \tag{3.2}$$

Moreover, a number of further physical processed have been implemented in GADGET-2, as radiative cooling/heating by photoionisation, star formation and associated feedback, galactic winds and metal enrichment.

Many cosmological simulations have been run using versions of GADGET, as the Millennium Simulation [61] (Figure 3.1), the Millennium II [11] and the Millennium XXL [3]. The features of the main simulations used in the field are listed in Table 3.1.

A simulated “real” universe

Several generations of publicly available models based on the Millennium Simulation have produced ever closer matches to the observed galaxy population and have been widely used by the community. This success reflects the fact that simulations of this kind make it possible to construct mock surveys where the simulated galaxy population is "observed" with a virtual telescope to produce a sample in which galaxy properties and the large-scale structure can be compared directly with those observed in real surveys. Such comparisons can be used to test the effectiveness of observational procedures for identifying galaxy groups and clusters and for measuring their masses. In Figure 3.2 [19] we see a proof of the accuracy of simulations: the mock catalogues constructed from the Millennium Simulation look amazingly similar to the real catalogues derived from galaxy surveys.

3.2 The GIF2 simulation

The GIF2 Simulation [20], run by Gao et al. (2004), adopts a ΛCDM cosmological model with $\Omega_m = 0.3$, $\Omega_\Lambda = 0.7$, $\sigma_8 = 0.9$ and $h = 0.7$. It follows 400^3 particles in a periodic cube of side $110h^{-1}$ Mpc from an initial redshift $z = 49$ to the present time; it contains only dark matter particles. The associated change in the linear theory growth factor is $D_+(z=0)/D_+(z=49) = 38.993$ and the individual particle mass $1.73 \times 10^9 h^{-1}\ M_\odot$. Initial conditions were produced by imposing perturbations on an initially uniform state represented by a glass distribution of particles [69]; based on the Zel'dovich approximation [71], a Gaussian random field is set up by perturbing the positions of the particles and assigning them velocities according to the growing model solution of linear theory. The critical value of the linear theory overdensity that is required for spherical collapse at the present time is $\delta_c = 1.6755$. In order to save computational time, the simulation was performed in two steps: until z = 2.2, with the parallel SHMEM version of HYDRA and then completed with GADGET [62], which has better performance in the heavily clustered regime.

Our group has access to all the 53 snapshots of the simulation: thus, we could directly analyse the data, running all the post-processing described in the following sections.

3.3 The Millennium XXL simulation

With a box side of 3 Gpc h^{-1} (4.1 Gpc), the Millennium XXL simulation (Angulo et al. 2012 [3]) was especially tailored to study massive haloes which can be only found in very large volumes, because of their nature of extremely rare objects and due to the dampening of large fluctuation modes in smaller boxes. It was produced with an optimised version of P-GADGET3, which improves the scalability and memory efficiency of the code considerably and it is very efficient for dark-matter-only simulations. The $6720^3 \approx 3 \times 10^{11}$ dark matter particles have a mass of 6.174×10^9 $\mathrm{M}_\odot h^{-1}$; the Plummer-equivalent softening length is $\epsilon = 13.7$ kpc. For reasons of consistency with the previous Millennium runs, the adopted ΛCDM cosmology is the WMAP one: total matter density $\Omega_m = 0.25$, baryons density $\Omega_b = 0.045$, cosmological constant $\Omega_\Lambda = 0.75$, power spectrum normalisation $\sigma_8 = 0.9$ and dimensionless Hubble parameter $h = 0.73$.

The simulation resolves large-scale structure with an unprecedented combination of volume and detail. The enormous statistical power of the simulation is hinted at in Figure 3.3, which shows the projected density field on very large scales and for the largest cluster found at z=0.

We used this simulation to study in detail the shapes of galaxy-cluster-size haloes, as will be explained in Chapter 7. Two snapshots (redshift 0 and 1) have been transferred to the servers at LAM (Laboratoire d'Astrophysique de Marseille), where Mario Bonamigo run the main analyses on the data.

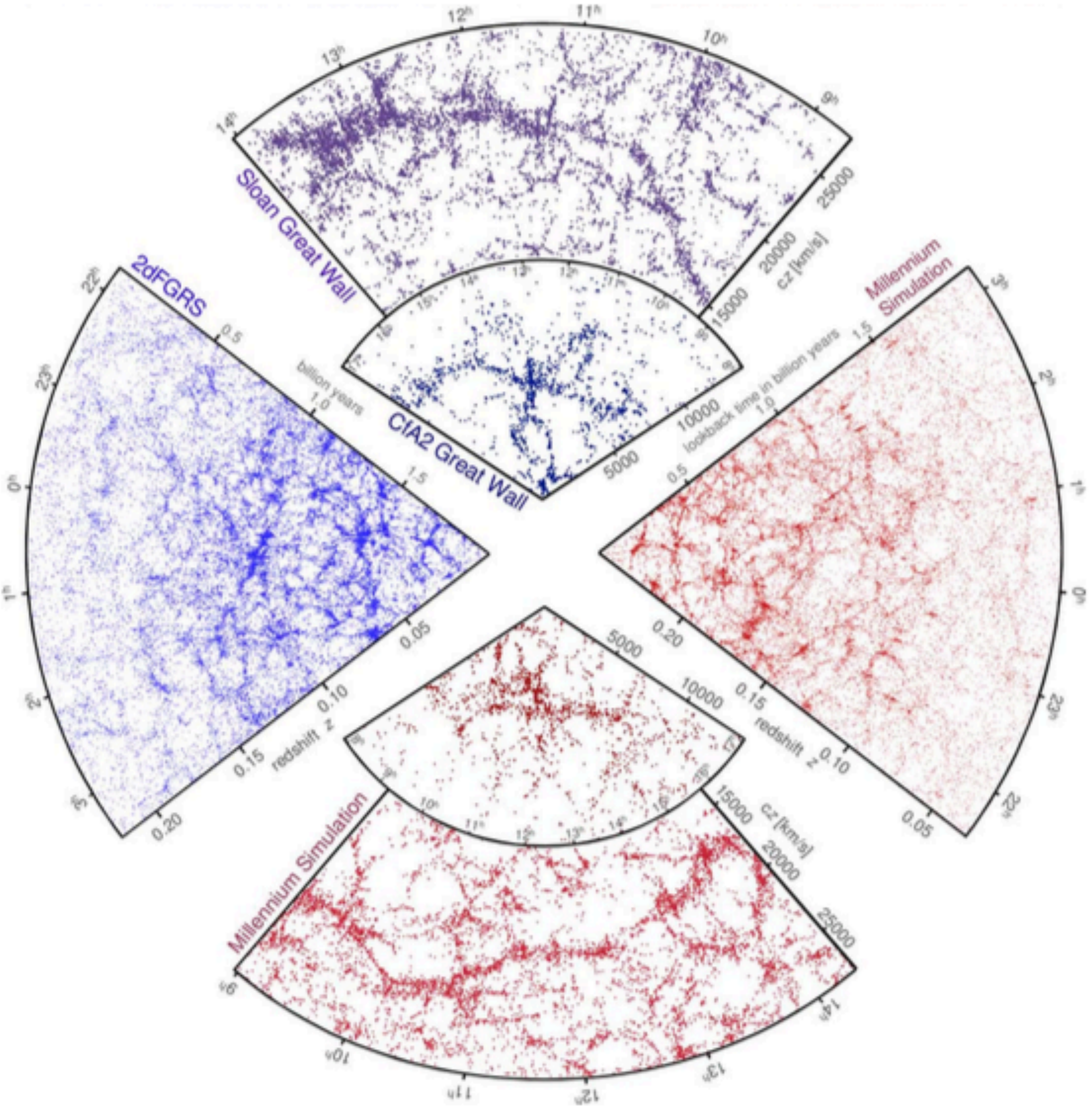

Figure 3.2: A proof of the accuracy of simulations: the galaxy distribution in redshift surveys and in mock catalogues constructed from the Millennium Simulation. The small slice at the top shows the CfA2 “Great Wall” , with the Coma cluster at the centre. Drawn to the same scale is a small section of the SDSS, with the even larger “Sloan Great Wall” . The cone on the left shows one half of the 2-degree galaxy redshift survey (the 2dFGRS) . The cones at the bottom and on the right correspond to mock galaxy surveys with similar geometries and magnitude limits constructed by applying semi-analytic galaxy formation simulation methods to the halo/subhalo assembly trees of the Millennium Simulation. From Frenk & White 2012 [19].

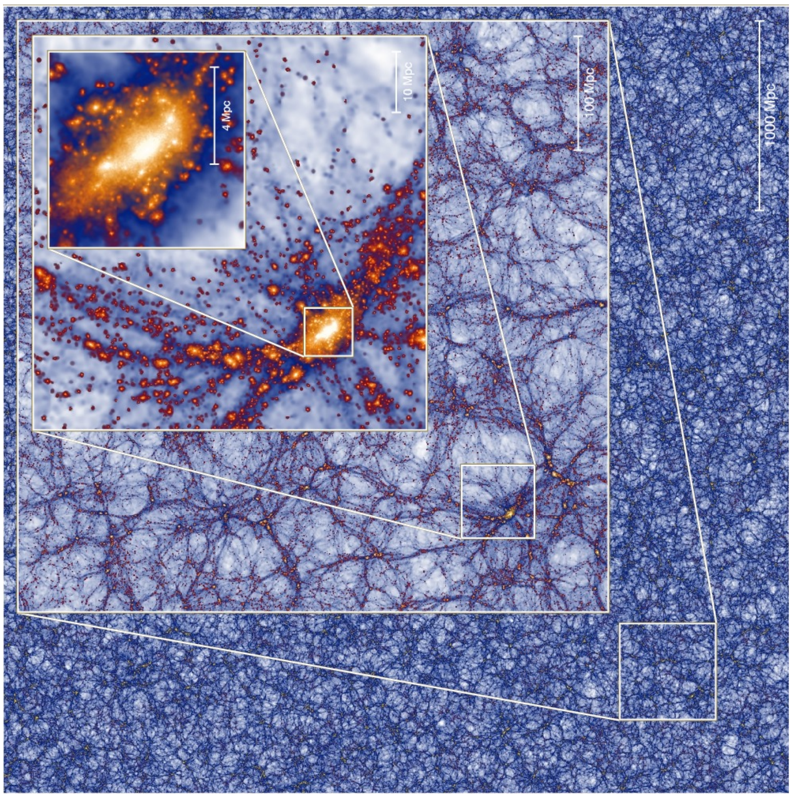

Figure 3.3: The mass density field in the Millennium-XXL focusing on the most massive halo present in the simulation at z=0. Each inset zooms by a factor of 8 from the previous one; the side-length varies from 4.1 Gpc down to 8.1 Mpc. All these images are projections of a thin slice through the simulation of thickness 8 Mpc.

3.4 Le SBARBINE simulations

In 2013 we decided to update our database with some new simulations: we run a set of 6 cosmological simulations, using the publicly available code GADGET-2 [61]; the simulations were completed in 2014. Their main features are listed in Table 6.1 and will be described in the following sections. We chose to use the latest cosmology from Planck [47]: $\Omega_m = 0.30711$, $\Omega_\Lambda = 0.69289$, $\Omega_b = 0.04825$, $h_0 = 0.6777$.

All the runs were made with 1 billion (1024^3) particles and the six simulations are named in alphabetical order, with increasing box sizes. On the whole, they contain more than 22 millions of haloes, which reduce to 250000 if we consider only haloes with more than 1000 particles. The SBARBINE simulations constitute an ideal set to study halo properties for a multiplicity of reasons:

1. a good spatial and mass resolution is granted by varying the box and the particle mass accordingly to each other: in this way, dark matter haloes of all masses will be formed by many particles, reducing the risk of resolution effect;

2. these simulations provide a large statistic, but are not too heavy to analise as some other recent simulations (as the Millennium XXL [2]) - each simulation weights 1.8 Tb and each of the 55 snapshots around 33 Gb;

3. since the mass range of each simulation overlaps with the one of the tow “neighbours”, we can again check for and take into account resolution effects.

name	box [Mpc h^{-1}]	z_i	$m_p[M_\odot h^{-1}]$	soft [kpc h^{-1}]	$N_{h-tot}(z=0)$	$N_{h>1000}(z=0)$
Ada	62.5	124	1.94×10^7	1.5	2264847	36561
Bice	125	99	1.55×10^8	3	2750411	44883
Cloe	250	99	1.24×10^9	6	3300880	54467
Dora	500	99	9.92×10^9	12	3997898	58237
Emma	1000	99	7.94×10^{10}	24	4739379	38636
Flora	2000	99	6.35×10^{11}	48	5046663	5298

Table 3.2: Main features of the simulations. The last two columns report the total number of SO haloes with more than 10 and 1000 particles, at redshift $z = 0$.

Initial conditions

The initial power spectrum for all the simulations was generated with the public software CAMB [33]. Apart from the main cosmological parameters, CAMB allows also to add some extra-features, as the primordial BAO. The resulting power spectrum can be seen in Figure 3.4, where is represented by the gray lines: the BAO are visible at the left tail of the lines. The initial conditions has been build with the public code N-GenIC, which requires as input parameters:

i) the initial $P(k)$
ii) a $glass$ file with positions
iii) the desired features of the simulation (number of particles, cosmological parameters, ...)
iv) a random number used to generate the Initial particle positions from the $glass$ file.

A $glass$ distribution of particles can be obtained using a special option of the publicly available GADGET-2 code [61]: a random distribution of particles evolves with the sign of Newton's constant changed, until it reaches equilibrium. This kind of distribution is random and does not introduce any preferred scale into the simulation, since the particles are not disposed on a lattice. We used a $glass$ file of 128^3 particles: then, in order to reach the desired number of particles, N-GenIC replicates the glass file and perturbes is with random displacements which depend on the input random number. This allows the user to reproduce the initial conditions of a simulation from a given $glass$ file, once known the random number. For each simulation, we chose a different random number to avoid the presence of recurrent features.

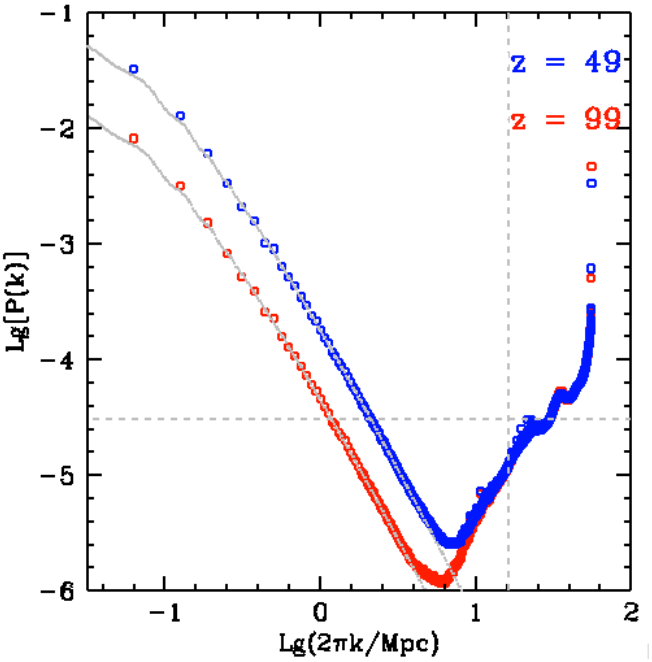

Figure 3.4: Initial power spectrum. Different colours show the results of two tests, done for 512^3 particles in a box of 100 Mpch^{-1}, at redshift 49 and 99. The gray line is the initial power spectrum obtained with CAMB, which was used for all the simulations.

In Figure 3.4, we show the measured initial power spectrum of two test runs, done with 512^3 particles in a box ok 100 Mpch^{-1}; we produced initial conditions for the same simulation at two different redshifts, to see if the initial time affects the noise level in the power spectrum. Given that no particular effect can be seen, we chose $z = 99$ as initial redshift for our simulations (apart from Ada which, due to its very small box, started from $z = 124$). This is supported also by the plots in Figure 3.5 where we show the $z = 0$ mass function of the two simulations and the density profiles of the most

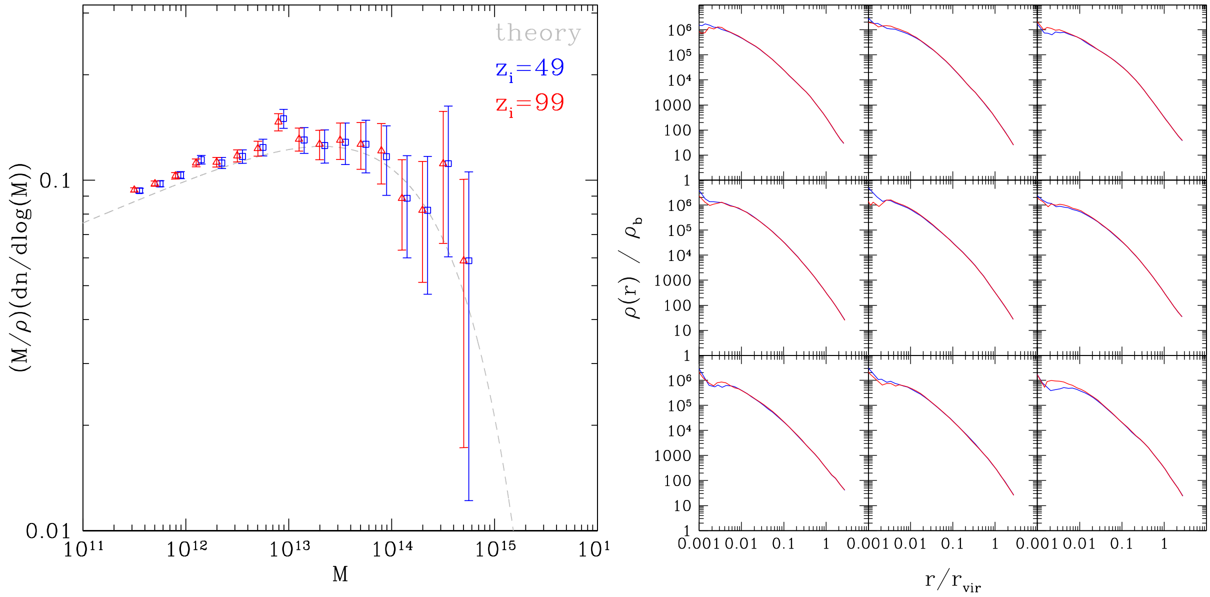

Figure 3.5: *Left*: final halo mass function of the two test (corresponding points are shifted of a small amount to allow to see them both); the Sheth & Tormen 1999 [60] mass function is represented in gray. *Right*: final density profiles of the most massive haloes; the color scheme is the same of the left panel. It is clear that there is no significant difference between the results of the two tests.

massive haloes of the two tests: it is clear that in this case the difference in initial redshift does not affect the final result.

Setting and tests

The six simulations have increasing box dimensions (doubled each time), in order to maintain a good resolution at any scale and to have a satisfying statistic at all masses: from 62.5 to 2000 Mpc. Since the total number of particles is always 1024^3, increasing the box dimension makes also the particle mass grow: from 1.94 $10^7 M_\odot h^{-1}$ to 6.35 $10^{11} M_\odot h^{-1}$.

Before running the simulations, we studied the properties of the main previous works in the field (Table 3.1) with the aim of choosing the best set of parameters and check the dependences between initial redshift, mass and spatial resolution. In the left panel of Figure 3.6 we see the initial redshift of some of the most recent simulations as a function of their mass resolution. We notice no regularity in the choice of z_{in}, since for example the Millennium-I and II runs have very different mass and spatial resolutions, but started at the same redshift for consistence. Thus, following the results of our tests (see the previous section) we chose $z = 99$ as a starting redshift for all our simulations, save from “Ada” which starts at $z = 124$ due to its very small scale and so to the possibility of stronger non-linear effects. In the right panel we seen the spatial resolution (or *softening*) as a function of the mass resolution: we show our simulations (red dots) among the ones of the previous plot. The two resolutions have a linear dependence, shown by the gray dashed line. The SBARBINE simulation are coherent with the most important recent simulations, as the Millennium runs.

Before the final set of simulations, we ran a few smaller tests to check the code performances. The last one of these was “Baby”, a cosmological simulation with 512^3 particles in 100 Mpch^{-1} and 5 kpc of softening, which has been used in [14]. The tests confirmed the expectations regarding the velocity and memory occupation of the code, as can be derived by the GADGET-2 user manual.

The initial power spectra of the simulations are shown in the left panel of Figure 3.7, where the

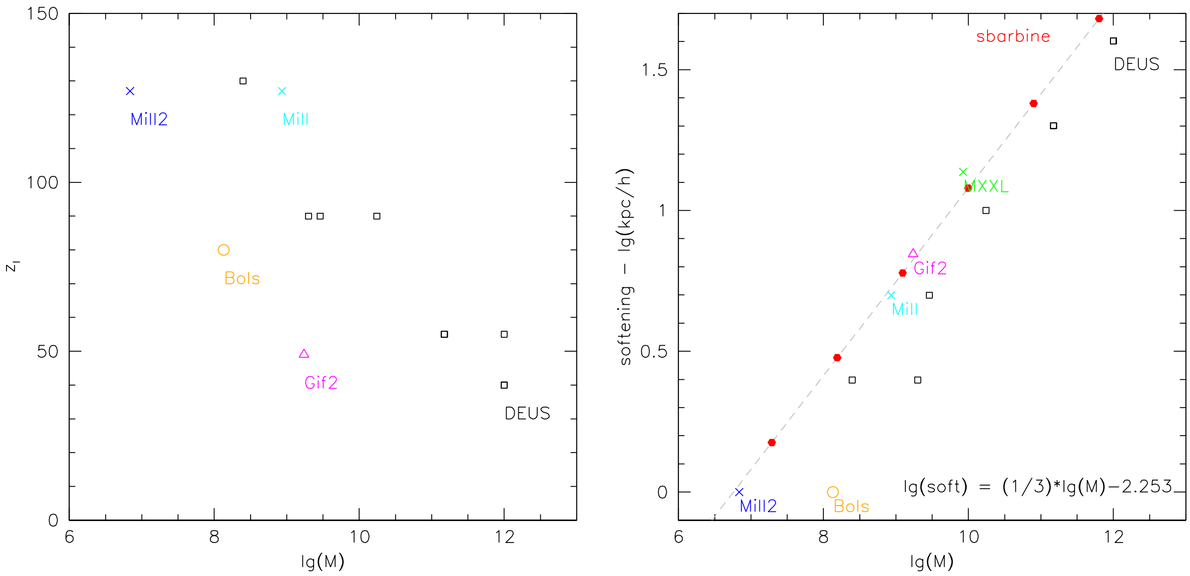

Figure 3.6: *Left*: Relation between the mass resolution and the initial redshift of some of the most recent simulations. *Right*: Relation between the mass resolution and the spatial resolution (softening); the six red dots show the feature of the SBARBINE simulations.

n snap	z	n snap	z	n snap	z	n snap	z
0	99	14	10.03	28	3.859	42	1.141
1	50	15	9.401	29	3.583	43	1.019
2	35	16	8.81	30	3.322	44	0.9041
3	20	17	8.252	31	3.076	45	0.7959
4	18.81	18	7.726	32	2.844	46	0.6937
5	17.68	19	7.23	33	2.626	47	0.5974
6	16.62	20	6.762	34	2.42	48	0.5066
7	15.62	21	6.32	35	2.225	49	0.4209
8	14.67	22	5.904	36	2.042	50	0.3401
9	13.78	23	5.511	37	1.869	51	0.2639
10	12.94	24	5.141	38	1.706	52	0.192
11	12.15	25	4.792	39	1.552	53	0.1242
12	11.4	26	4.463	40	1.407	54	0.0603
13	10.69	27	4.152	41	1.27	55	0

Table 3.3: List of the simulation snapshots and corresponding redshifts. Apart from the first 4 snapshots, the outputs are logarithmically spaced in redshift.

two black dashed lines show the input linear power spectrum at $z = 99$ and $z = 124$. It is easy to see how, increasing the box dimension, one gets more modes on large scales (small ks) and less on small scales (large ks).

3.5 Post processing: halo identification algorithms

In this section we present the most common algorithms for the identification of dark matter haloes in simulations - FoF (Friends-of-Friends) and SO (Spherical Overdensity) - and their main advantages and disadvantages.

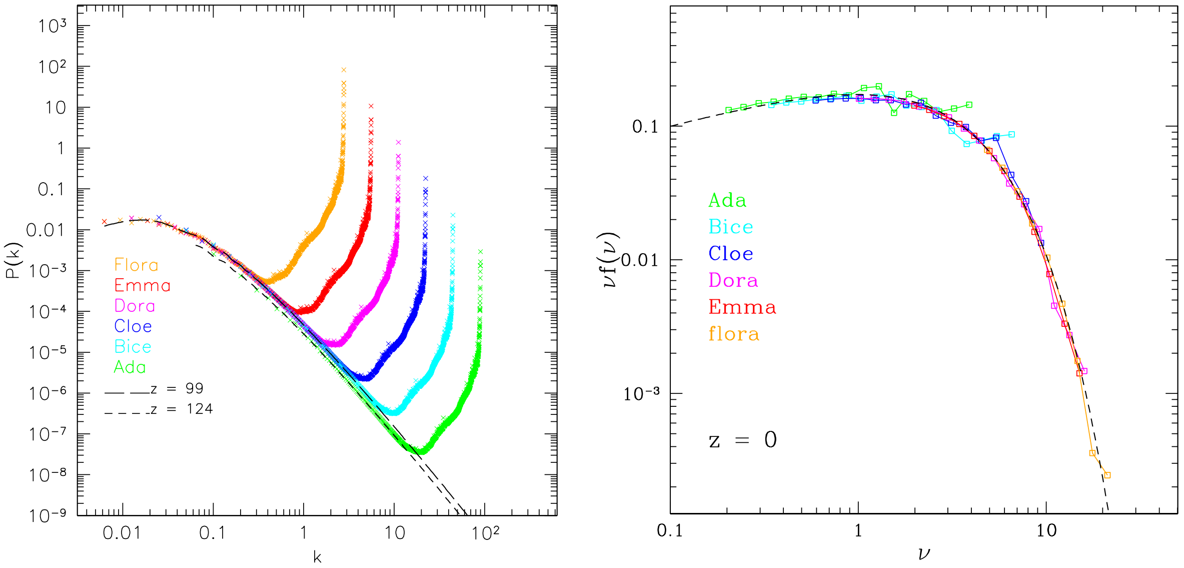

Figure 3.7: *Left*: Initial power spectrum: each colour represent one simulation, while the two black dashed lines show the input linear power spectrum at z=99 and 124. *Right* : Final mass function: different colours represent different simulations, while the black dashed line shows the theoretical prediction calculated as in [58]

Friends-of-friends

The friends-of-friends method (hereafter FoF) or percolation is a statistical method to define structures bounded by isodensity surfaces. It defines groups by linking together all pairs of particles with separation less than a certain values $b\bar{\rho} = bn^{-1/3}$, $\bar{\rho}$ being the mean particle density and b the linking length. This defines groups bounded approximately by a surface of constant local density $\rho/\bar{\rho} \sim 3/(2\pi b^3)$. Around each point, it traces a sphere of radius $r = bn^{-1/3}$ and we group together all the objects whose spheres intersect. Having N points, for $b << 1$ there are now N groups containing only one point; as b grows, the number of groups decreases and the number of points for each group increases. Thus, the linking length b defines the density threshold. This should correspond to the critical value predicted by the theory: for the spherical collapse model we know $\delta \simeq 178$. It has been argued that $b = 0.2$ is a good choice: it corresponds to $\rho/\bar{\rho} \sim 60$ and so, for a spherical halo with a density profile $\rho(r) \propto r^{-2}$, to a mean overdensity $< \rho > /\bar{\rho} \sim 180$, which is very close to the theoretical value.

This algorithm is simple, fast and has an important advantage: it does not make any assumption about the geometry of the groups. However it may happen that some of the selected groups are formed by two or more dense objects linked by low-density bridges of particles. This is a problem of the method, because these groups seem rather unphysical.

Spherical overdensity criterion

Another common choice is the spherical overdensity criterion (hereafter SO), which grows spherical shells around the center of mass and defines the radius of the halo taking the distance at which the overdensity first crosses a critical value. For each snapshot of the simulation the local dark matter density at the position of each particle ρ_i is estimated: our code (Denhf) which identify haloes in simulations takes the distance to the tenth closest neighbour of each particle, and assumes $\rho_i \propto (d_{i,10})^{-3}$. Then the particles are sorted in density and the densest particle is chosen as the center of the first halo. Around this center, spherical shells of matter are grown. The growth is stopped, and so we reach the boundary of the halo, when the overdensity first crosses the critical value (for example $\delta_{vir}(z=0) = 323.7$). All the particles within this radius belong to the same halo and can be used to compute its virial properties; the particles within the virial radius are removed from the list of possible choices for the subsequent idenfitications. The center of the second halo will be the second densest particle. The process continues until all the possible haloes have been identified and their properties computed; a particle index for each halo was also generated, in order be able to identify its particles at any redshift and thus to study the history of the haloes. It is also possible to create SO groups, after all haloes have been identified: any group that lie inside larger groups is merged together with the lardeer group. This method avoids the problem of the unphysical FOF groups, producing groups concentrated around a single center. Thus, it is more physical, but on the other hand it is also more complicated and so more time-consuming.

3.6 Padova's post-processing

Spherical overdensity: Denhf

The first step of our post-processing pipeline is running a SO halo finder (Denhf) - developed by Giuseppe Tormen - on all the snapshots of the simulations, listed in Table 3.3. We identified all haloes formed by more than 10 particles and saved catalogues containing their properties (mass, position, virial radius and so on) and the list of particles belonging to each halo. The virial overdensity δ_{vir}, used to define the halo boundaries, changes in time, proportionally to z. In the right panel of Figure 3.7 we show the present-day halo mass function for haloes with more than 200 particles: different colours represent different simulations, while the black dashed line shows the theoretical prediction which best fits the data, calculated as in [58].

A new halo finder: Ellipsoidal Overdensity

All the methods described so far are computationally convenient and widely tested, but they do not focus on halo shapes, which are the main interest of our work. As an advantage, the FoF algorithm does not impose a fixed shape to the haloes; on the other hand, this complete freedom makes it more complicated to assign geometricall properties to a halo. The SO algorithm identifies all objects as spheres, not giving a realistic view of structure formation.

A more recent and far less commonly used option is to define haloes as triaxial ellipsoids, as we do in the present work. Specifically, we will define haloes as triaxial structures with mean overdensity $\delta = \delta_{vir}$. Although computationally more costly, this method tries to retain the advantages of both previous ones: a theoretically motivated virial overdensity value and a more realistic description of the actual halo shape. This description is more consistent with the EC model, which naturally predicts triaxial rather than spherical haloes. Even if the SO algorithm has been proven to work very well in identifying haloes and it has also been shown that spherical haloes can be used to estimate the halo mass function and other properties quite precisely, it is also true that it is more realistic to describe haloes as triaxial ellipsoids, as within the context of the Ellipsoidal Collapse model ([70], [9], [59]). This is motivated by the fact that haloes are not isolated systems and that the surrounding gravitational field influences them during their collapse and formation phases; moreover during their hierarchical growth they experience different merging. All these effects stretch and modify the halo shape.

Thus, an ellipsoidal halo finder is particularly useful when one wants to study halo shapes, which are obviously more sensible than any other properties to the way in which haloes are identified.

We proceed describing our algorithm in detail. The volume V of a triaxial ellipsoid is defined by $V = (4\pi/3)abc$, with a, b, and c the longest, intermediate and shortest axis, respectively. In order to find the ellipsoidal shape which best fits a given halo, we first run an SO algorithm on the full simulation and find for each halo its virial radius R_V, enclosing an average overdensity δ_{vir} [64, 23]. We then calculate the mass tensor $M_{\alpha\beta}$ defined by the N_V particles found inside R_V as:

$$\boxed{M_{\alpha\beta} = \frac{1}{N_V}\sum_{i=1}^{N_V} r_{i,\alpha} r_{i,\beta}} \tag{3.3}$$

where $\mathbf{r}_i$ is the position vector of the ith particle and α and β are the tensor indices. Note that, even if the halo distribution can be recovered from both, this is different from the inertia tensor which is defined as:

$$I_{\alpha\beta} = \sum_{i=1}^{N} m_i(\mathbf{r}_i^2\delta_{\alpha\beta} - r_{i,\alpha} r_{i,\beta}). \tag{3.4}$$

As explained in [6], much of the literature confuses the two tensors and uses both interchangeably to describe the mass distribution.

The mass tensor so found will not be isotropic even for particles within a sphere if the particle distribution inside R_V is not isotropic. Therefore, by diagonalizing $M_{\alpha\beta}$ we will obtain eigenvalues and eigenvectors which give an initial guess for the true shape and orientation of the virialized structure: the axes of the best fitting ellipsoid are defined as the square roots of the mass tensor eigenvalues. We then modify the list of particles which make up the halo by performing a sort of *Ellipsoidal Overdensity* criterion: for each particle selected in the previous step, we calculate its ellipsoidal distance from the center as

$$r_E^3 = \frac{\Delta x^2}{l_1^2} + \frac{\Delta y^2}{l_2^2} + \frac{\Delta z^2}{l_3^2}, \tag{3.5}$$

where l_1^2, l_2^2 and l_3^2 are the eigenvalues of the mass tensor calculated at the previous step. (The eigenvalues of the inertia tensor would be $l_2^2 + l_3^2$, $l_1^2 + l_3^2$ and $l_1^2 + l_2^2$.) Sorting the particles by ellipsoidal distance from the center of the halo, we build up an ellipsoid which encloses an average overdensity δ_{vir}. We believe that using the overdensity to select the halo particles is more precise and consistent than requiring the volume of the ellipsoid equal that of the original SO sphere, or requiring the longest axis equal that of the initial sphere [67, 1, 56]. This also allows a more direct comparison with theoretical models. We recalculate the mass tensor for this new particle distribution, and obtain a new set of eigenvectors, which improve the previous description of the halo shape. We iterate this calculation until the algorithm converges to a set of eigenvectors to better than one percent in the axial ratios. We ran the EO finder on all the snapshots of the simulations, thus generating halo catalogues parallel to the spherical ones.

Protohaloes from the IC to the final time

With the algorithms described so far, we are able to identify spherical and ellipsoidal dark matter haloes at any snapshot of the simulations. Another interesting topic, is the evolution of protohaloes, meaning the evolutions of the original patches that led to the formation of haloes. To do this, instead of identifying from scratch dark matter haloes, we followed the particles of the final virialized haloes back in time. We analysed their distribution at any snapshot and found the best fitting ellipsoid (using the mass tensor) which describes them: in this way we neglect all the other particles that may have passed through the region, and keep only those which build up the final halo. The method is conceptually the same of the EO finder: the only difference is that here the iterations are used to find the best fitting ellipsoid always on the same set of particles, while the EO finder also refines the particle selection at each step. This allows a direct comparison with analytical models of gravitational collapse, which often do not consider the accretion process.

For each protohalo in the IC we then calculate the elements of the **deformation tensor**, defined at each position $\mathbf{q}$ as the second derivatives of the gravitational potential Φ. This, in the the Zel'dovich approximation [71] is equivalent to the evaluation of the first derivatives of the initial displacement:

$$\boxed{\xi_{ij}(\mathbf{q}) = -\frac{\partial^2\Phi}{\partial x_i \partial x_j}(\mathbf{q}) = -\frac{\partial\Psi}{\partial x}}. \tag{3.6}$$

These were calculated from the initial displacement grid and differentiated with respect to the spatial coordinates. A visual representation of the initial displacement field is given in Figure 3.8: a small line is drawn at every grid point, oriented as the corresponding displacement. This allows to see the overdense and underdense regions and the general flow of matter at the initial conditions. Specifically, for each halo we flagged the grid points occupied by particles and calculated the deformation tensor as:

$$\xi_{ij} = \frac{1}{V_L}\int_{V_L} \xi_{ij}(\mathbf{q})\, d^3x = \frac{1}{N_G}\sum_{k=1}^{N_G} \xi_{ij}(k) \tag{3.7}$$

where N_G is the sum of all the grid cells contained within the Lagrangian volume of the halo: i.e., those actually occupied by halo particles and those left empty, but still located inside the halo (with at least four neighbour cells occupied by particles). These last must be considered since the total potential field acting on the halo is affected by their contribution. Thus, we used an algorithm to select the correct set of empty cells and added their contribution to the deformation tensor of the halo. This results in a small change to the original value, which refines the one obtained using the particle grid points only. Since the shape of the protohalo regions is not symmetric nor regular, we could not choose a characteristic radius and use it to smooth the distribution in Fourier space (and calculate the value od the deformation tensor from it), since we need to maintain spatial resolution at each point.

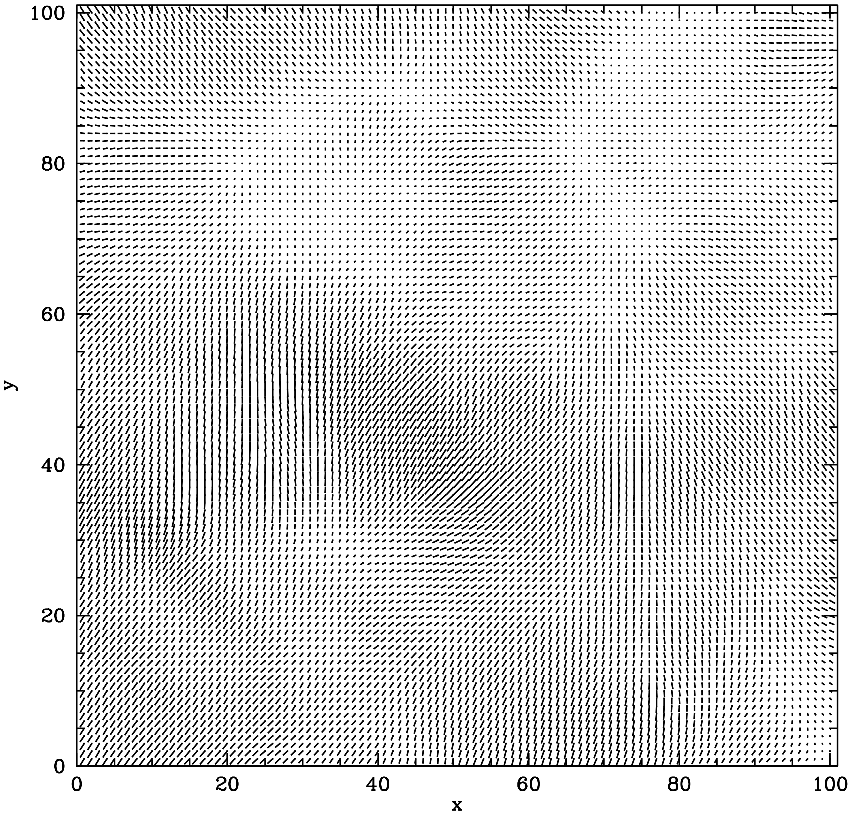

Figure 3.8: Representation of the initial displacement field: the plot is made from a piece of the GIF2 initial field. A small line in drawn at every grid point, oriented as the displacement of the corresponding grid point, to mark underdense and overdense regions.

The need for triaxiality in simulations and observations 4

4.1 The need for precise models for observations: galaxy clusters

Galaxy clusters are the most massive virialized structures in the universe and - following hierarchical clustering - also the last forming ones; almost 80% of their mass is attributed to dark matter, while the rest to baryons. Clusters of galaxies are considered one of the most important cosmological probes; they are still commonly modeled as spherical objects, even if the standard spherical modelling of the dark matter and the intracluster medium is only a rough approximation. Indeed, it is well established both theoretically and observationally that galaxy clusters are much better approximated as triaxial objects, even if the asphericity of galaxy clusters is still in its infancy: for this reason they constitute the perfect example of why we need to take into account triaxiality in cosmology.

Apart from the fact that haloes in simulations are found to be triaxial, there are many observational evidences for clusters not being spherical objects, since various probes are not well described by circular projections: optical observations (left panel of Figure 4.1), the density maps (right panel of Figure 4.1) and the distribution of galaxies, X-ray and surface brightness maps, Sunyaev Zel'dovich signal (Figure 4.2), strong and weak gravitational lensing.

In particular, strong lensing clusters are thought to constitute a biased population of triaxial haloes: their major axis is preferentially aligned with the line of sight, boosting the lensing efficiency. This orientation bias is due to the fact that, when haloes are oriented along the line of sight, a higher (projected) mass can produce the lensing effect, which then results stronger and easily visible to us: the bias seems to depend on cluster redshift, being stronger at those redshift that are least favourable for strong lensing.

This shows us the importance of a correct triaxial modelling of galaxy clusters: using spheres may lead to an underestimate of the halo mass, which then would not match the observed lensing effect.

The Abell 1689 puzzle

We report the findings of Limousin et al 2012 [34] on Abell 1689 (shown in Figure 4.1), to illustrate the difference between spherical and triaxial modelling. Abell 1689 is a massive galaxy cluster at redshift 0.18, with a very large Einstein radius and which have been extensively studied at different wavelengths. It appears as a complex structure, but still the main mass clumps seems to be dominant in the mass budget: all strong lensing studies find the mass centre to coincide with the brightest cluster galaxy, which also coincide with the peak of X-ray emission.

The cluster has been analysed assuming spherical symmetry, but it was shown to be problematic in two ways:

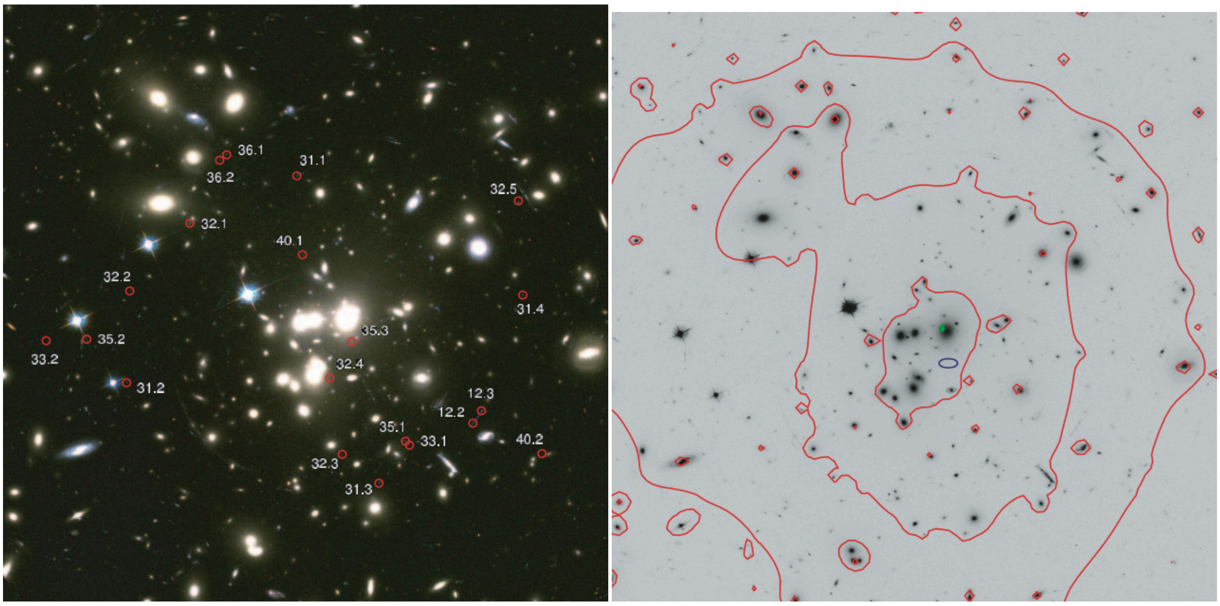

Figure 4.1: Abell 1689 (Limousin et al. 2007 [35])*Left*: Color image from F475W, F625W, and F775W observations; north is up, east is to the left. The size of the field of view is $160'' \times 160''$, corresponding to 485 kpc×485 kpc. *Right*: R-band image; The red contours show where the projected mass density equals $(1.6, 2.4, 4.0) \times 10^{10} M_{\odot} arcsec^2$. The green point shows where the peak of the mass map is found. The blue circle shows the location of the main dark matter clump

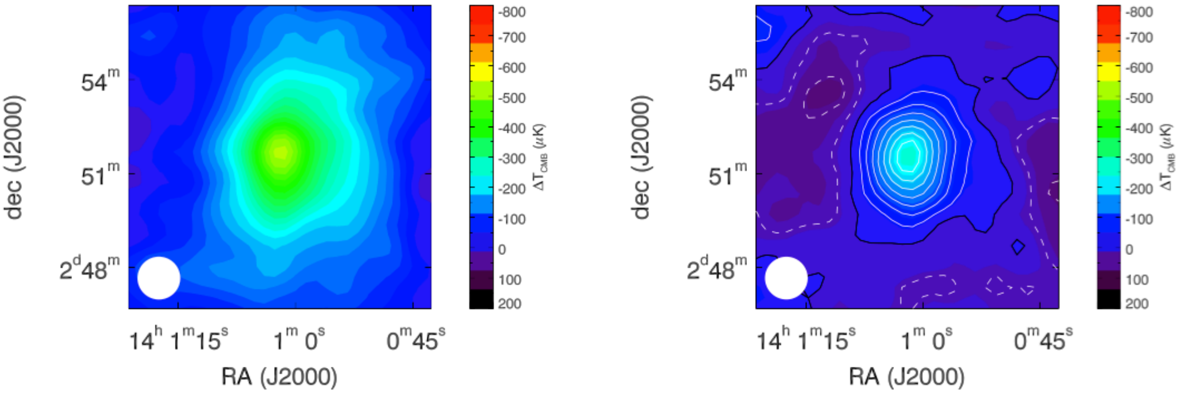

Figure 4.2: Abell 1835; from left to right we show the deconvolved SZ image of the cluster and the processed image of the cluster

- the lensing analyses yield very high concentration parameters, in contrast with the theoretical expectations from ΛCDM - even if there is a large variance between various works;
- the 2D mass derived from X-ray data is only half of the one derived from strong lensing, on which all the studies agree.

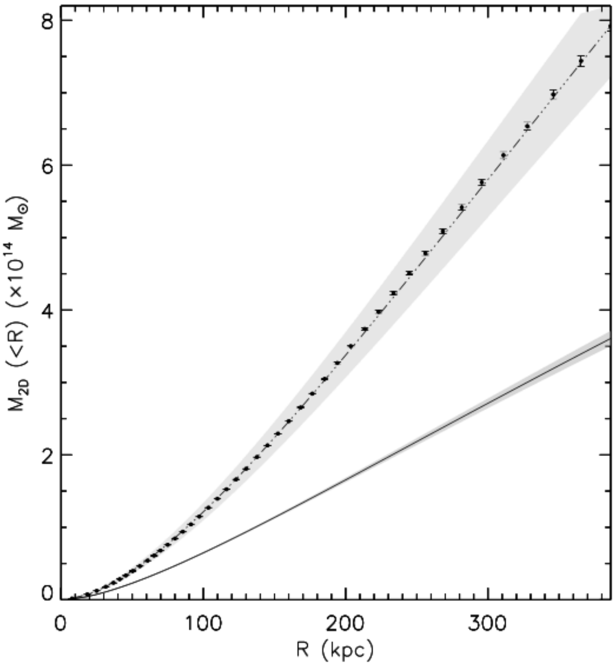

Figure 4.3: Abell 1689: 2D mass enclosed within a circular aperture of radius R from lensing data (points with error bars), from an X-ray only analysis under the assumption of spherical geometry (solid line with the 1ÏČ error grey shaded region), and from a joint X-ray+lensing analysis taking into account the 3D geometry (dot-dashed line with the 1ÏČ error cray shaded region). In this latter case, we see that both estimates agree with each other. [41, 34]

A possible way to reconcile the two mass measurements could be a triaxial mass model: it has already been found [45], considering triaxiality, that weak lensing measurements are indeed compatible with ΛCDM if the cluster represents a rare population. Morandi et al. 2011 [41] presented a determinations of intrinsic shapes and physical parameters of both dark matter and intracluster medium, by combining X-ray and strong lensing data. They showed that the halo of Abell 1689 could be elongated along the line of sight (an assumption justified by the "orientation bias"), with a minor/major axial ratio equal to 0.42 ± 0.02. Then, another analysis by the same group [38] confirmed the possibility of a triaxial halo by jointly analysing also weak lensing data and accounting for the non-thermal pressure of the IC gas.

Limousin et al. 2012 [34] extended the analysis, by allowing the DM and ICM ellipsoids to have an arbitrary orientation: the results indicate that Abell 1689 is indeed a triaxial galaxy cluster. The DM axial ratios are 0.56 ± 0.07 and 0.75 ± 0.08, the concentration $c_{200} = 5.27 \pm 0.46$ and the major axis is inclined with respect to the line of sight of $\theta = 27.3 \pm 7.1$ deg. Both the model proposed by Morandi et al 2011 [38] and this extension are able to solve the X-ray/lensing mass discrepancy: in Figure 4.3 we show the comparison between the 2D masses inferred using spherical and triaxial models.

Moreover, also the inner slope of the density profiles depends on the adopted geometry: a standard spherical modelling leads to 1.15 ± 0.04, while a triaxial one yields 0.92 ± 0.07. So far, four clusters has been studied with a triaxial modelling and their main features are listed in Figure 4.4. As we have seen, the parameters obtained with a triaxial modelling may significantly vary with respect to the ones obtained before.

4.2 Halo triaxiality in previous works

As we have already discussed, the collapse of overdensities in the cosmic density field is aspherical and so there is no reason to expect the resulting final haloes to be spherical. In the last few years, many works started to analyse halo triaxiality, identifying the best fitting ellipsoids in different ways: for example, it can be selected to have the same volume or mass of the spherical overdensity halo. This choice guarantees a fast convergence, but does not allow a free identification of the ellipsoid, as on the contrary our code does. Nevertheless, our results are compatible with those of previous works, which are summarised in this section.

Cluster	Abell 1835	Abell 383	Abell 1689	MACS 1423
c_{200}	4.32 ± 0.44	4.76 ± 0.51	5.27 ± 0.46	3.97 ± 1.0
R_s (kpc)	891.0 ± 114.3	511.2 ± 73.6	683.1 ± 84.7	644.7 ± 162.1
γ	1.01 ± 0.06	1.02 ± 0.06	0.92 ± 0.07	1.06 ± 0.1
$\eta_{DM,a}$	0.59 ± 0.05	0.55 ± 0.06	0.56 ± 0.07	0.62 ± 0.04
$\eta_{DM,b}$	0.71 ± 0.08	0.71 ± 0.10	0.75 ± 0.08	0.72 ± 0.06
ψ (deg)	3.8 ± 4.6	-13.6 ± 5.5	-35.5 ± 13.7	-34.4 ± 5.4
θ (deg)	18.3 ± 5.2	21.1 ± 10.1	27.3 ± 7.1	34.7 ± 8.7
ϕ (deg)	-55.0 ± 6.9	-16.9 ± 15.9	-11.1 ± 6.7	-72.3 ± 8.3
n_0 (cm^{-3})	0.018 ± 0.002	0.063 ± 0.003	0.017 ± 0.001	0.15 ± 0.02
r_{c_1} (kpc)	117.7 ± 10.1	26.4 ± 1.7	119.3 ± 5.3	20.6 ± 3.1
ε	0.68 ± 0.02	0.55 ± 0.01	0.72 ± 0.02	0.55 ± 0.02
δ	0.82 ± 0.03	0.02 ± 0.01	0.33 ± 0.01	0.02 ± 0.01
r_{c_2} (kpc)	1674.3 ± 266.7	-	-	-
υ	0.44 ± 0.04	-	-	-
ξ	0.177 ± 0.065	0.11 ± 0.05	0.24 ± 0.05	0.08 ± 0.03
n	0.77 ± 0.21	0	0	0
$\tilde{P}$ (erg/cm^3)	$(2.7 \pm 0.7) \times 10^{-13}$	-	-	-

Figure 4.4: Best-fit model parameters for the four clusters for which a full triaxial modelling exists. Error bars correspond to 1ĬČ confidence level. [41, 34]

Already in 1992, Warren et al. [67] studied the shapes of isodensity surfaces inside haloes. As later shown by Jing & Suto (2002) [27], halo isodensity surfaces are well described by ellipsoids, each characterised by the lengths of its axes ($a \le b \le c$). These axes can be used to specify some dimensionless shape parameters: the axial ratios

$$s = \frac{a}{c} \qquad q = \frac{b}{c} \qquad p = \frac{a}{b} \qquad ; \tag{4.1}$$

these can be then combines to give the triaxiality parameter

$$T = \frac{c^2 - b^2}{c^2 - a^2} = \frac{1 - q^2}{1 - s^2}. \tag{4.2}$$

An ellipsoid is considered oblate if $0 < T < 1/3$, triaxial if $1/3 < T < 2/3$, and prolate if $2/3 < T < 1$. In general, haloes do exhibit a rich variety of shapes, with a preference for prolateness over oblateness. Despite the natural difference between haloes, due to their personal merging history, systematic relations between the axial ratios and the threshold density ρ_s can be noticed:

1. **shape-mass** : haloes of cluster mass generally have smaller axial ratios than those of galactic mass, implying that the galactic mass haloes are rounder on average; this can be found in the left panel of Figure 4.7, where the three histograms slightly differ: the green one, corresponding to higher mass values, is located at smaller axial ratios. In particular, haloes that experienced a recent major merger have a tendency to be close to prolate, with the major axis reflecting the direction along which the last merger event occurred. Simulations suggest that the shape of a halo is tightly correlated with its merger history, with haloes that assembled earlier being more spherical. This implies - as already found - that less massive haloes (which form earlier in a hierarchical clustering scenario) are, in general, rounder, while more massive haloes tend to be less spherical and more prolate (probably because they are involved in more merging events).

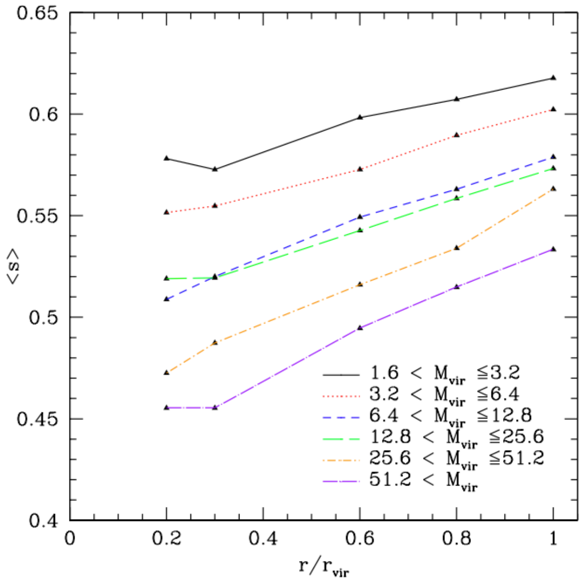

Figure 4.5: Shape as a function of radius, by means of the axial ratio $< s >$ for different mass bins - represented by different colours (from Allgood et al. 2006 [1]).

2. **shape-radius**: the axial ratios decrease with increasing density, meaning that the isodensity surface becomes more elongated in the central region of the halo. Thus, the triaxiality of dark matter haloes changes at different distances from the center [67, 1, 66] and haloes tend to be rounder in the outer parts and more elongated in the center: this happens because the outer regions are more influenced by the surrounding field and by gravitational interactions with other objects, while the cores - being more “protected” - maintain their original shapes.
3. **shape-time**: as predicted by the EC model, massive haloes are formed from almost spherical initial patches, while small protohaloes in the IC are generally more triaxial. At the final time the situation is reversed, as it is described in point 1: massive haloes are more triaxial since they formed recently and small haloes tend to be spherical. Thus, one must pay attention to do not mix the two situations, since from the IC to the present time the tendency is reversed.

Figure 4.5 shows the measurements of Allgood et al. 2006 [1], summarising both the dependence on mass and radius. Similar findings may be found in Bailin & Steinmetz 2005 [4], Muñoz-Cuartas et al. 2011 [42] and Vera-Ciro et al. 2011 [66].

The shape-density (radius) relation is described by a power-law in Jing & Suto 2002 [27]:

$$\begin{aligned} s &= \frac{a}{c} = 0.56\left(\frac{\rho_s/\rho_c}{2500}\right)^{-0.052} \\ q &= \frac{b}{c} = 0.71\left(\frac{\rho_s/\rho_c}{2500}\right)^{-0.040} . \end{aligned} \tag{4.3}$$

where they always refer to the surface with $\rho_s/\rho_c = 2500$. Galactic mass haloes should be denser than cluster mass haloes, implying larger values of the axial ratios; contemporary, within each halo, as density decreases moving outward, the axial ratios increase. This is confirmed by another relation, which shows a systematic dependence of s on the mass: the ratio is slightly larger for less massive haloes, and also decreases at higher redshift. The resulting law is:

$$r_{ac} = \left(\frac{a}{c}\right)_{sc} = \left(\frac{a}{c}\right)\left(\frac{M_{vir}}{M_\star}\right)^{0.07(\Omega(z))^{0.7}} \tag{4.4}$$

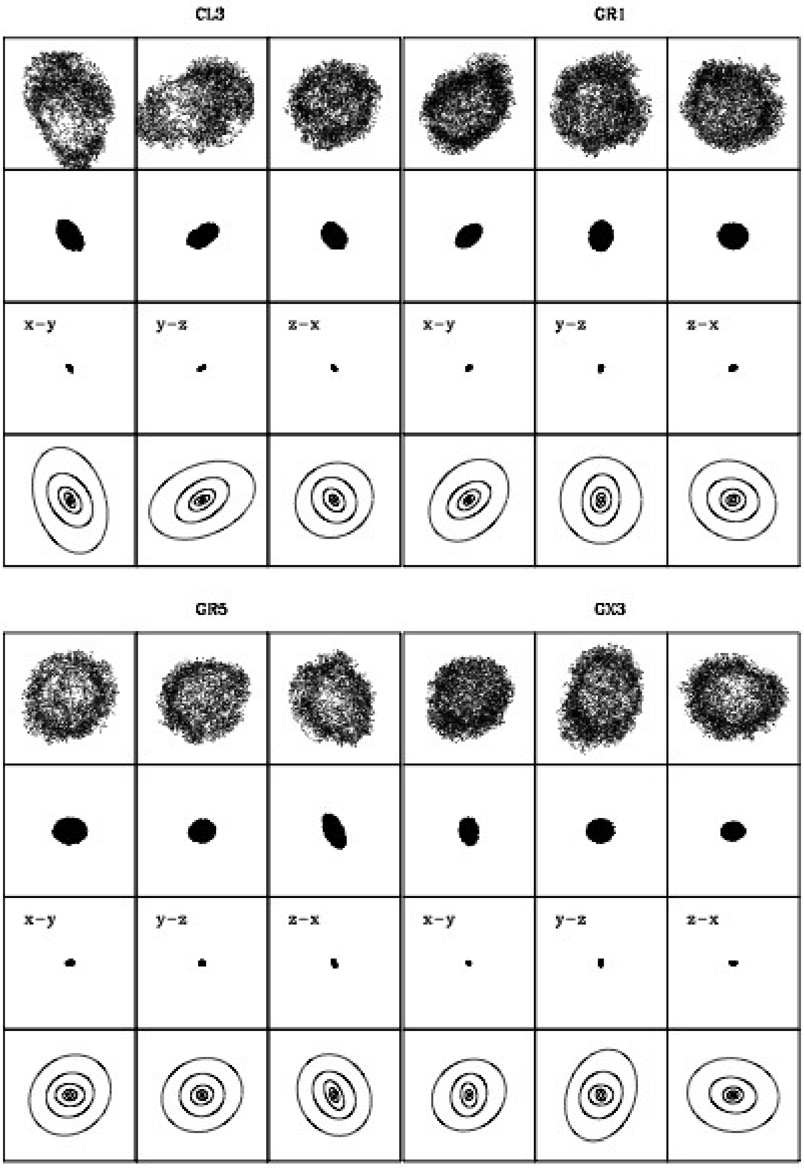

Figure 4.6: Example of projected particle distribution for four haloes used by Jing & Suto. The bottom panel shows the triaxial fit to five different isodensity surfaces that can be seen above. (Jing & Suto, 2002, [27])

where $M_\star$ is the characteristic halo mass. The scaled axial ratio r_{ac} show a fairly universal distribution independent of mass and epoch, as we can see in Figure 4.7 and 4.8. Allgood et al. (2006) extended this relation using numerical simulations, combining the mass and redshift dependence of $< s >$:

$$< s > (M, z) = (0.54 \pm 0.03) \left[\frac{M}{M_\star(z)} \right]^{-0.050 \pm 0.003} . \tag{4.5}$$

Another useful equation is the universal probability distribution function of r_{ac}, which turns out to be well fitted to the following Gaussian:

$$p(r_{ac}) dr_{ac} = \frac{1}{\sqrt{(2\pi)}\sigma_s} exp\left(-\frac{(r_{ac} - 0.54)^2}{2\sigma_s^2} \right) dr_{ac} \tag{4.6}$$

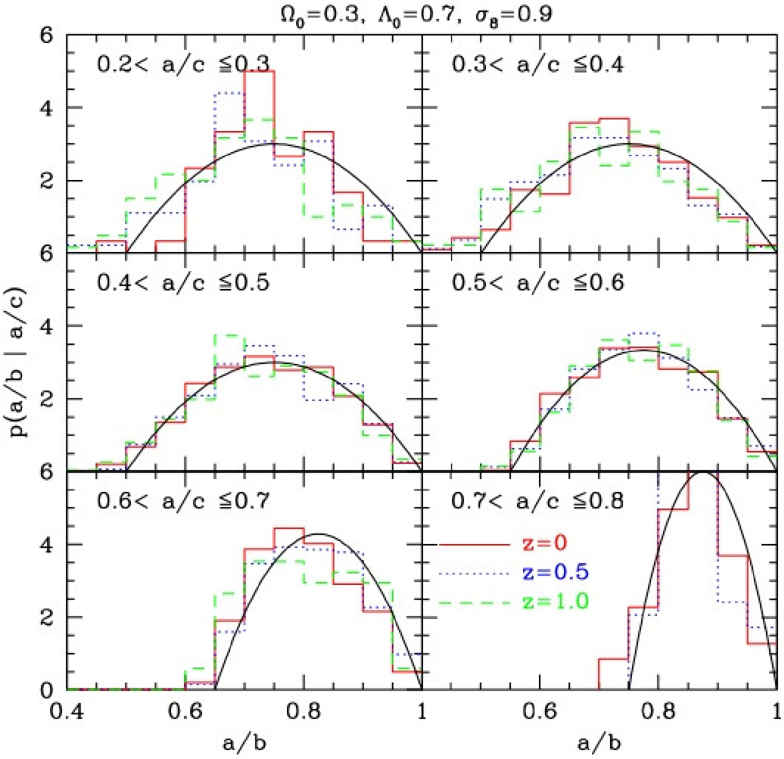

Figure 4.7: The distribution of the axis ratio a/c of the halos in the cosmological simulations of the LCDM model before (left) and after (right) the scaling described in the text. (Jing & Suto, 2002, [27])

with $\sigma_s = 0.113$. This allows us to predict the distribution of the axial ratio and so, in some way, of the halo shapes. We can decompose the joint probability function in terms of the conditional distribution and compute the probability of p, given s:

$$P(p|s) = \frac{3}{2(1-\tilde{s})}\left[1-\left(\frac{2p-1-\tilde{s}}{1-\tilde{s}}\right)^2\right] \tag{4.7}$$

with $\tilde{s} = max[s, 0.55]$ (Jing and Suto, 2002, [27]; Allgood et al., 2006, [1]).

Some works studied also the alignment of the ellipsoidal shells within each halo [4, 66]. The authors agree on the fact that shapes measured at different radii tend to be aligned with each other. Bailin & Steinmetz 2005 [4] found a good internal alignment (cos ≃ 0.9), becoming stronger for massive haloes. Vera-Ciro et al. 2011 [66] analysed the Aquarius haloes, considering the smooth main halo without substructures, finding perfect alignment between different shells. This suggests that, while the overall shape and orientation of an halo is the same at al radii, the presence of substructures alters the symmetry and leads to more complicated behaviours.

4.3 Results from our Ellipsoidal Halo Finder ar $z = 0$

The comparison between theoretical models and N-body simulations is a non-trivial problem, primarily because there is still no unanimous agreement about how to define a gravitationally bound object, i.e. of what a non-spherical dark matter halo is: the distribution of halo shapes measured from simulations depends critically on the halo definition. In this section we adress this problem, comparing spherical and ellipsoidal haloes, to show how the identification algorithm influences the

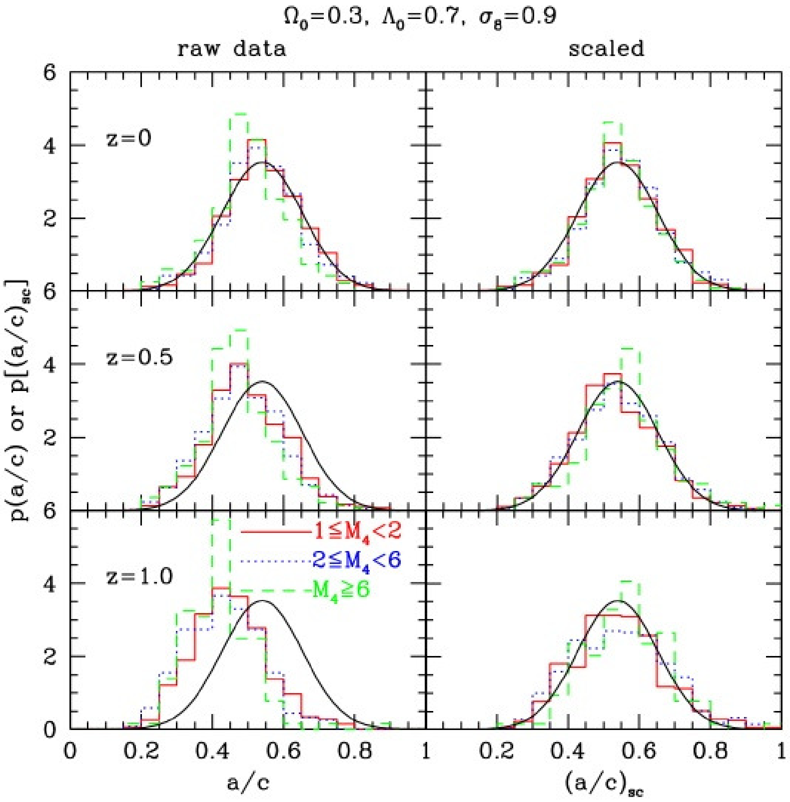

Figure 4.8: The conditional distribution of the axis ratio a/b of the halos in the cosmological simulations of the LCDM model for a given range of a/c. (Jing & Suto, 2002, [27])

results. We consider the Ellipsoidal Overdensity algorithm more suitable to study halo shapes, since it allows a variety of shapes and so a more realistic picture of large scale structure. For these reasons, the results presented in the next chapters have been obtained using mainly ellipsoidal haloes.

Figure 4.9 illustrates the difference between a spherical halo and its triaxial counterpart, as identified by our post-processing pipeline described in Chapter 3: black dots show the projected distributions of halo particles inside the final ellipsoid, while the red dashed circle indicates the virial radius R_V of the SO halo. The shape is obviously more elongated when measured inside an ellipsoidal volume (in this case particularly in the y-z plane), follows the natural orientation of the halo and its iso-density contours more accurately than does the SO halo: it is clear that the SO identification would add particles in the direction of the smallest axis and cut off the edges along the longest axis. We expect, therefore, an increase in virial mass M: this is true for the test halo of Figure 4.9 and also in general for the whole halo sample.

Difference in mass

In Figure 4.10 we plot, for the ellipsoidal haloes (thus obtained with the EO halo finder), the halo mass function of the GIF2, $Baby$ and $Flora$ simulations at four different z. The solid and dashed curves represent, respectively, the theoretical prediction for the GIF2 and Planck cosmology given as the Sheth & Tormen 1999 [60] mass function. In the lower panel, we show the relative residual between the mass functions obtained with the EO and SO finders at $z = 0$ - the behaviour at the other redshift is consistent with this one. Since the ellipsoidal and the spherical masses are positively biased with

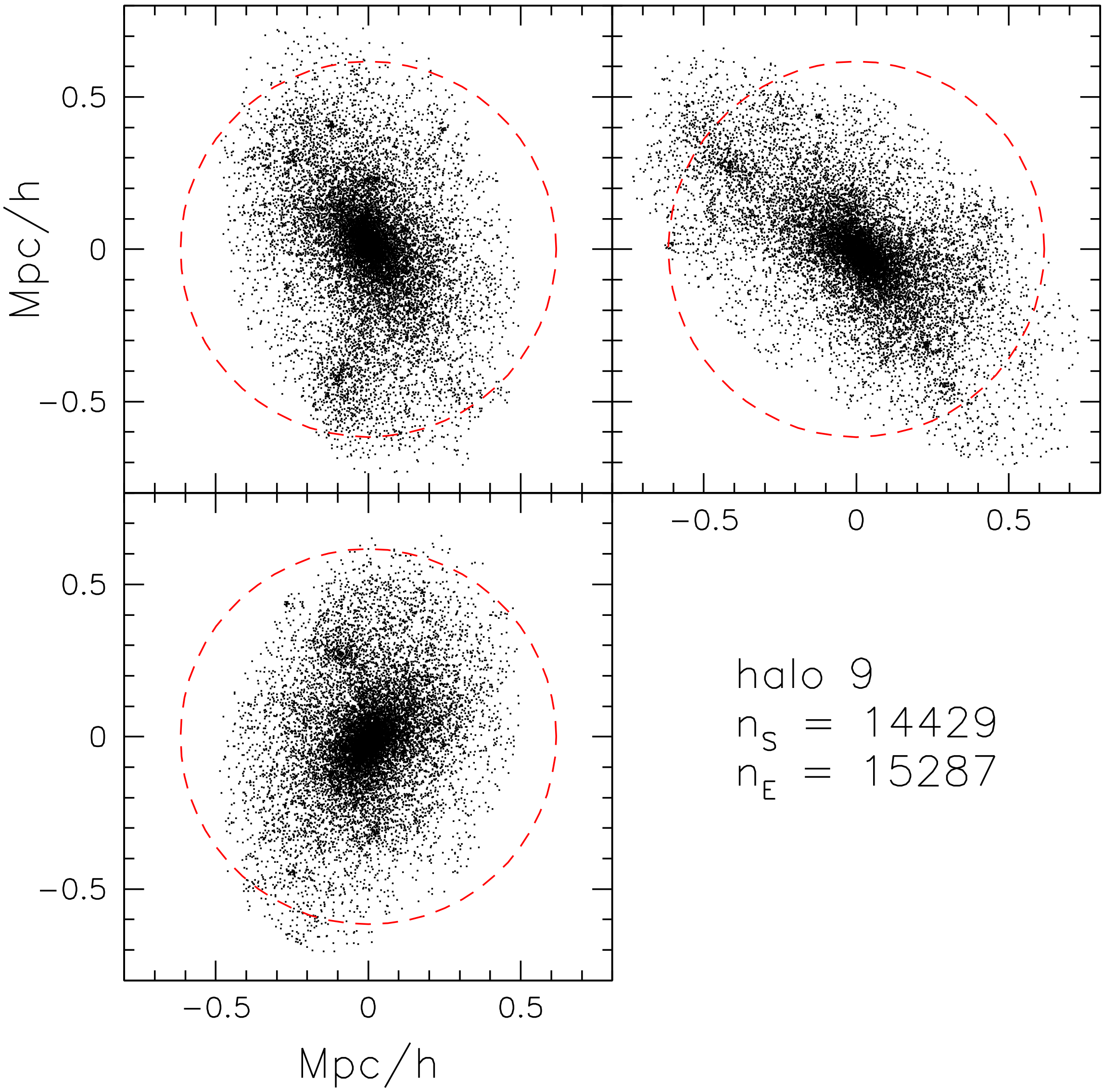

Figure 4.9: An example of the difference between a spherical halo and his triaxial counterpart: black dots show the projected distributions of halo particles inside the final ellipsoid, while the red dashed circle indicates the virial radius R_V.

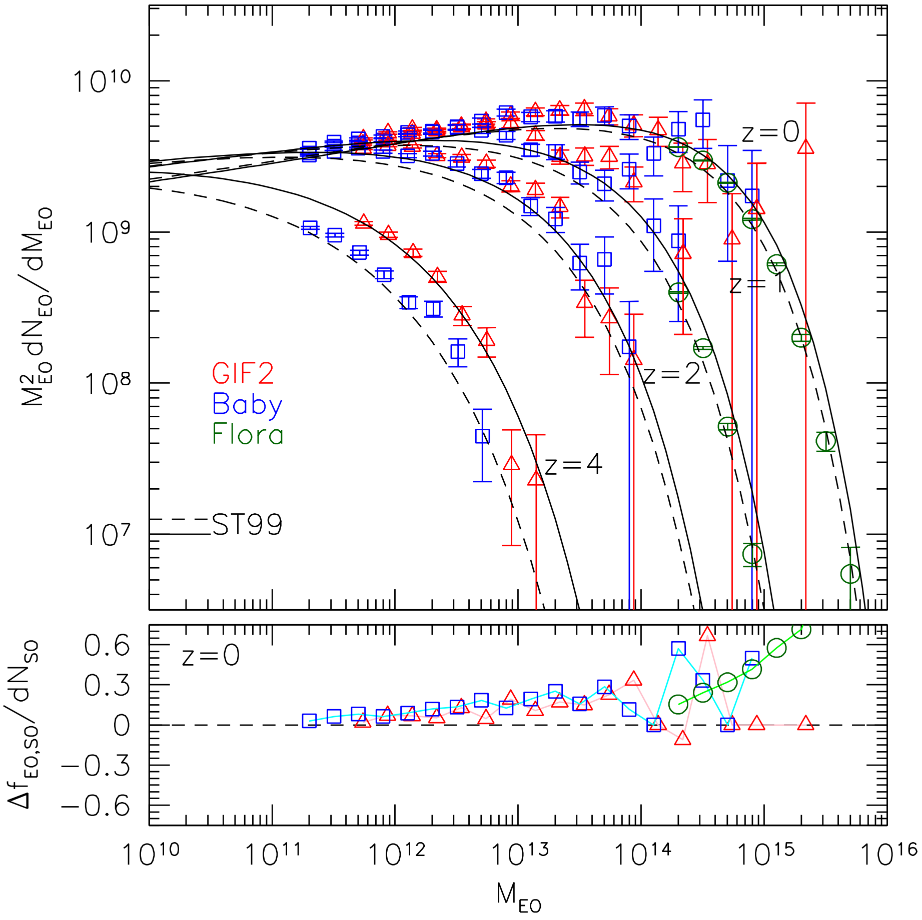

Figure 4.10: Halo mass function of the three simulations at four different z, obtained with the EO halo finder. Different data points and colours show the results for the three different simulations, and the error bars represent the Poisson uncertainty. The solid and dashed curves represent, respectively, the theoretical prediction for the GIF2 and Planck cosmology given by [60] mass function (ST99). The lower panel show the relative residuals between the halo abundance obtained with the EO and the SO finder for the three simulations at $z = 0$.

respect to each other of some percents, this results in a bias in the the halo abundance that can reach $10-30\%$. The bias increases with halo mass due to the fact that massive haloes are intrinsically more elongated and so their shapes are captured much better by an ellipsoid than by a sphere.

Notice that our new method indeed gives a different estimate of the mass: the ellipsoidal mass is clearly larger than the spherical one, as ellipsoids indeed trace the isodensity surfaces more precisely, and so include more particles. A detailed analysis of the best fitting mass function for the two mass definitions will be adressed in Chapter 7.

Difference in final shape

We now study the influence on halo shapes. Figure 4.11 shows the fractional difference in the axial ratios c/a and b/a (with $a \geq b \geq c$ the three eigenvalues of the mass tensor), as a function of the spherical axial ratios using the fractional differences

$$\frac{\Delta(c/a)}{(c/a)_S} = \frac{(c/a)_E - (c/a)_S}{(c/a)_S} \tag{4.8}$$

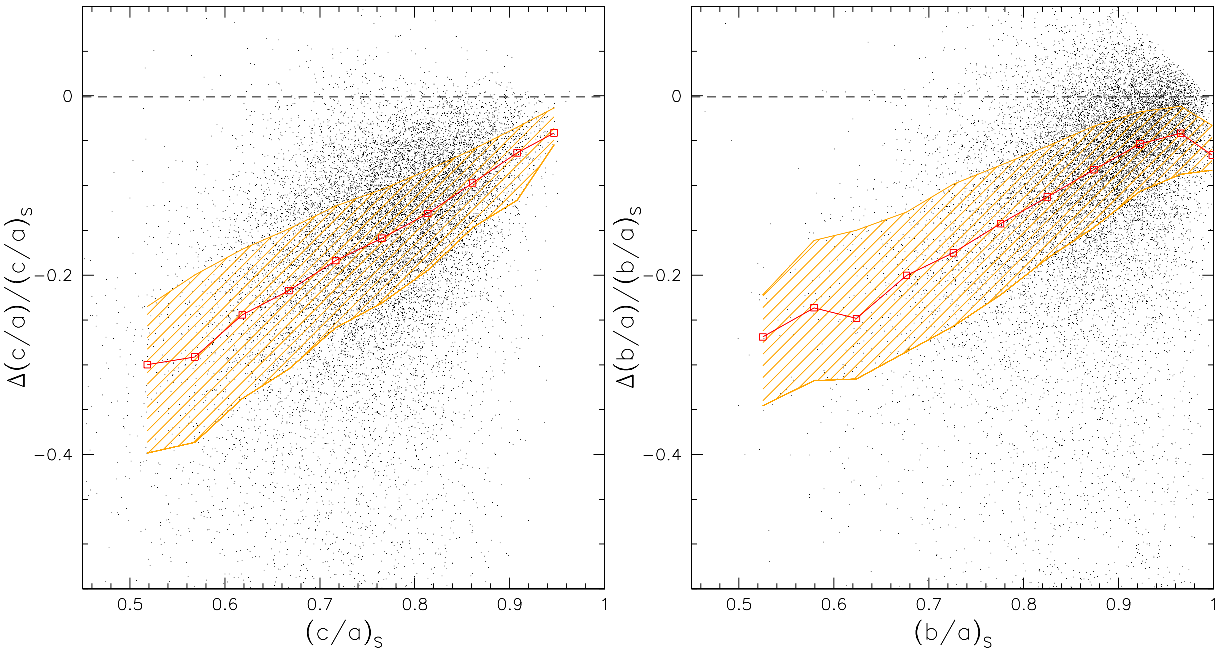

Figure 4.11: The difference in the final axial ratios *c/a* and *b/a* ($a \le b \le c$), as a function of the spherical ones. The orange shaded region lies between the first and third quartiles; red points show the median. The relative difference is generally negative, indicating that fitting ellipsoids yields more elliptical and prolate shapes than fitting spheres.

and similarly for b/a. Ellipsoidal haloes are obviously more elongated, and this means that it is always $\Delta(c/a)/(c/a), \Delta(b/a)/(b/a) \le 1$. When the axial ratio approaches 1, then haloes are almost spherical, so the ellipsoidal method correctly returns a spherical shape for the rounder objects. The difference increases as $(c/a)_S$ and $(b/a)_S$ decrease: in particular, ellipsoidal-based shapes become more prolate, since the shortest axis changes more than the others, as can be seen by comparing the two panels of Figure 4.12. This agrees with the recognised preference for prolate halo shapes in previous works.

In Figure 4.12 we show the differential and cumulative distributions for both c/a and b/a: the distribution obtained using final spheres is represented by the solid line, while the dashed line is for ellipsoids. There are more objects with small c/a when fitting ellipsoids, and the median is shifted to smaller values. This is also true for the b/a distribution, although the differences are smaller, implying a preference for more prolate shapes. This confirms what we already noticed in Figure 4.11. A similar result was obtained by Warren et al. 1992 [67], who compared the axial ratios of a spherical and an ellipsoidal halo, finding a change in the axial ratios in the direction of more ellipsoidal shapes.

Our analyses also confirm the general opinion that, on average, there is also a systematic dependence of shape on radius: haloes are more elongated closer to the center, and more spherical in the outskirts [1, 27, 67]. In addition, more massive haloes have a steeper gradient in axial ratios than lower mass haloes: this happens because the more massive haloes are less influenced by their environment. Since our findings agree with those of the previous works described in Section 5.2 [27, 4, 1, 42], we do not show our plots here.

4.4 Summary

As discussed in this chapter, the “true” shape of dark matter haloes is still an intriguing subject, far from being fully understood. In the era of precision cosmology, observational studies need more and

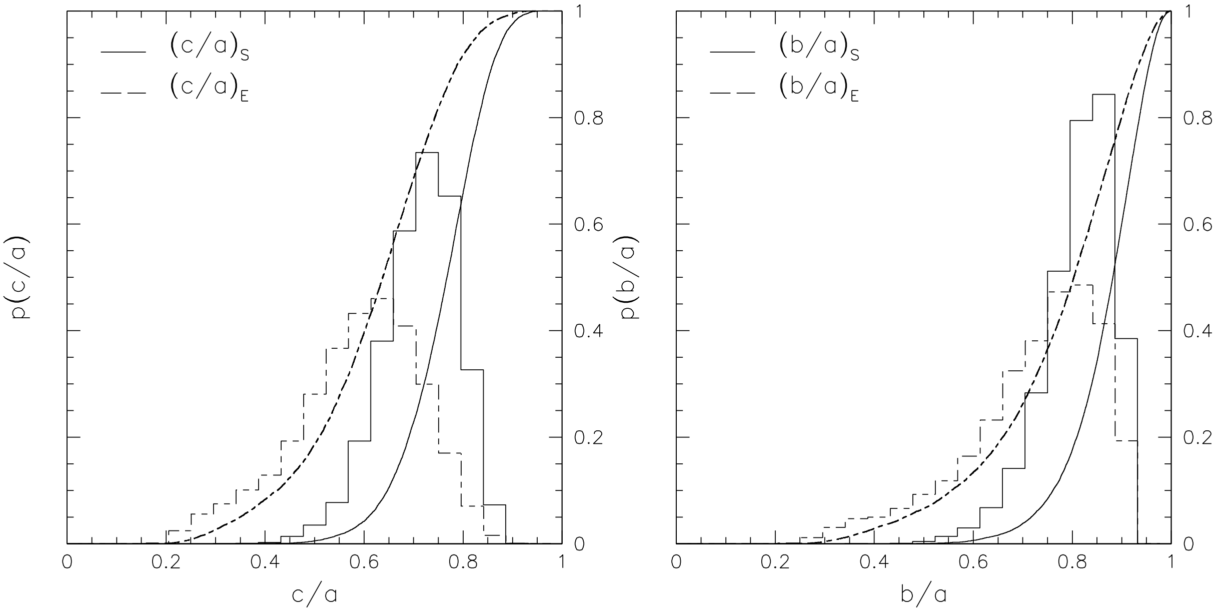

Figure 4.12: Cumulative and differential distribution of axial ratios *c/a* and *b/a* at the shape corresponding to the virial overdensity, from corresponding to a fitting ellipsoidal (dashed) and spherical (solid) volume: in both cases the enclosed mass distribution is not isotropic and so we are able to calculate the axial ratios. Haloes identified with the *EO* criterion have a smaller median value, with significantly more objects at small b/a and/or c/a. This difference is more significant for *c/a*, meaning that haloes become more prolate when fit with ellipsoids.

more precise estimates from theory and simulations; thus, even if the shape of haloes is not a first-order effect from a statistical point of view, we need to study it in more detail.

Moreover, we showed that the importance of finding the best halo identification algorithm. While its effect on the halo mass is present but not determinant, the distribution of halo shapes changes significantly: if one wants to adress the problem of halo shapes, then these must be calculated accurately.

Protohalo evolution in the ellipsoidal collapse model framework

5

As previously explained, the EC model predicts that the whole evolution of an halo can be determined by its initial properties, thus by the properties of the corresponding protohalo. Modelling the shape of initial protohaloes and that of the potential fields which surrounds them can shed light on the whole process of structure formation. In this chapter we will present an analysis of the protohalo shapes in the initial conditions and of their evolution in time; part of the results have been published in Despali, Tormen and Sheth 2013 [15]. Dark matter haloes are modelled as triaxial ellipsoids and have been identified in the GIF2 [20] and le SBARBINE (used only in section 5.2) simulations using the Ellipsoidal Halo Finder described in Section 3.6.

5.1 Does only potential matter? The importance of ICs.

Although the EC model [9] does not require it, all implementations of it assume that the mass distribution of a proto-halo is initially spherical. In this case, the evolution of the shape is determined by just three numbers (e,p,δ) which are specific combinations of the three eigenvalues of the initial 3×3 deformation tensor centered on the center of mass of the proto-halo. Because the shape of the object is determined by the initial deformation tensor, the mass and deformation tensors are perfectly aligned *by definition*. Measurements in simulations have shown that this vast simplification is actually a rather good approximation [50], as was argued in Chapter 2 (Figure 2.3). This means that tidal torques, induced by the misalignment between these tensors, are subdominant. Therefore, in this model, the proto-halo shrinks (in comoving coordinates) fastest along the axis corresponding to the direction of maximum compression, forming a pancake; this is followed by collapse along the second and then finally along the axis of least compression eventually resulting in a virialized object. I.e., the three axes collapse at different times, which depend on the local shape of the deformation tensor, but because the initial shape of the mass tensor was spherical, the ordering of the axis lengths is monotonic in time, and collapse times are determined by the initial compression factors: larger compression factor means earlier collapse. A final assumption of the model is that virialization corresponds to collapse along all three axes. Since the first axis to collapse and freeze-out from the expansion of the background Universe will have done so when the universe was denser, this first axis to collapse will also be the shortest axis of the virialized object, and the third will be longest. I.e., the shortest axis at virialization will be aligned with the direction of initial maximum compression, and vice versa. This is confirmed by measurements in simulations - as we will detail in this chapter - even if already Porciani et al. 2002 [50] found something unpredicted at the initial conditions: the direction of maximum compression is not aligned with the shortest axis of the protohalo, as it should be according to theory, but with its longest axis. This means that the halo may evolve through a serie of different ellipsoids and not just shrink maintaining the same shape and orientation.

The three numbers which determine the evolution in this model are the initial density contrast δ_i (the only number that matters for the spherical evolution model), and the ellipticity and prolateness parameters e and p of the deformation tensor (i.e. not the mass tensor) - as defined in Equation 2.14. Note that non-spherical effects always make $\delta_{ec}(e,p) > \delta_{sc} \simeq 1.686$; Sheth et al. 2001 [58] also showed that, in a Gaussian random fluctuation field, δ, e, p can vary from one position to another, with the consequence that even at fixed mass, δ_{ec} can vary from one protohalo to another. They then used the statistics of Gaussian fields to argue that, on average, δ_{ec} will be close to δ_{sc} at large masses, but it will increase as mass decreases. They showed that this mass dependence of δ_{ec} was indeed evident in their simulations, and so it is now commonly assumed that the EC model describes some of the physics which is relevant to the triaxial shapes of virialized haloes in simulations. In what follows, we test this in slightly more detail by checking if the dependence on e and p is as predicted.

What if the initial shape is not spherical?

We already know that there is one respect in which the EC model fails. This is because the model predicts that the large protohalo patches which collapse to form massive haloes should be more spherical. Therefore, the shape at virialization should also be more spherical [55]. But we showed that in simulations, in fact, the most massive virialized haloes can be quite triaxial [27, 1] and that they are on average more elongated than low mass haloes. This raises the question of whether the EC model has failed to identify the correct shapes in the initial conditions, or if its approximation of the evolution is incorrect. We will adress this problem in the next Sections.

For example, the next simplest model would begin with proto-haloes with triaxial rather than spherical mass distributions (as for example in [36, 10], but will keep the assumption that the mass and deformation tensors are perfectly aligned. In this case, the evolution of the shape, and hence the time required to collapse and virialize depends on δ, e, p as well as on the initial axis lengths (i.e., the square-roots of the eigenvalues of the mass tensor), and on whether or not the direction of maximum compression is oriented along the initially longest or the shortest axis. This correlation between the directions of the longest initial axis and the largest compression factor is indeed seen in simulations [50], in the sense that $\cos\theta_{11} \sim 1$ where θ_{11} is the angle between these two vectors.

In fact, despite the theoretical simplicity of these ‘perfect’ alignment models , the evolution of the shape can appear to be more complex because, e.g., if the axis that was longest initially also had the largest compression factor, then it may eventually become shorter than what was initially the second longest axis. So one might ask, even though the shortest axis initially may not be the shortest finally, is it still true that the shortest axis at virialization tends to be aligned with the direction of initial maximum compression (and vice versa)? If it does, then this would still be in agreement with an EC model for the evolution, only applied to a non-spherical initial mass distribution.

The Zel’dovich approximation [71], provides an easy way to see the qualitative features discussed above. In this case, the eigenvalues are assumed to evolve as $\lambda_j(t) = \lambda_j(t_i)D(t)/D(t_i)$, where $D(t)$ is the linear theory growth factor at time t. This means that the comoving axis lengths evolve independently of one another, as $R_j(t) = R_j(t_i)[1-\lambda_j(t)]$. Notice that in this approximation a positive eigenvalue implies contraction, whereas a negative eigenvalue implies expansion.

The nonlinear density is the ratio of the mass of the proto-halo to its volume. Mass conservation means that it satisfies

$$1+\delta(t) = \frac{M}{\bar{\rho}V(t)} = \frac{1}{\prod_{j=1}^{3} 1-\lambda_j(t)}. \tag{5.1}$$

Notice that this expression applies even if the $R_j(t_i)$ are not equal; it reduces to $\delta_i = \sum_{j=1}^{3} \lambda_j$ for very small values of λ_i.

In this approximation the collapse of axis j corresponds to the time when $1 - \lambda_j(t) = 0$. When the $R_j(t_i)$ are all equal, then the order of the axis lengths R_j at any given time is determined completely by the ordering of the λ_j at the initial time. But if they are not equal, then, although the order of the time to complete collapse is still determined by the order of the λ_j, the axis lengths at some time prior to complete collapse may not. E.g., if $R_j > R_k \; and \, \lambda_j > \lambda_k$ then R_j must collapse before R_k, so at some point it must become smaller than R_k. Notice that, despite this reordering of the axis lengths, the three fundamental directions of the principal axes of the mass tensor will *not* have changed. Of course, this means that if one studies the direction in which 'the longest axis' points, then this direction may change suddenly (e.g., at the time when it stops being the longest).

Although Shen et al. 2006[57] provide a simple approximation to the evolution predicted by the EC model when the initial shape is not a sphere, which can be thought of as a simple physically motivated modification to the Zel'dovich approximation, a complete understanding of these and related aspects of the EC model is still missing. Recently, Ludlow, Borzyszkowski and Porciani [36, 10] proposed a new extension to the EC model, which include initial triaxiality and the effects of the surrounding potential field, confirming part of the results presented in this Chapter.

5.2 Protohaloes at the IC: what defines them?

Since the properties of the initial fiels are so important in the EC model framework, in this Section we will try to understand what defines the protohaloes. The results of this chapter were obtained using the 6 simulations of our new set, Le SBARBINE simulations. Dark matter protohaloes are supposed to be located near the density peaks of the initial field, since they constitute the seeds of present-day haloes. If this is true, there should be a difference - for example - in the initial velocities between the particles that form the final virialized halo and those who remain unbound in the field or form other objects.

With this aim, we studied both the mass and velocity fields within and around protohalo centers (out to $3r_{Lag}$), to understand how haloes are built up from the initial field.

Particle positions

Protohaloes are commonly identified by tracing the halo particles back to the initial conditions; nevertheless, there may be particles which are located in the protohalo regions and its surrounding, but do not go into the final halo. In the top panels of Figure 5.2 we show the median percentage of protohalo particles with respect to the total number of particles in the region, as a function of the distance from the center, rescaled by the Lagrangian radius. The Lagrangian radius of a halo gives an estimate of the dimension of the protohalo and is defined as:

$$r_{lag} = \left(\frac{3M_{vir}}{4\pi\rho_c\Omega_{m0}} \right)^{1/3}. \tag{5.2}$$

The top-left panel shows the values obtained in 30 spherical shells around the center, each one of width $0.1 * r_{Lag}$, while the top-right panel shows the results for 30 ellipsoidal shells; different colours indicate different mass bins. To define the ellipsoidal shells, we first found the best fitting ellipsoid for the whole protohalo using the mass tensor: the method is conceptually the same of the EO finder described in Chapter 3; the only difference is that here the iterations are used to find the best fitting ellipsoid always on the same set of particles - since we are studying the IC position of the particles belonging to the virialized halo, while the EO finder also refines the particle selection at each step. Then, each ellipsoidal shell has the same shape (i.e. axial ratios) of the overall ellipsoid and is rescaled

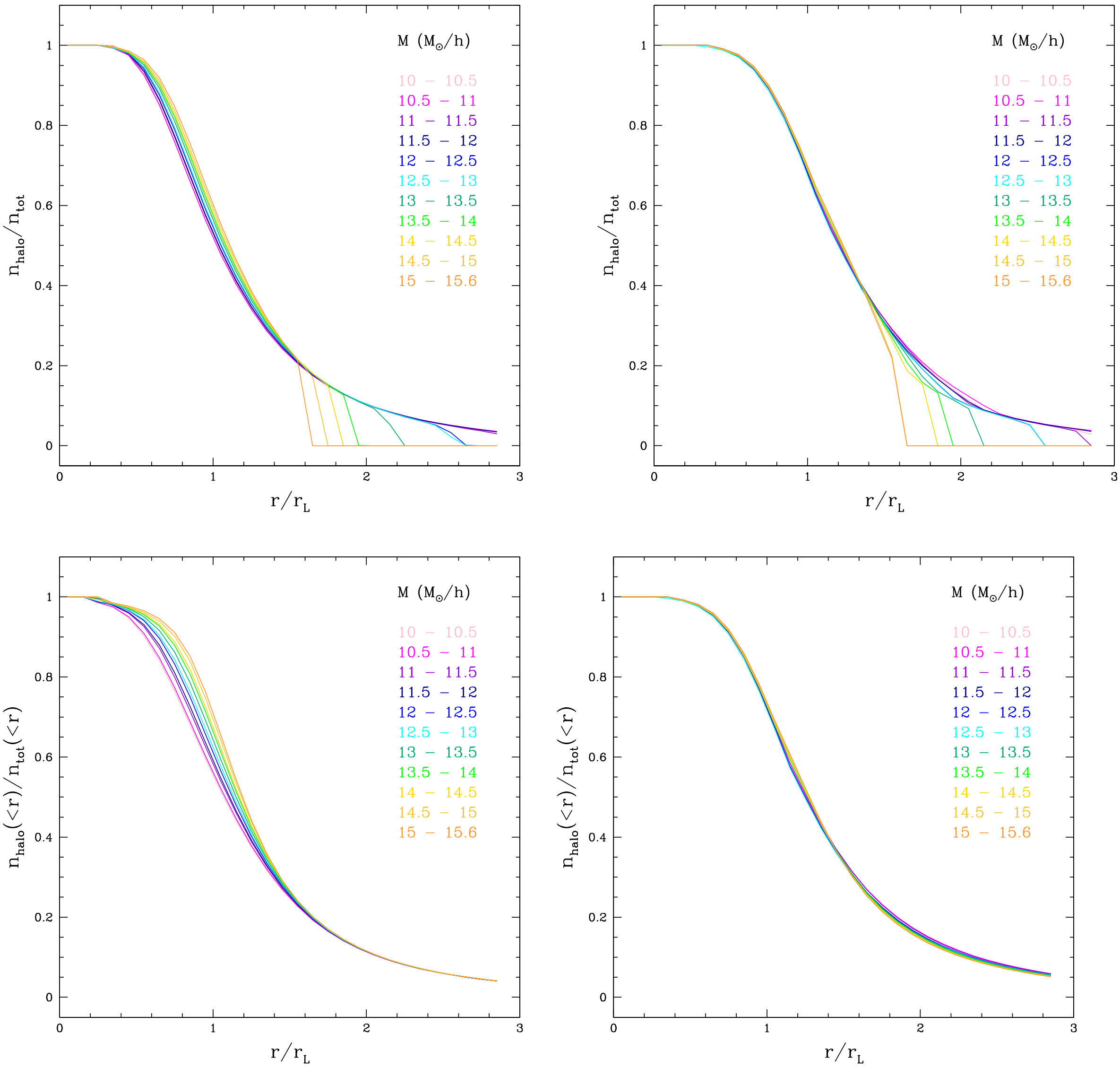

Figure 5.1: *Top*: As a function of the distance from the protohalo center, we show the percentage of protohalo particles with respect to the total number of particles in the region. The curves correspond for the results in 30 shells around the center, each one of width $0.1 * r_{Lag}$; the colours show different mass bins. *Left*: these curves have been obtained using SO haloes and spherical shells around the center of the protohalo. *Right*: in this case we used EO haloes and ellipsoidal shells, all with the same shape and orientation, which correspond to the ones of the best-fitting ellipsoid for all the protohaloes. Note that, due to the higher precision of the ellipsoidal description, the curves almost superpose to each other up to $1.5r_{Lag}$. *Bottom*: Cumulative versions of the top plots. Using ellipsoidal final haloes and ellipsoidal shells around the center, we find that all the curves become similar.

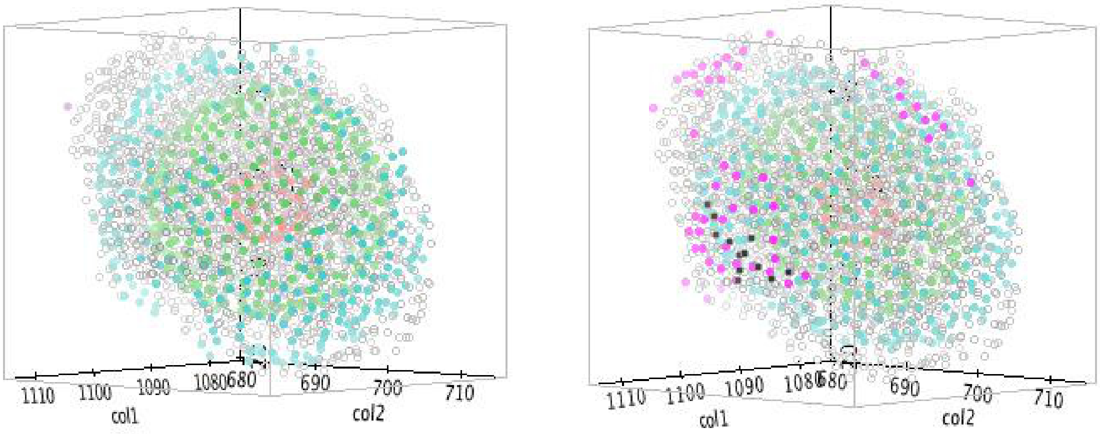

Figure 5.2: Visual 3D representation of the different effect of spherical ($left$) and ellipsoidal ($right$) shells, for one halo of our simulations. In both panels, the gray empty circles represent the particles of the whole protohalo; using different colours, we highlight tha particles belonging to some shells at a growing distance from the center. We see that ellipsoidal shells - elongated in the same direction of the halo - trace the true protohalo shape much better than the spherical ones.

to enclose the same volume of the corresponding spherical one; knowing $ar_1 = b/a$ and $ar_2 = c/a$ ($a \geq b \geq c$), this is equivalent to require that:

$$a = r\left(\frac{1}{ar_1 ar_2}\right)^{1/3}. \tag{5.3}$$

Note that, due to the higher precision of the ellipsoidal shapes, the curves in the top-right panel perfectly superposed to each other out to $1.5r_{Lag}$, while this is not the case for spherical shells. Even if the difference is not dramatic, it confirms the greater accuracy of the triaxial description: in Figure 5.2, we see a 3D representation of the different effect of spherical ($left$) and ellipsoidal ($right$) shells, for one test halo of our simulations. In both panels, the gray empty circles represent the particles of the whole protohalo; using different colours, we highlight tha particles belonging to some shells at a growing distance from the center. We see that ellipsoidal shells - elongated in the same direction of the halo - trace the true protohalo shape much better than the spherical ones. For example, there are no violet and black dots in the left panel, since those particles are included in an inner spherical shell.

From Figure 5.2 it is easy to see all the particles located at the very center of the protohalo are also part of the final virialized region: 100% of the particles inside $\simeq 0.4r_{lag}$ are part of he virialized halo, while the percentage decreases going outwards. Even within the initial Lagrangian radius, there are particles which “escape” from the final halo. The two bottom panels of Figure 5.2 show the cumulative version of the two top panels.

At this point, it is worth looking at one individual protohalo, which gives a more realistic picture of the process: Figure 5.3 shows the particle distribution in the region surrounding one protohalo of our simulation, at the IC ($top-left$) and at the present time ($top-right$). In this case we decided to show only the particles that are in the protohalo region, but that are not part of the final halo- thus we exclude all the protohalo particles. Different colours show particles in ellipsoidal shells at different distances from the protohalo center: green - inside r_{Lag}, blue - $r_{Lag} < d < 1.5r_{Lag}$, red - $1.5r_{Lag} < d < 2r_{Lag}$, orange - $2r_{Lag} < d < 3r_{Lag}$. The color-code is the same in both panels and a particles maintain the same colour in both: the particles in the $top-right$ panel are still coloured according to initial distance from the center. The two bottom panels show the distribution of the final distances from the halo center in units of r_{Lag} and of the final virial radius r_{vir}. The distance ranking is somehow maintained through the whole evolution: the green particles surround the final halo and will be probably accreted in the near future: they are located along the filaments and so are the next ones falling to the halo. The orange and red particles are instead scattered in the field. Figure 5.4 shows an enlargement of the central region of Figure 5.3, this time including the halo particles (at $z = 0$) in black. We examined other test haloes individually, finding the same results and so we believe that this halo can reasonably represent the average behaviour.

The velocity field

Thus, those particles which build the final virialized halo have something "special" already in the initial field: this is confirmed also by looking at the velocity field around protohaloes. In Figure 5.5 we show the distribution of infall velocity both for the particles of our test halo - the same of Figure 5.3 and for the field particles. The infall velocity of a particle, with respect to the center of mass of the protohalo, is defined as:

$$v_{inf} = \frac{(vx_p - vx_{CM}) * (x_p - x_{CM})}{d} + \frac{(vy_p - vy_{CM}) * (y_p - y_{CM})}{d} + \frac{(vz_p - vz_{CM}) * (z_p - z_{CM})}{d}, \quad (5.4)$$

where $d = |r_p - r_{CM}|$ is the distance of the particles from the protohalo center of mass. Thus, v_{inf} is negative if a particle is moving toward the center of mass, and positive in the opposite situation. In the left panel of Figure 5.5, the velocity distribution of halo particles is represented by the black histogram, while the other histograms are color-coded as in the previous Figures (see Fig. 5.3). All the particles which belong to the protohaloes are already infalling toward the center of the halo: none of them has a positive velocity. This is true also for the field particles located inside one Lagrangian radius (green), which reinforces our hypothesis that they will be the next particles accreted by the haloes. The other coloured histograms have higher means and start to show a tail at positive values. Given the high mass of the test halo ($M_{vir} = 1.9\ 10^{15} M_{\odot}/h$), the attraction due to its potential well is still strong far from the center. However, as shown by Figure 5.5, the orderin in mean infall velocities holds for all masses, even if with a smaller gradient.

The right panel of Figure 5.5 shows the median values of infall velocities as a function of distance from the center, for the same mass bins of Figure 5.2 and the same four shells of Figure 5.3. The triangles represent the median infall IC velocity of the protohalo particles, for haloes of different mass bins (plotted at x=0.8 for convenience). The squared points show instead the median IC velocity of the particles which do not belong to the final halo, but which are located near the initial protohalo. This plot gives us a more general picture, clearly showing that there is a selection effect which determines which are the particles of the virialized object: the median infall velocities of the halo particles are systematically lower than the ones of the field particles, for the same mass bin.

A comparison with linear theory

Colberg et al. 2000 [12] derived an accurate approximation of the linear predictions for the peculiar velocity field. According to linear theory the peculiar velocity evolves as

$$v \propto a\dot{D}, \quad (5.5)$$

where $a(t)$ is obtained from the Friedmann equation

$$\left(\frac{\dot{a}}{a}\right)^2 = \Omega_0 a^{-3} + (1 - \Omega_0 - \Lambda_0) a^{-2} + \Lambda_0 \quad (5.6)$$

and $D(t)$ is the growth factor for linear density perturbations. A number of accurate approximate forms are known for the relations between D and a, which can be used to rewrite the equation in a

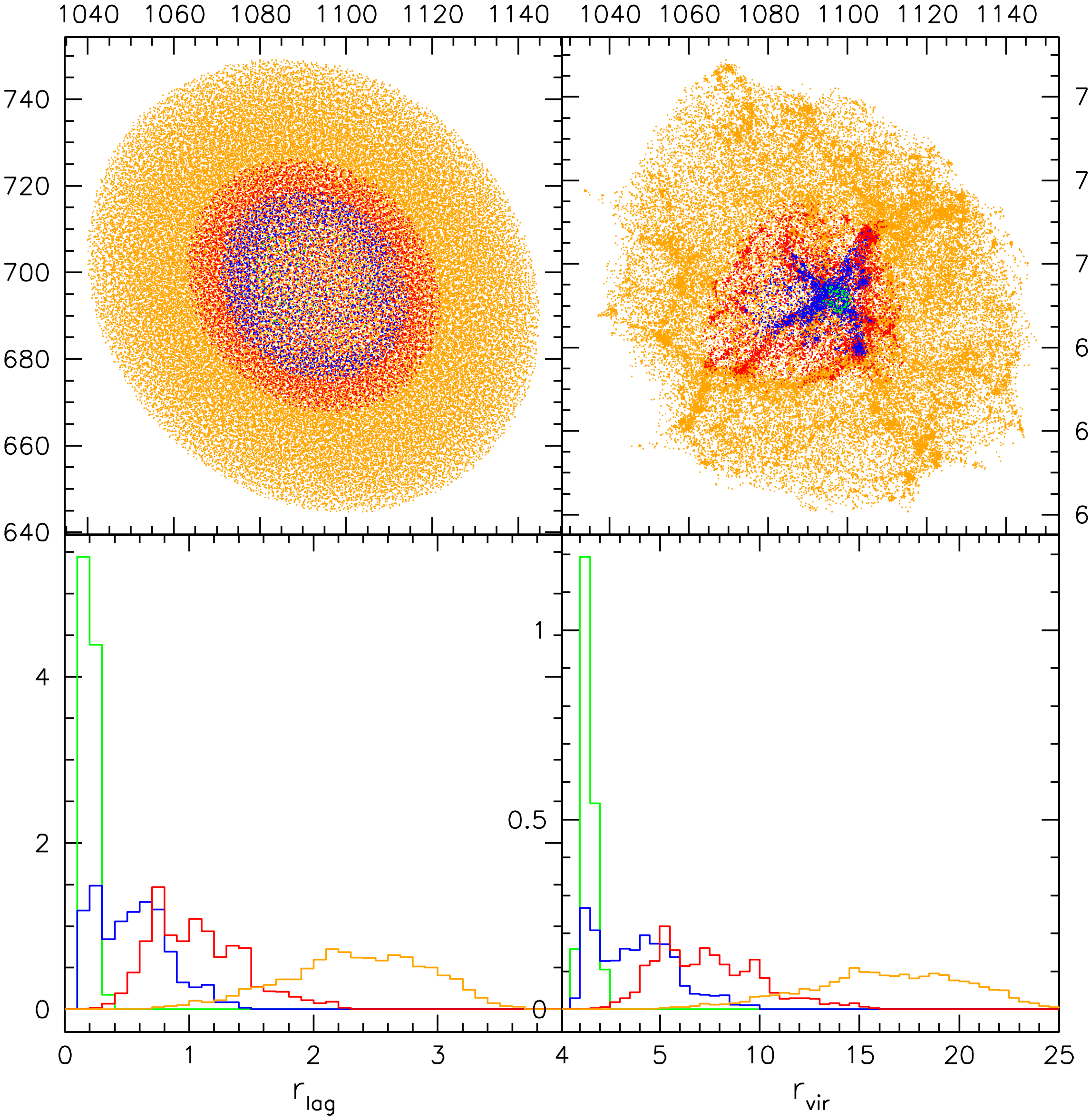

Figure 5.3: Evolution in time of the particle distribution in the region surrounding one protohalo of our simulation, excluding the protohalo particles. Different colours show particles in ellipsoidal shells at different distances from the protohalo center: green - inside r_{Lag}, blue - $r_{Lag} < d < 1.5r_{Lag}$, red - $1.5r_{Lag} < d < 2r_{Lag}$, orange - $2r_{Lag} < d < 3r_{Lag}$. *Top left*: 2D projection of the IC particles in the region surrounding the protohalo; *Top right*: 2D projection of the positions of the same particles at $z = 0$. *Bottom left*: distribution of the final distances from the halo center, rescaled by the IC Lagrangian radius; *Bottom right*: same distribution, but with values rescaled by the final virial radius; this last plot makes more clear that none of these particles is going into the final halo.

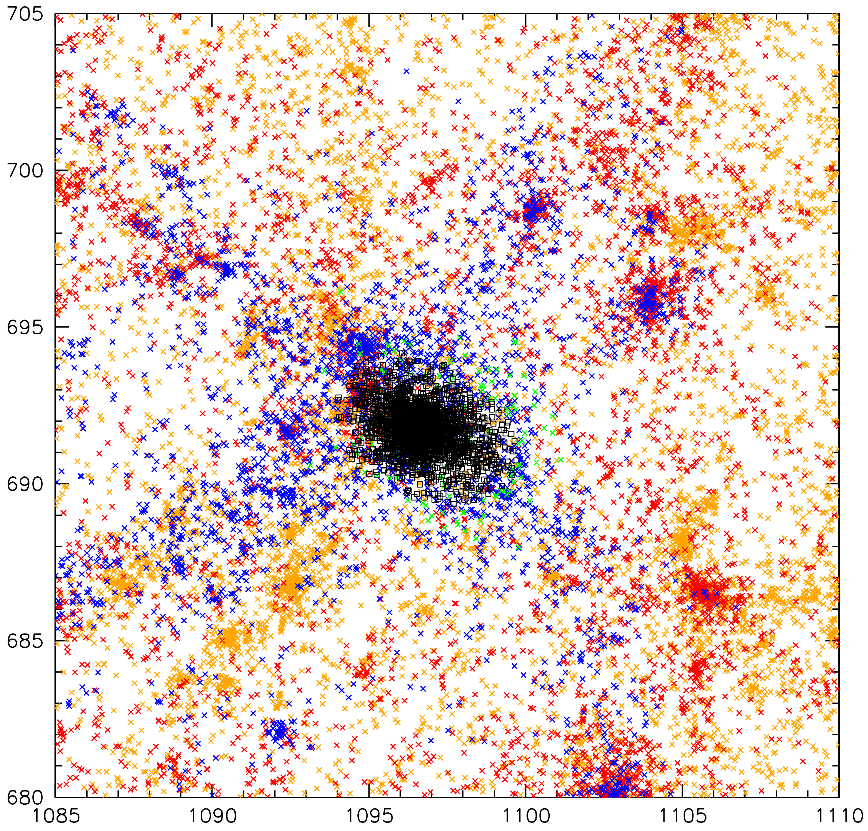

Figure 5.4: Enlargement of the central region of the top right panel of Figure 5.3. The color code is the same of the previous Figure and the black points show the particles of the final halo.

more convenient form. The resulting form for the growth of peculiar velocities is:

$$v \propto f(a)g(a)a^2\sqrt{\Omega_0 a^{-3} + (1-\Omega_0-\Lambda_0)a^{-2} + \Lambda_0}, \tag{5.7}$$

where

- $$f(a) = \frac{dD}{da}\frac{a}{D} \simeq \left[\frac{\Omega_0 a^{-3}}{\Omega_0 a^{-3} + (1-\Omega_0-\Lambda_0)a^{-2} + \Lambda_0}\right]^{0.6} \tag{5.8}$$
- $$g(a) = \frac{5}{2}\frac{\Omega(a)}{\Omega(a)^{4/7} - \Lambda(a) + \left(1+\frac{\Omega(a)}{2}\right)\left(1+\frac{\Lambda(a)}{70}\right)} \tag{5.9}$$
- $$\Omega(a) = \frac{\Omega_0}{a + \Omega_0(1-a) + \Lambda_0(a^3-a)} \tag{5.10}$$
- $$\Lambda(a) = \frac{\Lambda_0 a^3}{a + \Omega_0(1-a) + \Lambda_0(a^3-a)}. \tag{5.11}$$

For an Einstein-de Sitter universe, this approximation reduces to $v \propto \sqrt{a}$.

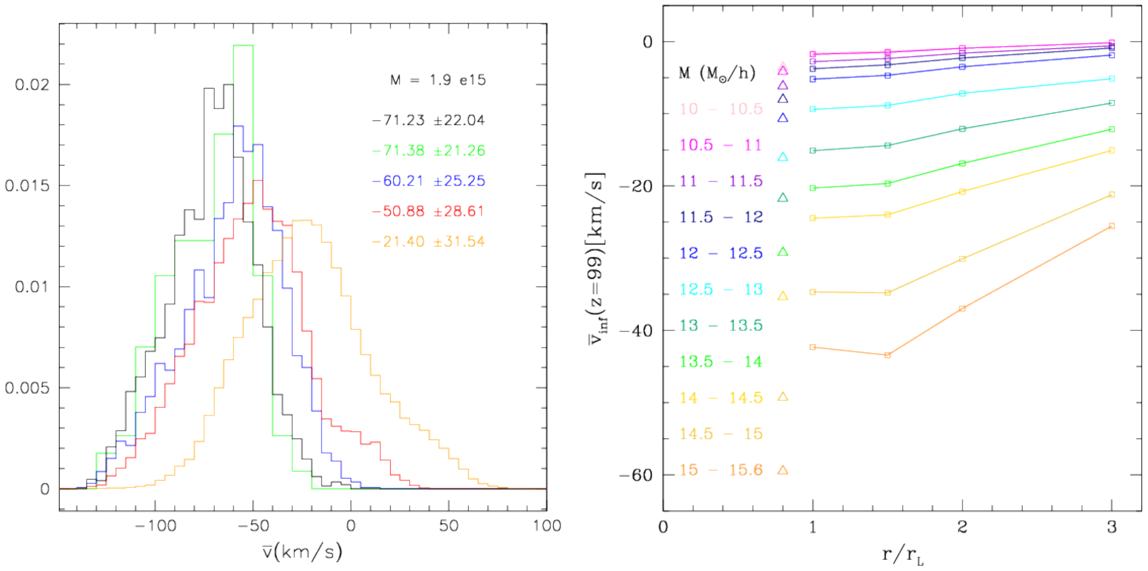

Figure 5.5: *Left*: The black histogram shows the distribution of the initial infall velocities of the particles of the final halo. The coloured histogram (with the sam colour code of Figure 5.3) show the same distribution for the field particles which will not be a part of the final halo, divided in four shells. We see that the median value of the distribution increases while going farther from the protohalo center and that at large distances the particles also have positive velocities. *Right*: Infall velocities of the halo particles and of the particles belonging to the surrounding region. The triangles represent the median infall IC velocity of the particles of the final halo, for haloes of different mass bins (plotted at x=0.8 for convenience). The squared points show the median IC velocity of the particles which do NOT belong to the final halo, but which are located near the initial protohalo. The median is measured in 4 shells, which are $d < r_{Lag}$, $r_{Lag} < d < 1.5r_{Lag}$,$1.5r_{Lag} < d < 2r_{Lag}$ and $2r_{Lag} < d < 3r_{Lag}$.

The linear predictions for the initial ($z = 99$) and final ($z = 99$) snapshots of le SBARBINE simulations are, respectively 0.3853 and 0.05542; thus

$$\frac{v_0}{v_{99}} \simeq 6.952. \tag{5.12}$$

In Figure 5.6, we compare the actual ratio measured in simulations with the one predicted by linear theory, for the velocity of halo centers. The red squared points stand for the median values of the distribution and the red solid lines for the quartiles. The solid horizontal line shows the linear prediction for the evolution of velocities, the dotted line the median of the whole distribution and the dashed line the mean. We find a qualitative agreement between the linear prediction and out measurements, even if - due to the non-linearity of structure formation - the measured ratio is on average a bit higher and differs significantly from linear theory in the case on massive haloes.

5.3 The properties of the initial density and potential fields

As already seen in the previous Section, the protohalo regions are defined by tracing all halo particles, identified at $z = 0$, back to their unperturbed (Lagrangian) positions. For each protohalo patch we calculated both the mass tensor and the deformation tensor which descrive, respectively, the physical shape of the protohalo and the potential field within/around the protohalo. The computational methods are described in detail in Section 3.6, as part of our post processing pipeline. All the results of the following Sections of this Chapter make use of the GIF2 simulations only.

Recall that the mass tensor $M_{\alpha\beta}$ is defined by the N_V particles found inside R_V as:

$$M_{\alpha\beta} = \frac{1}{N_V} \sum_{i=1}^{N_V} r_{i,\alpha} r_{i,\beta} \tag{5.13}$$

where $\mathbf{r}_i$ is the position vector of the ith particle and α and β are the tensor indices. Note that, in the simplest EC model, the initial mass distribution is spherical, so the mass tensor at any later time is determined completely by the initial tidal tensor defined by its constituent particles.

The left panel of Figure 5.7 shows that the protohaloes are indeed not spherical: the axis ratios as determined from the square-roots of the initial mass tensor only approach unity for the most massive haloes. This is due to the fact that the higher potential of massive haloes attracts particles more uniformly from the surroundings, originating more spherical patches in the IC. Note also that, even if massive haloes are more spherical at the IC, they become very triaxial at virialization, as shown by the axial ratio distributions of Figure 4.5 (while the opposite change is seen for less massive haloes).

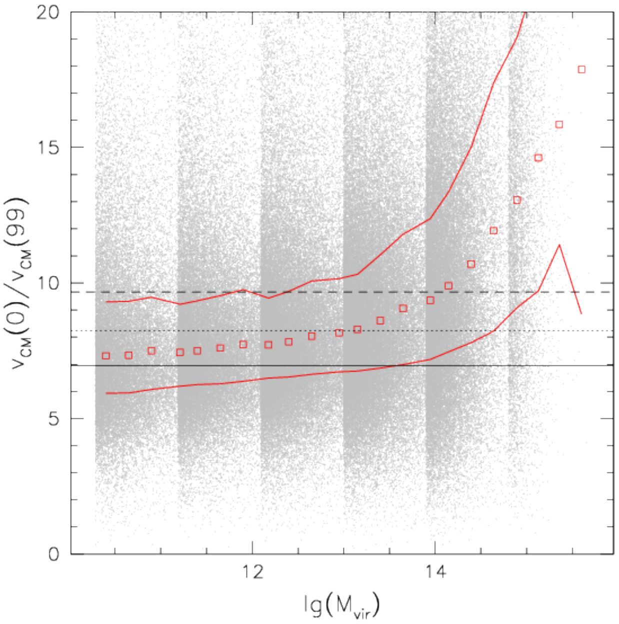

Figure 5.6: Velocity evolution of the center of mass of ellipsoidal haloes. We plot the ratio of the final (z=0) and initial (z=99) velocities as a function of the virial mass. The red squared points stand for the median values of the distribution and the red solid lines for the quartiles. The solid horizontal line shows the linear prediction for the evolution of velocities, the dotted line the median of the whole distribution and the dashed line the mean.

For each protohalo we then calculate the elements of the deformation tensor, defined at each position $\mathbf{q}$ as the second derivatives of the gravitational potential Φ. This, in the the Zel'dovich approximation [71] is equivalent to the evaluation of the first derivatives of the initial displacement:

$$\xi_{ij}(\mathbf{q}) = -\frac{\partial^2 \Phi}{\partial x_i \partial x_j}(\mathbf{q}) = -\frac{\partial \Psi}{\partial x}. \tag{5.14}$$

These were calculated from the initial displacement grid and differentiated with respect to the spatial coordinates, using the procedure described in Section 3.6. Specifically, for each halo we flagged the grid points occupied by particles and calculated the deformation tensor as:

$$\xi_{ij} = \frac{1}{V_L} \int_{V_L} \xi_{ij}(\mathbf{q}) d^3x = \frac{1}{N_G} \sum_{k=1}^{N_G} \xi_{ij}(k) \tag{5.15}$$

where N_G is the sum of all the grid cells contained within the Lagrangian volume of the halo: i.e., those actually occupied by halo particles and those left empty, but still located inside the halo (with at least four neighbour cells occupied by particles).

While doing this, we also studied the profiles of haloes in the initial conditions. Since the particles belonging to each halo are selected at the present time, they do not necessarily form a single simply connected *lump* in the initial conditions. We found that haloes are indeed more fragmented in the initial conditions, but in most cases the mass of the main lump is more than 90% of the total mass of the halo. Thus in this case, to calculate the initial properties, we decided to use the particles contained in the main lump, and to exclude from our sample those haloes for which less than 90% of the mass is in the main lump. In some rare cases, this fraction can be as small as 50% of the mass: these haloes

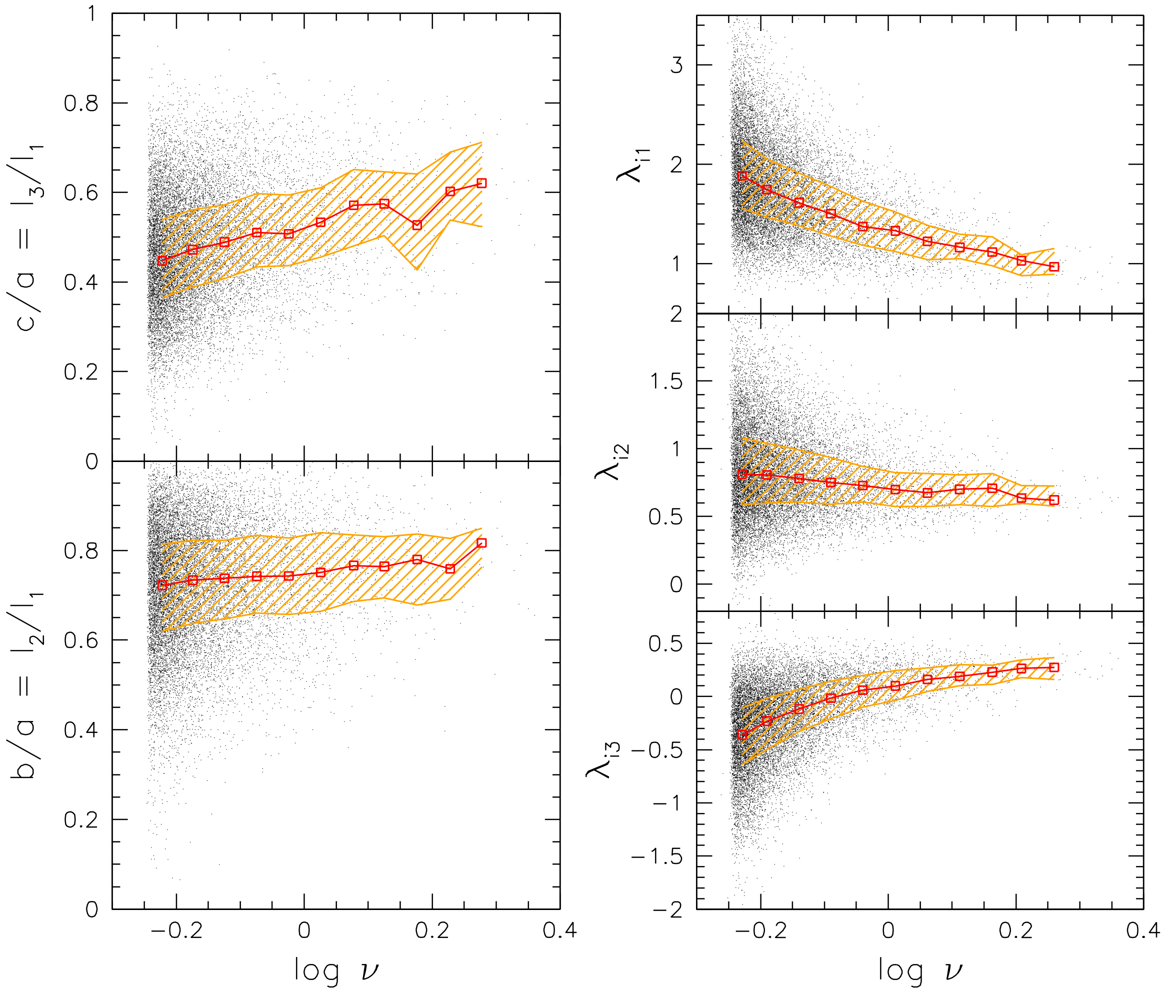

Figure 5.7: *Left*: Axis ratios calculated from the square root of the mass tensor eigenvalues of the protohaloes at the initial time. *Right*: The eigenvalues of the deformation tensor for the ellipsoidal proto-haloes, as a function of mass (which has been scaled to ν). The median of each distribution is shown in red, while the orange shaded region lies between the first and the third quartiles. Note that, while the first two eigenvalues are positive, the third one is almost always negative, especially at low mass, indicating that haloes are not contracting with the same strength along all the three directions and that the potential along the third axis may slow down the contraction in that direction.

probably formed through a recent merging process or have undergone some transformations in time, so they do not correspond to a sufficiently compact region in the initial conditions. They are only 8% of the total sample: removing them does not affect the mean behaviour, but it does reduce the scatter around this mean. Summing up, here N_G is the sum of all the cells (full and empty) contained in the main lump of the each halo.

Non-positivity of the initial eigenvalues

The right panel of Figure 5.7 shows the distribution of the eigenvalues of the deformation tensor (λ_i) as a function of halo mass, which we express in scaled units $\nu = \delta_{sc}/\sigma(M)$. Recall that $\sigma^2(M)$ represents the variance in the initial density fluctuation field when smoothed on scale $R = (3M/4\pi\bar{\rho})^{1/3}$. The λ_is are rescaled to $z = 0$ to allow an easier comparison with the distribution of δ_i shown in Figure 5.8: the "true" values are multiplied by the linear growth factor $D_+(z=0)/D_+(z=49) = 38.993$ and so become comparable with the reference for the Spherical Collapse model ($\delta_i \simeq 1.686$). In principle, this expression assumes a spherically symmetric filter. Although [32] provide the relevant expression for non-spherical filters, and note that it only makes a small difference, our main purpose here is to rescale the mass variable, so using the spherical expression is appropriate. In these units and for the cosmology adopted in the GIF2 simulation, $\nu = 1$ corresponds to a mass M_* is $8.956 \times 10^{12} M_\odot h^{-1}$. Later on, we will study halo properties for broader bins in mass; Table 5.1 shows the correspondence between these mass bins and ν.

ν	mass	n
0.53	$M_\star/16$	6607
0.67	$M_\star/4$	3890
0.84	$M_\star$	1061
1.06	$2-4M_\star$	348
1.33	$8-16M_\star$	109

Table 5.1: Correspondence between mass bins and ν; M_* is $8.956 \times 10^{12} M_\odot h^{-1}$. The third column shows the number of haloes in each bin.

The right panel of Figure 5.7 shows that while the first and the second eigenvalues are mostly positive, the third one is negative for the majority of the haloes, especially at lower masses. This indicates that, on average, protohaloes in the initial conditions are not contracting with the same strength along all their axes, and that, in the direction of λ_3 the potential may act slowing down the contraction or even causing an expansion. More precisely, only 30% show $\lambda_{1,2,3} \geq 0$, while 70% have $\lambda_3 \leq 0$ and $\lambda_{1,2} \geq 0$. A small fraction ($< 1\%$) of haloes behave very differently from these two categories.

We found that, as for the mass, the two identification schemes (SO and EO finders) yield very similar results also for the potential field: although there are haloes (especially at low mass) with significant differences, even larger than 40%, the median of the distributions remains around zero. The variance is larger in the case of λ_3, and, of course for lower masses. This shows that the spherical overdensity criterion traces the potential (and so the mass) quite well and that the best fitting ellipsoid is useful mainly for the description of the geometrical shape of the haloes and its evolution. The greater discrepancy for the values of λ_3, which is the one showing an unexpected behaviour, suggests that our new procedure provides a more realistic description of the halo structure.

Protohalo overdensities: the trace of the initial deformation tensor

In the EC model, the fundamental quantities which influence the evolution are not the eigenvalues of the deformation tensor themselves, but their combinations (δ, e, p) - defined by Equation 2.14. The most important of these is the overdensity δ, which is the trace of the deformation tensor.

The left panel of Figure 5.8 shows the distribution of δ as a function of halo mass, here scaled to ν. For ease of comparison with equation 2.15, the overdensity within the initial proto-halo has been rescaled to the present time, as was done for the eigenvalues λ_i. It is clear that the initial overdensity is a decreasing function of mass, in qualitative agreement with previous works [58, 53, 18], and with the prediction which comes from combining the *EC* model with the statistics of Gaussian random fields [58]. The required overdensity for collapse is higher for low mass haloes which must be able to hold themselves together against tidal effects. Although the overdensity values can be substantially higher than the critical value associated with the SC model, especially at small masses, they are almost never smaller. This represents a nontrivial success of the EC model.

Nevertheless, qualitative success does not guarantee quantitative agreement. In the EC model, the initial density of protohalo regions depends on the shape parameters e and p (equation 2.15). A simple estimate of the mass dependence comes from replacing $e\delta$ and $p\delta$ in equation (2.15) with a naive estimate of their mean values. If averaged over all possible positions in a Gaussian field, this gives $\sigma/\sqrt{5}$ and zero as characteristic values of $e\delta$ and $p\delta$, making $\delta/\delta_{sc} = 1 + \beta\nu^{-2\gamma} = 1 + 0.25\sigma^{1.2}$. The median values shown in the left panel of Figure 5.8 are smaller than this most naive prediction.

Most of the mass dependence in Figure 5.8 is removed by rescaling to $\Delta_h \equiv (\delta/\delta_{sc} - 1)/\sigma$. The right panel of Figure 5.8 shows that, in these scaled units, the mean and rms values are approximately

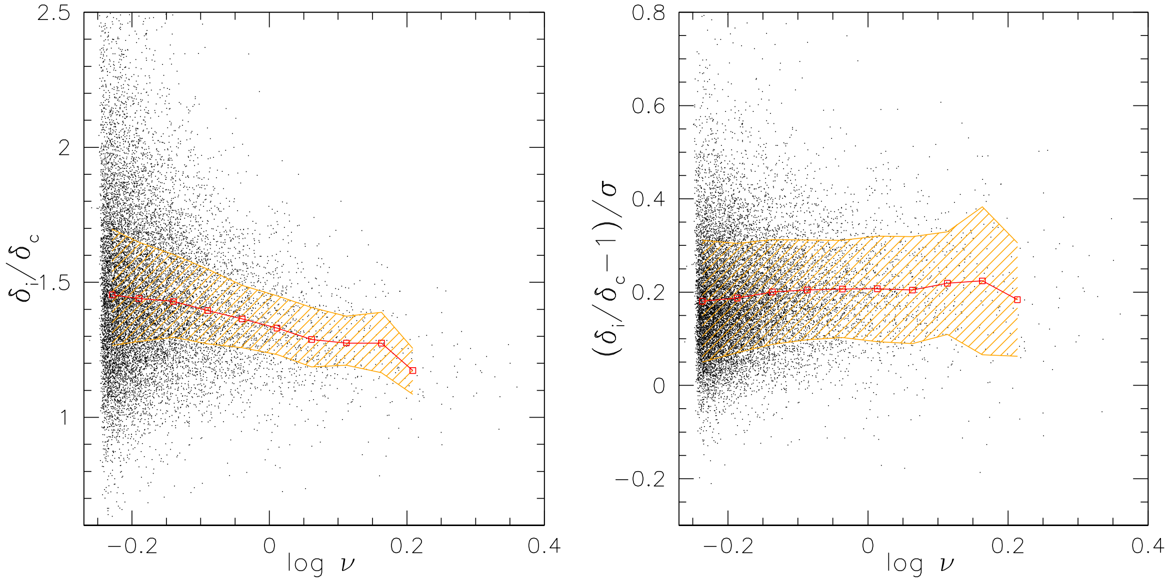

Figure 5.8: *Left*: Distribution of the initial overdensity as a function of halo mass (here scaled to ν). The overdensity is expressed in units of the critical value in the SC model, for ease of comparison with the EC prediction that it should always be greater than δ_{sc}, and increasingly so at small masses. *Right*: Same as previous figure, except that now the initial overdensity has been scaled to Δ_h, in terms of which most of the mass dependence has been removed.

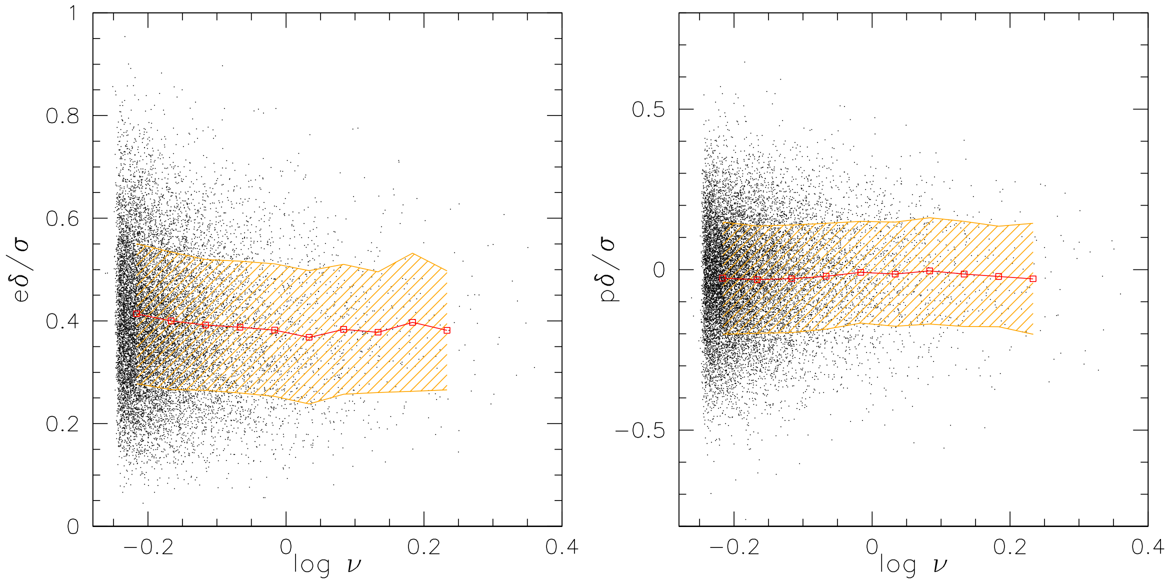

Figure 5.9: Distribution of the initial ellipticity and prolateness of the haloes as a halo mass (here scaled to ν). e and p have been scaled by δ/σ for more direct comparison with the EC prediction that $e\delta/\sigma$ and $p\delta/\sigma$ should be independent of protohalo mass.

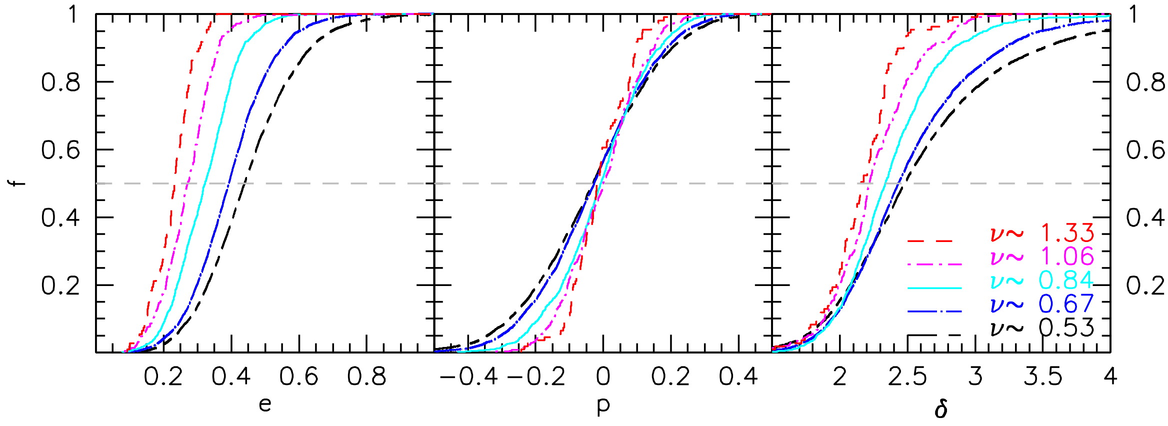

Figure 5.10: Cumulative distribution of initial ellipticity, prolateness and overdensity, for five different mass bins indicated by colours and line types; the bins have the same width in log(ν). They clearly show that ellipticity is a decreasing function of mass, as is the overdensity. In contrast, prolateness is almost the same, on average, for all mass bins. The gray dashed line is drawn to help identify the median values in the cumulative distributions.

0.2 and 0.12. These values are smaller than those reported by [53] ($0.48/\delta_c = 0.28$ and $0.3/\delta_c = 0.18$). Some of this is due to the fact that we use the actual particle distribution in the initial conditions to determine (δ, e, p), rather than assuming the initial shape was spherical. In addition, we use EO rather than SO derived quantities. We believe these differences matter, since the shape of the distribution is expected to encode information about the quantities in the initial conditions which determine halo formation.

Ellipticity and prolateness of the deformation tensor

In the EC model, the fundamental quantities which influence the evolution are not the λ_j themselves, but the combinations δ, e, p. Since we have already discussed δ, we now turn to a study of e and p in our protohaloes. Recall that, if the shape is caused entirely by the deformation tensor, then a prolate mass configuration corresponds to $p < 0$ and an oblate one to $p > 0$. (This classification differs from the one given by the geometrical mass distribution, in which a physically prolate/oblate halo has $p > 0/p < 0$.)

The distributions of ellipticity and prolateness are shown in the two panels of Figure 5.9 as a function of halo mass (always represented by ν). Recall that the combination of the EC model with Gaussian field statistics means that lower mass haloes should, on average, have larger values of e with a larger rms around this mean, while the most naive averaging procedure suggests that $e\delta/\sigma$ should have mean $\approx 1/\sqrt{5} = 0.447$ and rms 0.14 independent of mass. The lack of mass dependence in the mean and rms values is in good agreement with our measurements, although their actual values, 0.4 and 0.13, are slightly smaller than predicted. Similarly, $p\delta/\sigma$ has mean zero as predicted, but the measured rms of 0.15 is smaller than the predicted value of 0.22.

Inserting these values to obtain the EC prediction for the typical overdensity of protohaloes yields $\delta/\delta_{sc} = 1 + \beta(4/5)^{\gamma}\nu^{-2\gamma} = 1 + 0.22\sigma^{1.2}$. Comparison with the bottom panel of Figure 5.9 shows that this is about 10% higher that what we see. Our measurements indicate that $\delta/\delta_{sc} - 1 \approx 0.2\sigma$, with an rms scatter around this mean of 0.12σ (also see Figure 5.8).

Before moving on, note that $e\delta \equiv (\lambda_1 - \lambda_3)/2$, so, on average, $\lambda_1 - \lambda_3 \sim 0.8\sigma$. In addition, $p = 0$ implies $\lambda_1 + \lambda_3 = 2\delta/3$ or $\lambda_1 - \lambda_2 = \lambda_2 - \lambda_3$. While this latter is interesting itself, it is also worth noting that the mean values we see imply mean values of $\lambda_1 = \delta/3 + 0.4\sigma$, $\lambda_2 = \delta/3$ and $\lambda_3 = \delta/3 - 0.4\sigma$. This shows that the mean value of λ_3 will be less than zero once σ exceeds $5\delta/6$. Inserting the mean trend $(\delta/\delta_c - 1) \sim 0.2\sigma$ implies $\sigma \geq (5\delta_c/6)(1 + 0.2\sigma)$ or $\sigma \geq (5\delta_c/6)/(1 - \delta_c/6)$. So, a significant fraction of haloes with $\nu \equiv \delta_c/\sigma \leq (6 - \delta_c)/5 \sim 13/15$, will tend to have $\lambda_3 < 0$ (as shown in Figure 5.7).

Finally, Figure 5.10 shows the cumulative distributions of the three initial parameters, as a function of halo mass: the haloes were divided into five mass bins, described in Table 5.1. This confirms that, on average, both the initial overdensity δ and initial ellipticity e are larger at small mass, while the initial prolateness p is distributed around a mean value of zero.

We believe we have demonstrated that the combination of the EC model with the statistics of the Gaussian potential field works reasonably well. Because the potentials of the most massive proto-haloes are indeed more spherical, whereas the shapes of the most massive virialized haloes are less spherical ([1]; [56]), we conclude that we have a puzzle. Either the EC model is incorrect in its description of the evolution, or the proto-haloes are non-spherical even initially, and this influences the final shapes.

5.4 Evolution of halo shapes

The simplest *EC* model assumes that haloes evolve and collapse through a series of homologous triaxial configurations [70]: the directions of the three axes of the ellipsoid do not change, and they are determined by the initial deformation tensor. Therefore, the mass tensor is perfectly correlated with the initial (Lagrangian space) tidal tensor. But, as discussed in the previous sections, shapes are not spherical initially. This raises the question of whether or not the EC assumption that the directions of the principal axes of the mass and deformation are aligned is justified.

Initial alignment of the mass and deformation tensors

To quantify the correlation between the mass and deformation tensors, we study the distribution of $\mu_{ij} = |\cos(\widehat{\lambda_i l_j})|$, the cosine of the angle between axis i and j of the initial deformation and mass tensors. Recall that the mass and deformation tensor eigenvalues are ordered, as in the previous Sections, as $1 \geq 2 \geq 3$; we use l_i for the three axes calculated from the mass tensor (here we prefer to call them l_i instead of a, b, c, for uniformity of notation with the λ_is). The directions are said to be correlated if they are well-aligned ($\mu_{ij} \simeq 1$), while they are $anticorrelated$ in the opposite case ($\mu_{ij} \simeq 0$): the maximum misalignment happens when the two vectors (representing the semi-axes of the ellipsoid) are perpendicular to each other, while they are considered aligned when $\cos(\widehat{\lambda_i l_j}) \simeq 1, -1$, since a misalignment of more than 90 degrees corresponds in fact to an alignment on the other side.

Previous measurements in simulations (Porciani et al. 2002 [50]) have shown that while this correlation is indeed very good, the two tensors are not perfectly correlated. The left panel of Figure 5.11 confirms this. For our protohaloes, the longest axis of the mass tensor l_1 is very well-aligned with λ_1 of the deformation tensor, which corresponds to the direction of maximum compression; similarly the shortest mass tensor axis l_3 is aligned with the direction of minimum compression λ_3. To quantify this, the median values of the distributions in Figure 5.11 are:

$$p[\cos(\theta_{ij})] = \begin{pmatrix} 0.898 & 0.396 & 0.081 \\ 0.406 & 0.853 & 0.109 \\ 0.070 & 0.120 & 0.985 \end{pmatrix}. \tag{5.16}$$

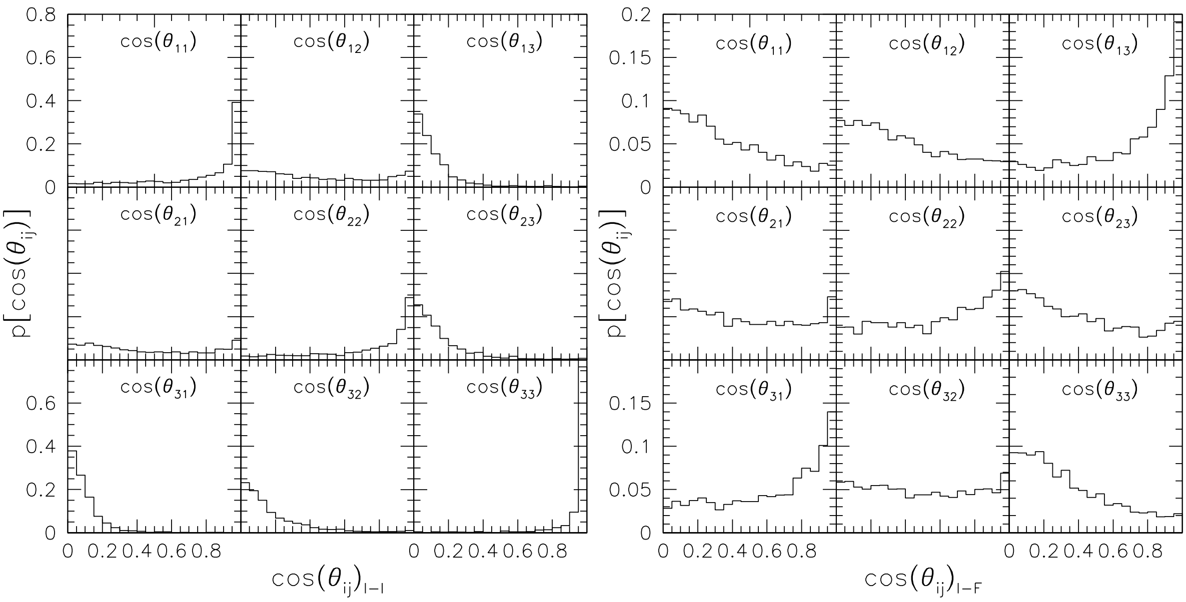

Figure 5.11: *Left*: alignment between the principal axes of the initial mass tensor and the initial deformation tensor. *Right*: alignment between the principal axes of the initial deformation tensor and the final mass tensor.

Thus, it is no longer obvious that the halo will turnaround first along the direction of its initial minor mass axis, then along the second and finally along the major mass axis, as it would be predicted by the model. Rather, the differences in the turnaround (or collapse) times of the three axes may be smaller than they were for the case of collapse from a sphere. Moreover, it is probable that the first axis to reach turnaround will be the major mass axis l_1, since it is aligned with the direction of maximun compression.

Alignment of the final mass tensor with the initial deformation tensors

Therefore, it is also interesting to study the alignment between the initial and final axes to check how the evolution affects the axis orientation. At the initial time, both the mass and the deformation tensor can be used to approximate protohaloes, while the final orientation and dimension of the haloes can be described only by the mass distribution (since the [71] approximation used to calculate the λ_i can be applied only at the initial time). Hence, the right panel of Figure 5.11 compares the alignments between the principal axes of the final mass tensor with that of the initial deformation tensor.

For this particular analysis we only chose haloes with more than 1000 particles in the GIF2 simulation - so as to ensure accurate determination of the mass eigenvectors - and haloes with smooth evolution and mass accretion history. This last condition arises because we have found that a significant fraction of haloes presents an irregular evolution history, probably due to the occourence of important merging events, which of course influence the final orientation of the halo. We identified these using an objective automated algorithm, which searches for irregularities in the evolution of the amplitudes of the axes of the best fitting ellipsoid. We exclude them from the sample for this specific case, because their final properties could be influenced by the merging history more than by the initial distribution, unlike regular haloes. Thus, they constitute a different population which should be studied separately. An example of such an halo is shown in Figure 5.16: a quick comparison with the haloes of the other similar Figures is enough to note some irregularities in its evolution. First of all, the protohalo at the IC is formed by two big clumps, with the top-left one falling onto the other (even though irregular, this halo was not excluded by our initial selection since the two clumps are already connected to each other); moreover, during its evolution the three axis lengths cross many times and the final orientation of the halo is not well correlated with the initial one, as for other haloes.

Returning to Figure 5.11, it is clear that at the final time the axes of the two tensors are not so well-aligned as in the initial conditions: the top-right box, for $\cos(\theta_{13}) = \cos(\widehat{\lambda_{I1} l_{F3}})$, shows that the final shortest axis of the mass tensor seems to be aligned with the direction of initial maximum compression λ_1. The bottom right panel shows that it is almost anticorrelated with the direction of initial minimum compression. This sort of inversion occurs also in the case of the first axes: the bottom-left box shows that the final longest mass axis l_{F1} is better aligned with λ_3 than with λ_1 (top-left box).

The tendency shown in the left panel of Figure 5.11 is thus completely reversed. Now, the median values of the (cosines of the) alignment angles are:

$$p[\cos(\theta_{ij})] = \begin{pmatrix} 0.310 & 0.360 & 0.779 \\ 0.463 & 0.613 & 0.365 \\ 0.677 & 0.497 & 0.300 \end{pmatrix} \tag{5.17}$$

confirming that whereas before the 11 and 33 correlations were strongest, now it is the 13 and 31 correlations which are strongest.

The left panel of Figure 5.12 shows how this behaviour depends on halo mass, plotting the same distributions of Figure 5.11 (but here cumulative and not differential) for haloes of three mass bins: black (solid), blue (dot - long dash) and red (short dash) curves show results for mass bins centered on $M_\star$, $M_\star/16$ and $8-16M_\star$. Clearly, the evolution pattern that we have suggested is strongest for the most massive haloes. We also checked the alignment between the initial and final axes of the mass tensor, but we do not present the result here since the correlations are weaker and only the behaviour of the shortest axis is well defined: this seems to indicate that the potential field is a better tracer of the initial shape, since it shows what will be the evolution tendency more than the actual initial position of particles.

Evolution of the alignment

To study more closely if and when the axes invert, the right panel of Figure 5.12 shows the evolution of the misalignment between the major axis of initial deformation tensor λ_{I1} and the shortest axis of the mass tensor l_3 (i.e., the strongest alignment shown in the matrix 5.17) calculated at each time step of the simulation and for all the haloes of our selection. The points show the median value of the cosine of the angle between the principal axes of the two tensors at each time and the dashed lines the first and third quartiles of the distribution. At high redshift the two axes are almost perpendicular to each other: the median misalignment is $cos(\theta) \simeq 0.12 \simeq 83^\circ$; on the contrary by $z = 0$ they are almost perfectly aligned. I.e., the halo collapses in the direction of maximum compression and, by the end, the shortest axis of the halo lies in this direction (which is almost perpendicular to the direction of the initial shortest axis). There is, in fact, an intermediate period of rapid misalignment, followed by a stable period at late times. Note that the best alignment happens some time before $z = 0$, probably because it corresponds to the mean formation time. While the right panel of Figure 5.12 shows the median behaviour, some examples of the evolution of individual haloes can be found in Figures 5.13, 5.14, 5.15,5.16 and 5.17 - which will be described in detail in the next Section.

We believe that this inversion in direction is rather generic to the collapse process, but there are a number of ways in which this can happen:

1. if the mass and deformation tensors are perfectly aligned, then this is just a consequence of the compression due to the tidal field. I.e., early-on, the protohalo contracts most rapidly along the direction of λ_1, while contracting more slowly along the direction of λ_3. Eventually, the protohalo collapses first along the direction of λ_1, then along λ_2 and finally along λ_3; the resulting mass distribution ends up being more compressed along the direction of maximum initial

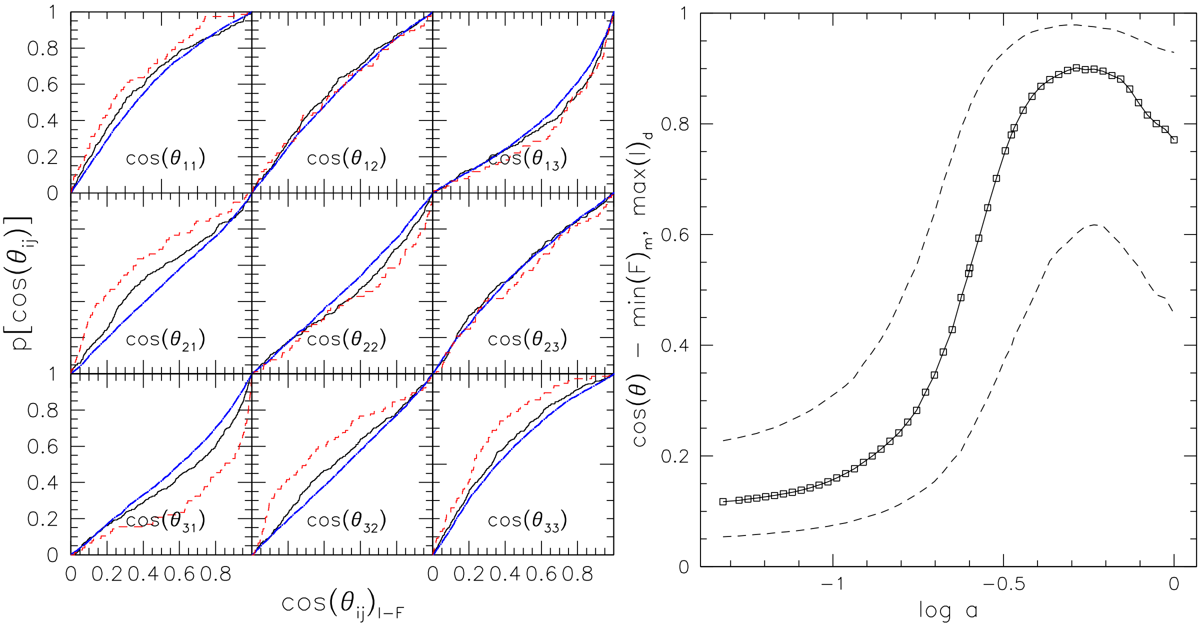

Figure 5.12: $Left$: Same distributions as in Figure 5.11, but in cumulative rather than differential form; haloes are now split according to their mass: $M_\star/16$ in blue (dot - long dash), $M_\star$ in black (solid) and $8-16M_{star}$ in red (short dash). The alignments or misalignments are enhanced at higher masses. $Right$: Misalignment between the longest axis of initial deformation tensor and the the shortest axis of the mass tensor of the haloes at as a function of time, represented by log(a): the points represent the median values at each time and the dashed lines the first and third quartiles of the distribution.

compression, λ_1, and more elongated in the direction of initial minimum compression λ_3. As a result, the longest axis of the mass tensor of the final object, which is perpendicular to the shortest axis, ends up being perpendicular to its initial direction, even though there is no rotation. In this case, there should be a time during the evolution when the axis lengths are equal.

2. If the mass and deformation tensors are not well-aligned initially, then the object may rotate. For example, if the second axes are well-aligned but the first and third are not, then the object may rotate about the second axis. This rotation will be most effective if the sum of the first and third deformation vectors is perpendicular to the sum of the first and third mass vectors. I.e., rotation will be most efficient if λ_1 and λ_3 have opposite signs. Once the axes are aligned, the rotation stops. In this case, the exchange of direction of the axes need not be accompanied by an exchange of lengths. Note that although we showed that $\mu_{11} \sim 1$, suggesting that the initial misalignments are small, $\mu_{11} = 0.9$ still allows misalignments as large as 20°. Since the rotation depend on the cross- rather than dot-product of the two vectors, rotation might be more common than one might have concluded on the basis of the statement that $\mu_{11} \sim 1$.

3. Finally, there could be an intermediate case: it may be that the halo does not actually rotate, in the sense of having an overall angular momentum: rather, as the particle distribution is squeezed by different amounts in different directions, the relative lengths of the mass axes change, the particle distribution deforms (maybe not exactly along the directions of the λ_is due to the initial misalignment between the two tensors) and so the direction in which the longest axis points can evolve.

We looked at the evolution of many haloes in 3D, using animations which cannot be - obviously - printed here. Figure 5.17 shows some snapshot of one of these 3D animations: by looking at them, it seems clear that haloes do not show an overall rotation - ruling out hypothesis 2. We think that the best choice would be a combination of hypothesis 1 and 3: surely the initial compression factors have a major effect, but the deformation also induces peculiar motions in the particle distribution.

In summary: the major axis of a protohalo is initially aligned with the direction of maximal compression [50, in agreement with]. For a few haloes, the compression is sufficiently large that this longest axis ends up being the first one to turnaround and collapse, and so it becomes the shortest axis. Whether or not the axis lengths invert, for most haloes, the axis directions do: the shortest axis of the final object ends up being well-aligned with the initial direction of maximal compression. As will be argued from the examples in the next section, haloes show a general behaviour, but they differ in the details of the evolution: further analyses are needed to provide a more complete description of the process.

5.5 Evolution of the particle distribution

We described the mean behaviour of the halo population, which is indeed representative of individual haloes. To illustrate this, we show how the shape and orientation of the particle distribution in a few test haloes evolves in time. We followed the change in axis lengths snapshot by snapshot, but since the best fitting ellipsoid is calculated independently at each time step, we had to decide how to associate each axis with its corresponding “self” at the next step: at each time step we calculated the angles between the axes and the axes at the previous time step, and then associated the couples of axes which align the most. In this way, the axis system of the halo is allowed to rotate and follow the modifications in shape.

In Figures 5.13, 5.14 and 5.15 we show the 2D projections of the particle distributions with respect to a fixed coordinate system; the axes are rescaled so that the halo maintains almost the same dimension in each plot, to concentrate on the evolution of its shape. In addition, in the bottom-left panel we show how the (square-roots of the) eigenvalues of the mass tensor evolve. These are the lengths of the principal axes of the object; if two of these cross, then this signals that the compression due to the deformation tensor has managed to change the relative axis lengths. This information about how the size of the object changes gives no insight into the spatial orientation of the object. To see if the principal axes of the mass tensor change direction - from the combined effects of compression and rotation - we also show how the angle between the mass tensor axis l_i and the initial deformation tensor axis λ_i evolves.

Figures 5.13 and 5.15 show the evolution of haloes of mass M_* and $16M_*$ respectively. Despite the order of magnitude difference in mass, both objects evolve rather similarly. In both cases, the initial particle distribution is rather non-spherical, after which gravitational collapse occurs along the preferred directions as discussed in the main text, creating a pancake; the directions of the three principal axes of the best-fitting ellipsoid change with time; there is an axis inversion feature, such that the longest and shortest axes exchange directions. Notice that the evolution is not identical, even though the values of $\delta \sim 2$, $e \sim 0.2$ and $p \sim 0$ are approximately the same. This shows that the initial deformation tensor does not uniquely determine the evolution – the initial shape also matters, as does the degree of initial misalignment. For these haloes, b/a and c/a were $(0.94, 0.59)$ and $(0.91, 0.72)$, respectively, and although the initial alignments are all within 10° for the first object, they are much worse for the second.

In more detail, the top panels show the projected particle distribution at nine time steps between $z = 49$ and $z = 0$. Red, magenta and yellow show the longest, intermediate and shortest axes of the mass tensor. Projecting from three to two dimensions means that the relative lengths are not always obvious in such a plot, so the bottom left panels show how the lengths of the three mass axes evolve. Red, blue and black curves show the evolution of the longest, intermediate and shortest axes, in units of

$$r_{Li} = (l_{1i} l_{2i} l_{3i})^{1/3}. \tag{5.18}$$

In some cases the axis which was initially the longest may become the second longest; this sort of length-inversion occurs in only a few of our haloes (which were excluded from the analysis regarding the axes alignments, to have a more homogeneous sample): an example is given in Figure 5.16. Halo 6 has been discarded from our analysis since it is clearly disturbed: its initial patch is formed by two near lumps, with the smaller one fallin on the other. This modifies the whole evolution, as can be noted by the irregularities in the two bottom plots and from the fact that the longest axis (in red) remains always in the same direction (the same of the infall). The time at which the axes lengths cross does not necessarily coincide with the time when the long axis starts becoming better aligned with the direction of minimum initial compression; squares connected by dashed lines show the moment when the exchange in direction occurs.

The bottom right panels illustrate the evolution of the alignment angle in more detail. They show the angle between the mass axes and the direction of the corresponding initial deformation axis. Red, blue and black show the longest, middle and shortest axes ($\widehat{l_1\lambda_{i1}}$, $\widehat{l_2\lambda_{i2}}$ and $\widehat{l_3\lambda_{i3}}$, respectively). Thus, Figure 5.13 shows that halo 252 appears to rotate about its shortest axis initially; by the time the other two axes have exchanged directions, they have also reached turnaround. Thereafter, the object rotates about its longest axis, until the other two have approximately exchanged directions. The net result is that the longest and shortest axes have exchanged directions. In contrast, the more massive halo 14 shown in Figure 5.15 is slightly simpler. The initial misalignment in this case was larger, but its second axis soon aligns with the intermediate axis of the initial deformation tensor, after which the object appears to rotate about this second axis until the first and third axes have exchanged directions.

Figure 5.14 shows another example of evolution: the initial parameters are again similar to the ones of the two previous haloes, but in this case $\lambda_3 < 0$. We see that the evolution follows a similar pattern, even if the evolution is more rapid at the beginning and the change in direction happens more than once, involving also the medium axis. However, at the end even this halo has a stronger misalignment for the shortest and longest axes, while the medium returns back towards its initial direction. In all three cases, the misalignment angles are tens of degrees. This is in apparent contradiction with our finding in the main text that $\mu_{11} \sim 1$, which suggested perfect alignment. However, note that $\cos 20° = 0.93$ which is very close to unity.

Finally, in Figure 5.17 we show some stages of the evolution of a protohalo in 3D, hoping that this could further clarify our conclusions; the particle distribution is shown on the left, while the best fitting ellipsoid on the right.

5.6 Summary

In this Chapter we presented an analysis of the properties of protohaloes in the Initial Conditions and of the influence of such properties on the whole history of haloes.

We first tried to understand what defines protohaloes, since they are supposed to correspond to special regions (density peaks) in the initial field: these are usually found in simulations by tracing the halo particles back in time to the IC. Thus, the region which will then form the virialized halo is a shapeless clump of particles. Nevertheless we found that those particles possess some special properties that distinguish them from the surrounding ones: for example, all the halo particles are already infalling toward the halo center, while the surrounding particles show a broader distribution.

In the EC model, the properties of the initial field are usually expressed not in terms of the three eigenvalue of the deformation tensor λ_i but using the trace, and the shape parameters e and p. We plotted their distributions, finding that:

- for most protohaloes the eigenvalues of the deformation tensor do not have the same sign; the fraction of protohaloes for which this is true increases at low masses;
- at fixed mass, protohaloes have a range of initial overdensities; these are almost always larger than the critical overdensity associated with spherical collapse; the mean overdensity increases as mass decreases, scaling approximately as $\delta_c(1+0.2\sigma)$, and the rms distribution around this mean is 0.2σ (it is broader for lower mass haloes);
- the median ellipticity e of the deformation tensor decreases as mass increases: the distribution of $e\delta/\sigma$ is approximately independent of halo mass, having mean ~ 0.4 and rms 0.14;
- the median prolateness of $p\delta/\sigma \simeq 0$ with rms 0.15;
- the mass tensors are increasingly non-spherical as protohalo mass decreases.

The middle three findings are in good qualitative agreement with the triaxial collapse model in which low mass haloes need a higher initial overdensity so as to collapse by the present time, because they tend to be less spherical.

The final part of this work aimed at understanding how the initial potential field interacts with haloes and influences their evolution, since the initial properties are the dominant ingredient in the *EC* model. Thus, we studied the cross-talk between the mass tensor and the deformation tensor: the first gives an estimate of the particle distribution of haloes and so of their actual shape and orientation, while the second (calculated only at the initial time) describes the potential field. We showed that:

- At the initial time, the principal axes of the two tensors are very well-aligned; the longest axis of the mass tensor (l_1) is aligned with the direction of maximum compression λ_1, l_2 is aligned with λ_2, and l_3 with λ_3. However, although cos of the misalignment angle is ~ 1, the angle itself can still be of order tens of degrees.
- At the final time ($z = 0$) the alignment between the axes is reversed, as a consequence of the collapse process and the associated deformation of the particle distribution.
- The change in directions of the first and third axes are sometimes dominated by the different compression factors, and others by what appears to be rotation, although it is still unclear if the apparent rotation is actually an asymmetrical deformation of the particle distribution.

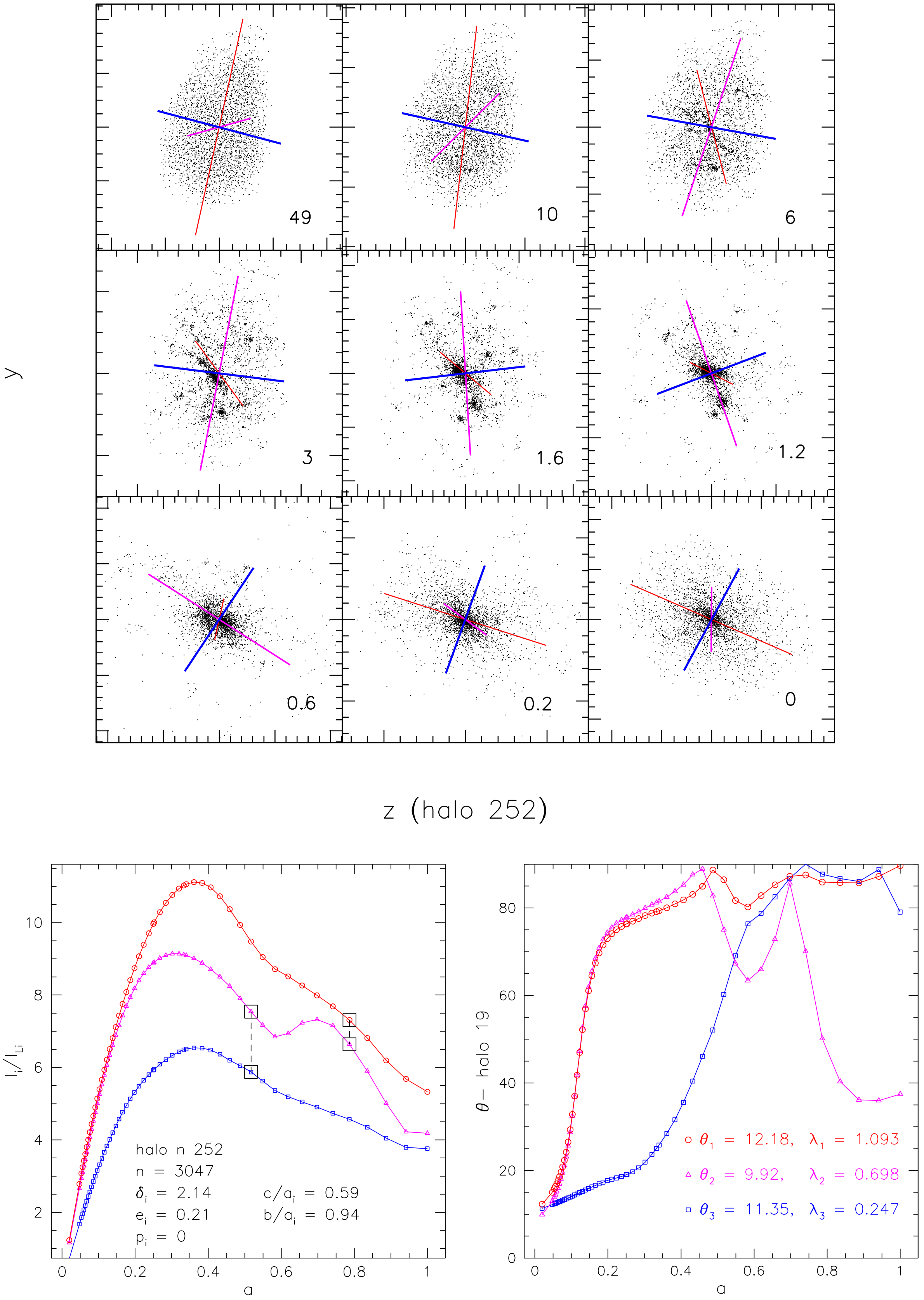

Figure 5.13: Evolution of an object of mass M_*. Top panels show the projected particle distribution at different redshifts (as labeled); bottom left shows the evolution of the three mass axes; bottom right shows the evolution of the angle between the mass tensor axes and the initial deformation tensor axes (the misalignment of the longest axis is shown in red, the medium in blue and the shortest in black).

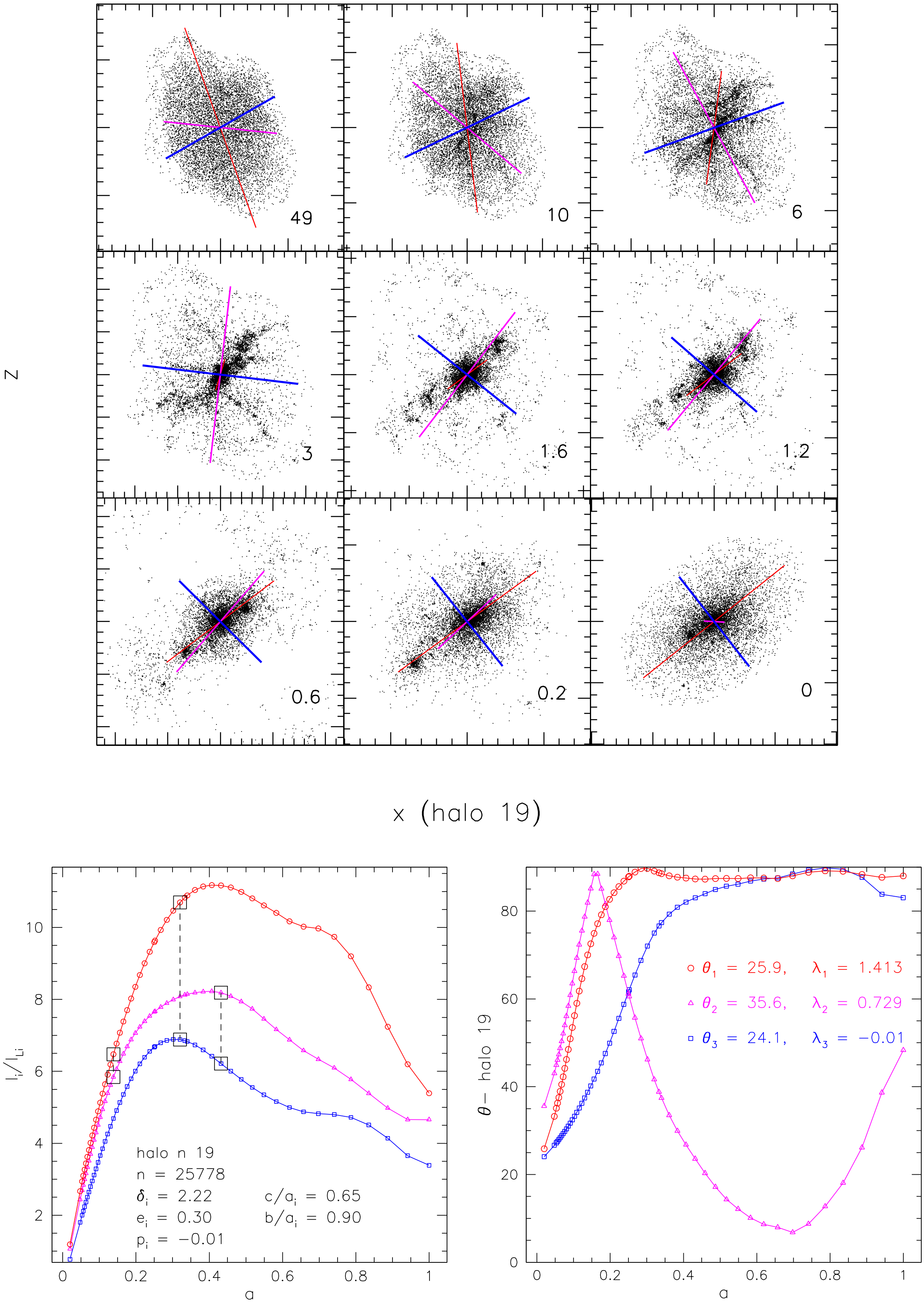

Figure 5.14: Same as previous figure, but now for an object of mass $4M*$. Notice in particular that in this case $\lambda_3 < 0$.

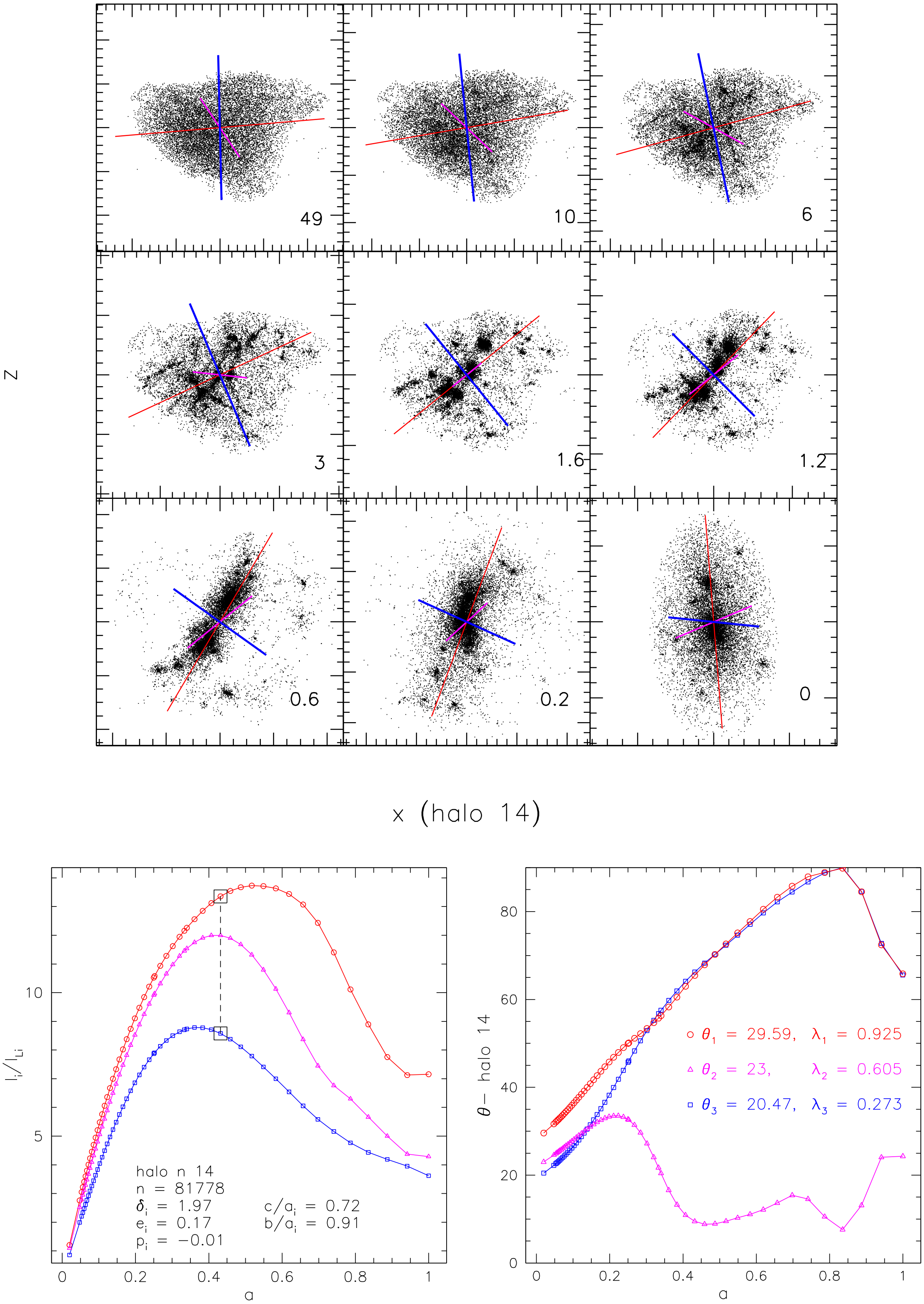

Figure 5.15: Same as previous figure, but now for an object of mass $16M*$.

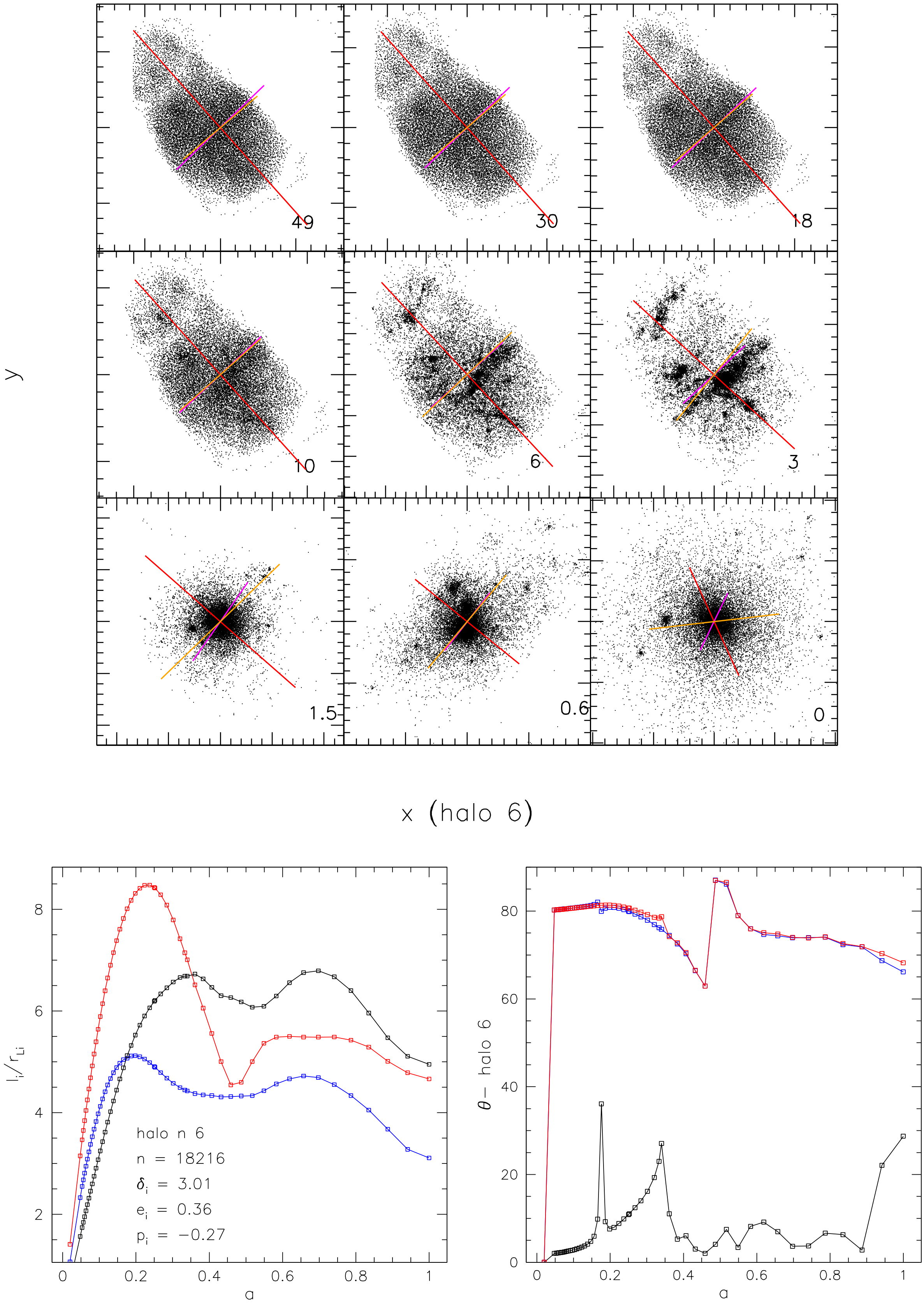

Figure 5.16: Same as previous figure, but now for an object which has been discarded from our selection: it is clearly formed by two big lumps in the initial conditions, with the smaller one falling on the other. This also result in an unusual axis evolution.

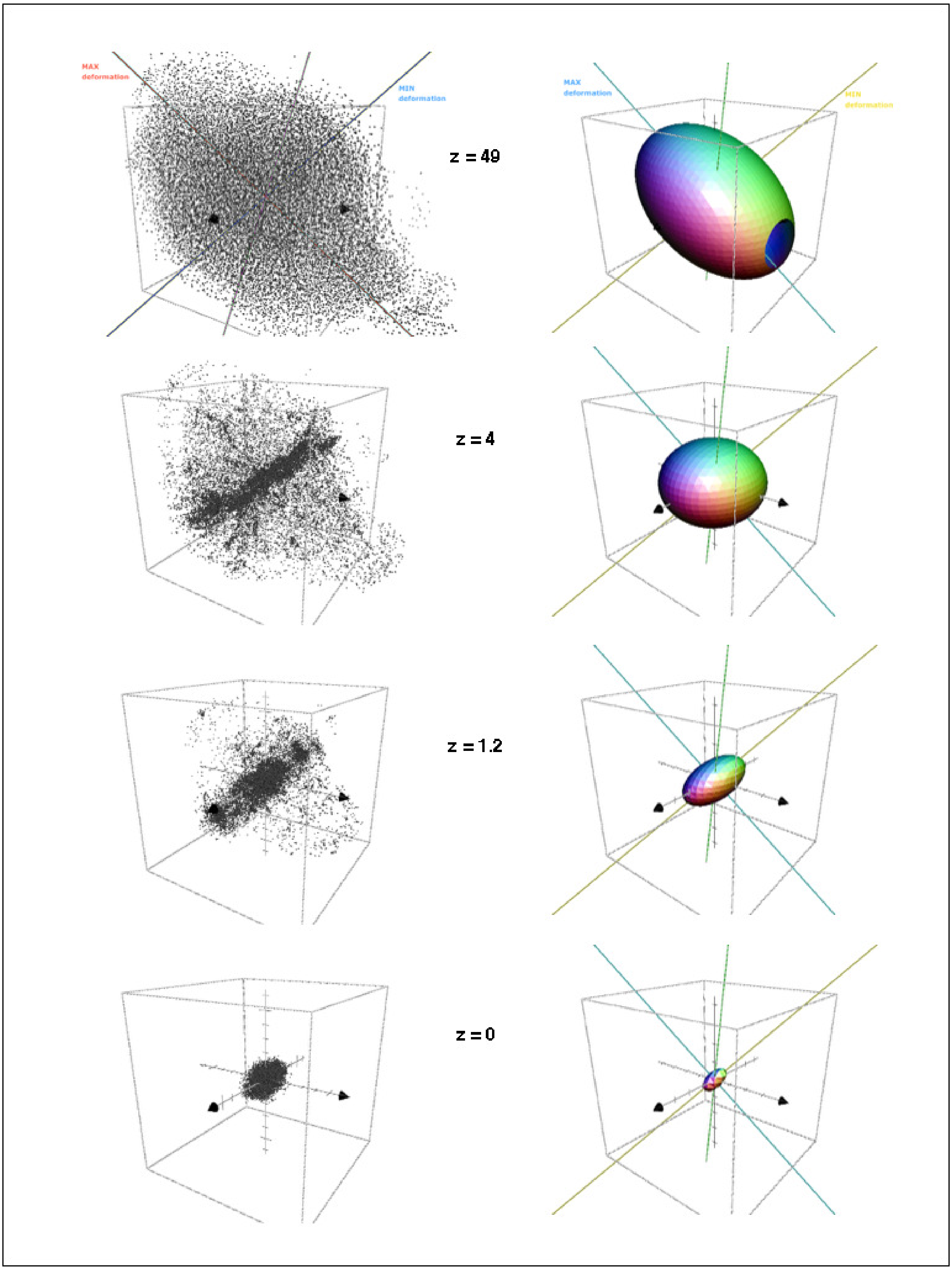

Figure 5.17: *Left*: evolution of a test halo in 3D. *Right*: best fitting ellipsoid to the particle distribution.

Universal distributions for the shape parameters 6

The interpretation of observations requires a comparison with the predictions coming from theory and simulations [34]. For this reason, it is becoming more and more important to model the results of simulations with as much detail as possible, even if this is computationally more expensive. In particular, precise knowledge of the ellipticity and of the axial ratio distributions of galaxy cluster-size halos is fundamental to compare with observational studies which combine different bands to recover - for example - cluster masses [40, 39].

The aim of this chapter is to present an analysis of the shape of triaxial haloes, its evolution with redshift and dependence on cosmology. In particular, we will analyse the distribution of the shape parameters (axial ratios, ellipticity and prolateness) as a function of halo mass and redshift; we will then present some universal relations and fitting formulae which may be used to retrieve the typical shape distribution at a certain time or for a certain mass bin - when a comparison with observations or a prediction is needed. For this work, we used both the GIF2 simulation [20] and two simulations (Baby and Flora) from LE SBARBINE simulations set, described in Chapter 3. This allowed us to compare two different cosmological models and test the universality of our results. Part of these results hase been published in Despali, Giocoli and Tormen 2014 [14]. The mean features of the three simulations are summarised in Table 6.1.

Moreover, in Bonamigo et al. 2015 [7] we provided the first statistically significant predictions in the unexplored mass range above 3×10^{14} $M_\odot h^{-1}$, using haloes from two redshifts ($z = 0$ and $z = 1$) of the Millennium XXL simulation [3]. The size of this cosmological dark matter only simulation (4.1 Gpc) allows the formation of a statistically significant number of massive cluster scale haloes (≈ 500 with $M > 2\times10^{15}$ $M_\odot h^{-1}$, and 780 000 with $M > 10^{14}$ $M_\odot h^{-1}$). Then we extended this investigation to lower masses in order to look for universal predictions across nearly six orders of magnitude in mass, from 10^{10} to almost 10^{16} $M_\odot h^{-1}$. For this purpose we use the SBARBINE simulations, allowing to model haloes of masses starting from $\approx 10^{10}$ $M_\odot h^{-1}$.

In this Chapter we will consider only ellipsoidal haloes, identified with our Ellipsoidal halo finder (Section 3.6); Mario Bonamigo run an equivalent code on the Millennium XXL snapshots. Thus, all the masses that we refer to are *ellipsoidal masses*.

	Ω_m	Ω_Λ	H[km s^{-1}]	box [Mpc h^{-1}]	z_i	N	$m_p[M_\odot h^{-1}]$	σ_8
GIF2	0.3	0.7	70	110	49	400^3	1.73×10^9	0.9
Baby	0.307	0.693	67.7	100	99	512^3	6.36×10^8	0.829
Flora	0.307	0.693	67.7	2000	99	1024^3	6.35×10^{11}	0.829

Table 6.1: Main features of the three simulations used in this work.

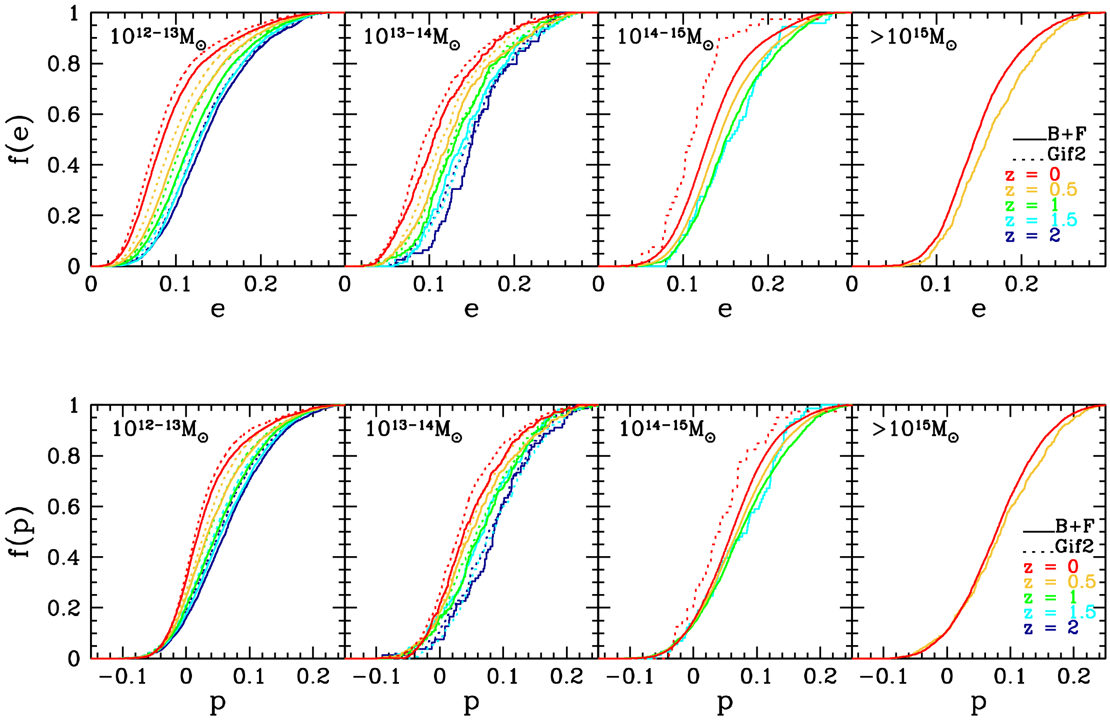

Figure 6.1: Ellipticity and prolateness cumulative distributions. Each panel shows the distribution at five redshifts for a different mass bin, with increasing mass from left to right. The haloes of Baby and Flora are represented by the solid lines, while those of the GIF2 by the dotted lines. We notice that both ellipticity and prolateness decrease to low redshift and also to lower masses.

6.1 Halo populations at different z

In this section we will describe how the halo ellipticity and prolateness change as a function of redshifts for different halo masses and how it is possible to obtain universal relations for the shape parameters.

Distributions of e and p at different times

In Figure 6.1 we show the ellipticity and the prolateness cumulative distributions: in each panel we present the results for five different redshifts - $z = 2, 1.5, 1, .5, 0$ - (or less at high masses) for a given mass bin. The haloes of Baby and Flora are represented together - since they have the same cosmology - by the solid lines, while those of the GIF2 by the dotted lines. Flora is determinant to have enough data at $M > 10^{14} M_{\odot} h^{-1}$: it contains around 150000 systems more massive than 10^{14} and 1390 still more massive than $10^{15} M_{\odot} h^{-1}$. Looking at each panel it is clear how both ellipticity and prolateness peak at higher values at high redshift; on the other hand, comparing the curves of the same colour in the four panels, we see that, at any given redshift, the median of e and p increases with mass: as already shown in other works using the axial ratios [1, 42], at the present time – and also at each previous epoch – the most massive systems are also the least spherical. They are still in the formation phase and so their shape is still be influenced by the direction of the last major merger or of the material falling in through the filaments, making them more elongated. Smaller haloes, formed at higher redshifts and typically more concentrated, lived for enough time to relax and lose memory of

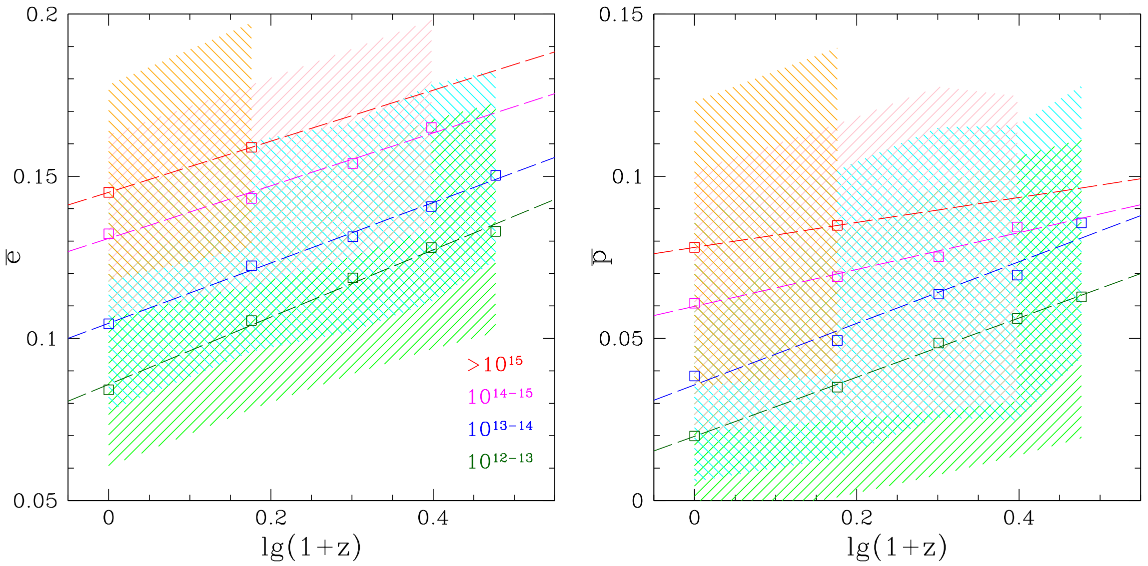

Figure 6.2: Medians and quartiles of the cumulative distributions of Figure 6.1 both for the ellipticity (left panel) and the prolateness (right panel), for Baby and Flora as a function of redshift. Each set of point shows the median relation for a different mass bin and the shaded regions the quartiles. The dashed lines represent the linear fit to each set of points.

the directions of the different merging events experienced during their history. To stress these two dependencies, in Figure 6.2, we show, as a function of z - only for Baby and Flora - the medians of the ellipticity and of the prolateness distributions of Figure 6.1: each set of point shows the median relation for a different mass bin and the shaded regions the quartiles; the dashed lines represent the linear fit to each set of points.

In Figure 6.1, we observe also a slight dependence on cosmology, with Baby and Flora having an higher average value for both e and p; this was expected since, in a universe with a lower value of σ_8 (Baby+Flora), haloes tend to form later and so, when we look at them at a given time, they are still more ellipsoidal than those which form with in an higher-σ_8-universe (GIF2).

A universal rescaling for halo shape evolution

In Figure 6.3 we show how the ellipticity and prolateness distributions evolve in time for haloes of different masses: in the top panel the median ellipticity is plotted against the halo mass for eleven snapshots of each simulation (a part from Flora, we have a significant number of haloes only at six snapshots). We can notice both a dependence on mass and on time as in Figure 6.1: first, looking at each set of points independently, it is clear that more massive haloes are on average less spherical than the smaller ones. Then, looking at the whole plot, the median ellipticity decreases in time, leading to a more spherical distribution at the present time. In the bottom panel, we show the same results for prolateness. At all times haloes tend to be prolate ($p > 0$), even if this trend weakens at low redshifts.

Since the virial mass is a cosmology and redshift-dependent definition, Press and Schechter (PS) and extended-PS approaches [52, 8, 30] have shown that an universal generalisation of the mass function can be obtained by using the variable $\nu(z)$. An analogous approach has also been used by [51] to rescale the concentration for different cosmologies and various redshifts. Also in our case, using ν instead of the virial mass, allows to obtain an universal relation: in Figure 6.4 we show the same points of Figure 6.3, but as a function of ν instead of mass. It is easy to see that the use on ν remove the dependence on both cosmology and time: this is due to the fact that $\sigma(M)$ retains the information of the mass and is higher for low masses, while $\delta_c(z)$ changes in time, increasing at high z. The combination of the three simulations allows us to span an order of magnitude in ν and we verify that, in these unit, all the points move on the same median relation. The effect is the same also on the prolateness and the axial ratios and so we believe that it is not worth showing all of them. Thus, in Figure 6.5 we decided to average over all the points at all the eleven redshifts, for each one of the simulations: the coloured points show the medians for each simulation and the corresponding shaded regions enclose the first and third quartile of each distribution. The black dashed line represents the best fit to all the points, which can be written as:

$$\boxed{\begin{aligned} e &= 0.098^{+0.001}_{-0.001}\,\mathrm{lg}(\nu) + 0.0940^{+0.0002}_{-0.0001} \\[6pt] p &= 0.079^{+0.003}_{-0.003}\,\mathrm{lg}(\nu) + 0.025^{+0.001}_{-0.001}. \end{aligned}} \tag{6.1}$$

The parameters and the errors were obtaining by fitting the distributions in both directions and then taking the mean values. For e, the interquartile difference goes from 0.05 al low values of ν to 0.08 at high ν; for p it changes from 0.05 to 0.1. This reflects the fact that haloes at different redshifts populate different regions due to their relative mass limits, but they remain around it.

In Figure 6.6 we show the same results for the axial ratios (λ_3/λ_1 and λ_2/λ_1), which can be more useful for the comparison with observations. Looking at the axial ratios we recognise the same trends in the evolution of shapes that we noticed studying e and p. The best fit relations to all the data points are:

$$\boxed{\begin{aligned} \frac{\lambda_3}{\lambda_1} &= -0.282^{+0.003}_{-0.004}\,\mathrm{lg}(\nu) + 0.567^{+0.001}_{-0.001} \\[6pt] \frac{\lambda_2}{\lambda_1} &= -0.293^{+0.007}_{-0.005}\,\mathrm{lg}(\nu) + 0.736^{+0.002}_{-0.002}. \end{aligned}} \tag{6.2}$$

In this case the interquartile difference for λ_3/λ_1 goes from 0.17 at low ν to 0.19 at high ones; for λ_2/λ_1 it changes more, from 0.17 to 0.25.

e-*p* relation

As discussed in [5], [50] and [13], the definition of e and p, together with the range of the eigenvalues, introduces a correlation between them at high ellipticities (which in particular it has been studied at the initial conditions). In what follows, we present the same distribution but using the catalogues of virialized haloes at each z. The ellipticity and prolateness of haloes still form a triangular region in the $e-p$ plane and it is interesting that the median distribution almost does not change with time (Figure 6.7): at high redshift, due to the limited mass resolution of the simulation, we have few haloes in our mass range, but nevertheless they already form a triangle; moving to lower redshift we have more and more haloes, which keep populating the triangle, but leave the median relation almost unchanged. The data points in Figure 6.7 show the median distributions at eleven different redshifts, represented by the different color points. The small gray dots show the whole distribution at $z = 0$, for all the three simulations together. The points at $z = 0$ are fitted by the relation:

$$\boxed{p = 0.01 - 0.7e + 10.57e^2 - 19.1e^3}. \tag{6.3}$$

which is represented by the black dashed line; to fit the relation at the other snapshots it is enough to introduce a the dependence on redshift of the order of $(1+z)^{-0.05}$. The flat initial part, up to the fourth median point, corresponds to haloes for which both relative differences between the axes $((\lambda_1 - \lambda_3/\lambda_1)$ and $(\lambda_1 - \lambda_2/\lambda_1))$ are less than 25%, while the linear growth at $e \geq 0.1$ is represented by haloes with $(\lambda_1 - \lambda_3/\lambda_1)$ greater than 50%. These two regions are marked in the figure by the dotted lines. This

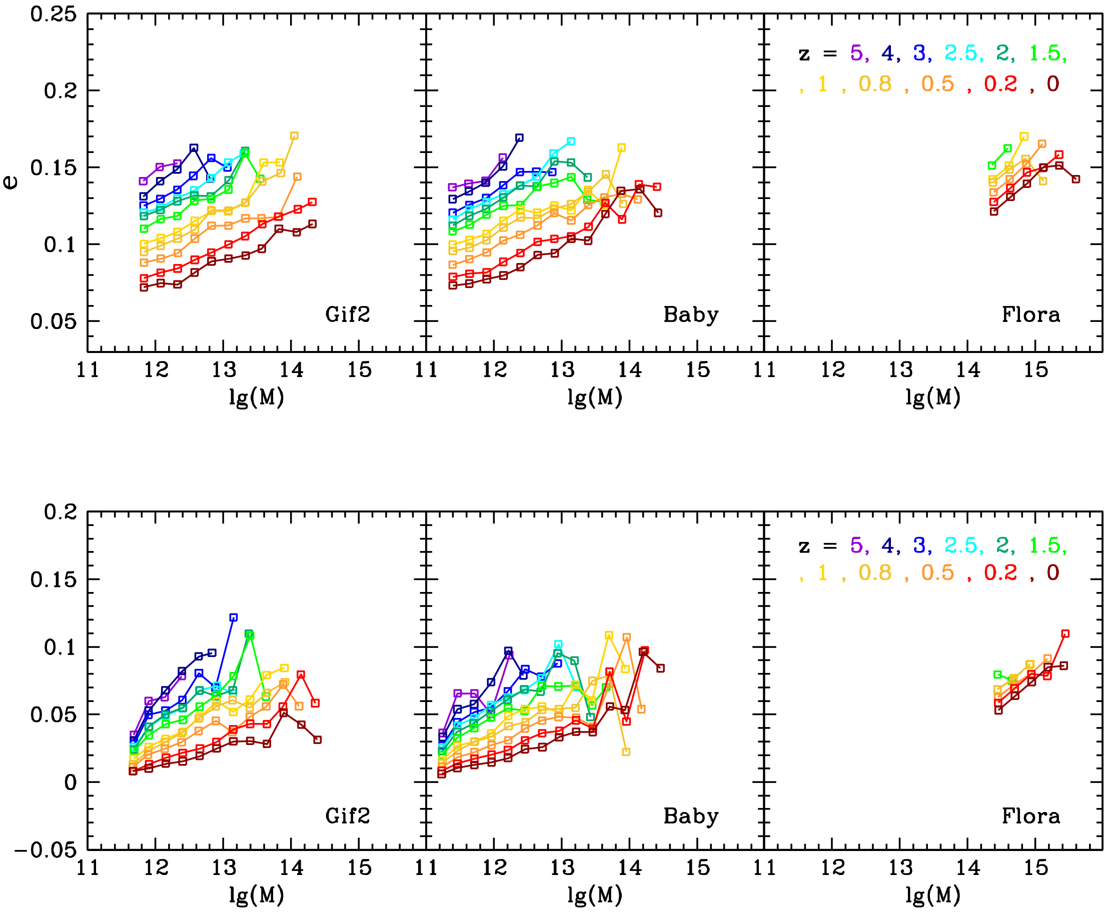

Figure 6.3: Ellipticity (*top*) and prolateness (*bottom*) median distributions as a function of mass for 13 outputs of both simulations: the three panels refer respectively to the GIF2, Baby and Flora simulations.

also confirms the tendency to prolateness already shown in other works: on average, the second axis λ_2 is not large enough to have $p < 0$. The slope of the linearly growing part is close to unity: assuming to neglect λ_3 as a first approximation, both e and p depend primarily on λ_1, which is larger for high values of e, but p is lowered a bit by the contribution of the second axis, as can be seen in Equation 2.14.

This quasi-universality of the $e - p$ relation is useful to estimate the shape properties of the halo population at a certain redshift and to create mock catalogues performing Monte Carlo realisations

How to use these universal relations

These linear (Equations 6.1 an 6.2) or parametric (Equation 6.3) fitting functions are universal, meaning that they do not depend on redshift and cosmology. Apart from the conceptual grace of this definitions, they may be very useful to observers to extract predictions and prior: one can choose a preferred cosmological model and a mass range, then convert the mass into the universal variable ν and pick up the corresponding (median) predicted shape. Just one relation can satisfy all the requests. The next important step, which is discussed in the next Section, is to model the whole distribution of shapes - not only the mean behaviour - and find appropriate fitting functions.

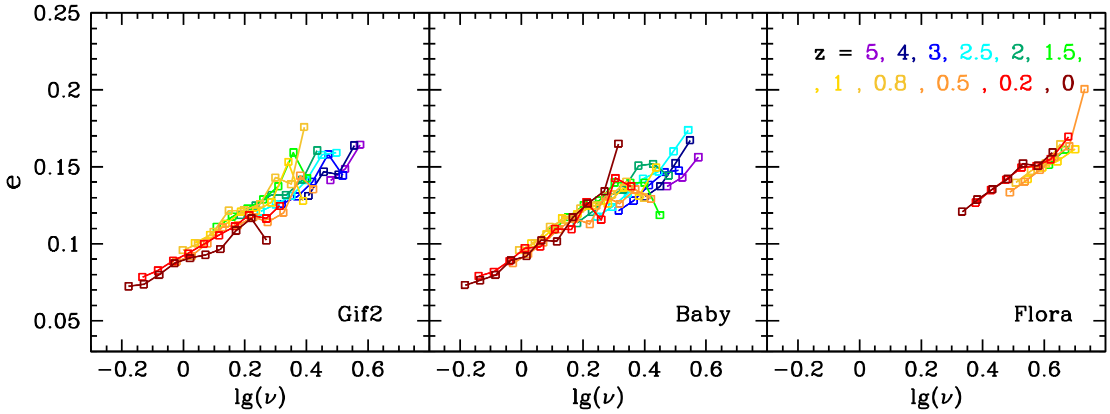

Figure 6.4: Median Ellipticity as a function of ν: we show the effect of rescaling the mass to the variable ν: since it contains the dependence on epoch and cosmology, all the ellipticity distributions of the previous Figure now lie on the same relation. The color scheme is the same of Figure 6.3. The rescaling has also the same effect on the prolateness and on the axial ratios.

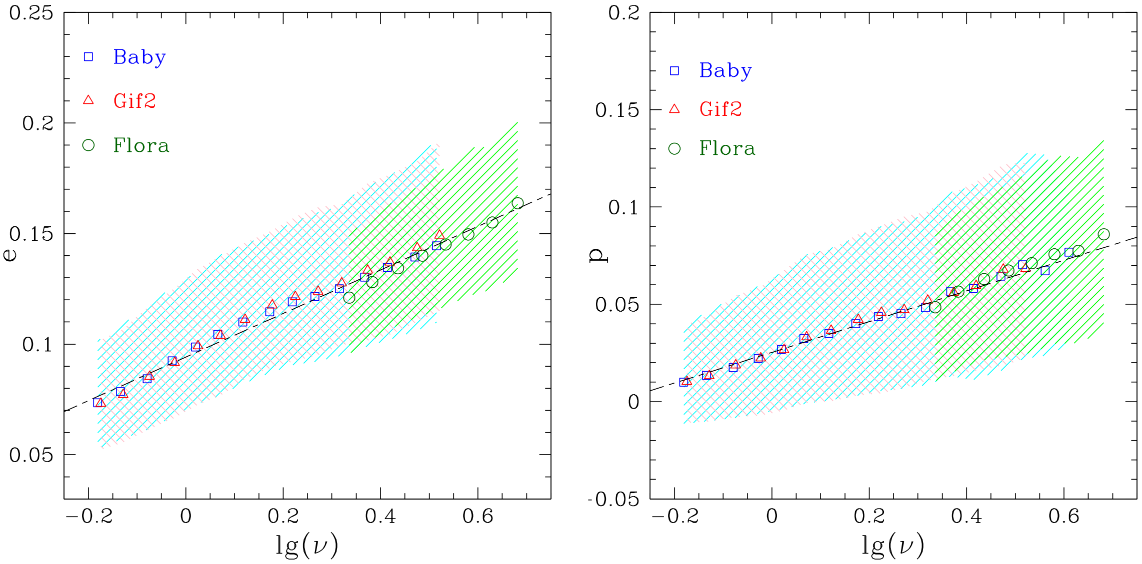

Figure 6.5: *Universal* ellipticity and prolateness distribution. e and p are shown as a function of the variable $\nu = \delta_c/\sigma$: this choice eliminates the dependence on epoch and, as we see, the distributions at all times lies on same relation. The coloured points show the medians for each simulation and the corresponding shaded coloured regions enclose the first and third quartile of each distribution; the black dashed line represents the best fit to all the points.

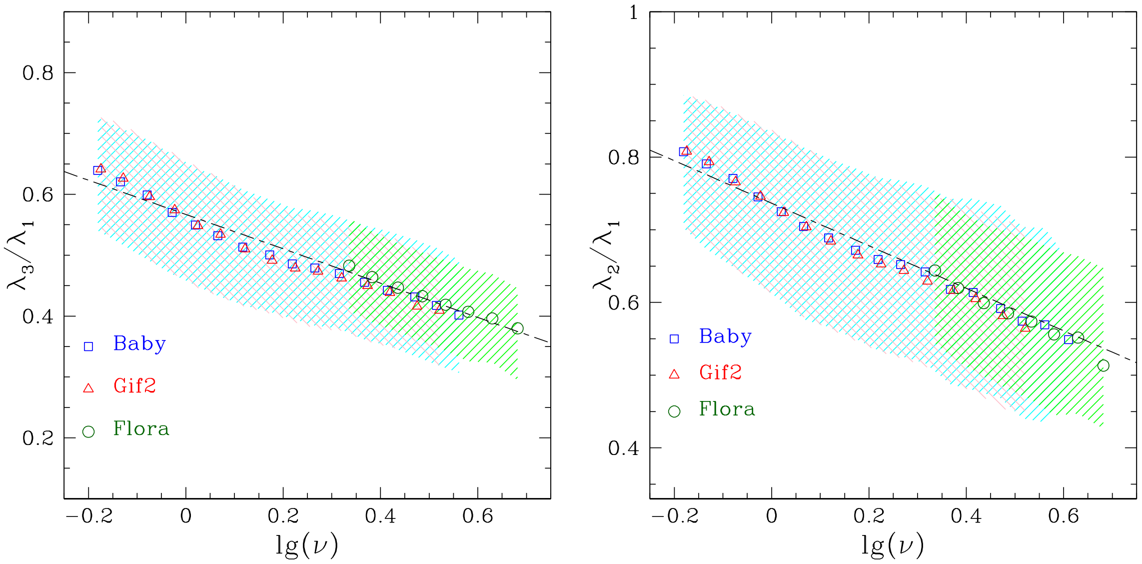

Figure 6.6: *Universal* axial ratio distributions. The color scheme is the same as in Figure 6.5

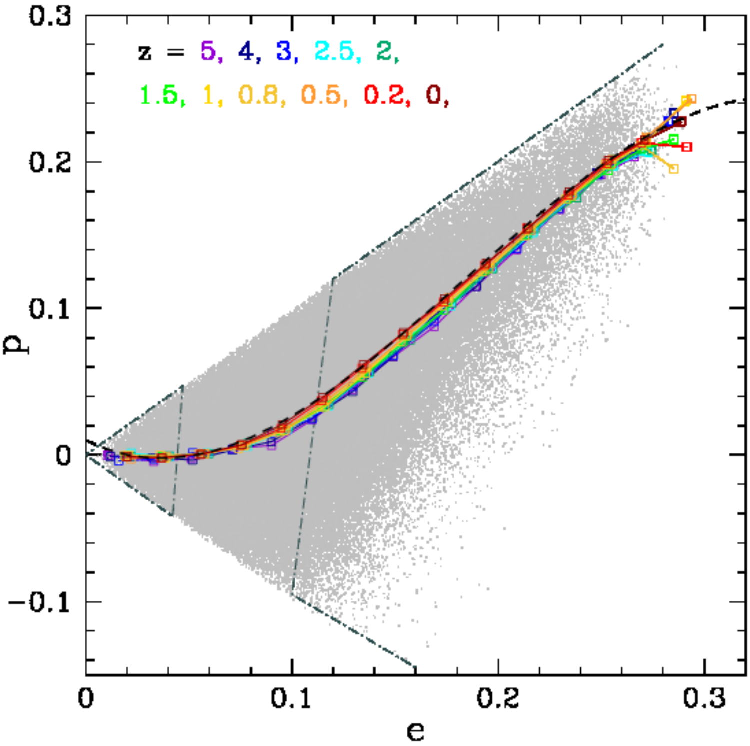

Figure 6.7: e-p distribution at eleven different redshifts, the same of Figure 6.3: the coloured points show the medians at a certain redshift taken on all the data of the three simulations together. The black dashed curve shows the fitting function to the points at $z = 0$. The gray dots represent the $e-p$ distribution at $z = 0$ for all the simulations; the dotted lines delimit the regions for which the relative difference between λ_1 and λ_3 is less than 25% (in the triangle on the left) or more than 50% (in the region on the right).

6.2 Axial ratios distributions: a parametrisation over six order of magnitude in mass

The results obtained so far can be further extended, by searching for universal functional forms to describe the axial ratio distributions. In this Section we present an extension of the work of Jing & Suto 2002 [27], who provided a first universal distribution for the axial ratios. They show a systematic dependence of $s = c/a$ on the mass: the ratio is slightly larger for less massive haloes, and also decreases at higher redshift. The resulting law is:

$$r_{ca} = \left(\frac{c}{a}\right)_{sc} = \left(\frac{c}{a}\right)\left(\frac{M_{vir}}{M_\star}\right)^{0.07(\Omega(z))^{0.7}} \tag{6.4}$$

where $M_\star$ is the characteristic halo mass. The scaled axial ratio r_{ca} show a fairly universal distribution independent of mass and epoch, as we can see in Figure 4.7. Allgood et al. (2006) extended this relation using numerical simulations, combining the mass and redshift dependence of $< s >$:

$$< s > (M,z) = (0.54 \pm 0.03)\left[\frac{M}{M_\star(z)}\right]^{-0.050\pm0.003}. \tag{6.5}$$

The analysis of Jing & Suto [27] was based on simulations with 512^3 particles in a 100 Mpc h^{-1} box, which contained hardly any halo above 10^{14} M$_\odot h^{-1}$ and some higher resolution runs which provided only 12 haloes with more than 10^6 particles. Thus, due to the low statistic, they were not able to fully resolve the details of the distribution and therefore assumed a Gaussian distribution - which gave a good fit. Recently, Schneider et al. 2012 [56] provided a fit all the masses with a single beta distribution, although, even after a rescaling of s there is some residual mass dependence. The mass range between 10^{12} M$_\odot h^{-1}$ and 10^{14} M$_\odot h^{-1}$ has been widely explored in all these works, while only recently small haloes down to 10^{10} M$_\odot h^{-1}$ [42, 56] and some massive haloes of 10^{15} M$_\odot h^{-1}$ - as for example in the previous Section - [14] have been included in this kind of analysis. So far, no statistically significant predictions are available above $3 \times 10^{14}\, h^{-1}$ M$_\odot$ and we rely on extrapolations from lower mass haloes when it comes to predict the shapes of massive galaxy clusters.

Thanks to the high statistic in the Millennium XXL simulation [3] (300 billion particles and a box size of 3 Gpc h^{-1}) we are able to reconstruct the distributions with greater detail, even at large masses. In this Section, we first use the Millennium XXL [3] haloes to specifically explore the range of cluster-size haloes and then we extend our results over six order of magnitudes (from $10^{10} M_\odot/h$ to $10^{16} M_\odot/h$) using both the Millennium XXL and the SBARBINE simulations.

Halo selection

For the first analysis regarding the clusters mass range, we chose to use only a portion of the available MXXL data [3], due to the huge number of haloes in the simulation (almost 68 millions at redshift 0): for each logarithmic mass bin of size 0.2 (mass inside a spherical overdensity of $200\Omega_{crit}$) we chose, from the FoF catalogues, either 10^5 random objects or all, if the number of haloes is lower (as for the higher masses bins). The cut at low masses excludes haloes less massive than $10^{14.4}$ and $10^{14.0} M_\odot h^{-1}$ for redshifts 0 and 1 respectively. After the selection in the FoF catalogue, we have re-identified all haloes using the Ellipsoidal Halo Finder.

To ensure a good resolution in the determination of shapes, we kept only haloes with more than 1000 particles in the ellipsoidal identification, both for the MXXL and Le SBARBINE simulations.

In this case, for our analysis we cleaned the halo catalogue from many unrelaxed systems, trying to exclude the most irregular and asymmetrical ones, whose shape cannot be well captured by a single ellipsoid (this must be kept in mind when comparing with the results of the previous Section). For this purpose, we used a selection criterion commonly adopted to identify “relaxed” haloes: the offset between centre of mass and the most bound particle of the halo, associated with the minimum of potential. This means that, if a significant number of massive substructures is present and perturbs the whole halo distribution, there will be an offset between the centre of the ellipsoid and the centre of mass. We decided to select only haloes for which the offset is less than 5 per cent of their virial radius:

$$\frac{|\bar{x}_{MBP} - \bar{x}_{cm}|}{R_{vir}} < 0.05. \tag{6.6}$$

Table 6.2 shows the total number of haloes in each mass bin and the percentage of selected relaxed (or regular) haloes. As expected, the number of perturbed haloes increases with the mass, due to more massive haloes being assembled recently and so being more perturbed.

Generally, "relaxed" haloes are selected using both this and two other criteria: the amount of mass in substructures and the ratio of kinetic to potential energy as measurements of the dynamical state of an halo. However, previous works[44] show that the selection in the centre offset is responsible for the majority of the rejected haloes: this means that our selection is still able to eliminate the most unrelaxed and irregular objects. Ludlow et al. 2012 [37] used a similar selection ($N_{200} > 5000$ and spherically defined haloes) and found a different results: the fraction of objects with an offset less than 5 per cent is 0.536, while, combining all the three relaxation criteria, the fraction of selected haloes is 0.285. Thus, the choice of the criteria to distinguish between relaxed and unrelaxed haloes is still different in different works. Since we are interested in the overall shape of haloes we decided to use only the center offset as a selection criterion, since it is able to exclude very irregular haloes which could not be well fitted by an ellipsoid; we believe that adding the other two criteria would not change our results more than a few percent. Moreover, our choice is motivated also by the fact that we do not want to restrict out analysis to a very limited and regular sample, since our future plans include a comparison with observational results, which are far from being homogeneous and regular.

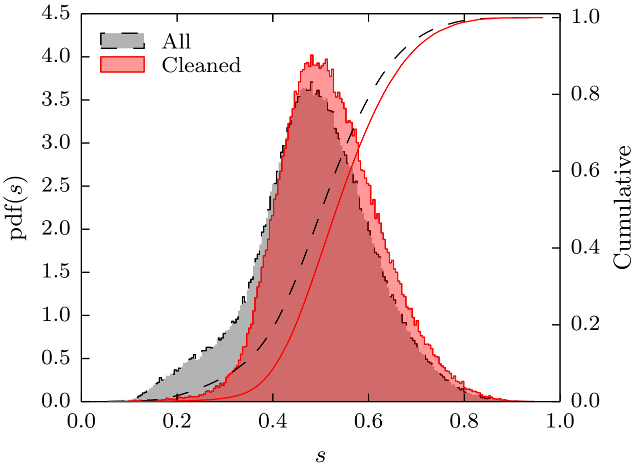

Figure 6.8: Probability distribution functions – differential and cumulative - of $s = a/c$. The distributions for the entire haloes population is shown in grey (and with dashed lines), while the red (solid) ones refer to the cleaned population.

In Figure 6.8 we show the effect of our halo selection on the axial ratio distribution: the distributions for the entire haloes population is shown in grey (and with dashed lines), while the red (solid) ones refer to the cleaned population. Our selection eliminates the left bump of the distribution, due to very disturbed haloes (which are modelled by an extremely prolate ellipsoid by our code), making the overall shape more regular.

Results for cluster-size haloes: MXXL

The full shape of a triaxial halo is described by the two axial ratios $s = c/a$ (minor to major) and $q = b/a$ (intermediate to major). Thus, modelling their distribution with functional forms would allow to reconstruct the whole distribution of halo shapes.

The left panel of Figure 6.9 shows the logarithm of the first axis ratio versus ν for the selected haloes; medians of $\log(s)$ for the two redshifts are shown in red squares and blue circles. This Figure shows the same result of Figure 6.6, but in a different mass range. The idea of providing results that are independent of the redshift and valid for different cosmologies was already in the original [27] paper, as the mass was given in units of M_*, but the use of ν is more general and gives a more direct

	$z=0$		$z=1$	
$\log(M)\,[\mathrm{M}_\odot h^{-1}]$	N_h	N_{rel}/N_h	N_h	N_{rel}/N_h
14.0 - 14.2	57759	58.56 %	30823	41.19 %
14.2 - 14.4	56083	56.61 %	13271	39.11 %
14.4 - 14.6	42951	53.52 %	3914	38.24 %
14.6 - 14.8	20715	50.60 %	919	39.39 %
14.8 - 15.0	7823	48.50 %	134	36.81 %
15.0 - 15.2	2305	46.46 %	6	19.35 %
15.2 - 15.4	523	45.84 %		
15.4 - 15.6	84	46.15 %		

Table 6.2: Number of haloes in each logarithmic mass bin (in $\log(M/M_\odot h)$) and percentage of relaxed haloes for redshifts $z=0$ and $z=1$.

connection to the theory of structure formation. As a result, we can safely treat the two datasets as a single population, shown by the box and whiskers plot for a given ν bin (horizontal error bars). This plot confirms the previously mentioned trend: more massive haloes (higher ν) are more aspherical - even in this restricted mass bin.

We have looked for a linear relation between ν and axis ratio in the log-log space: $\log(s) = f\log(\nu)+g$; the green line in Figure 6.9 is a fit to the median values, with inclination $f = -0.255 \pm 0.01$ and intercept $g = 0.61 \pm 0.01$. It is easy to invert this linear relation to obtain a power-law, following the work of previous authors: $\tilde{s}(M_\star) = 10^g = 10^{\log s - f\log(\nu)} = s\nu^{-f}$. The fit then yields to a scaled axis ratio of:

$$\tilde{s} = s\nu^{0.255}; \tag{6.7}$$

as ν takes care of any time and cosmology dependence, this rescaling is valid also for different redshifts and cosmologies. As Figure 6.9 shows, distributions of the rescaled axis ratios (coloured histograms) are nearly indistinguishable from each other, meaning that we have eliminated all the dependence on the mass, in contrast with the findings of Schneider et al. 2012 [56]. This rescaled distribution of the minor to major axis ratio can be fitted by a log-normal:

$$\boxed{p(x,\mu,\sigma) = \frac{1}{x\sqrt{2\pi}\sigma} exp\left(-\frac{(\ln x-\mu)^2}{2\sigma^2}\right)}, \tag{6.8}$$

which is the probability distribution function of a variable which is normally distributed in the logarithmic space. The resulting parameters are:

$$\begin{aligned} \mu &= -0.49 \\ \sigma &= 0.20. \end{aligned} \tag{6.9}$$

They can be converted to more familiar quantities, as the median and the standard deviation:

$$\begin{aligned} \text{median } &= e^{\mu} = 0.61, \\ \text{std } &= \sqrt{(e^{\sigma^2}-1)e^{2\mu+\sigma^2}} = 0.13\,. \end{aligned} \tag{6.10}$$

Once modelled the first axial ratio s, we need to do the same with the second on q. There is a correlation between s and a scaled version of q - $\tilde{q} = (q-s)/(1-s)$ - and this helps to model the distribution. The Left panel of Figure 6.11 shows the distributions: it is quite evident that $\tilde{q}$ strongly depends on the first axial ratio, with higher values at higher s, which is in agreement with haloes that tend to be prolate. Moreover the scatter is larger at higher s, though this is mostly due to the rescaling which extends the allowed interval of $\tilde{q}$. Given the large differences in the shapes of the

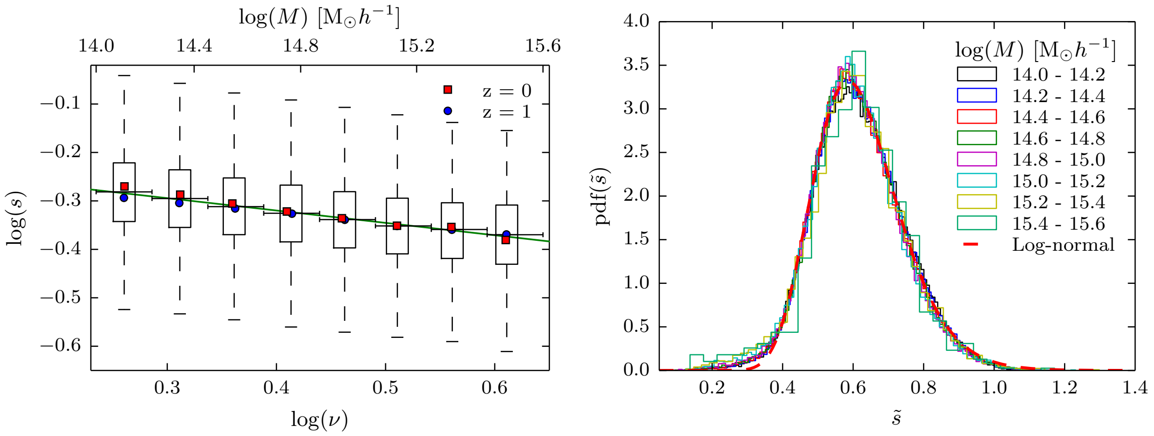

Figure 6.9: *Left*: Distribution of s as function of peak height: the black boxes and whiskers represent the quartiles and 1.5 the quartiles range of the combined distributions. The horizontal error shows the different bins, while the green solid line is the linear fit to the medians. Red squares and blue circles are redshift 0 and 1 sub-samples. *Right*: Distribution of the scaled axial ratio $\tilde{s}$ for masses shown in Table 6.2. It can be easily seen that the distributions at all masses are well represented by an unique fitting function.

distributions of $\tilde{q}$ at a given s, modelling them with a single functional form is not trivial. Therefore, we decided to fit each single histogram with a different beta distribution, which has the following analytical expression:

$$\boxed{p(x,\alpha,\beta) = \frac{1}{B(\alpha,\beta)} x^{\alpha-1}(1-x)^{\beta-1}}. \tag{6.11}$$

This function has two shape parameters α and β; the factor $1/B(\alpha,\beta)$ is a normalisation constant that can be computed by requiring that the integral of the probability distribution function is equal to unity. The solid curves in Figure 6.11 represent the resulting fitting functions.

Extending the mass range: all the simulations

The next step is to extend the recipes for dark matter halo shapes to lower masses, combining the MXXL data with Le SBARBINE simulations: the overall mass range goes from 3×10^{10} M$_\odot h^{-1}$ to 6×10^{15} M$_\odot h^{-1}$.

On left panel of figure 6.10, the logarithm of the minor to major axial ratio s is shown as a function of the logarithm of ν. As before, horizontal error bars represent the interval in ν and the box and whiskers are the quartiles and 1.5 the quartiles range for the combined sample, while coloured points are medians of individual catalogues. s shows a nearly linear dependence on log(ν), with a hint of flattening at both high and low masses.

For each bin, we extracted the probability distribution function of log(s), shown in the right panel of Fig. 6.10). The resulting curves exhibit an interesting pattern: high and low ν histograms are mirrored with respect to a central symmetric distribution which corresponds to $\nu \simeq 1.21$ ($M \approx M_*$). The rescaling adopted for cluster-size haloes does not compensate this effect and so it is not able to remove entirely the mass dependence. Instead of using a different rescaling relation to obtain a single pdf, we decided to fit each distribution and then we relate the resulting parameters to the binning quantity. In order to keep the procedure simple we fit with a linear relation both μ and $\log\beta$:

$$\begin{aligned} \mu(\nu) &= -0.322\log\nu + 0.620 \\ \log\big(\beta(\nu)\big) &= 0.560\log\nu + 0.836. \end{aligned} \tag{6.12}$$

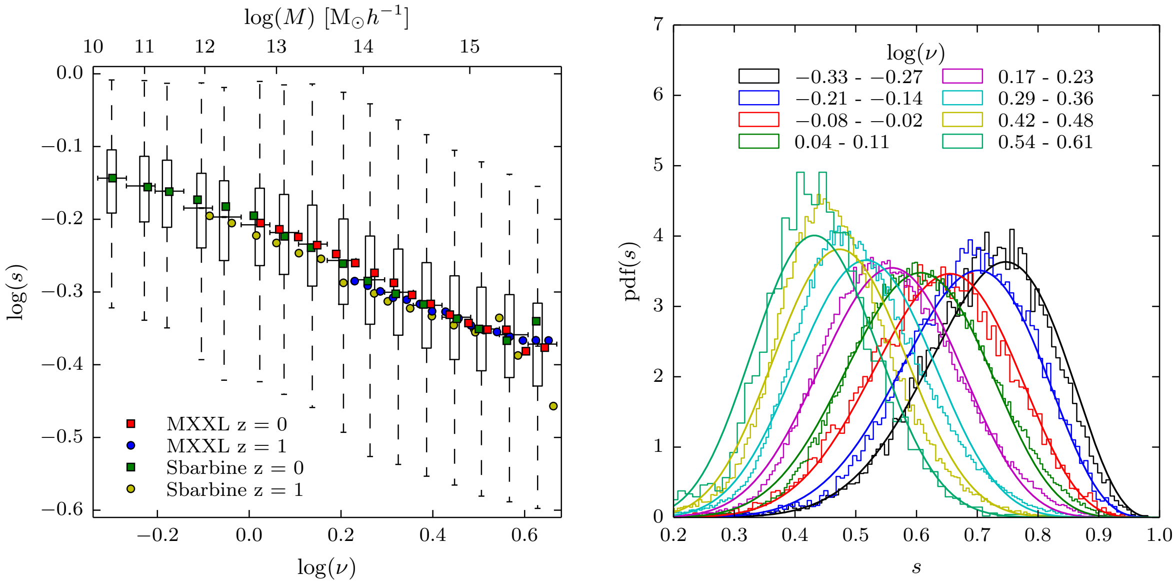

Figure 6.10: *Left*: Distribution of s as function of peak height for all the haloes selected from both redshifts the two simulations: the black boxes and whiskers represent the quartiles and 1.5 the quartiles range respectively computed within the bins shown by the horizontal error bars. The coloured points represent the medians for individual redshifts for the two simulations. *Right* : Differential distribution of s for 8 bin in ν (histograms) and the respective approximating functions obtained as shown in the section (curves).

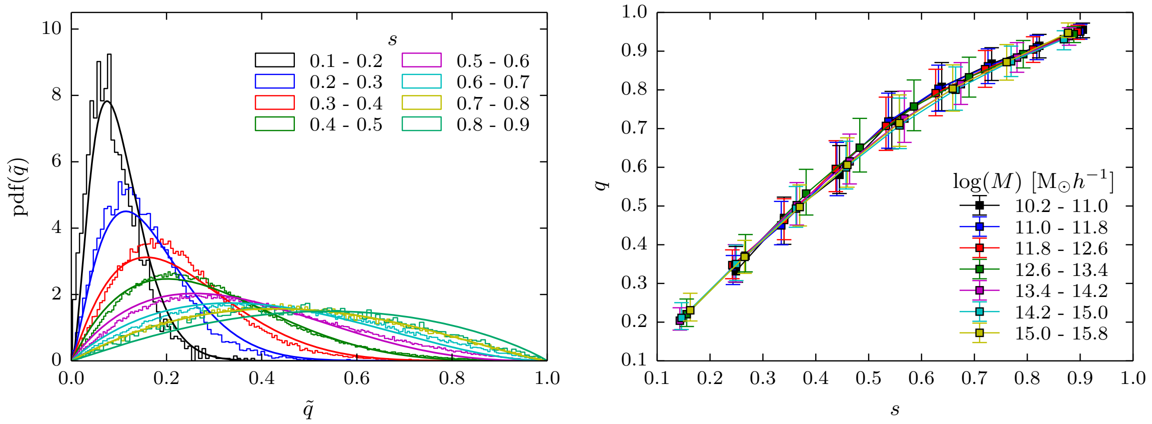

Figure 6.11: *Left*: Distributions of scaled axial ratio $\tilde{q}$ for different values of s (histograms) and fitting function resulting from the mode. *Right*: Axis ratio q as function of s for different masses, represented by the points of different colours. Since there is no residual mass dependence in the conditional distribution, we get the same result as in the MXXL with all the simulations, confirming that this relation is universal.

Using this fits we are now able to approximate the probability distribution function of the first axial ratio with a Beta function with parameters $\alpha = \beta/(1/\mu - 1)$ and β, over a range in mass of almost 6 orders of magnitudes. Moreover the use of ν allows us to extend these results to different cosmologies and different redshifts.

Finally, as the right panel of Figure 6.11 shows, the relation between q and s at redshift $z = 0$ does not depend on the mass: the curves of different colours represent different mass bins and still trace the same relation. The fact that all the mass dependence is already inside s, allows us to use for $p(q|s)$

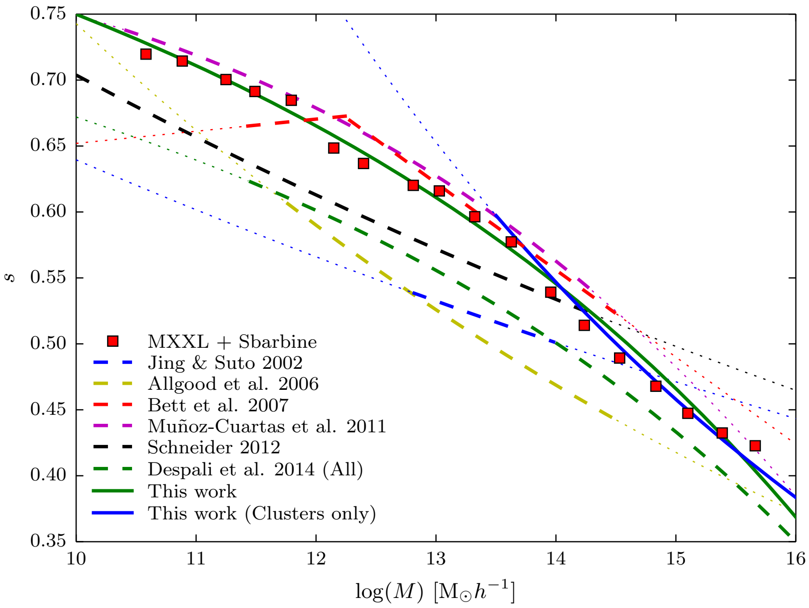

Figure 6.12: Comparison between previous works (dashed lines) and the results of Bonamigo et al. 2015 (solid lines) [7]. Red squares represent the data from both redshifts of the MXXL and the SBARBINE simulations, converted to redshift $z = 0$ for the Millennium cosmology. The blue solid line is the model for clusters; the green solid line is the fit for the entire mass interval. The dotted parts of the curves show the mass ranges outside where the relations have been derived from.

the same functional form of cluster size haloes, independently of the mass we choose. The same applies to different redshifts, with the relation between the two quantities being indistinguishable from the one in Fig. 6.11. Moreover, this independence of the conditional distribution from both mass and redshift is in agreement with the theoretical predictions from [54].

6.3 Comparing results from many works

In Figure 6.12 we compared our results with measurement of axis ratios from other authors. The results obtained with the Millennium XXL and SBARBINE simulations are shown with red squares, the median result form the analysis on cluster masses is the blue solid line and the green solid line is from the combined datasets spanning six order of magnitudes. Results from other authors are shown with dashed lines in the mass range where their analysis was carried out and with dotted lines when extrapolated beyond it. As it can be seen, there is a general agreement in the dependence of s on the mass, with more massive haloes being less spherical. Although there seems to be a scatter of about 15 per cent, this is due more to the differences in the method of measuring shapes (different finders, radius, cleaning procedure, mass definition), than an error on the measurement. The most important difference comes from the radius at which the shape is measured. Jing & Suto 2002 [27] (blue dashed line) used particles of the isodensity surface corresponding to $2500\delta_c$, roughly at a radius of $0.3R_{\rm vir}$; this analysis is different from all the following authors, as it reflects the shape of an ellipsoidal shell, and not of all the mass inside the ellipsoid. Studying a larger mass interval, $6\times10^{11} - 3\times10^{14}$ M$_\odot h^{-1}$, Allgood et al. 2006 [1] (yellow dashed line) derived axis ratios of particles distribution inside $0.3R_{\rm vir}$ diagonalizing the normalised mass tensor (weighted by the distance from the centre); because of this their measure reflects the shape at a even closer radius. If we restrict the comparison to works that used particles within the virial radius the agreement becomes much more strong. This is the case of the magenta dashed line [42], derived studying shapes with an ellipsoidal overdensity algorithm similar to the one adopted in this work.

The other difference can arise from the cleaning of the sample; the green dashed line show our prediction from Equation 7.2 [14], which is obtained from all haloes, regardless of their state of relaxation. As expected the values are lower, since unrelaxed haloes are typically irregular and so they appear more elongated with lower axial ratios.

6.4 Merger Tree and Formation Redshift

From the halo catalogues, we built the merging history tree for all haloes in the simulations with more than 200 particles: starting from each halo at redshift $z = 0$, we define its progenitors at the previous output $z = z_i$ as all the haloes containing at least one particle of the $z = 0$ halo; we term as "main progenitor" the halo that provided the largest mass contribution to the final one. Then we repeat the same procedure, now starting from the main halo progenitor at the snapshot $z = z_i$ and going backwards in time in this way from snapshot to snapshot, until all the particles are lost in the field (i.e. the main halo progenitor possesses fewer than 10 particles). We stress that our approach to follow the main halo progenitor back in time until it has fewer than 10 particles is in agreement with previous works and theoretical models developed to interpret the halo mass growth history [65, 68, 21]. In Figure 6.13 we show the fit to the formation redshift proposed by [22] for the Baby and the GIF2 cosmologies, given by the equation:

$$\delta_c(z_f) = \delta_c(z_0) + \tilde{w}_f \sqrt{S(fM) - S(M)}\,, \tag{6.13}$$

where z_f is obtained by inverting the relation between δ_c and z_f. The parameters are

$$\tilde{w}_f = \sqrt{2\ln(\alpha_f + 1)}\,, \tag{6.14}$$

and

$$\alpha_f = \alpha_0 \exp(-2f^3)/f^{0.707} \tag{6.15}$$

where $\alpha_0 = 0.937$ – corresponding dashed curves for the two cosmologies. The value of α_0 in this case is different from the one computed by [22] by circa 15% because of the different halo sample considered. While [22] considered all bounds haloes that never exceed more than 10% their present-day mass along their mass accretion history, in this work we consider all identified systems at the present time. A higher value of α_0 modifies the normalisation of the formation redshift-mass relation mainly for large value of f in order to take into account the accretion histories of haloes characterised by major merging events excluded by [22]. In each panel the data points represent the median formation redshift z_f at the time at which the main halo progenitor assembles a fraction f of its present-day mass; the shaded regions of the corresponding colour enclose the first and the third quartiles. From the figure we note that, since the cosmology adopted for Baby (and Flora) has a lower value of σ_8, its haloes have typically a lower formation redshift. Going from the top left panel to the bottom left one, thus decreasing the value of f, the difference between the two simulations increases up to almost 25% for the redshift at which the main halo progenitor assemble a fraction $f = 0.04$ of its present-day mass.

In Figure 6.14 we show the relation between the ellipticity of haloes at $z = 0$ and their generalised formation redshifts. The points (squares for Baby and triangles fo the GIF2) show the medians of the distribution at a fixed z_f for the four definitions, as in Figure 6.13, while the coloured shaded regions enclose the first and third quartile. We can see that, using any of the definitions of formation redshifts, final ellipticity and z_f anti-correlate: this is consistent with the behaviour already seen and discussed in Figure 6.1. It is also interesting to notice that even if Baby and GIF2 simulations have been run with

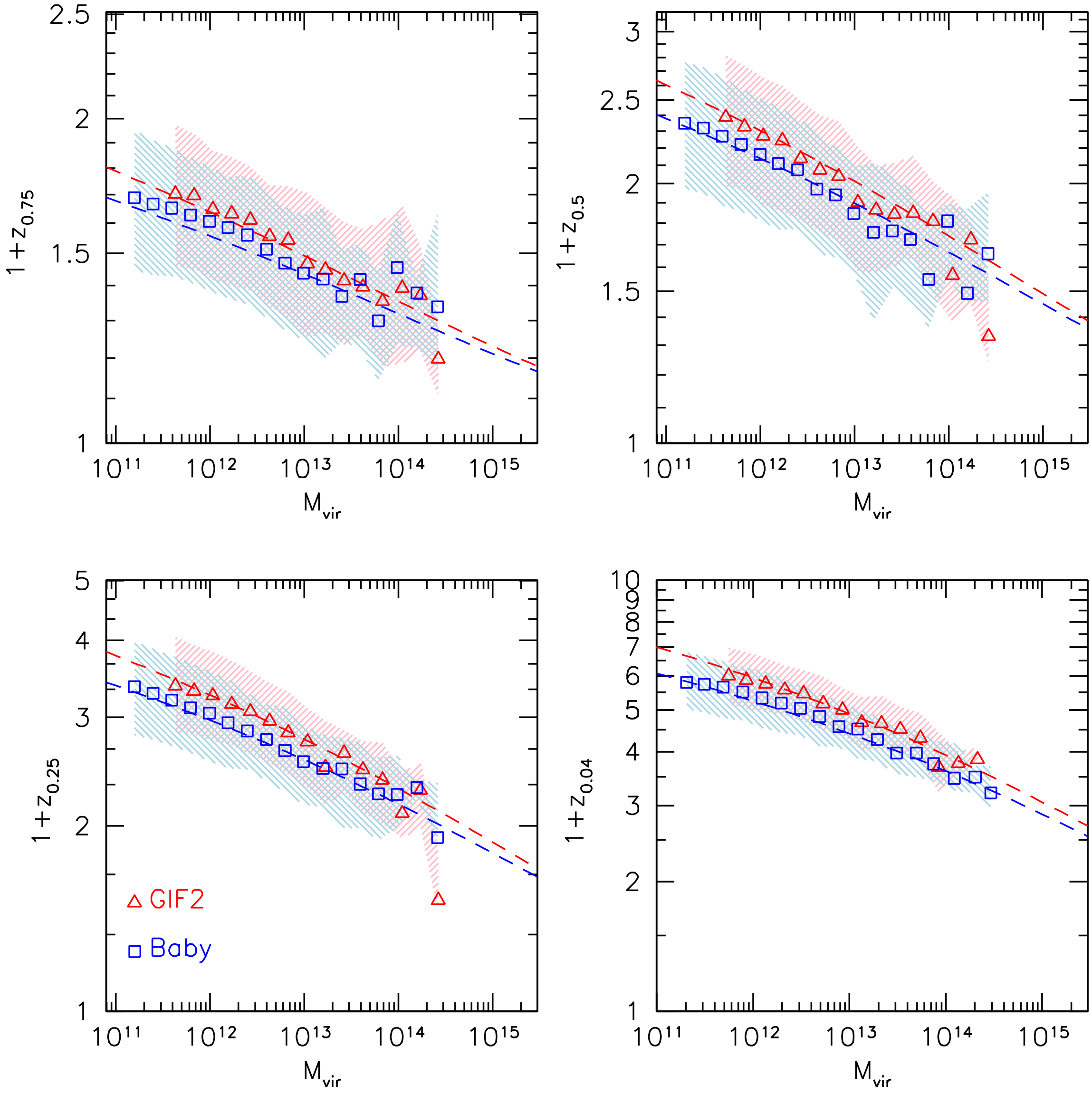

Figure 6.13: Formation redshift as a function of the halo mass. In the different panels we show the results derived from four definition of formation redshift z_f, defined as the moment at which the main halo progenitor assembles a fraction $f = 0.75, 0.5, 0.25, 0.04$ of its mass. The data points show the median of the measurements performed on the two simulations while the shaded regions enclose the first and third quartiles. The dashed curves represent the predictions for the formation redshift mass relations, for the two cosmologies, using the model by [22].

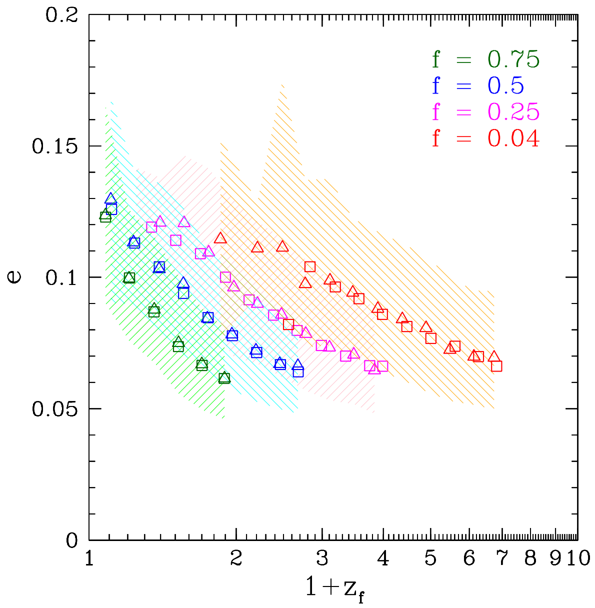

Figure 6.14: Relation between the ellipticity of haloes at $z = 0$ and the redshift at which haloes assemble different fraction of their mass. The points show the medians of the distribution for all the four definition of z_f, already seen in Figure 6.13, while the corresponding coloured shaded regions enclose the first and third quartile. The squares show the results for Baby, while the triangles for the GIF2, as in the other figures.

different cosmological parameters, the relation $e - z_f$ is similar once adopted the same formation redshift definition.

6.5 Summary

The main result of the work presented in this chapter is the existence of universal distributions of the shape parameters (e, p and the axial ratios), when rescaling the mass to the universal variable $\nu = \delta_c/\sigma$. It allows to eliminate the dependences on cosmology and epoch, moving the distributions of all redshifts all on the same linear relations. Then we report and study other properties of halo shapes, which can be summarised as follows:

- at fixed mass, halo shapes become more elongated at high redshifts; the behaviour is qualitative the same for both cosmologies, with a slight difference in the median values due to the difference in formation times of haloes;

- haloes of similar mass possess larger ellipticity and prolateness at higher redshifts: on average e and p from redshift $z = 2$ to the present time change of about $40-50\%$;

- at any given time, the more massive is an halo, the less spherical it is: this is due to the fact that massive haloes still retain memory of their "original" shape, which has not been yet contaminated or rounded by other events and which is related to the direction of filaments or of the last major merger; thus, at any given time, massive haloes show higher values both of e and p – clearly the same trend is reflected in the axial ratios);

- another quasi-universal distribution is given by the relation between p and e, which remains on average with a slight redshift dependence;

- halo ellipticity is a decreasing function of the generalised formation redshifts z_f – as the redshift when the main halo progenitor assembles a fraction f of its present-day mass, with no particular dependence on cosmology: both GIF2 and Baby cosmology lie on the same relation;
- for clusters, the distribution of the rescaled minor to major axis ratio is well described by a lognormal distribution, in contrast to previous extrapolations from lower masses that found a simple Gaussian fit;
- over the whole examined mass range, s can be approximated by a beta distribution that depends only on the peak height ν;
- the conditional intermediate to major axis ratio distribution $p(q|s)$ can also be described by a beta distribution that depends only on the first axis ratio and not on the mass, thus the same approach can be used for both clusters and the whole mass range of haloes;
- overall, the probability distribution function of the shape of a dark matter halo is given by one single parameter ν, related to its mass, that incorporates the dependence on redshift and cosmology. This goes in support of methods that allows to change the cosmology of a numerical simulation, as within good approximation most of halo properties depend only on ν.

To conclude, halo triaxial properties show a dependence on cosmological parameters since related to the halo assemble histories. In this chapter we have presented how ellipticity, prolateness and axial ratios correlate with the universal variable ν: in a way that these quantities are independent on halo mass, redshift and background cosmology. We find our results useful to be implemented in a Monte Carlo method to generate mock haloes with given triaxial properties, and in triaxial mass reconstruction methods that require priors for the axial ratio distributions.

The universality of the halo mass function: a systematic analysis 7

There has always been considerable interest in the modelling of the mass function of collapsed dark matter haloes (Press & Schechter 1974[52], Bond et al. 1991 [8], Lacey & Cole 1993 [30], Sheth & Tormen 1999 [60] and 2001 [58], Jenkins et al. 2001 [26], Tinker et al. 2008 [63]). In all these models it is implied that haloes are biased tracers of the underlying dark matter distribution and the predicted shape of the mass function is generally in agreement with the results of numerical simulations. The majority of theoretical predictions use the virial mass of haloes to model the halo mass function. Nevertheless, other definitions of the halo mass - corresponding to different overdensity thresholds - do exist and are used by both theoretical and observational works: for example the halo mass can be defined using an overdensity of 200 times the background density ρ_b or some multiples of the critical density ρ_c. This debate on the definition of the "true" halo mass may cause inconsistencies between the theoretical model and the predictions from numerical simulations and observations. In this Chapter we present a detailed analysis of how the identification of haloes at different overdensity thresholds affects the halo mass function. Moreover, we show how the parameters of the halo mass function varies due to the mass definition and some relations to convert from one mass definition to the other.

7.1 The halo mass function - an overview

As it was already discussed in Chapters 1 and 2, the halo mass function has evolved through the years: by far the most widely used analytic formulae for halo mass functions are based on extensions of the theoretical framework first developed by Press & Schechter 1974 [52]; this then evolved to include the excursion sets model [8] and the ellipsoidal collapse [60, 59].

In particular, the shape of the unconditional mass function is expected to depend on the initial fluctuation distribution [52]; if the initial distribution is Gaussian with a scale-free spectrum, then the mass function can be expressed in a universal form, independent of redshift and power spectrum. For initially scale-free spectra

$$\nu f(\nu) = m^2 \frac{n(m,z)}{\bar{\rho}} \frac{\mathrm{d}log m}{\mathrm{d}log \nu} = \sqrt{\frac{2}{\pi}} \nu^{1/2} \exp -\nu/2 \tag{7.1}$$

has a universal shape. Here $\nu = (\delta_c(z)/\sigma(m))^2$ and δ_c=1.686. Since it was not obvious that the scaling would hold for more general initial power spectra, Sheth & Tormen 1999 [60] tested the PS model on

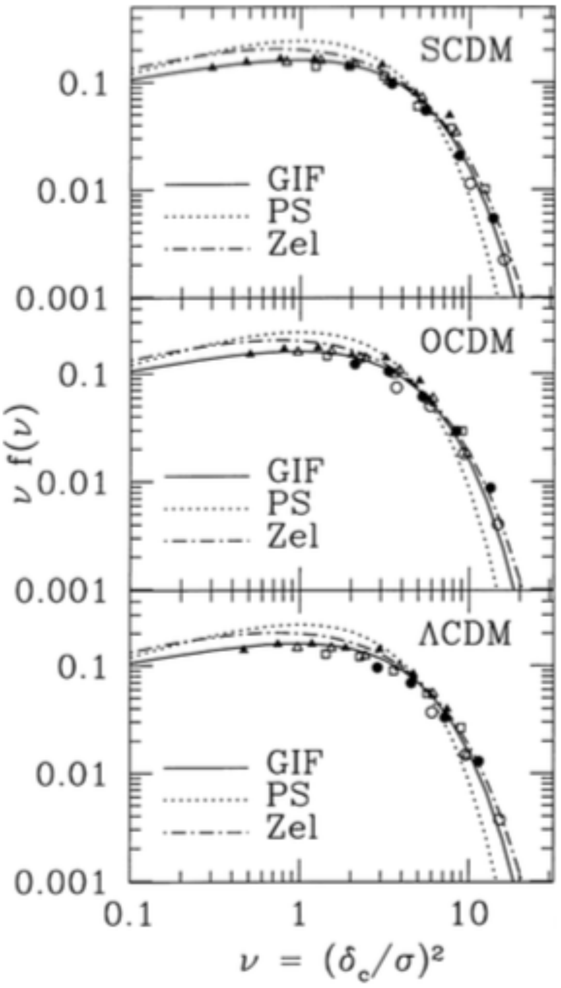

Figure 7.1: Unconditional halo mass functions from Sheth & Tormen 1999 [60]. Different points show from five output times (filled triangles, open triangles, open squares, filled circles, open circles show results for $z = 0$, $z = 0.5$, $z = 1$, $z = 2$ and $z = 4$) in the GIF simulations. The dotted curve shows the Press & Schechter prediction, the dot-dashed curve shows the mass function associated with the Zel'dovich approximation, and the solid curve shows the modified fitting function.

numerical simulations, finding some discrepancies both at high and low values of ν, as can be seen in Figure 7.1. A modification of the PS function that fits the data can be written as:

$$\nu f(\nu) = A\left(1+\frac{1}{\nu'^{p}}\right)\left(\frac{\nu'}{2}\right)^{1/2}\frac{e^{-\nu'/2}}{\sqrt{\pi}} \tag{7.2}$$

where $\nu' = a\nu$, $a = 0.707$, $p = 0.3$ and $A \simeq 0.322$. Note that in principle the shape of $\nu f(\nu)$ could depend on the initial power spectrum, but from Figure 7.1 we see that the analytic form of the unconditional mass function is universal: the same function and parameters can be used to predict halo abundance for different redshifts and cosmologies. This suggests that the dynamics of collapse is sensitive o the value of ν and not to the mass scale itself.

As explained in Chapter 3, Sheth, Mo & Tormen 2001 [59] extended the excursion set derivation of the PS formula by Bond et al. 1991 [8] to include the ellipsoidal collapse and showed that this produce a mass function almost identical in shape to the last equation.

Jenkins et al. 2001 [26] obtained another fitting formula for the mass function, expressed as a function of σ:

$$f(M) = 0.315 \exp - |\ln \sigma^{-1} + 0.61|^{3.8}, \tag{7.3}$$

valid over the range $-1.2 \leq \ln \sigma^{-1} \leq 1.05$. This formula is very close to the one proposed by Sheth & Tormen 1999 [60] - Equation 7.2 - with a small difference in the high-mass tail. The fit can be improved by adjusting the parameters (A, p, a) of Equation 7.2, obtaining a better constraint if all three parameters are allowed to vary freely. Their results are based both on FoF and SO haloes, where in the latter case the overdensity for ΛCDM was set to 324 (at $z = 0$).

A work by Tinker et al. 2008 [63] claimed the need for a recalibration of the mass function in the era of precision cosmology, since the accuracy of previous fitting formulae is 10%-20% [26]. They used a SO algorithm to identify haloes and chose many density thresholds ranging from $200\rho_b$ to $3200\rho_b$. In Figure 7.2 we can see the measured mass function at two different redshifts ($z = 0$ and $z = 1.25$), using a density threshold of $200\rho_b$: it's easy to see that, while the analytical model fits very well the data points at $z = 0$, this is no longer true at $z = 1.25$ where the points lie 20% lower than the solid line. The authors then tried the same procedures with other density thresholds, multiples of ρ_b, finding an offset with respect to the best fitting mass function: Figure 7.3 shows the residuals of the measured mass functions with respect from the best-fitting analytical model at $z = 0$, the blue line represents the Jenkins et al. 2001 [26] mass function - rescaled from 324 to the desired overdensity - and the red dashed line the Sheth & Tormen 1999 [60] mass function.

This result has been used by Tinker et al. 2008 [63] to claim a $non-universality$ in redshift (or cosmology) of the halo mass function. We find it a rushed conclusion: the universality of the halo mass function has been widely tested for virial masses, but was not claimed for haloes identified at other overdensity thresholds. In the following sections we will show a detailed analysis of how the mass definition may influence the shape of the mass function and its universality.

7.2 The dependence on the density threshold

Analysis

We used Padova's spherical and ellipsoidal halo finders [14, 14, 7], described in Chapter 3, to identify spherical and ellipsoidal haloes at six different density thresholds (in increasing order): $200\rho_b$, δ_{vir} (already used in the previous analyses), $200\rho_c$, $500\rho_c$, $1000\rho_c$ and $2000\rho_c$. Recall that $\rho_c(0) \simeq 2.77 \times 10^{11} M_\odot h^{-1} Mpc^{-1}$ and that the following relations hold (in a comoving cosmological box):

$$\rho_b = \rho_c(0)\Omega_m(0), \tag{7.4}$$

$$\rho_c(z) = \frac{3H^2}{8\pi G} = \frac{\rho_c(0)\Omega_m(0)}{\Omega_m(z)}. \tag{7.5}$$

This has been done for all the snapshots, allowing us to study the evolution in time of the halo mass function: for each simulation-snapshot-density-shape combination, we saved a catalogue containing all the information about the identified haloes. We limited the selection to haloes with at least 300 particles, to ensure a good resolution. For this reason, while the $z = 0$ catalogues of each simulation contain many haloes, at higher redshift the simulations on larger scales start to loose haloes and maintain only the high mass tail. As we will show in the next section, apart from studying the universality of the halo mass function as a function of redshift, these catalogues will allow us to find a way to convert from one mass to the other.

Using different density thresholds is equivalent to looking at inner or outer parts of each halo. As an example, Figures 7.4 and 7.6 show the projected distribution of particles of two haloes (at $z = 0$),

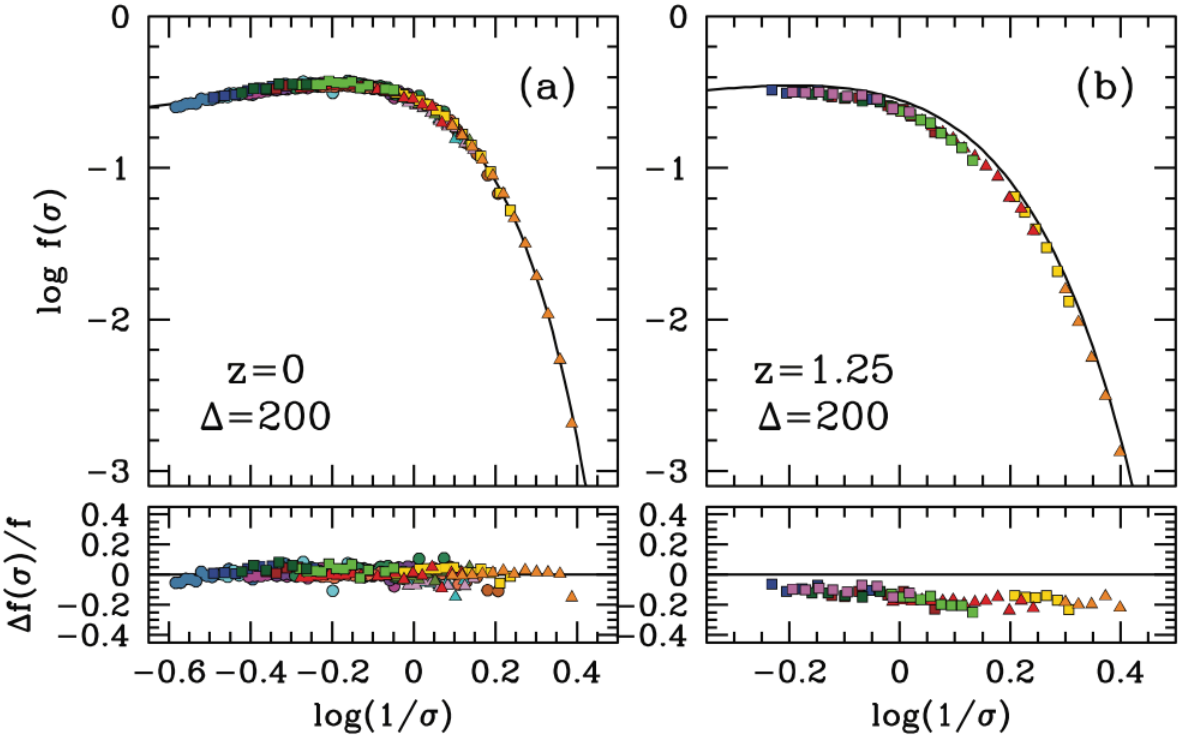

Figure 7.2: Halo mass functions from Tinker et al. 2008 [63]. We see the mass function measured at $\Delta = 200\rho_b$, at $z = 0$ ($left$) and $z = 1.25$ ($right$). The percentage residual to the best fitting theoretical model (represented by the black solid line) are shown in the lower panels.

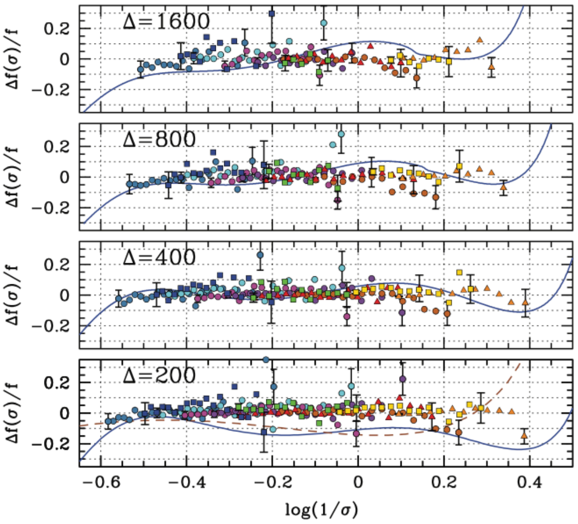

Figure 7.3: Residuals of the measured mass functions with respect from the best-fitting analytical model at $z = 0$, from Tinker et al. 2008 [63] The blue line represents the Jenkins et al. 2001 [26] mass function - rescaled from 324 to the desired overdensity - and the red dashed line the Sheth & Tormen 1999 [60] mass function.

of virial masses M=5.322 $10^{14} M_{\odot} h^{-1}$ and M=3.683 $10^{12} M_{\odot} h^{-1}$. Different colours show the particles selected at different density thresholds, superposed to each other from the outer to the inner one. The circles show the corresponding radii, whose value - together with the masses - are listed in Tables 7.1 and 7.2. As we can see, despite of the mass difference, the mass-radius trend is very similar. The same holds for the ellipsoidal identification, shown in Figures 7.5 and 7.7: here the colour code is the same and the circles still represent the radii of the spherical identification. The chosen overdensities are commonly used in different astrophysical situations; for example:

- $200\rho_b$ is the virial overdensity derived from spherical collapse with $\Lambda = 0$: the exact value is 178, but it is usually approximated to 200 for simplicity. It has also been used to define heuristically the linking length of the FoF algorithm to b=0.2;
- $\delta_{vir} \simeq 324\rho_b$ has been derived by Eke et al. 1996 [17], solving the spherical collapse for the case ($\Lambda > 0$;$\Omega_m + \Omega_\Lambda = 1$). This value is correct of a standard ($\Omega_m = 0.3, \Omega_\Lambda = 0.7$) cosmology. For the Planck cosmology, $\delta_{vir} \simeq 319$. The resulting overdensity is higher than the one obtained without the cosmological constant: in a universe that is expanding faster due to Λ, haloes need to be even denser to collapse;
- $200\rho_c$ is commonly used to define galaxy cluster masses in observational studies; ρ_c has the advantage of being cosmology-independent, while ρ_b is not : $\rho_b = \rho_c \Omega_{m0}$. Moreover, it can resemble the virial overdensity, even if it does not exactly correspond to it;
- $500 rho_c$ is important for X-ray observations of galaxy clusters, since it defines a more central (and so brighter) region: it has been chosen since, nowadays, the X-ray data are usually able to trace the ICM out to this radius and it has been shown that inside a region of $\simeq r_{500}$ randomized galaxy and mass particle orbits dominate clearly over infalling material;
- the last more used value is $2500\rho_c$ - again with X-ray data; in particular, the x-ray gas fractions in the central regions of galaxy clusters, tend to a constant value around r_{2500}. The majority of our simulations were not resolved enough to define this very central region of the haloes with enough particles, and so we chose to analyse them at $1000\rho_c$ and $2000\rho_c$.

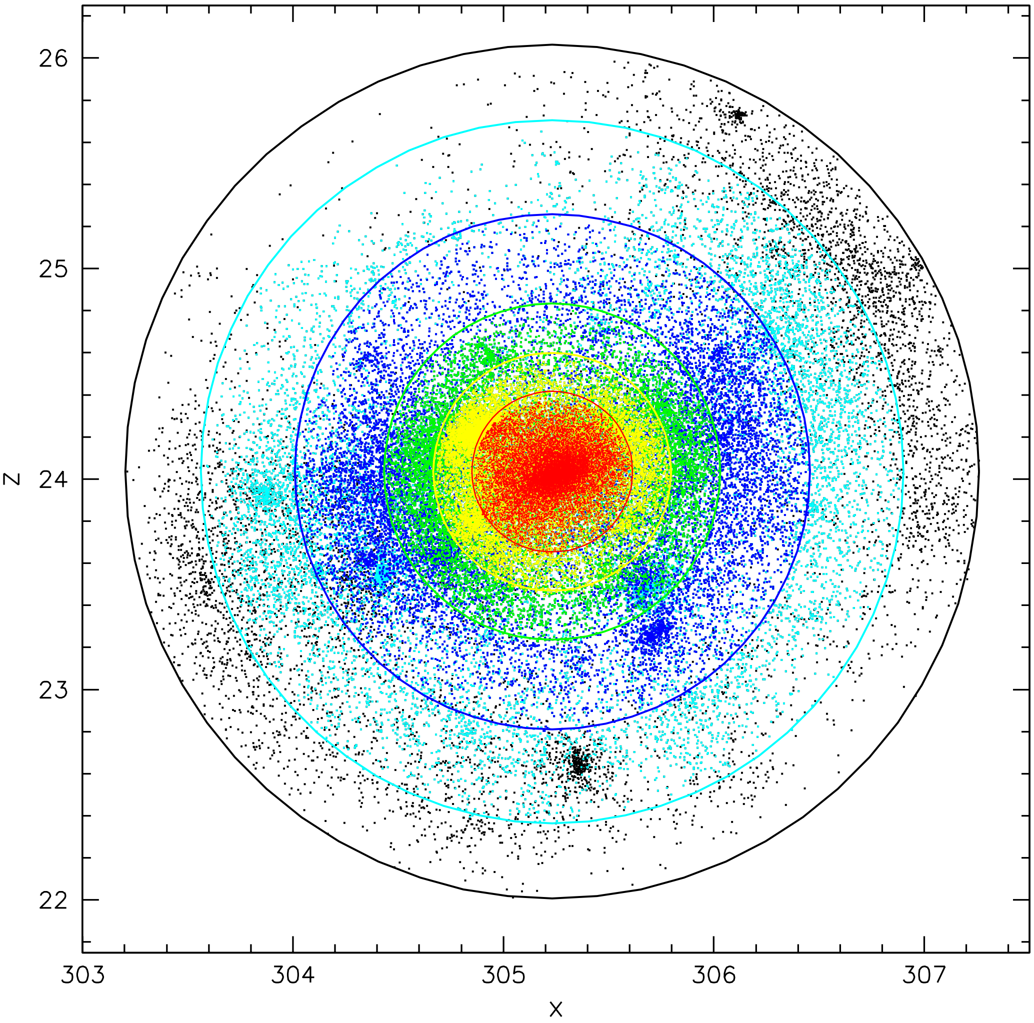

Figure 7.4: Projected 2D distribution of the particles of halo 1 in “Dora”: the virial mass of the halo is M=5.322 $10^{14} M_{\odot} h^{-1}$ and the virial radius r=1.670 Mpc. Different colours show the particles selected at the 6 density thresholds, superposed to each other from the outer to the inner one; in particular, the virial halo is represented in cyan. The circles show the corresponding radii, whose value - together with the masses - are listed in Table 7.1.

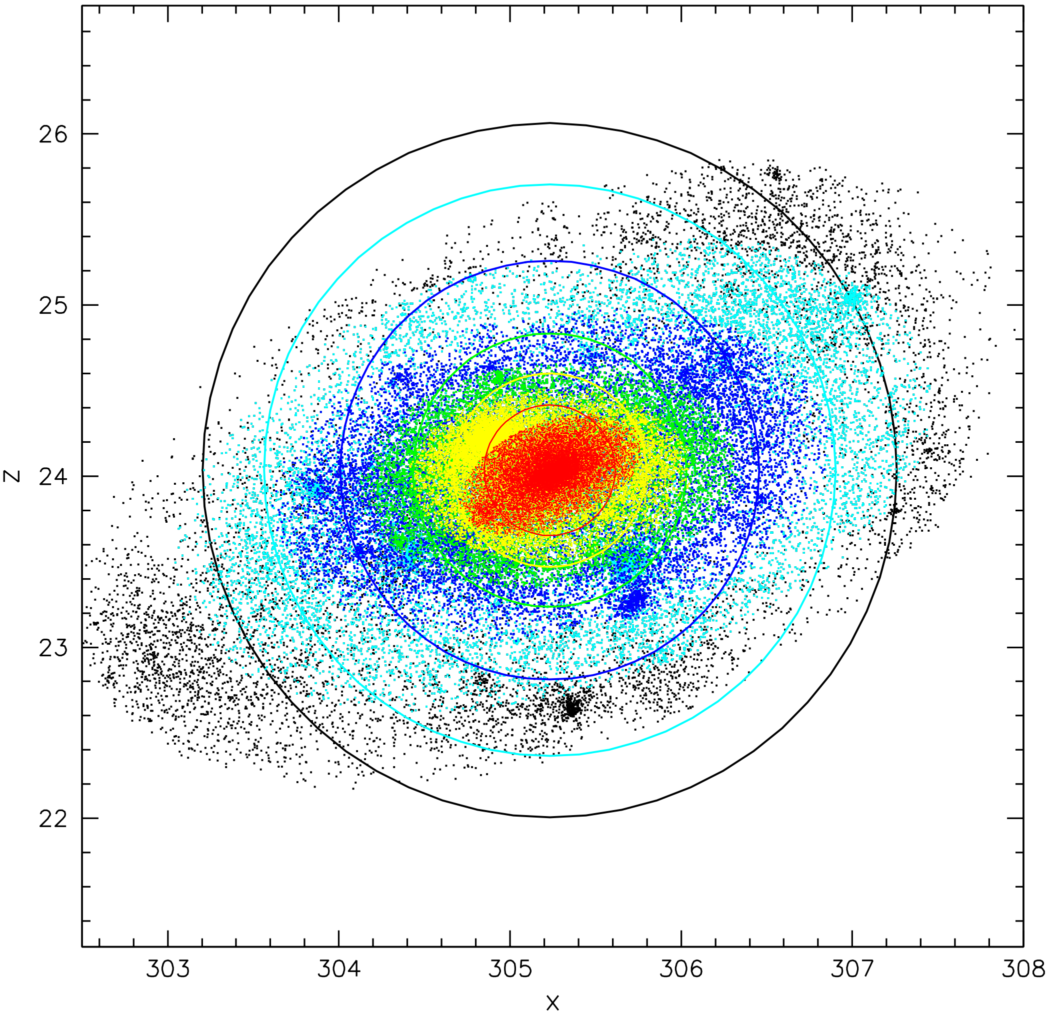

Figure 7.5: Projected 2D distribution of the same halo of Figure 7.4, but for the ellipsoidal identification. The circles show the radii of the corresponding spherical identification, whose value - together with the masses - are listed in Table 7.1. Here we note the dazzling difference between the two identifications and we can note that the virial radius (in cyan) is not completely filled even at a lower density. As in the previous Figure, the colour scheme is black - $200\rho_b$, cyan - δ_{vir}, blue - $200\rho_c$, green - $500\rho_b$, yellow - $1000\rho_b$, red - $2000\rho_b$.

halo 1 (dora)	M_{sph} $[M_\odot h^{-1}]$	M_{ell} $[M_\odot h^{-1}]$	r [Mpc]
$200\rho_b$	$5.964\ 10^{14}$	$6.275\ 10^{14}$	2.029
δ_{vir}	$5.322\ 10^{14}$	$5.569\ 10^{14}$	1.670
$200\rho_c$	$4.264\ 10^{14}$	$4.407\ 10^{14}$	1.224
$500\rho_c$	$2.965\ 10^{14}$	$3.085\ 10^{14}$	0.799
$1000\rho_c$	$2.098\ 10^{14}$	$2.255\ 10^{14}$	0.565
$2000\rho_c$	$1.294\ 10^{14}$	$1.383\ 10^{14}$	0.382

Table 7.1: For each density threshold, we list the radii and the corresponding enclosed masses of halo 1 from "Dora", represented in Figure 7.4.

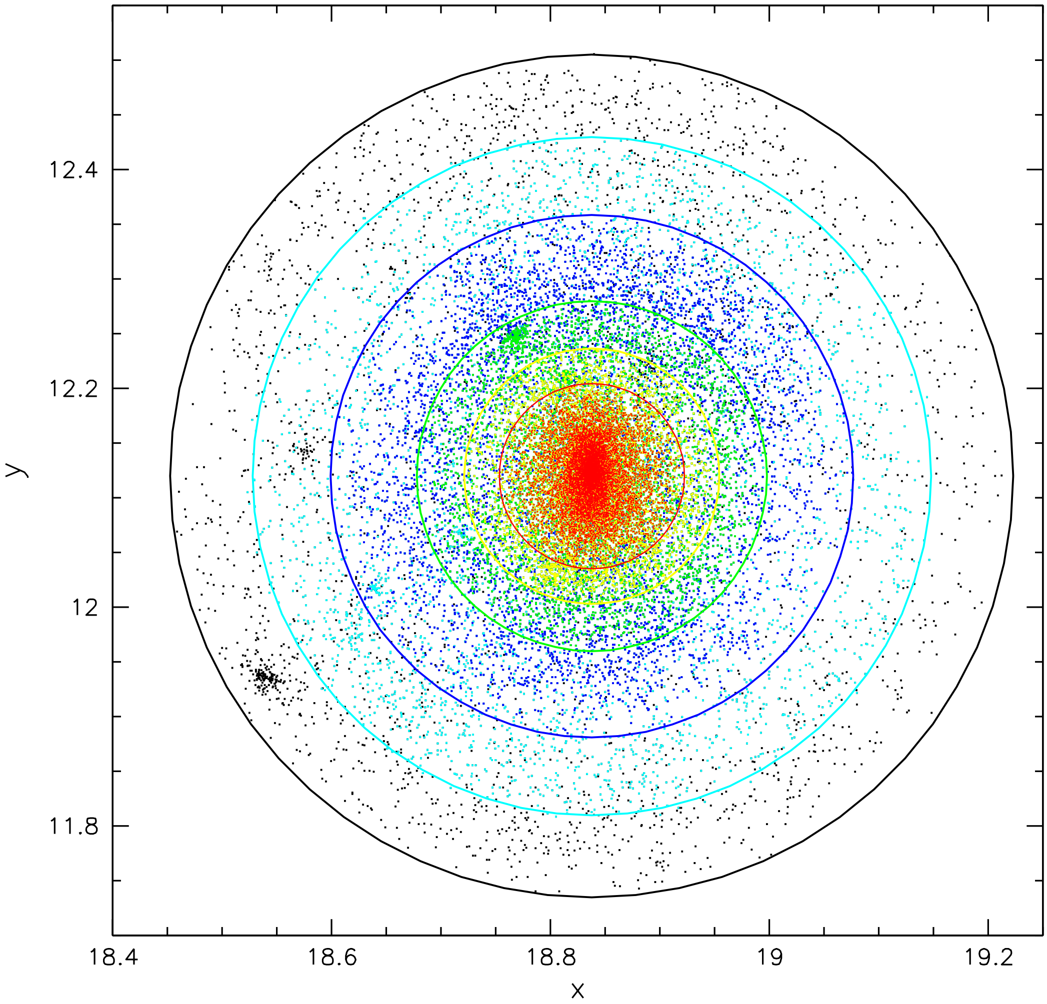

Figure 7.6: Same as Figure 7.4, but for halo 48 from "Bice". This halo is less massive than the previous one, having a virial mass of M=3.683 $10^{12} M_{\odot} h^{-1}$. Masses and radii of all the shells are listed in Table 7.2.

halo 48 (bice)	M_{sph} $[M_{\odot} h^{-1}]$	M_{ell} $[M_{\odot} h^{-1}]$	r [Mpc]
$200\rho_b$	4.084 10^{12}	4.196 10^{12}	0.385
δ_{vir}	3.683 10^{12}	3.796 10^{12}	0.318
$200\rho_c$	3.170 10^{12}	3.238 10^{12}	0.239
$500\rho_c$	2.379 10^{12}	2.516 10^{12}	0.160
$1000\rho_c$	1.848 10^{12}	1.913 10^{12}	0.117
$2000\rho_c$	1.411 10^{12}	1.469 10^{12}	0.085

Table 7.2: For each density threshold, we list the radii and the corresponding enclosed masses of halo 48 from "Bice", represented in Figure 7.6.

The uniqueness of the virial overdensity

In Figure 7.8 we show the evolution of the halo mass function of the spherical virial haloes, from $z = 0$ to $z = 5$. Figure 7.10 show the same results for ellipsoidal virial haloes. The virial overdensity is higher than $200\rho_b$ (corresponding to $\simeq 98\rho_c$) and lower than all the other ones that we considered. Different colours show data points from each one of the six simulations (green = Ada, cyan = Bice,

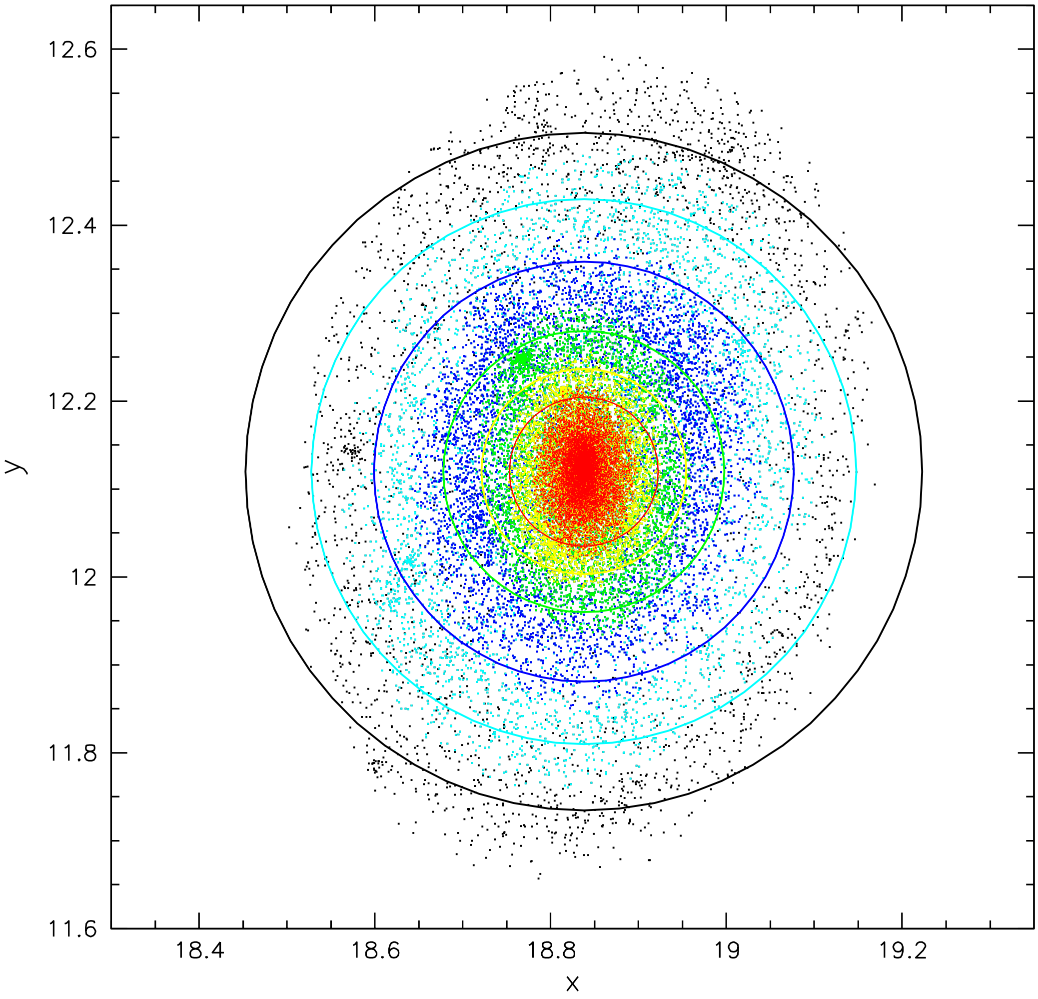

Figure 7.7: Same as Figure 7.6, but for the ellipsoidal identification.

blue = Cloe, magenta = Dora, red = Emma, orange = Flora). The black solid line in all panels shows the best fit to the $z = 0$ points, following the Sheth & Tormen mass function [60, 59]: the resulting set of parameters is specified at the bottom of each Figure. The lower panels show the percentual residuals from the best fit. It is easy to see that the mass function is actually universal for virial haloes, since the residuals' mean is around zero and the scatter remains within the limit of 10% at all redshifts. We found the best fit parameters using a chi-squared method and weighting each point by the associated poissonian error (represented by the error bars). We let the three parameters (A, a, p) vary freely; alternatively, one could vary only (a, p) and then derive the normalisation A from p: this allows to maintain the whole distribution normalised to 1. This last option is coherent with the assumption that all the mass is contained in haloes, which in turns holds only for the virial overdensity. Thus, we decided to use the three parameters estimation for all the overdensities, since haloes identified at high density thresholds cannot contain all the mass. For comparison with other works, the results obtained varying only two parameters for the virial overdensity are: $a = 0.769$, $p = 0.292$ and $A = 0.330$ - thus very similar to the adopted three-parameters fit.

Finally, once demonstrated the universality (within 10% scatter) of the virial halo mass function, we found another set of fest-fit parameters by using the data at all the eight redshift together to obtain the fit. Figure 7.9 shows the resulting curve, whose parameters are: $a = 0.8065$, $p = 0.1814$ and 0.3436.

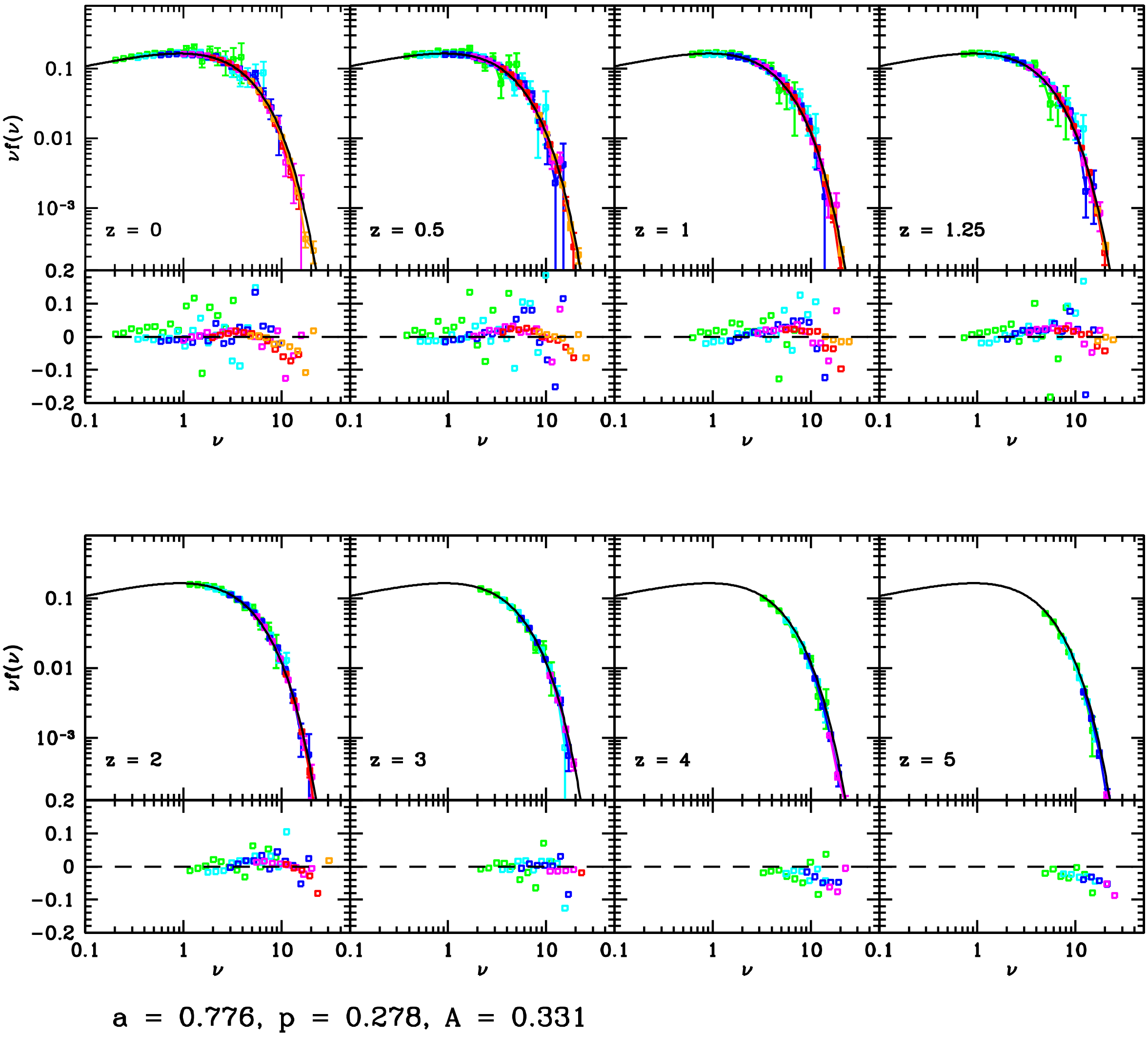

Figure 7.8: Halo mass function at eight redshifts, for all haloes with more than 300 virial particles in the Spherical Overdensity catalogues. The points belonging to each simulation are represented in different colours (from Ada in green to Flora in orange). The black solid line in all panels shows the best fit to the $z = 0$ points, following the Sheth & Tormen mass function [60, 59]; the parameters of the fit are given at the bottom. The lower panels show the residuals from the best fit.

The universality is maintained and reinforced: the scatter both at high masses and high z is reduced, allowing a better fit.

We then proceeded to study the mass functions for the other density thresholds, finding that they vary with z, moving away from the present-day distribution. Figure 7.12 and Figure 7.13 show the nass function of spherical haloes, identified respectively at $200\rho_b$ and $200\rho_c$. Figure 7.12 reproduces the result of Tinker et al. 2008 [63], shown in Figure 7.2: at high redshift, the $z = 0$ best fit overestimates the real population of haloes identified at $200rho_b$. The opposite is true for the haloes of Figure 7.13, whose abundance is underestimated by the $z = 0$ best fit relation. The present day mass functions at all the other density thresholds (both for SO and EO haloes) are shown in Appendix B. Table 7.3 summarises the parameters of the $z = 0$ best fitting relations, which are also plotted in Figure 7.11 - as a function of ρ/ρ_c: the three parameters depend on density in a very regular way. We derived some

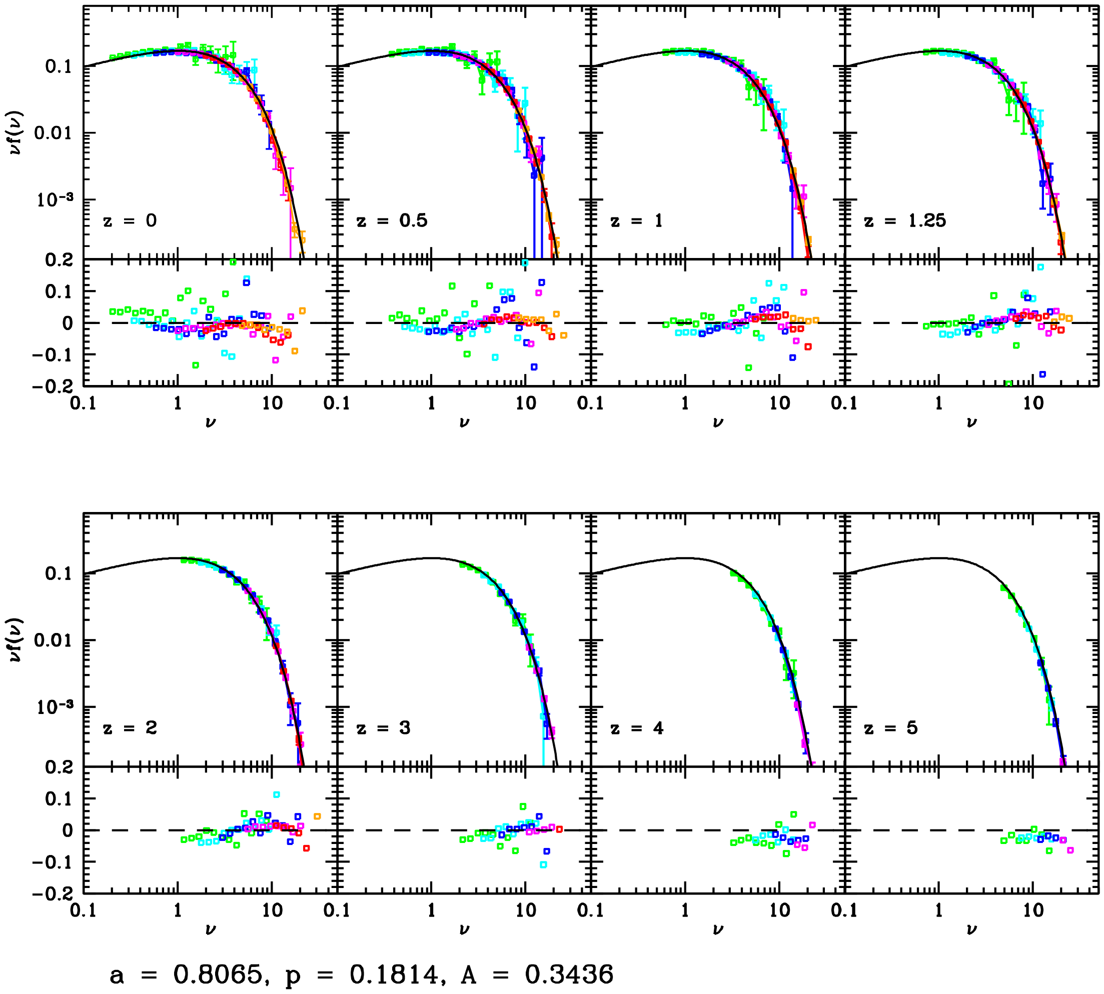

Figure 7.9: The data points and the colour code are the same of Figure 7.8, while the best-fit relation is different: we obtained it fitting all the points at all the eight redshifts together, as a proof of the universality of the halo mass function for virial haloes. With respect to the previous fit, the scatter both at high masses and at high z is a bit reduced

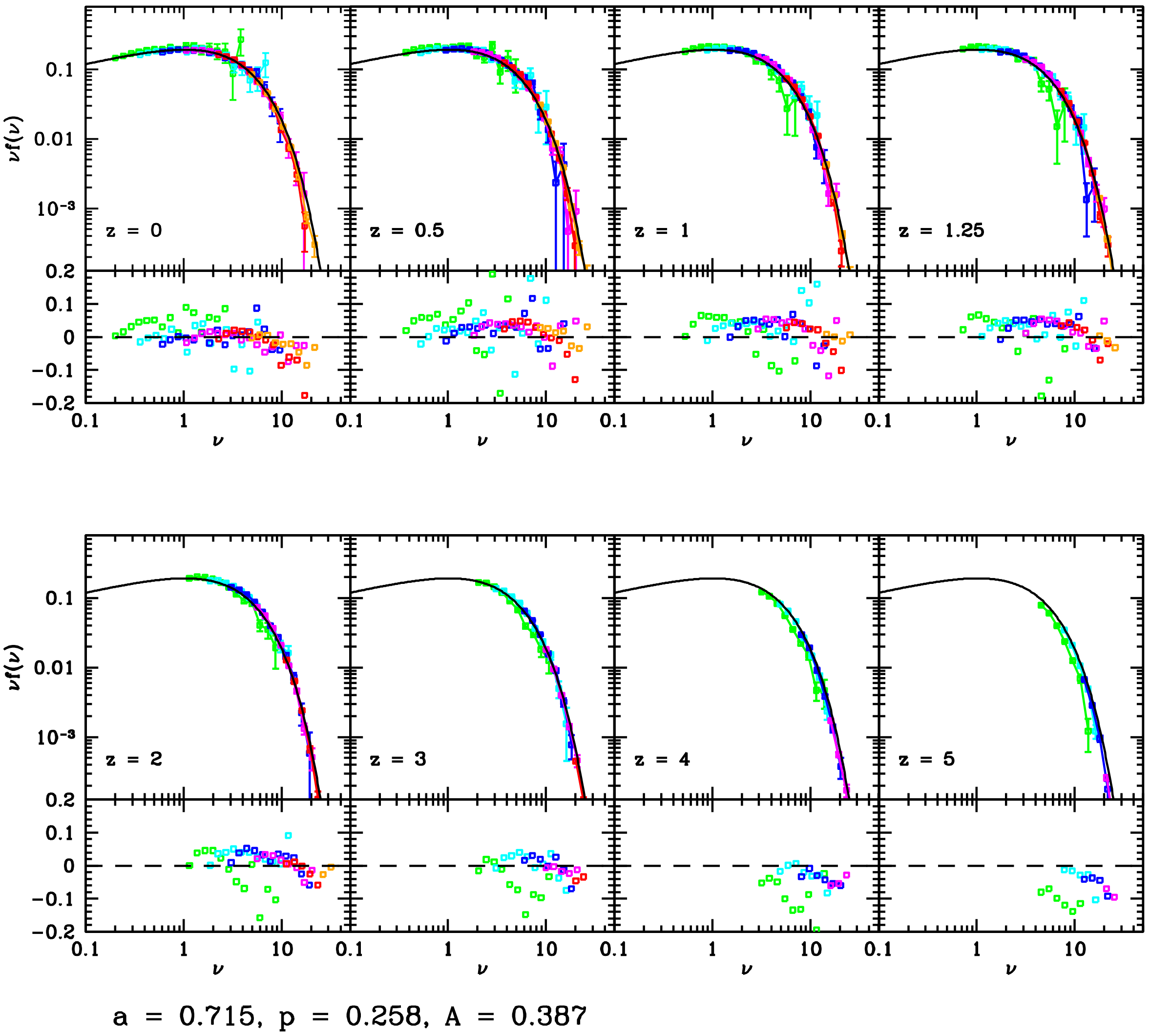

Figure 7.10: Same as Figure 7.8, but for the haloes in the Ellipsoidal Overdensity catalogue.

simple fitting formulae for the $z = 0$ mass functions; for the case of SO haloes these are:

$$\begin{aligned} a &= 1.9113 - 1.3927x + 0.4116x^2 & \chi^2 &= 1.485 \times 10^{-4}, \\ p &= -0.4647 + 0.5148x - 0.0733x^2 & \chi^2 &= 1.5113 \times 10^{-4}, \\ A &= 0.5994 - 0.1346x & \chi^2 &= 2.934 \times 10^{-5}, \end{aligned} \tag{7.6}$$

where $x = \rho/\rho_c$. For EO haloes we have analogous relations:

$$\begin{aligned} a &= 1.7142 - 1.2174x + 0.3563x^2 & \chi^2 &= 1.19 \times 10^{-3}, \\ p &= -0.3647 + 0.4158x - 0.0549x^2 & \chi^2 &= 2.653 \times 10^{-4}, \\ A &= 0.712 - 0.1636x & \chi^2 &= 3.255 \times 10^{-5}. \end{aligned} \tag{7.7}$$

These relations may be used as a general model to derive the predicted mass function at any overdensity.

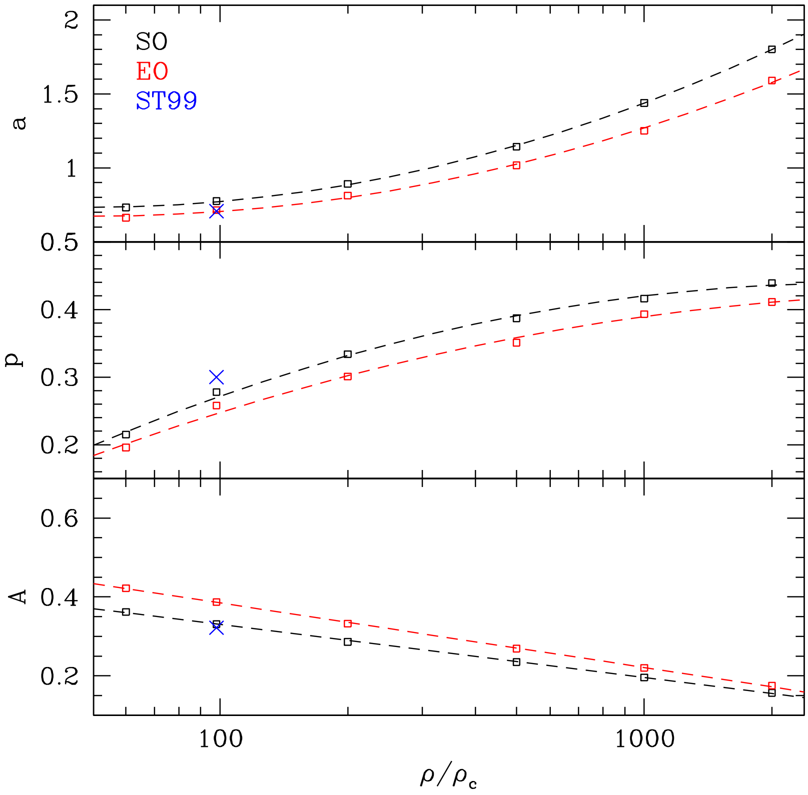

Figure 7.11: Best fit parameters of the $z = 0$ halo mass functions, as a function of ρ/ρ_c. The results for spherical haloes are represented in black, while those for ellipsoidal haloes in red. The blue crosses show the best fit parameters obtained by Sheth & Tormen 1999 [60]. The dashed curves represent the best fit relations from Equations 7.6 and 7.7.

ρ (SO)	a	p	A	ρ (EO)	a	p	A
$200\rho_b$	0.732	0.215	0.362	$200\rho_b$	0.663	0.196	0.422
δ_{vir}	0.776	0.278	0.331	δ_{vir}	0.715	0.258	0.387
$200\rho_c$	0.891	0.334	0.286	$200\rho_c$	0.813	0.301	0.332
$500\rho_c$	1.143	0.387	0.235	$500\rho_c$	1.017	0.351	0.269
$1000\rho_c$	1.439	0.416	0.196	$1000\rho_c$	1.250	0.393	0.220
$2000\rho_c$	1.801	0.439	0.157	$2000\rho_c$	1.590	0.411	0.175

Table 7.3: Parameters of the best-fitting mass function at $z = 0$, for the SO haloes on the left and the EO haloes on the right.

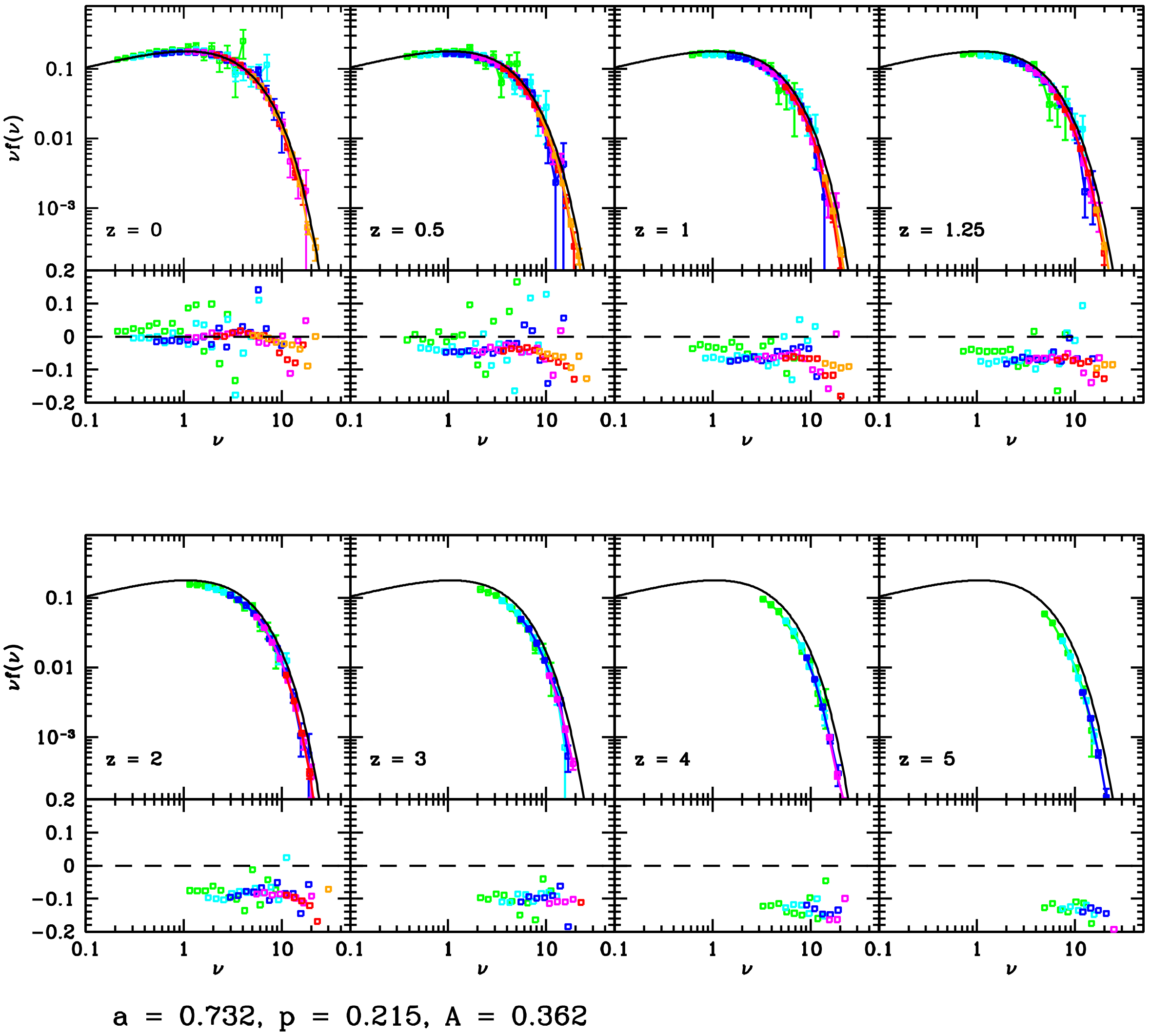

Figure 7.12: Same as Figure 7.8; in this case haloes has been identified using $200\rho_b$ instead of δ_{vir} as density threshold, which breaks the universality of the mass function at all redshifts.

7.3 A comparison between SO and EO halo identifications

Figure 7.14 shows the best fitting relations to the $z = 0$ mass functions for the SO haloes: different colours represent different density thresholds. The ordering of the mass functions perfectly reflect the increase in density from $200rho_b$ to $2000\rho_c$: haloes identified at higher density will be enclosed in smaller regions, with a lower mass. in the bottom panel we show the percentual difference between our best fit for virial haloes and the mass function from Sheth & Tormen 1999 [60]: while their fit was very accurate at low and intermediate masses, it overpredicts massive haloes; this is probably due to a lack of high mass haloes in their simulations.

Figure 7.15 shows the same curves of the previous Figure, but for the case of EO haloes: this allows us to analyse the effect of the identification method on the halo mass function. As has already been discussed, ellipsoidal haloes are systematically more massive than spherical haloes, since the ellipsoidal approximation is able to follow more precisely the isodensity curves.

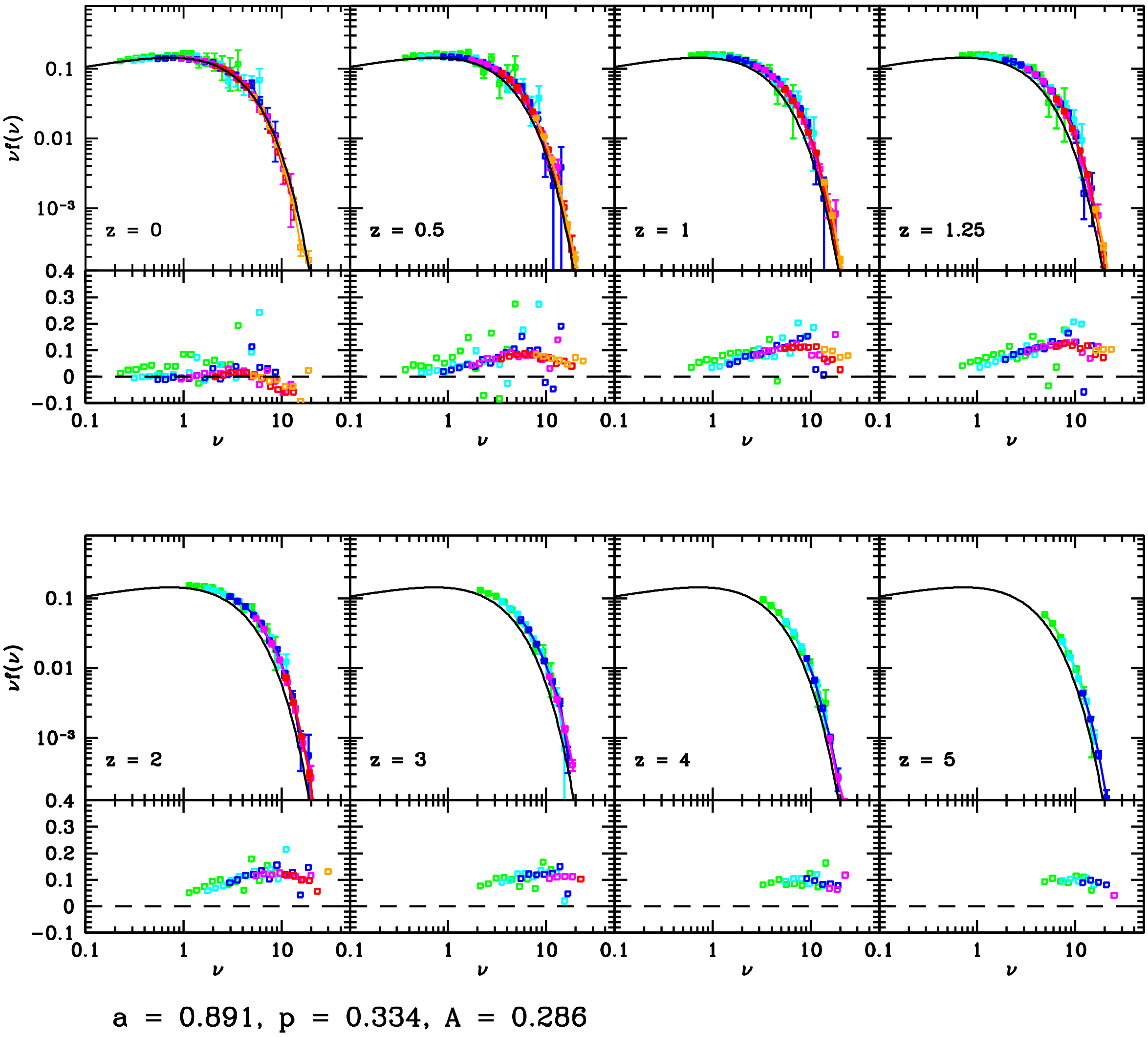

Figure 7.13: Same as Figure 7.8, but for haloes identified at $200\rho_c$; the universality is again broken.

7.4 Matching haloes

The halo catalogues at various density threshold can be use to study the dependence of halo properties on density. Thus, we selected the virial haloes with more than 1000 particles and we checked whether they had a corresponding halo at all the other densities: to do so, we used an algorithm that find, in the other catalogues, the nearest haloes to the center of mass of the virial halo. We selected only the virial haloes with a corresponding identification in all the other five catalogues: in this way we can look at the same halo in different shells.

In the left panel of Figure 7.16 we show the halo mass (of the matching haloes) as a function of density. Each colour represent a different bin in mass; squared points show the medians, while the dashed lines mark the interquartile region. The halo mass decreases at higher densities (thus towards the center of the halo) in a similar way for all the mass bins, even if the variation is bigger for high mass haloes. The right panel shows the percentual variation in mass: while for low mass haloes the mass contained in the inner shell ($2000\rho_c$) is still $\simeq 60\%$ of the virial mass, for high mass haloes it is between 30% and 40%. This behaviour reflects the shape of the density profile, which is steeper for

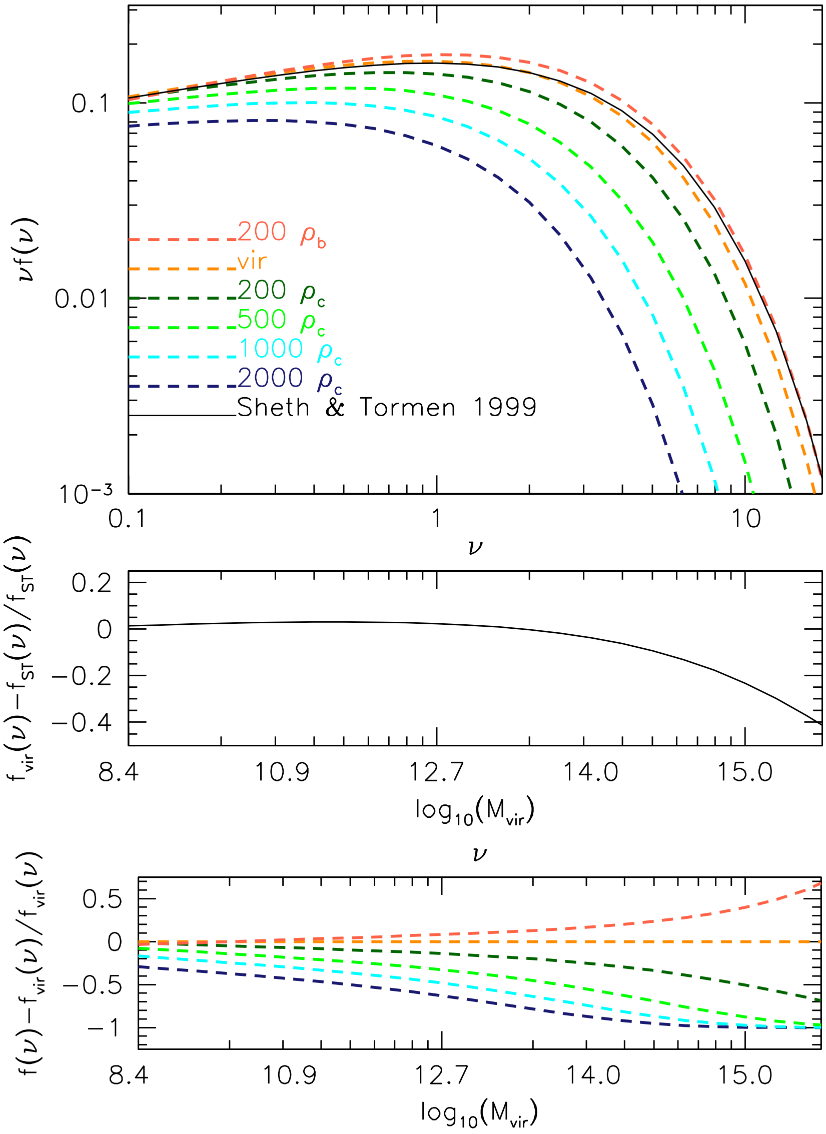

Figure 7.14: Halo mass function at the six different density thresholds for SO haloes. In the two bottom panels we show: (*i*) the percentual difference between our best fit for virial haloes and the mass function from Sheth & Tormen 1999 [60]; (*ii*) the all the mass functions and the virial one.

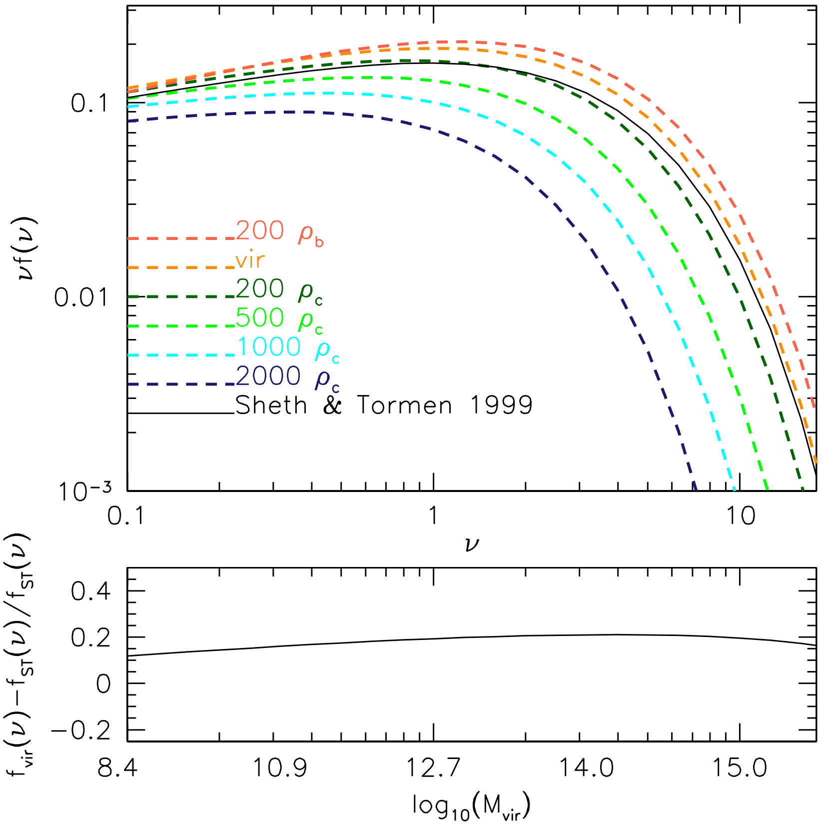

Figure 7.15: Same as Figure 7.14, but for the EO haloes.

massive haloes, and the fact that low mass haloes are more concentrated. Figure 7.17 shows the same results for the radius instead of the mass. The variation in radius between different shells is almost the same for all the mass bin: this again shows that the differences in Figure 7.16 are due to different concentrations.

7.5 Summary

In this Chapter we adressed the definition and the universality of the halo mass function, analysin in detail its dependence on the halo identification. We found that:

- the effect of the halo identification on the halo mass function is very strong; all the mass functions can be modelled with ST99-like fitting formulae;
- the halo mass function for virial haloes is indeed universal, so independent from z; our final best fit parameters are $a = 0.8065$, $p = 0.1814$ and 0.3436;
- the best fit parameters exhibit a regular behaviour as a function of density (ρ/ρ_c), which can be modelled with first or second order equations (Eq. 7.6 and 7.7). These relations may be used as a general model, since they allow to predict the expected mass function at any density.

We plan to extend this analysis to all the other redshifts, modelling the dependence of the halo mass function on z and ρ to find a general conversion method from the virial mass function to the other ones. Moreover, we will use simulations with a different cosmology (and possibly with extreme values) to test again the independence from the assumed cosmological model.

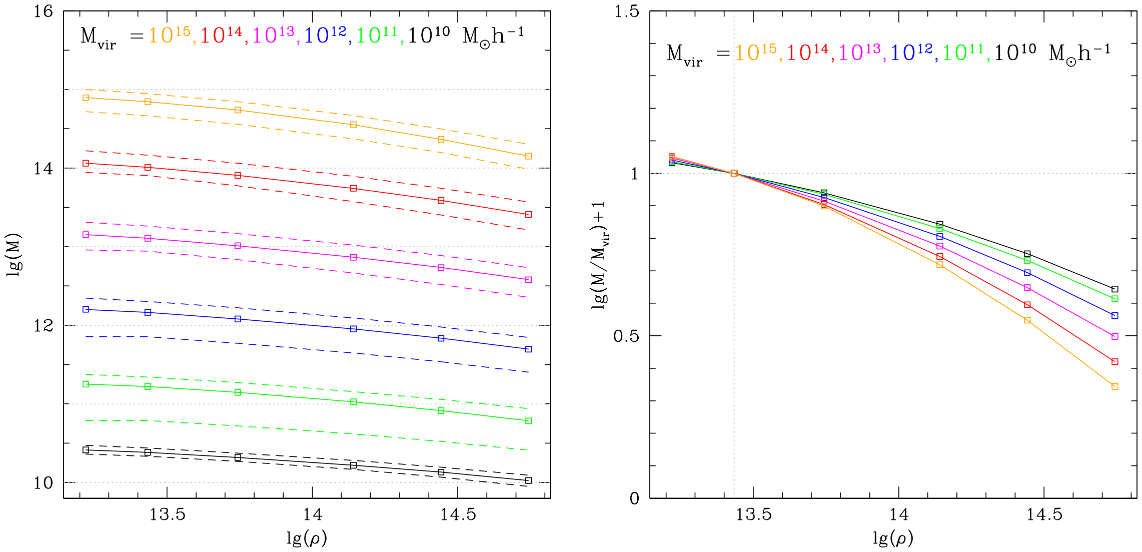

Figure 7.16: *Left*: halo mass as a function of density, from the matching haloes catalogues. Each colour represent a different bin in mass; squared points show the medians, while the dashed lines mark the interquartile region. *Right*: percentual variation in mass as a function of density. This plot contains the same data of the left panel, but rescaled to the value of the virial mass. The color scheme is the same of the left panel and the squared points show the medians of the distribution.

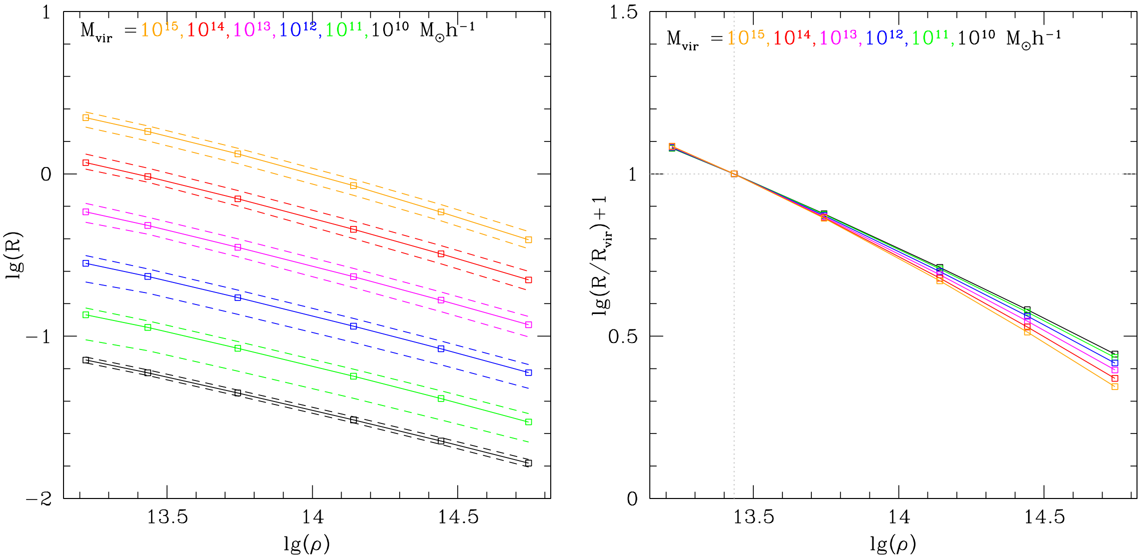

Figure 7.17: *Left*: radius as a function of density. *Right*: percentual variation in radius as a function of density. For both panels the colour scheme is the same of Figure 7.16

Useful formulae A

A.1 Calculation of the growth factor

The growing solution of perturbation theory can be approximated as:

$$\boxed{\delta_+ \propto D(z) \propto g(z)(1+z)^{-1}} \tag{A.1}$$

where

$$g(z) \simeq \frac{5}{2}\frac{\Omega_m(z)}{(\Omega_m(z))^{4/7} - \Omega_\Lambda(z) + \left[1+\frac{\Omega_m(z)}{2}\right]\left[1+\frac{\Omega_\Lambda(z)}{70}\right]}. \tag{A.2}$$

Here again

$$\Omega_m(z) = \frac{\Omega_m(0)(1+z)^3}{E^2(z)} \tag{A.3}$$

$$\Omega_\Lambda(z) = \frac{\Omega_{Lambda}(0)}{E^2(z)} \tag{A.4}$$

$$E(z) = \left[\Omega_\Lambda(0) + (1-\Omega_0)(1+z)^2 + \Omega_m(0)(1+z)^3 + \Omega_r(0)(1+z)^4 + ...\right]^{1/2}. \tag{A.5}$$

From the scale factor, we can also calculate $f(\Omega)$ as:

$$f(\Omega_m) = -\frac{\mathrm{d}\ln D(z)}{\mathrm{d}\ln(1+z)} \simeq \Omega_m^{0.6}. \tag{A.6}$$

A.2 Calculation of ν

For a virialized halo with mass M at redshift z for a given cosmological model the definition of ν is the following:

$$\nu \equiv \frac{\delta_c(z)}{\sigma(M)}, \tag{A.7}$$

where $\delta_c(z)$ is the critical overdensity of the spherical collapse model, the initial density required for a fluctuation to collapse at redshift z. This in turn can be expressed as the collapse overdensity at redshift $z=0$ rescaled to a given time: $\delta_c(z) = \delta_c/D(z)$, with $D(z)$ being the linear growth rate of a density fluctuation normalised to unity at $z=0$ - thus the one just derived in the previous section. The denominator $\sigma(M)$, depends on the mass but not on redshift. It is the variance in the initial density field smoothed on a linear scale R, which corresponds to the radius of a uniform sphere of mass M.

The collapse overdensity δ_c has an extremely weak dependence on cosmology, that can be expresse as in Kitayama & Suto [28]:

$$\boxed{\delta_c(z) \approx \frac{3}{20}(12\pi)^{2/3}[1+0.0123\lg\Omega(z)] \approx 1.686\,[\Omega_m(t_c)]^{0.0055}} \tag{A.8}$$

For realistic cosmologies this can be approximated to $\delta_c \approx 1.686$. Therefore, at $z = 0$ the collapse overdensity is δ_c and it increases with redshift, due to $D(z)$.

The other quantity required, the variance $\sigma^2(M)$, is defined from the power spectrum as:

$$\sigma^2(M) = \frac{1}{2\pi^2}\int_0^\infty P(k)\tilde{W}^2(kR)k^2\mathrm{d}k; \tag{A.9}$$

where $\tilde{W}$ is the Fourier transform of a window function. Typically, W is a Top Hat (sphere) in the coordinates space, so that its Fourier transform $\tilde{W}$ is:

$$\tilde{W}(kR) = 3\frac{\sin(kR) - kR\cos(kR)}{(kR)^3}; \tag{A.10}$$

with the radius R given by $M = \rho_b 4\pi/3R^3$. The power spectrum $P(k)$ of the density fluctuations is the main input; given a set of cosmological parameters it can be computed from a software like CAMB [33]. As it is function of initial conditions only, $\sigma(M)$ needs to be computed only once for a given cosmology: all the redshift dependence is inside $D(z)$.

Mass functions at various density thresholds B

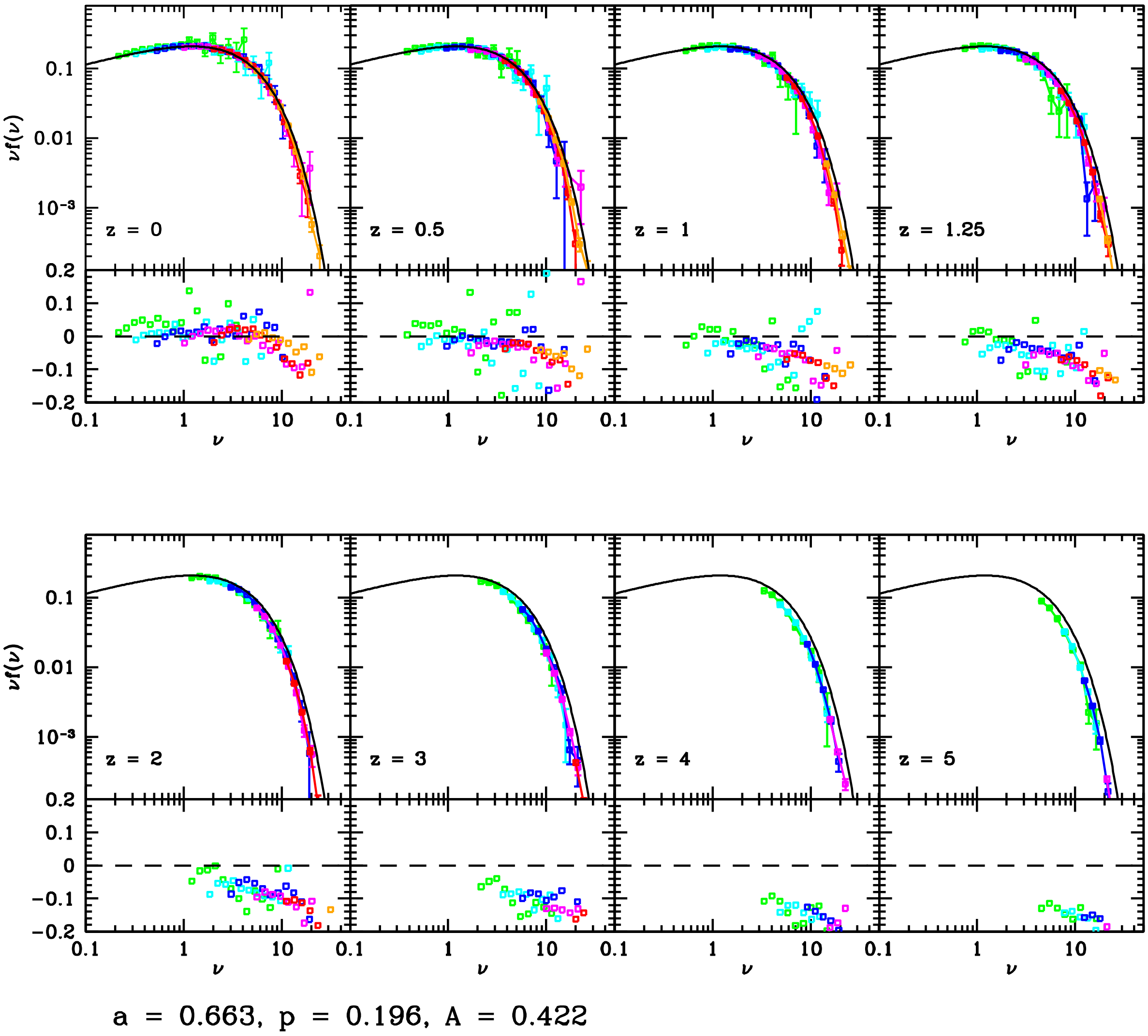

Figure B.1: Same as Figure 7.10, but for EO haloes identified at $200\rho_b$

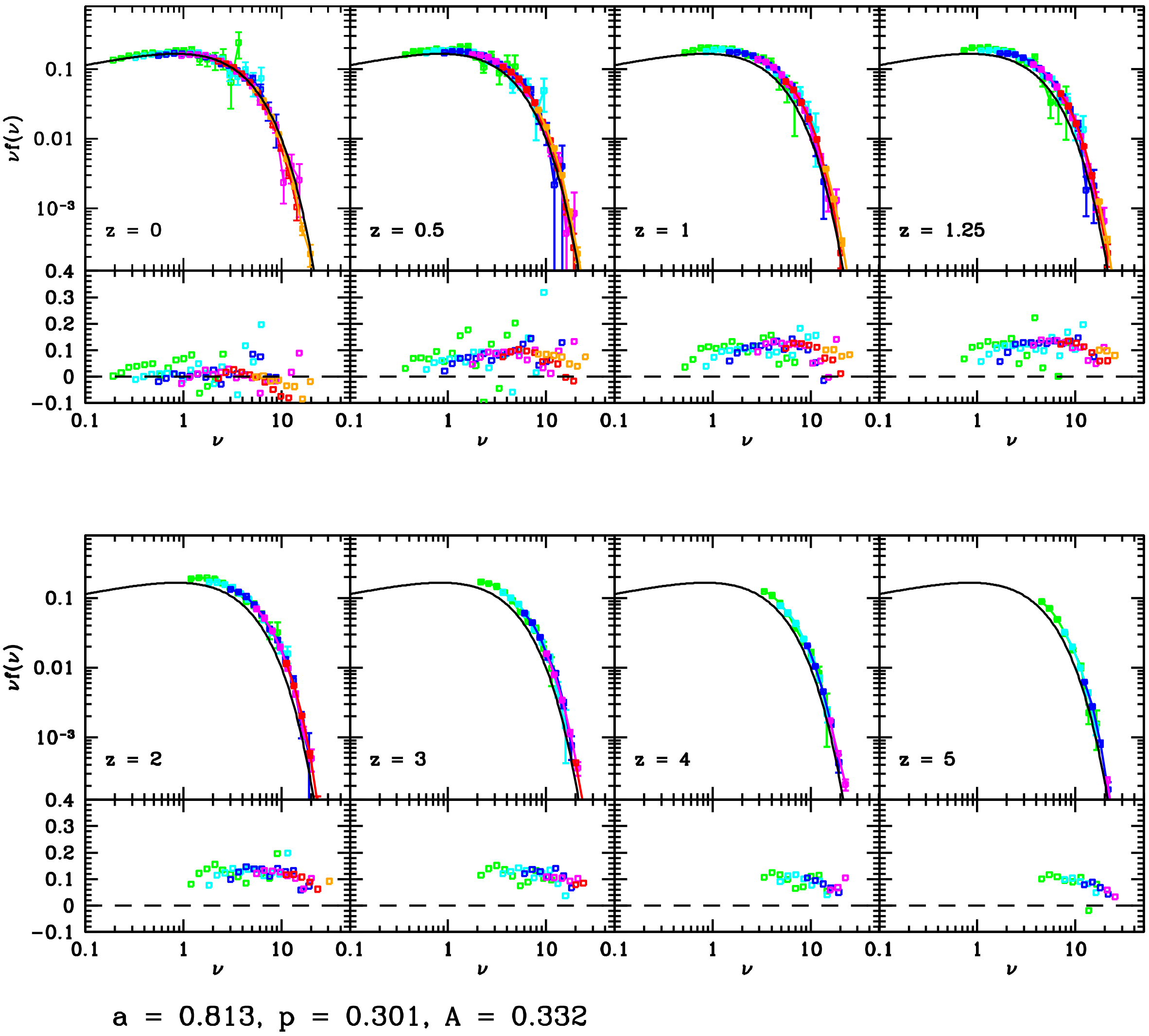

Figure B.2: Same as Figure 7.10, but for EO haloes identified at $200\rho_c$

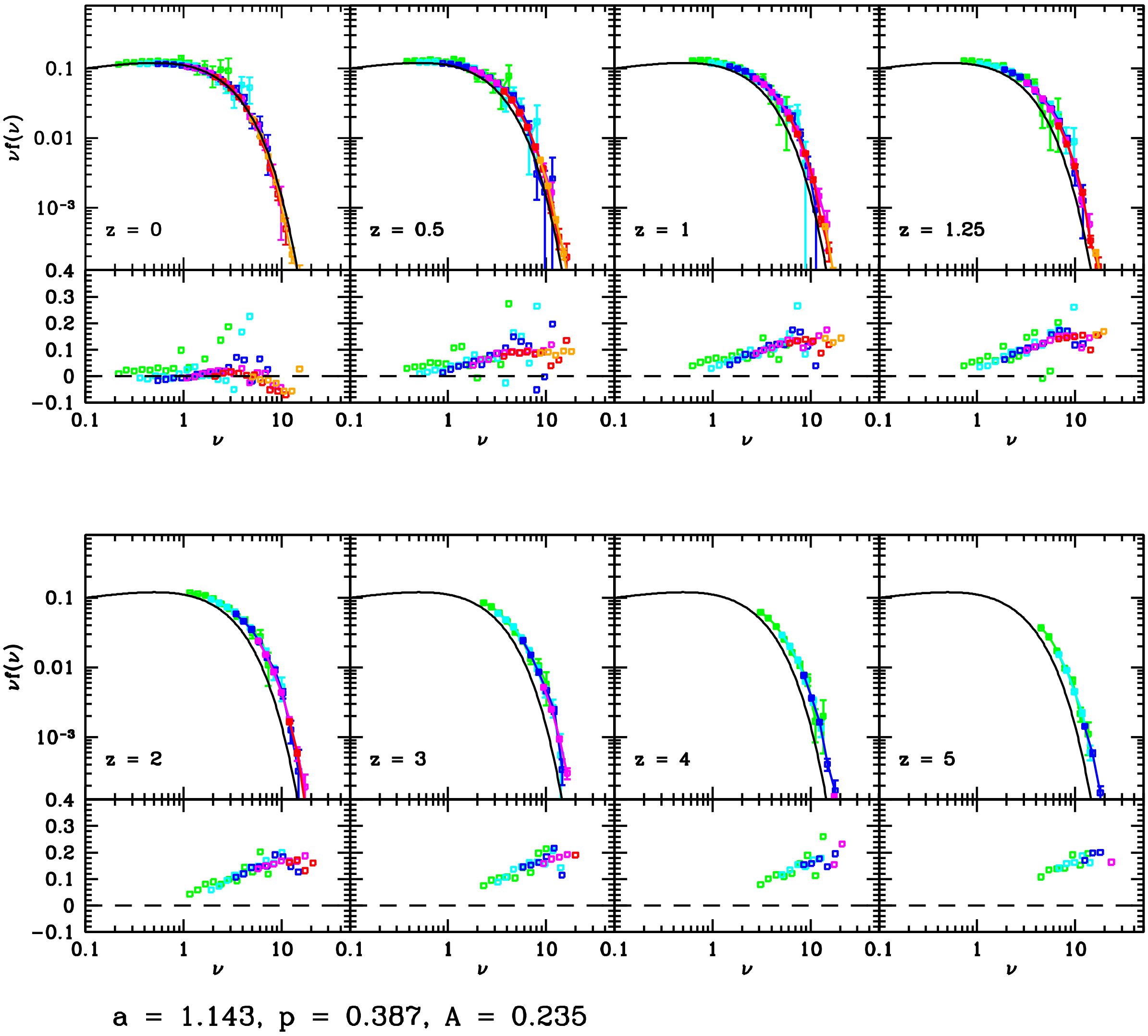

Figure B.3: Same as Figure 7.8, but for SO haloes identified at $500\rho_c$.

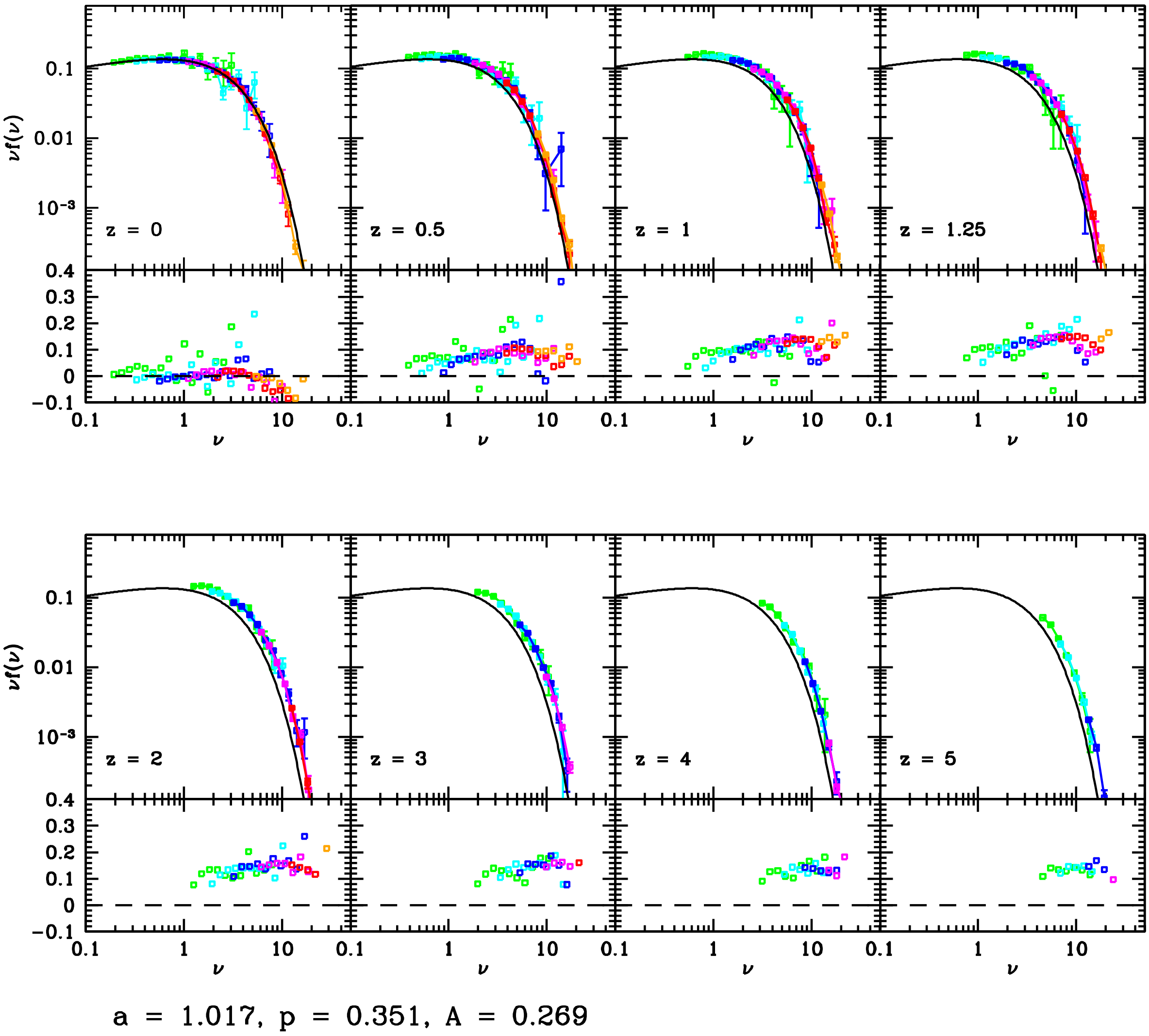

Figure B.4: Same as Figure B.3, but for EO haloes identified at $500\rho_c$..

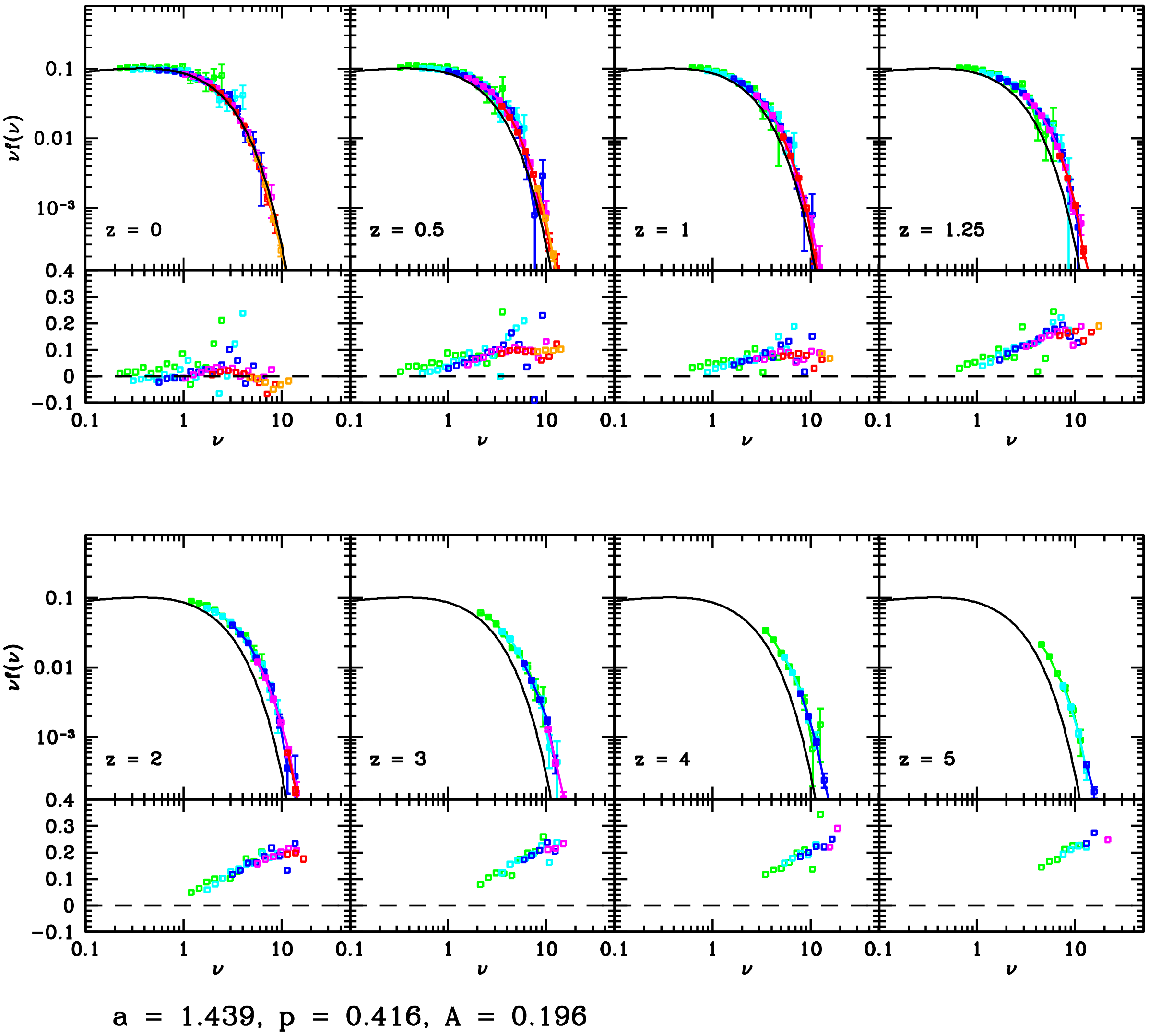

Figure B.5: Same as Figure B.3, but for SO haloes identified at $1000\rho_c$.

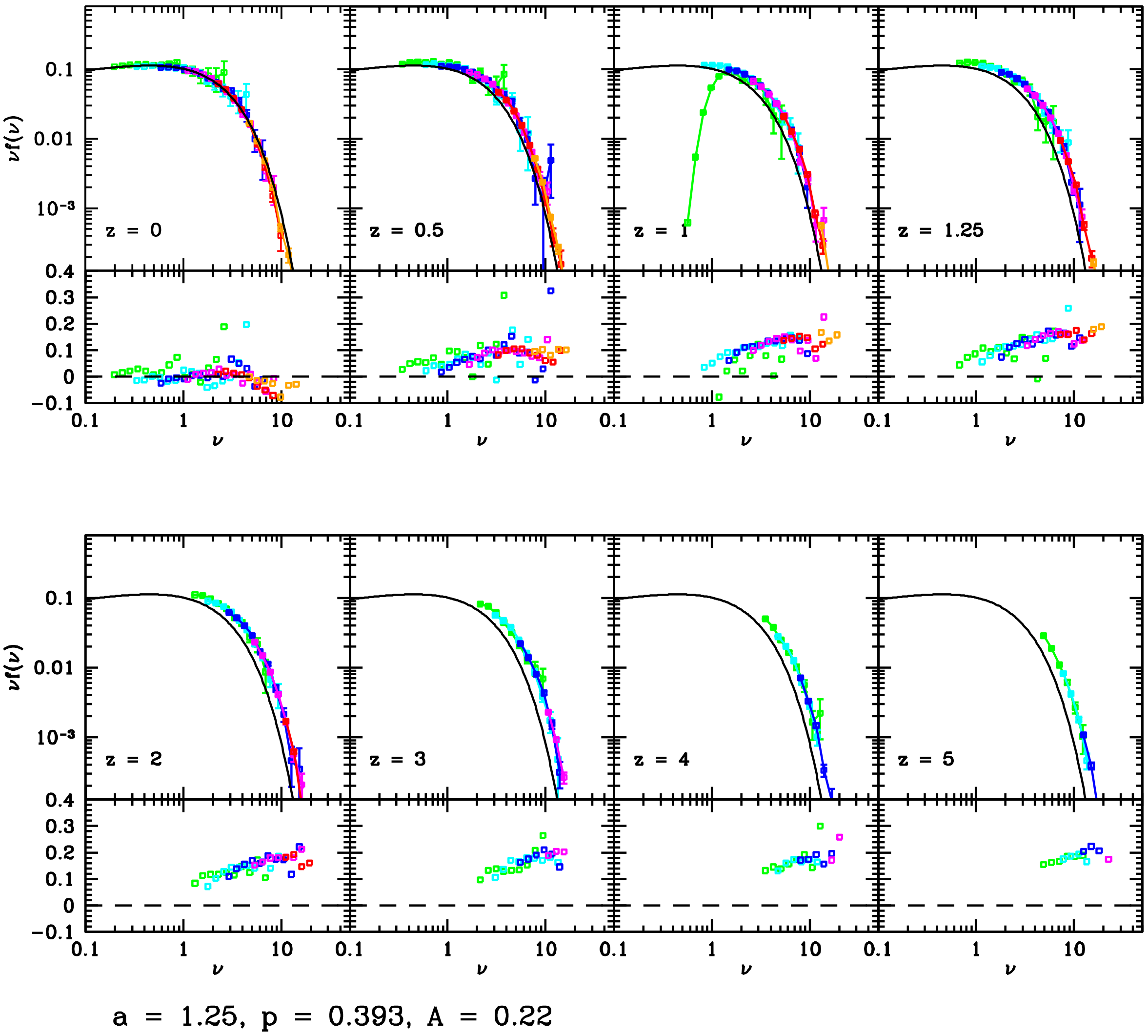

Figure B.6: Same as Figure B.4, but for EO haloes identified at $1000\rho_c$.

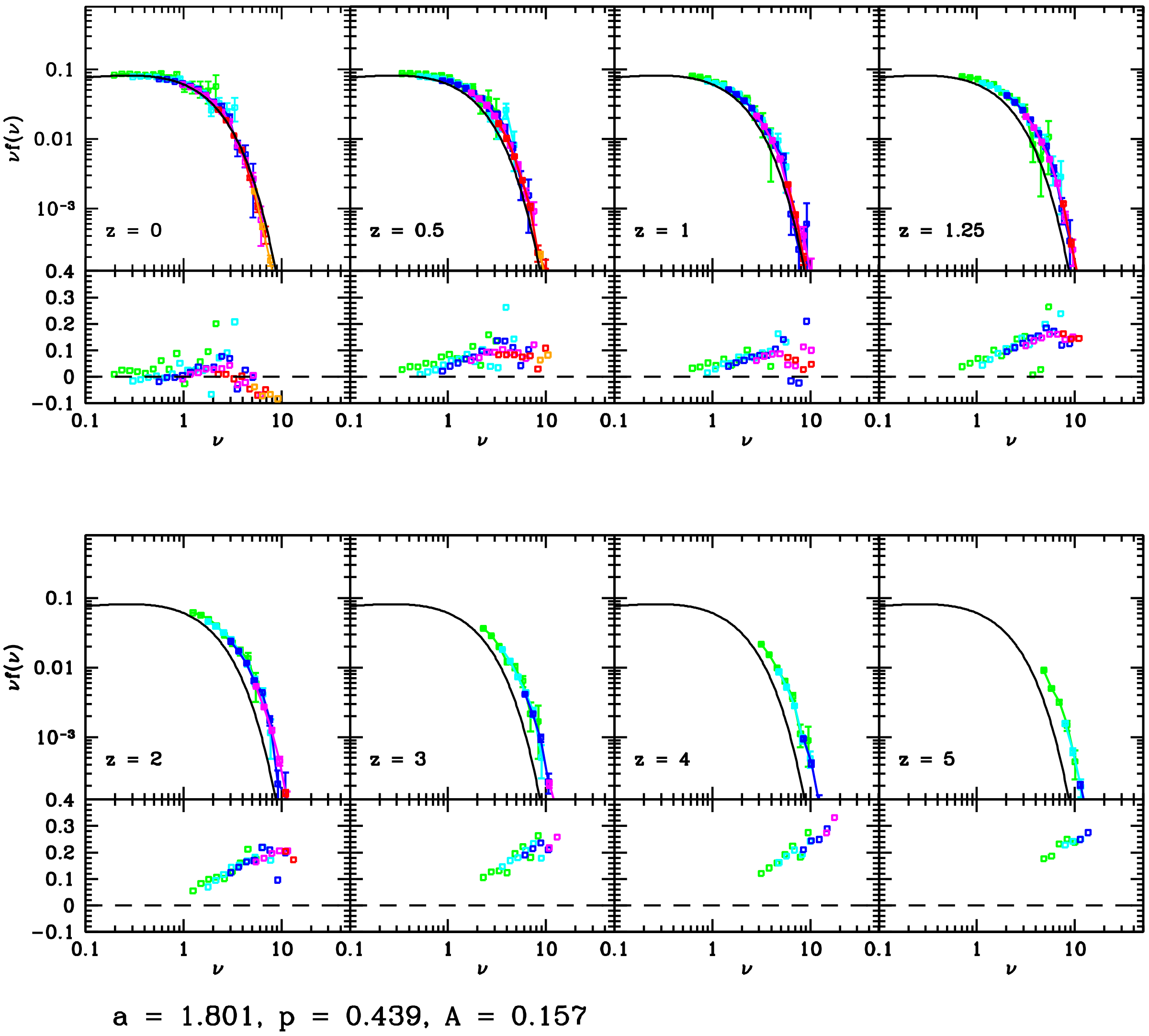

Figure B.7: Same as Figure B.3, but for SO haloes identified at $2000\rho_c$.

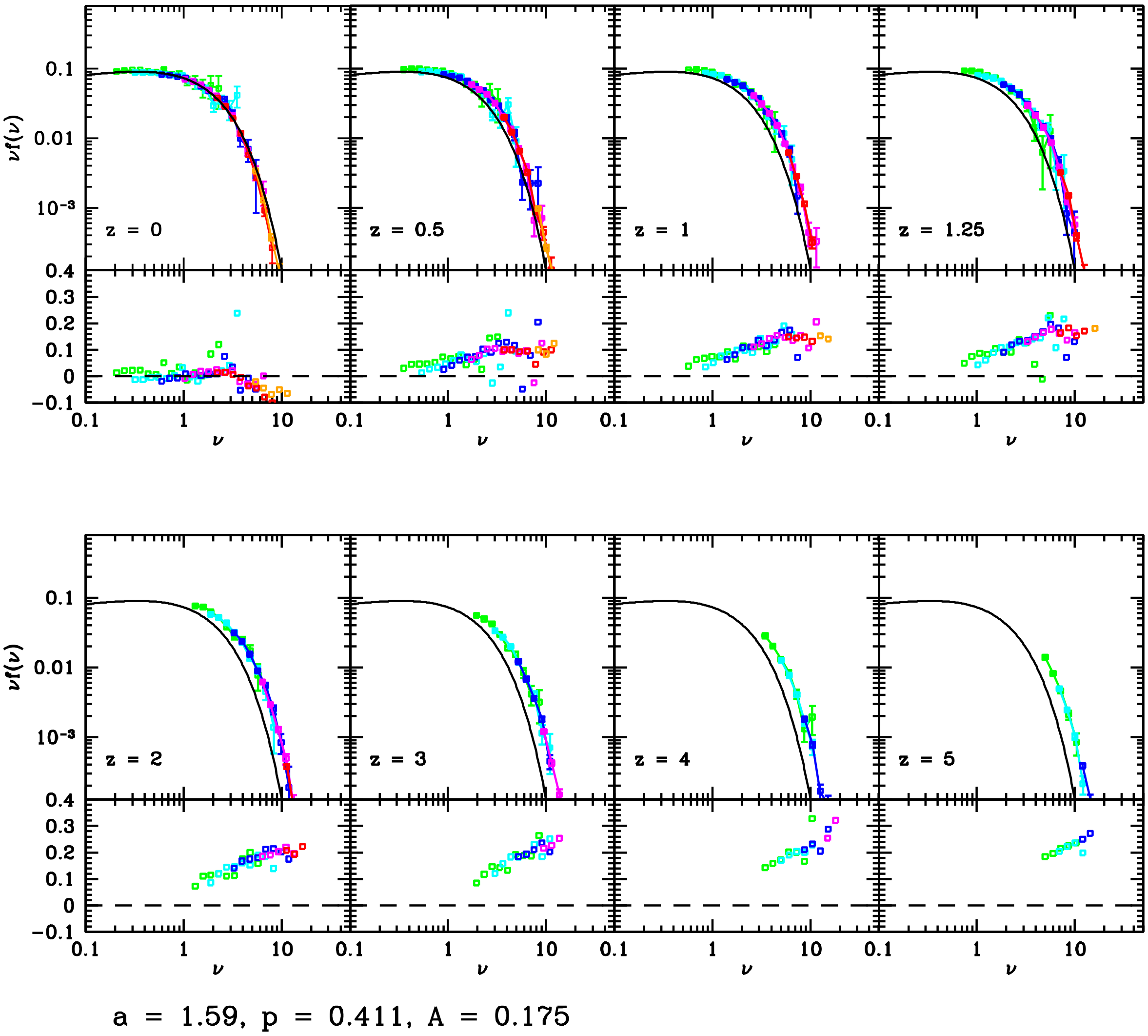

Figure B.8: Same as Figure B.4, but for EO haloes identified at $2000\rho_c$.

List of Figures

List of Tables

Bibliography

[1] B. Allgood, R. A. Flores, J. R. Primack, A. V. Kravtsov, R. H. Wechsler, A. Faltenbacher, and J. S. Bullock. The shape of dark matter haloes: dependence on mass, redshift, radius and formation. *MNRAS*, 367:1781–1796, April 2006.

[2] R. E. Angulo, C. G. Lacey, C. M. Baugh, and C. S. Frenk. The fate of substructures in cold dark matter haloes. *MNRAS*, 399:983–995, October 2009.

[3] R. E. Angulo, V. Springel, S. D. M. White, a. Jenkins, C. M. Baugh, and C. S. Frenk. Scaling relations for galaxy clusters in the Millennium-XXL simulation. *MNRAS*, 426(3):2046–2062, November 2012.

[4] J. Bailin and M. Steinmetz. Internal and External Alignment of the Shapes and Angular Momenta of ΛCDM Halos. *ApJ*, 627:647–665, July 2005.

[5] J. M. Bardeen, J. R. Bond, N. Kaiser, and A. S. Szalay. The statistics of peaks of Gaussian random fields. *ApJ*, 304:15–61, May 1986.

[6] P. Bett, V. Eke, C. S. Frenk, A. Jenkins, J. Helly, and J. Navarro. The spin and shape of dark matter haloes in the Millennium simulation of a Λ cold dark matter universe. *MNRAS*, 376:215–232, March 2007.

[7] M. Bonamigo, G. Despali, M. Limousin, R. Angulo, C. Giocoli, and G. Soucail. Universality of dark matter haloes shape over six decades in mass: Insights from the Millennium XXL and SBARBINE simulations. *ArXiv e-prints*, September 2014.

[8] J. R. Bond, S. Cole, G. Efstathiou, and N. Kaiser. Excursion set mass functions for hierarchical Gaussian fluctuations. *ApJ*, 379:440–460, October 1991.

[9] J. R. Bond and S. T. Myers. The Peak-Patch Picture of Cosmic Catalogs. I. Algorithms. *ApJS*, 103:1–+, March 1996.

[10] M. Borzyszkowski, A. D. Ludlow, and C. Porciani. The formation of CDM haloes II: collapse time and tides. *ArXiv e-prints*, May 2014.

[11] M. Boylan-Kolchin, V. Springel, S. D. M. White, A. Jenkins, and G. Lemson. Resolving cosmic structure formation with the Millennium-II Simulation. *MNRAS*, 398:1150–1164, September 2009.

[12] J. M. Colberg, S. D. M. White, N. Yoshida, T. J. MacFarland, A. Jenkins, C. S. Frenk, F. R. Pearce, A. E. Evrard, H. M. P. Couchman, G. Efstathiou, J. A. Peacock, P. A. Thomas, and Virgo Consortium. Clustering of galaxy clusters in cold dark matter universes. *MNRAS*, 319:209–214, November 2000.

[13] V. Desjacques. Environmental dependence in the ellipsoidal collapse model. *MNRAS*, 388:638–658, August 2008.

[14] G. Despali, C. Giocoli, and G. Tormen. Some like it triaxial: the universality of dark matter halo shapes and their evolution along the cosmic time. *MNRAS*, 443:3208–3217, October 2014.

[15] G. Despali, G. Tormen, and R. K. Sheth. Ellipsoidal halo finders and implications for models of triaxial halo formation. *MNRAS*, 431:1143–1159, May 2013.

[16] J. Einasto. On the Construction of a Composite Model for the Galaxy and on the Determination of the System of Galactic Parameters. *Trudy Astrofizicheskogo Instituta Alma-Ata*, 5:87–100, 1965.

[17] V. R. Eke, S. Cole, and C. S. Frenk. Cluster evolution as a diagnostic for Omega. *MNRAS*, 282:263–280, September 1996.

[18] A. Elia, A. D. Ludlow, and C. Porciani. The spatial and velocity bias of linear density peaks and protohaloes in the Λ cold dark matter cosmology. *MNRAS*, 421:3472–3480, April 2012.

[19] C. S. Frenk and S. D. M. White. Dark matter and cosmic structure. *Annalen der Physik*, 524:507–534, October 2012.

[20] L. Gao, S. D. M. White, A. Jenkins, F. Stoehr, and V. Springel. The subhalo populations of ΛCDM dark haloes. *MNRAS*, 355:819–834, December 2004.

[21] C. Giocoli, F. Marulli, M. Baldi, L. Moscardini, and R. B. Metcalf. Characterizing dark interactions with the halo mass accretion history and structural properties. *MNRAS*, 434:2982–2998, October 2013.

[22] C. Giocoli, G. Tormen, and R. K. Sheth. Formation times, mass growth histories and concentrations of dark matter haloes. *MNRAS*, 422:185–198, May 2012b.

[23] C. Giocoli, G. Tormen, and F. C. van den Bosch. The population of dark matter subhaloes: mass functions and average mass-loss rates. *MNRAS*, 386:2135–2144, June 2008.

[24] J. E. Gunn. Massive galactic halos. I - Formation and evolution. *ApJ*, 218:592–598, December 1977.

[25] L. Hernquist. An analytical model for spherical galaxies and bulges. *ApJ*, 356:359–364, June 1990.

[26] A. Jenkins, C. S. Frenk, S. D. M. White, J. M. Colberg, S. Cole, A. E. Evrard, H. M. P. Couchman, and N. Yoshida. The mass function of dark matter haloes. *MNRAS*, 321:372–384, February 2001.

[27] Y. P. Jing and Y. Suto. Triaxial Modeling of Halo Density Profiles with High-Resolution N-Body Simulations. *ApJ*, 574:538–553, August 2002.

[28] T. Kitayama and Y. Suto. Formation rate of gravitational structures and the cosmic X-ray background radiation. *MNRAS*, 280:638–+, May 1996.

[29] A. Klypin, S. Trujillo-Gomez, and J. Primack. Halos and galaxies in the standard cosmological model: results from the Bolshoi simulation. *ArXiv e-prints*, 1002.3660:–, February 2010.

[30] C. Lacey and S. Cole. Merger rates in hierarchical models of galaxy formation. *MNRAS*, 262:627–649, June 1993.

[31] C. Lacey and S. Cole. Merger Rates in Hierarchical Models of Galaxy Formation - Part Two - Comparison with N-Body Simulations. *MNRAS*, 271:676–+, December 1994.

[32] T. Y. Lam and R. K. Sheth. Ellipsoidal collapse and the redshift-space probability distribution function of dark matter. *MNRAS*, 389:1249–1258, September 2008.

[33] Antony Lewis, Anthony Challinor, and Anthony Lasenby. Efficient computation of CMB anisotropies in closed FRW models. *Astrophys. J.*, 538:473–476, 2000.

[34] M. Limousin, A. Morandi, M. Sereno, M. Meneghetti, S. Ettori, M. Bartelmann, and T. Verdugo. The Three-Dimensional Shapes of Galaxy Clusters. *Space Sci.Rev.*, May 2013.

[35] M. Limousin, J. Richard, E. Jullo, J.-P. Kneib, B. Fort, G. Soucail, Á. Elíasdóttir, P. Natarajan, R. S. Ellis, I. Smail, O. Czoske, G. P. Smith, P. Hudelot, S. Bardeau, H. Ebeling, E. Egami, and K. K. Knudsen. Combining Strong and Weak Gravitational Lensing in Abell 1689. *ApJ*, 668:643–666, October 2007.

[36] A. D. Ludlow, M. Borzyszkowski, and C. Porciani. The formation of CDM haloes I: collapse thresholds and the ellipsoidal collapse model. *ArXiv e-prints*, July 2011.

[37] A. D. Ludlow, J. F. Navarro, M. Li, R. E. Angulo, M. Boylan-Kolchin, and P. E. Bett. The dynamical state and mass-concentration relation of galaxy clusters. *MNRAS*, 427:1322–1328, December 2012.

[38] A. Morandi, M. Limousin, Y. Rephaeli, K. Umetsu, R. Barkana, T. Broadhurst, and H. Dahle. Triaxiality and non-thermal gas pressure in Abell 1689. *MNRAS*, 416:2567–2573, October 2011.

[39] A. Morandi, M. Limousin, J. Sayers, S. R. Golwala, N. G. Czakon, E. Pierpaoli, E. Jullo, J. Richard, and S. Ameglio. X-ray, lensing and Sunyaev-Zel'dovich triaxial analysis of Abell 1835 out to R_{200}. *MNRAS*, 425:2069–2082, September 2012.

[40] A. Morandi, K. Pedersen, and M. Limousin. Unveiling the Three-dimensional Structure of Galaxy Clusters: Resolving the Discrepancy Between X-ray and Lensing Masses. *ApJ*, 713:491–502, April 2010.

[41] A. Morandi, K. Pedersen, and M. Limousin. Reconstructing the Triaxiality of the Galaxy Cluster A1689: Solving the X-ray and Strong Lensing Mass Discrepancy. *ApJ*, 729:37, March 2011.

[42] J. C. Muñoz-Cuartas, A. V. Macciò, S. Gottlöber, and A. A. Dutton. The redshift evolution of Λ cold dark matter halo parameters: concentration, spin and shape. *MNRAS*, 411:584–594, February 2011.

[43] J. F. Navarro, C. S. Frenk, and S. D. M. White. The Structure of Cold Dark Matter Halos. *ApJ*, 462:563–+, May 1996.

[44] A. F. Neto, L. Gao, P. Bett, S. Cole, J. F. Navarro, C. S. Frenk, S. D. M. White, V. Springel, and A. Jenkins. The statistics of Λ CDM halo concentrations. *MNRAS*, 381:1450–1462, November 2007.

[45] M. Oguri, M. Takada, K. Umetsu, and T. Broadhurst. Can the Steep Mass Profile of A1689 Be Explained by a Triaxial Dark Halo? *ApJ*, 632:841–846, October 2005.

[46] Planck Collaboration, P. A. R. Ade, N. Aghanim, M. I. R. Alves, C. Armitage-Caplan, M. Arnaud, M. Ashdown, F. Atrio-Barandela, J. Aumont, H. Aussel, and et al. Planck 2013 results. I. Overview of products and scientific results. *A&A*, 571:A1, November 2014.

[47] Planck Collaboration, P. A. R. Ade, N. Aghanim, C. Armitage-Caplan, M. Arnaud, M. Ashdown, F. Atrio-Barandela, J. Aumont, C. Baccigalupi, A. J. Banday, and et al. Planck 2013 results. XVI. Cosmological parameters. *ArXiv e-prints*, March 2013.

[48] Planck Collaboration, P. A. R. Ade, N. Aghanim, M. Arnaud, M. Ashdown, J. Aumont, C. Baccigalupi, M. Baker, A. Balbi, A. J. Banday, and et al. Planck early results. I. The Planck mission. *A&A*, 536:A1, December 2011.

[49] C. Porciani, A. Dekel, and Y. Hoffman. Testing tidal-torque theory - I. Spin amplitude and direction. *MNRAS*, 332:325–338, May 2002.

[50] C. Porciani, A. Dekel, and Y. Hoffman. Testing tidal-torque theory - II. Alignment of inertia and shear and the characteristics of protohaloes. *MNRAS*, 332:339–351, May 2002.

[51] F. Prada, A. A. Klypin, A. J. Cuesta, J. E. Betancort-Rijo, and J. Primack. Halo concentrations in the standard LCDM cosmology. *ArXiv e-prints*, April 2011.

[52] W. H. Press and P. Schechter. Formation of Galaxies and Clusters of Galaxies by Self-Similar Gravitational Condensation. *ApJ*, 187:425–438, February 1974.

[53] B. E. Robertson, A. V. Kravtsov, J. Tinker, and A. R. Zentner. Collapse Barriers and Halo Abundance: Testing the Excursion Set Ansatz. *ApJ*, 696:636–652, May 2009.

[54] G. Rossi, R. K. Sheth, and G. Tormen. Modelling the shapes of the largest gravitationally bound objects. *MNRAS*, 416:248–261, September 2011.

[55] G. Rossi, R. K. Sheth, and G. Tormen. Modelling the shapes of the largest gravitationally bound objects. *MNRAS*, 416:248–261, September 2011.

[56] A. Schneider, R. E. Smith, A. V. Macciò, and B. Moore. Non-linear evolution of cosmological structures in warm dark matter models. *MNRAS*, 424:684–698, July 2012.

[57] J. Shen, T. Abel, H. J. Mo, and R. K. Sheth. An Excursion Set Model of the Cosmic Web: The Abundance of Sheets, Filaments, and Halos. *ApJ*, 645:783–791, July 2006.

[58] R. K. Sheth and A. Diaferio. Peculiar velocities of galaxies and clusters. *MNRAS*, 322:901–917, April 2001.

[59] R. K. Sheth, H. J. Mo, and G. Tormen. Ellipsoidal collapse and an improved model for the number and spatial distribution of dark matter haloes. *MNRAS*, 323:1–12, May 2001.

[60] R. K. Sheth and G. Tormen. Large-scale bias and the peak background split. *MNRAS*, 308:119–126, September 1999.

[61] V. Springel. The cosmological simulation code GADGET-2. *MNRAS*, 364:1105–1134, December 2005.

[62] V. Springel, N. Yoshida, and S. D. M. White. GADGET: a code for collisionless and gasdynamical cosmological simulations. *New Astronomy*, 6:79–117, April 2001a.

[63] J. Tinker, A. V. Kravtsov, A. Klypin, K. Abazajian, M. Warren, G. Yepes, S. Gottlöber, and D. E. Holz. Toward a Halo Mass Function for Precision Cosmology: The Limits of Universality. *ApJ*, 688:709–728, December 2008.

[64] G. Tormen, L. Moscardini, and N. Yoshida. Properties of cluster satellites in hydrodynamical simulations. *MNRAS*, 350:1397–1408, June 2004.

[65] F. C. van den Bosch. The universal mass accretion history of cold dark matter haloes. *MNRAS*, 331:98–110, March 2002.

[66] C. A. Vera-Ciro, L. V. Sales, A. Helmi, C. S. Frenk, J. F. Navarro, V. Springel, M. Vogelsberger, and S. D. M. White. The shape of dark matter haloes in the Aquarius simulations: evolution and memory. *MNRAS*, 416:1377–1391, September 2011.

[67] M. S. Warren, P. J. Quinn, J. K. Salmon, and W. H. Zurek. Dark halos formed via dissipationless collapse. I - Shapes and alignment of angular momentum. *ApJ*, 399:405–425, November 1992.

[68] R. H. Wechsler, J. S. Bullock, J. R. Primack, A. V. Kravtsov, and A. Dekel. Concentrations of Dark Halos from Their Assembly Histories. *ApJ*, 568:52–70, March 2002.

[69] S. D. M. White. Violent Relaxation in Hierarchical Clustering. In O. Lahav, E. Terlevich, & R. J. Terlevich, editor, *Gravitational dynamics*, pages 121–+, 1996.

[70] S. D. M. White and J. Silk. The growth of aspherical structure in the universe - Is the Local Supercluster an unusual system. *ApJ*, 231:1–9, July 1979.

[71] Y. B. Zel'Dovich. Gravitational instability: An approximate theory for large density perturbations. *A&A*, 5:84–89, March 1970.

" I can see the bright green strip of grass beneath the wall, and the clear
blue sky above the wall, and sunlight everywhere. Life is beautiful.
Let the future generations cleanse it of all evil, oppression and violence,
and enjoy it to the full. " (L.T.)